SCIENTIFIC REPORT

2014-2020

Laboratorio

National Enterprise for nanoScience and nanoTechnology

NEST

Graphical project: A. Freccioni, D. Leccese - Scuola Normale Superiore
Editing: C. Bertini - Scuola Normale Superiore

LABORATORIO NEST

NATIONAL ENTERPRISE FOR NANOSCIENCE AND NANOTECHNOLOGY

LABORATORIO NEST

Scientific report and five-year proposal

Index

Executive summary

The present document provides a scientific, financial and institutional report of Laboratorio NEST, the National Enterprise for nanoScience and nanotechnology, for the period 2014-2020.

The report illustrates the evolution of the NEST initiative at the Scuola Normale Superiore: NEST has grown into a multi-institutional enterprise through formal long-term partnerships with Consiglio Nazionale delle Ricerche, Istituto Italiano di Tecnologia, and Scuola Superiore Sant'Anna. This evolution was motivated by the objective to make available a competitive, well-equipped, multidisciplinary research environment ideally suited to train undergraduate and graduate students in the dynamic field of nanoscience and nanotechnology. Critical mass would be impossible to reach with staff and resources from SNS only, but the multi-institution format adopted was able to achieve this goal. This will be illustrated also by providing a description of the laboratory facilities currently available at NEST.

The main research activities will be presented together with selected related publications that demonstrate the degree of success and the breadth of the scientific activities: from the bibliographical point of view, in the period here examined the number of yearly NEST citations continued to rapidly grow and proponents wish to underline also the significant growth in technology-transfer activities, industrial collaborations and patenting. Another important aspect is the continued direct involvement of SNS students in all activities and the fruitful interactions within Scuola Normale Superiore. Indeed, the impact of NEST on SNS educational activities remains one of the main indicators of success for us and will be addressed in several points, in particular by providing the complete list of students that carried out their thesis work (laurea or PhD theses) at NEST.

The foreseen evolution of NEST builds on the nanotechnological expertise acquired in these years in a broad range of fields on one side, and on the extensive modeling and theoretical knowledge accumulated on the other. We intend to align NEST goals to the emerging quantum technologies and their applications. We believe the time is ripe to collect the fruits of the knowledge developed in the laboratory and exploit nanoscience to actively tackle socially and economically relevant issues, from innovation in industry to health and environment.

1. Scientific report
2014 - 2020

Presented by

Prof. Fabio Beltram
Prof. Vittorio Giovannetti
Prof. Luigi Rolandi
Dr. Pasqualantonio Pingue

1.1 The NEST initiative

NEST, the National Enterprise for nanoScience and nanoTechnology, is an interdisciplinary research and training center where physicists, chemists and biologists investigate scientific issues at the nanoscale. This knowledge is exploited to develop innovative nanobiotechnological tools, nanoelectronic and photonic devices and architectures.

NEST is located in the San Silvestro building, the seat of Scuola Normale Superiore at the time of its foundation in 1810. Scuola Normale Superiore entered the field of nanoscience in 2001 by applying to the Istituto Nazionale per la Fisica della Materia (INFM) for the establishment of one of its centers of excellence. The proposal was selected and funded, as a result NEST was created. Since then a number of institutional changes occurred: INFM itself does not exist anymore and was absorbed by the Consiglio Nazionale delle Ricerche. Scuola Normale Superiore, however, never abandoned its target of creating a competitive center for research and training in nanoscience and nanotechnology. This objective was pursued by consistently investing in this initiative, but, even more importantly, by forming a stable network of collaborations that made NEST an attractor for other institutions that found it the ideal location to establish related and closely integrated research entities that all share the NEST "brand".

Today the NEST initiative comprises four distinct institutions: Scuola Normale Superiore, Istituto Italiano di Tecnologia, Consiglio Nazionale delle Ricerche and Scuola Superiore Sant'Anna. Although each institution has its own staff and administration (Laboratorio NEST of SNS, IIT@NEST Center for Nanotechnology Innovation of IIT, the Istituto Nanoscienze of CNR, and nanoPlant of Scuola Sant'Anna) facilities and activities are closely coordinated and scientists team up for specific scientific objectives regardless of their affiliation. An additional important institutional development is the establishment of the *Centro di Competenza Regionale sulle Nanotecnologie* at Laboratorio NEST. This was the starting point for an intense effort towards technology transfer that has brought significant results in this period in terms of collaborative contracts with industry and the establishment of NEST spin-offs.

The presence and integration of different institutions has proved a powerful asset for NEST that was able to sum resources and coordinate investments making it possible to reach a critical mass in terms of technological platforms available and sheer number of scientists working and interacting all together under the same roof. This concentration of efforts and flexibility allowed NEST scientist to address a rather broad range of experimental and theoretical research activities that span from semiconductor/superconductor nanostructure design, 3D, 2D and 1D materials growth and investigation to single-molecule studies in live cells and tissues. Just as importantly, this led to the creation of a very competitive environment that attracted significant funding from national and international funding agencies. In the period covered by this report NEST scientists were awarded six ERC (advanced, consolidator, starting) grants, 28 Horizon2020 EC-funded projects, 9 international, 25 National (Ministry of Research, Health, Economic Development), 14 Regional projects and 12 projects funded by private entities (AIRC, bank foundations etc.). This success translated into significant resources for research (over 34 million euros) and a dynamic environment, where cutting-edge research is carried out and, importantly, Scuola Normale students

are exposed to the state of the art in research themes and methods. The relevance of this should not be underestimated as it represents a crucial tool in the hands of the Scuola to ensure that its students find research and training conditions that are at the highest level and fully comparable to the best university laboratories worldwide.

In the following a selection of the research and technology-transfer activities will be presented as a means to assess the degree of success of the NEST initiative and to present what proponents believe are the solid foundations onto which the future of Laboratorio NEST is planned.

The years covered by this report saw several changes in the Scuola, but NEST managed to ensure continuity of operation and continued collaboration with all partner institutions. In this period three Scuola Normale professor acted as Directors of the Laboratory and have jointly prepared this report:

2014-2016	Fabio Beltram
2016-2018	Vittorio Giovannetti
2018-2020	Luigi Rolandi

During the whole period Dr. Pasqualantonio Pingue was the Chief Operational Officer of the Lab and participated to the redaction of this report.

1.2 People and technology platform @ NEST

The following data are relative to year 2020.

1.2.1 People at NEST

The **Scuola Normale Superiore** staff comprises:

Professors	Fabio Beltram Francesco Cardarelli Vittorio Giovannetti Giuseppe La Rocca	Stefano Luin Luigi Rolandi Alessandro Tredicucci*
Research Fellow	Francesco Rossella	
Fellowships	Matteo Agostini Rosy Amodeo Alberto Bonisoli Valeria Demontis	Gianmarco Ferri Andrea Guerrini Luca Medda Aldo Moscardini
PhD students	Federica Anastasi Gian Marcello Andolina Omer Arif Mahdi Asgari Luca Basta Federico Belliardo Mario Bernardi Gianmichele Blasi Lennart Bours Annalisa Carretta Roberta Cecchi Stefano Chessa Sara Chiarugi Gaia Ciampalini Elena Corradi Francesca D'Elia Marco Fanizza Giulia Giannone	Andrea Iorio V. O. Khaustov Farzad Kianvash Didi Lamers Ana Katrina Mapanao Francesco Margheriti Elisa Martino Giulia Matteoli Nicola Melchioni Roberta Mezzena Gabriele Nardi Giulia Piccinini Domenic Prete Chiara Schirripa Spagnolo Paolo Maria Tentori Ayush Tyagi Isha Verma Agata Zamborlin
Undergraduate students SNS/Pisa University	Annachiara Albanese Riccardo Bertini Luca Buoni Marta Cagetti Giulio Cappelli Luigi Caputo Michele Cardelli Alessio Cargioli	Federico Massarelli Chiara Massetti Jacopo Menconi Giorgio Orlandini Elisa Ottalagana Luca Palumbi Alessandro Passera Sara Passuti

	Alessia Colosimo Monica Coraggioso Davide Degli Esposti Fabio Dispinzeri Filippo Giovanni Fabozzi Letizia Ferbel Luca Fusar Bassini Lorenzo Lavista Enio Mangiacotti Niccolò Martinolli	Alessandro Porcelli Salvatore Ragusa Marco Santucci Luca Scaccini Matteo Sestini Giorgia Silvestrelli Daniele Sonaglioni Teresa Tommasini Giacomo Venturi
Other universities	Luca Monari	
Technical Staff	Pietro Barnini Franco Carillo Daniele Ercolani	Paolo Faraci Claudio Lelli Pasqualantonio Pingue
Administrative staff	Chiara Bertini	Gianluca Giannico

* on a part-time, temporary basis with an agreement with the University of Pisa

In order to assess size and diversity of the NEST community, however, it is necessary to consider the contribution from all participating institutions: the following chart provides the numbers relative all four partners: IIT, CNR, Sant'Anna, and SNS. Under "Scientists" we count professors and ricercatori.

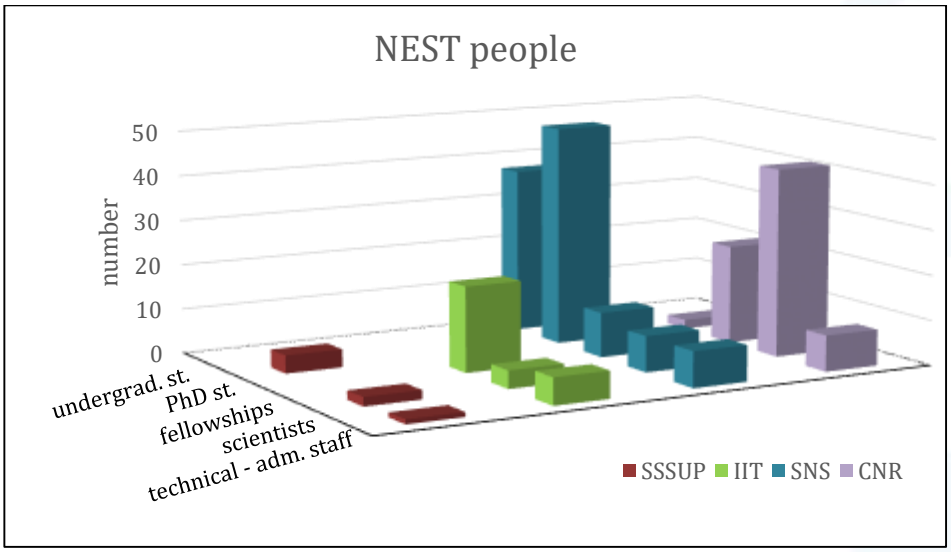

This sizable community comprises a wide variety of experiences from different disciplines and different institutions. It is instructive to see the distribution of master's degree majors in this community:

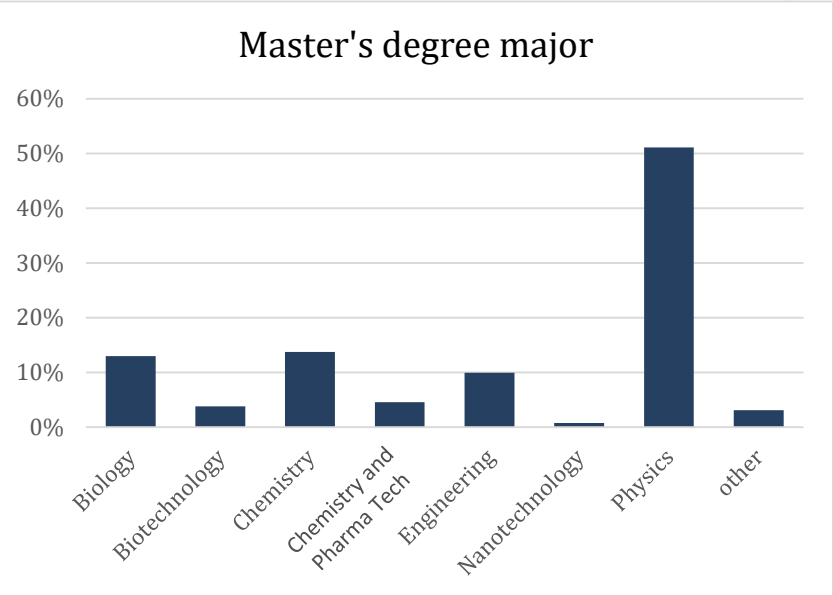

Data show that about half of the people have a (self-declared) master's degree in Physics while the rest of the people at NEST come from a wide range of disciplinary backgrounds.

1.2.2 NEST technology platform

A detailed description of each laboratory is available on the Laboratory's web site (www.laboratorionest.it/facilities), in this section floor maps with a synthetic description of the present destination of each room/laboratory are provided.

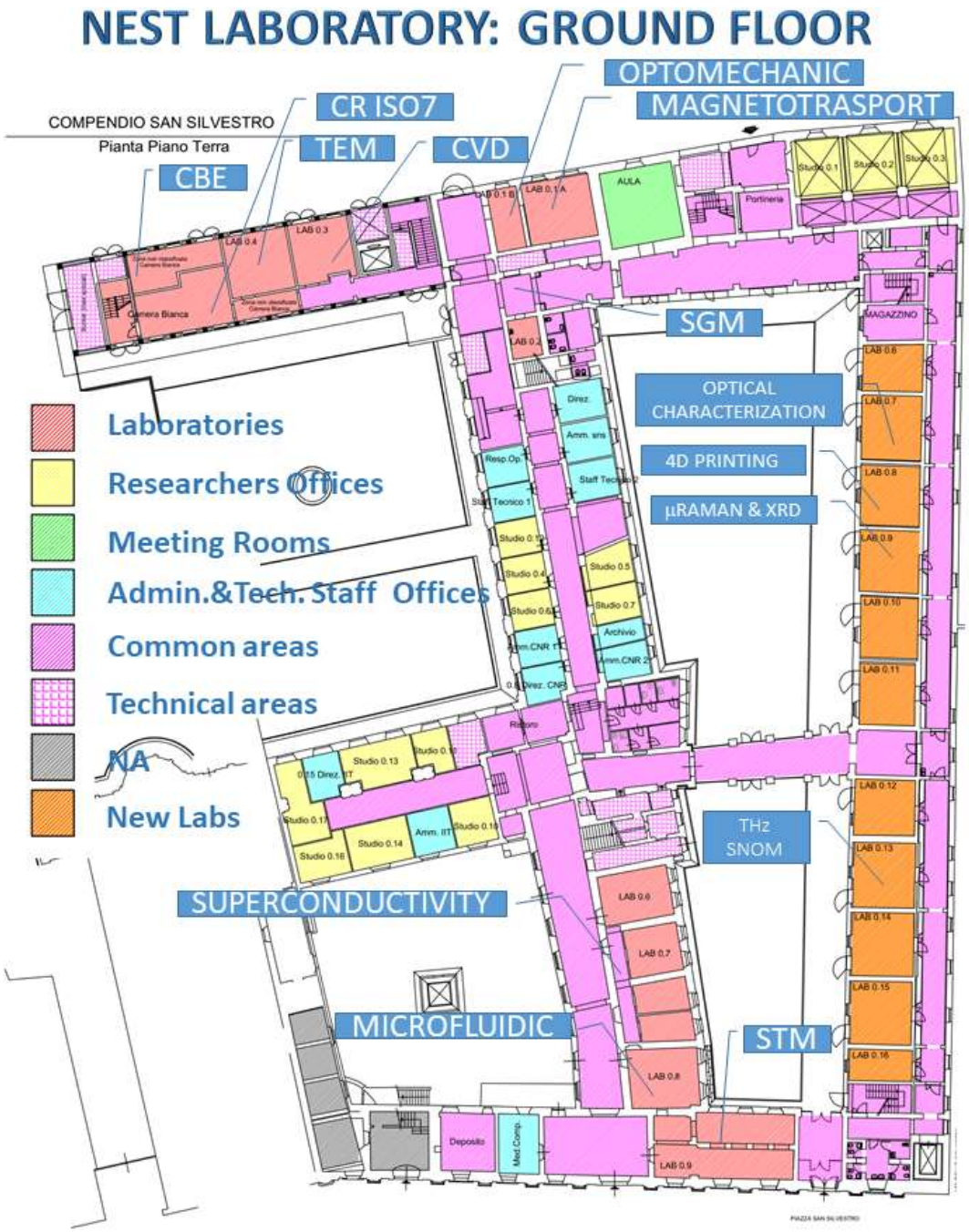

NEST LABORATORY: FIRST FLOOR

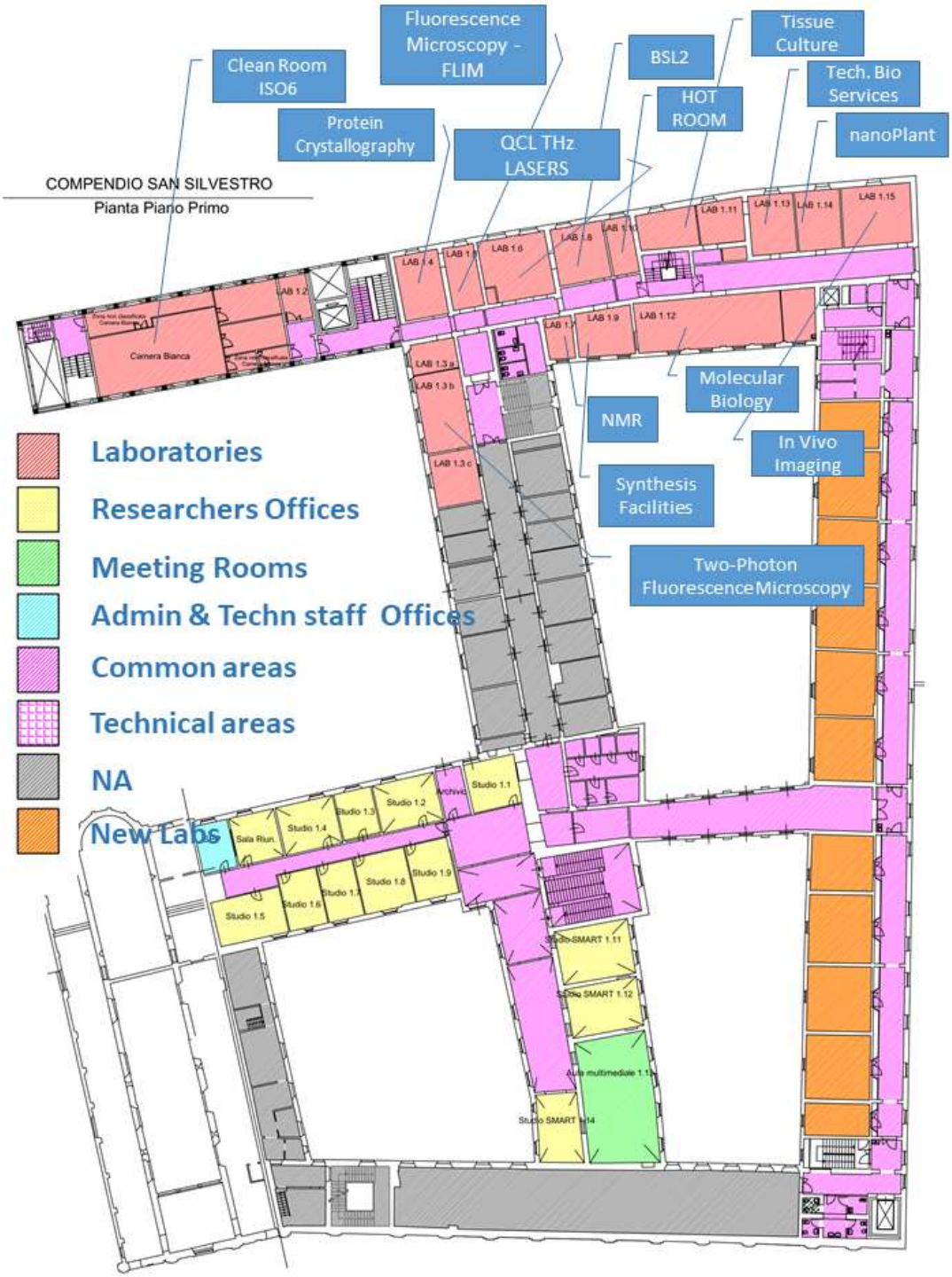

NEST LABORATORY: SECOND FLOOR

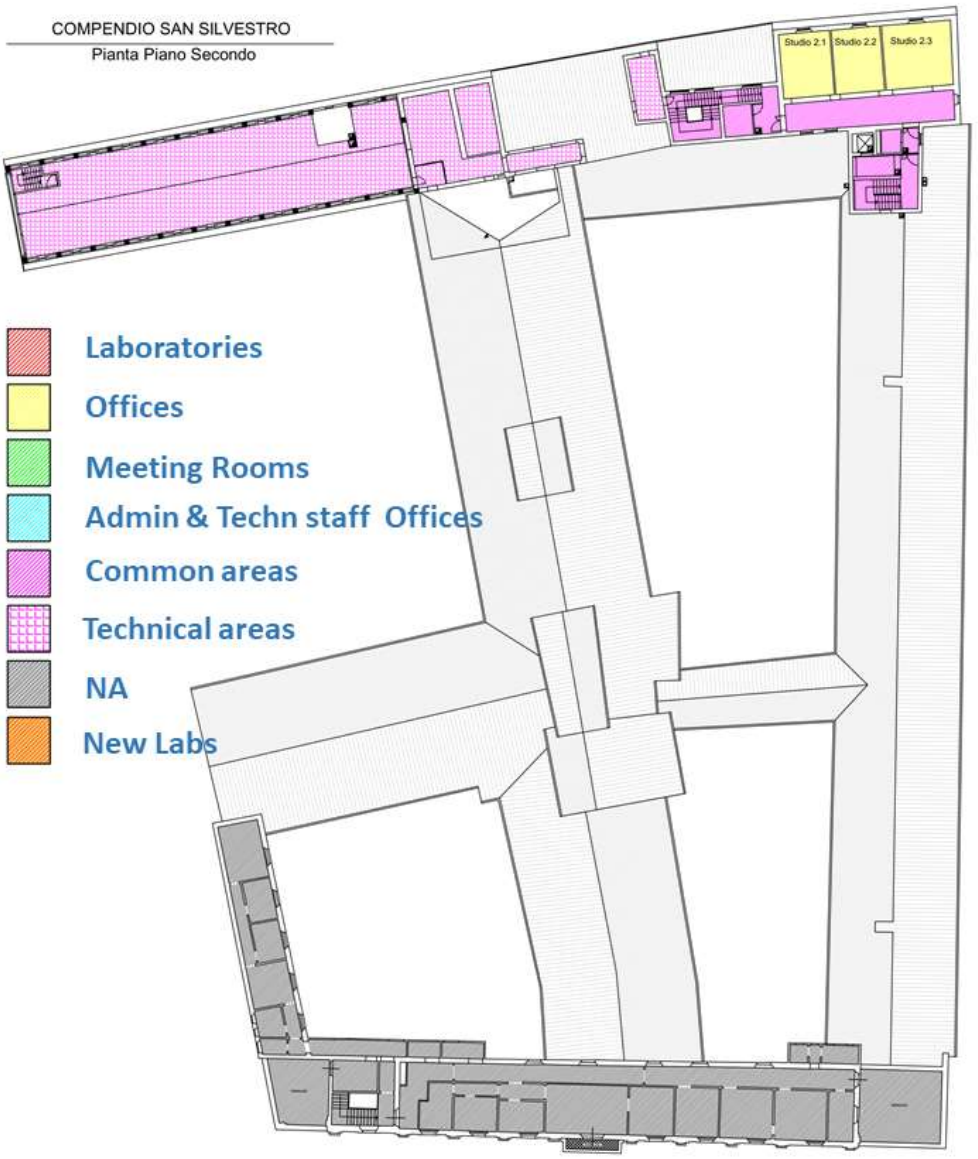

1.3 Research highlights 2014-2020

In the following sections the activities carried out within some selected research lines are reported. Each section includes the main related NEST publications that appeared in the scientific literature during the reference period.

1.3.1 Semiconductor nanowires: growth mechanisms and dynamics

Semiconductor nanowires (NWs) are strongly anisotropic single crystals that can be obtained by exploiting bottom-up growth techniques. This approach allows to obtain NWs with very high aspect ratio and also complex axial and radial heterostructures in which materials that are incompatible in standard epitaxy can be combined together with a large flexibility. These properties make NWs attractive both for fundamental studies and for device applications in the field of electronics, photonics, chemical sensing and energy conversion. NW-related activities at NEST started in 2008 with the installation of the chemical beam epitaxy laboratory dedicated to the growth of III – V semiconductor NWs. Since then, research activities have involved an increasing number of other laboratories at NEST, from the nanofabrication facilities to the transport and superconductivity labs, making NEST nowadays an important player in the international NW community.

Within the class of 1D nanostructures, semiconductor NWs possess several unique characteristics, representing one key area in nanoscience and nanotechnology [1-3]. Their very high surface-to-volume ratio makes them interesting for efficient interaction with light, energy conversion, catalysis and sensing application. Another peculiarity of semiconductor NWs is their nanometer-sized diameter, which gives the opportunity for quantum confinement of the charge carriers. Moreover, it allows an unprecedented degree of freedom in the growth of dissimilar materials in defect-free axial heterostructures, thanks to the efficient relaxation of the stress on the sidewalls. Radial heterostructures where the chemical composition of the material is modulated perpendicularly to the wire axis can also be grown. In this case, the controlled growth of one or more shells can passivate existing surface states, enable new interface properties, and introduce unique electronic, phononic and plasmonic features. In the last 5 years, NWs activities at NEST focused on two complementary fronts: (i) the progress of growth processes for the synthesis of innovative nanostructures and (ii) the development of novel devices based on NWs and related heterostructures. In this contribution we will describe the main results related to the growth activities.

At the heart of the success of NWs as versatile building blocks for nanoscience and nanotechnology is the development of a general strategy for the controlled growth of these materials. The most widespread approach for the growth of NWs is the nanoparticle (NP)-mediated growth technique known as vapor-liquid-solid (VLS) mechanism. Usually Au is used to catalyze the NW growth, because of its chemical inertness and its capability of forming liquid eutectic alloys with major semiconductor materials at the growth temperature. Au NPs can be obtained with various methods, like the annealing of Au films (Fig. 1a), dispersion of colloidal solutions and electron beam lithographic techniques. Different NP preparation methods result in different NW size distribution and areal densities, therefore the choice of the growth method is crucial for controlling NWs density, diameter, length and crystal structure, as we have demonstrated for Au-assisted InAs NWs [4, 5].

The possibility to expand the range of material combinations in defect-free heterostructures not achievable in standard thin film epitaxy is one of the most attractive properties of NWs. Some examples of axial NW heterostructures realized at NEST in the last years are GaAs/InAs NWs (Fig. 1b), InAs NWs with built-in InP barriers forming quantum dot systems within a single NW (Fig. 1c), InP NWs with embedded InAs quantum dots and quantum wells (Fig. 1d), InAs/InSb NWs (Fig. 1e).

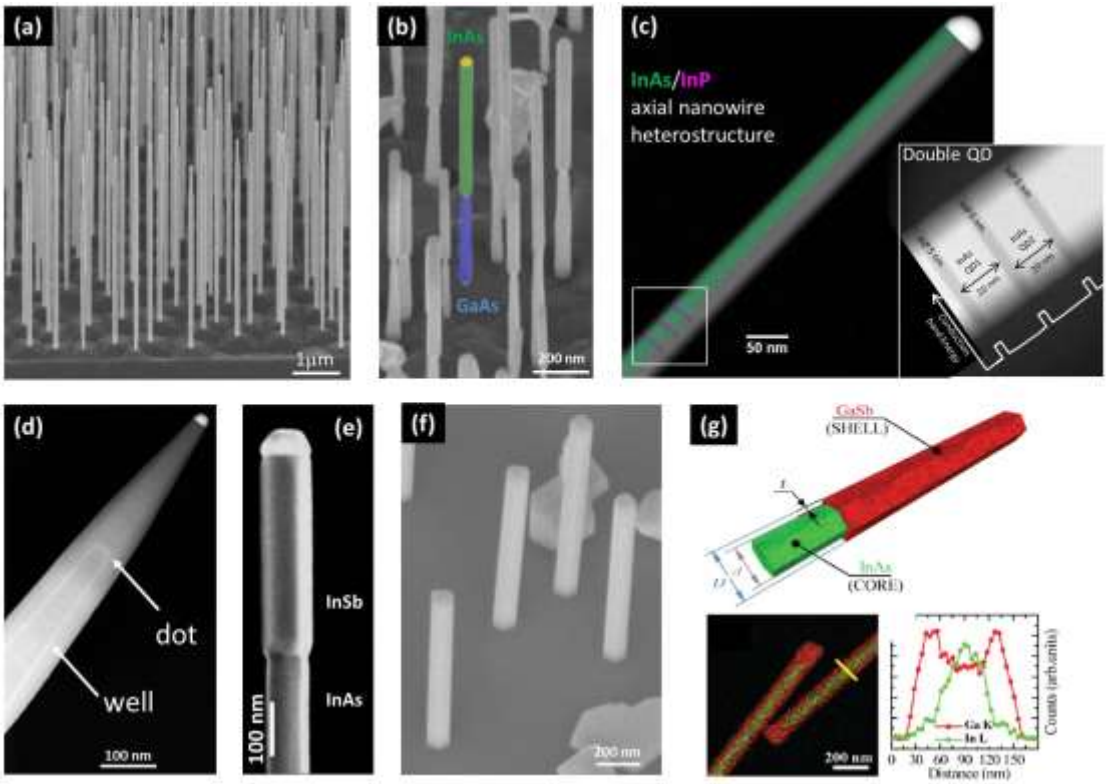

Figure 1. (a) 45°-tilted SEM image of Au-assisted InAs NWs grown on InAs(111)B substrate with 0.5 nm thick Au film. (b) 45°-tilted SEM image of GaAs/InAs axial heterostructured NWs grown on GaAs(111)B. The false-colors highlight the presence of the 2 materials in the same NW. (c) InAs NW with built-in InP barriers defining a double QD system (the inset is a STEM image of the double QD structure). (d) STEM image of a single tapered InP NW with an InAs quantum dot and well (bright contrast). (e) InAs/InSb axial heterostructured NW. (f) 45°-tilted image of catalyst-free InAs NWs grown on Si(111) substrate. (g) InAs/GaSb core/shell NWs (schematics of the single NW structure (top) and EDX elemental map and cross-sectional profile of the grown NWs (bottom).

The Au-assisted VLS growth approach allows an extremely high flexibility to grow different materials in axial NW heterostructure with very good crystal quality, size and shape control. However, the different interactions among the Au NP and the growing materials may affect the growth mode and the interface sharpness. Indeed, many axial NW heterostructures suffer from compositional gradients at the heterointerfaces and kinking or downward growth. Understanding such interactions is fundamental to achieve a full control over the morphology and the properties of the NW heterostructures. In this context, we have investigated the Au-assisted growth of GaAs/InAs and InAs/InP axial NW heterostructures and we found that the nanoparticle composition controls the growth mode and dynamics. In particular, for the straight growth of InAs segments on top of GaAs NWs, we found that the NP stability that determines the straight or downward growth is related to the change of composition of the III/Au alloy NPs at the flux commutation. Only high group III concentrations, hence large NP contact angles allow to obtain straight GaAs/InAs axial NW heterostructures [6]. Similarly, for the growth of InP segments on InAs NW stems we demonstrated that the sole parameter affecting the growth mode is the NP composition that changes at the material exchange. As a consequence, straight untapered InAs/InP NW heterostructures can be obtained only when the In/Au ratio in the NPs and hence the contact angle is kept under a certain critical value by properly choosing the

growth conditions [7]. Moreover, the NP reconfiguration at the InAs/InP switch strongly affects the growth of thin alternating InAs/InP segments. We analyzed the growth dynamics, the nucleation delay and the thickness/diameter dependence of thin alternating InAs/InP segments and we found a strategy to control the growth rate by forcing the nanoparticle reconfiguration before starting the next NW segment. This allows for the realization of InAs/InP nanowire heterostructures with a precise control over the segment thicknesses [8], essential for their implementation in quantum devices.

Despite the very good control of NWs aspect ratio and the high flexibility for the growth of NWs with the desired parameters, the Au-assisted growth may introduce the potential for unintentional incorporation of impurities degrading electronic and optical properties of the grown semiconductors and is not compatible with current CMOS technology. Consequently, Au-free techniques for the growth of III–V NWs are required to overcome these challenges. For this purpose, in the last few years we have developed two different strategies for the Au-free growth of InAs NWs on silicon substrates: the so-called catalyst-free and self-catalyzed growth. In the first case the NWs are grown without any NP (Fig. 1f). We have investigated experimentally and theoretically the heterogeneous nucleation and the growth mechanism of InAs NWs on Si(111), finding that surface defects, whose density can be controlled by the substrate preparation technique, act as nucleation sites and that the growth conditions (temperature and precursor fluxes) play a major role in driving the anisotropic NW growth and determining the final NW aspect ratio [9, 10]. In the second approach, Indium NPs are generated by using In-rich growth conditions and used to drive the NW growth via the VLS mechanism [11]. Also, in this case we have described the growth with a theoretical model that allowed us to extract relevant growth parameters, providing useful guidelines to rationally control the growth of Au-free InAs NWs for various applications.

Catalyst-free NWs are particularly suitable for the realization of radial heterostructures (core-shell NWs) because the axial growth can be almost completely suppressed and the radial growth enhanced by properly choosing the growth conditions. In this context, a very interesting material system consists of InAs/GaSb core/shell NWs (Fig. 1 g). InAs and GaSb have a very low lattice mismatch (0.6%), broken-gap band alignment (type-II) and small effective masses of electrons and holes in InAs and GaSb regions, respectively. Indeed, electronic devices fabricated with these heterostructures combine closely-spaced n-type and p-type conductors, and can display negative differential resistance due to transport across the broken gap junction, as we have demonstrated in [12].

References

[1] M. Law, J. Goldberger, P. Yang, *Semiconductor nanowires and nanotubes*, Annual Review of Materials Research **34**, 83 (2004).

[2] C.M. Lieber, *Semiconductor nanowires: a platform for nanoscience and nanotechnology*, 3rd international nanoelectronics conference (INEC), 5 (2010).

[3] N.P. Dasgupta, J. Sun, C. Liu, S. Brittman, S.C. Andrews, J. Lim, H. Gao, R. Yan, P. Yang, *Semiconductor Nanowires – Synthesis, Characterization, and Applications*, Advanced materials **26**, 2137 (2014).

[4] U.P. Gomes, D. Ercolani, V. Zannier, F. Beltram, L. Sorba, *Controlling the diameter distribution and density of InAs nanowires grown by Au-assisted methods*, Semiconductor science and technology **30**, 115012 (2015).
[5] V.G. Dubrovskii, N.V. Sibirev, Y. Berdnikov, U.P. Gomes, D. Ercolani, V. Zannier, L. Sorba, *Length distributions of Au-catalyzed and In-catalyzed InAs nanowires*, Nanotechnology **27**, 375602 (2016).
[6] V. Zannier, D. Ercolani, U.P. Gomes, J. David, M. Gemmi, V.G. Dubrovskii, L. Sorba, *Catalyst Composition Tuning: The Key for the Growth of Straight Axial Nanowire Heterostructures with Group III Interchange*, Nano Letters **16**, 7183 (2016).
[7] V. Zannier, F. Rossi, V.G. Dubrovskii, D. Ercolani, S. Battiato, L. Sorba, *Nanoparticle Stability in Axial InAs–InP Nanowire Heterostructures with Atomically Sharp Interfaces*, Nano Letters **18**, 167 (2018).
[8] V. Zannier, F. Rossi, D. Ercolani, L. Sorba, *Growth dynamics of InAs/InP nanowire heterostructures by Au-assisted chemical beam epitaxy*, Nanotechnology **30**, 094003 (2019).
[9] U.P. Gomes, D. Ercolani, V. Zannier, S. Battiato, E. Ubyivovk, V. Mikhailovskii, Y. Murata, S. Heun, F. Beltram, L. Sorba, *Heterogeneous nucleation of catalyst-free InAs nanowires on silicon*, Nanotechnology **28**, 065603 (2017).
[10] U.P. Gomes, D. Ercolani, N.V. Sibirev, M. Gemmi, V.G. Dubrovskii, F. Beltram, L. Sorba, *Catalyst-free growth of InAs nanowires on Si (111) by CBE*, Nanotechnology **26**, 415604 (2015).
[11] U.P. Gomes, D. Ercolani, V. Zannier, J. David, M. Gemmi, F. Beltram, L. Sorba, *Nucleation and growth mechanism of selfcatalyzed InAs nanowires on silicon*, Nanotechnology **27**, 255601 (2016).
[12] M. Rocci, F. Rossella, U.P. Gomes, V. Zannier, F. Rossi, D. Ercolani, L. Sorba, F. Beltram, S. Roddaro, *Tunable Esaki Effect in Catalyst-Free InAs/GaSb Core–Shell Nanowires*, Nano Letters **16**, 7950 (2016).

1.3.2 Quantum transport in semiconductor nanowires

Semiconductor nanowires (NWs) are strongly anisotropic single-crystalline nanostructures that can be grown using a bottom-up approach. This class of nanostructures can embed complex axial and radial heterostructures with materials that would be rather hard to combine in standard epitaxy owing to excessive lattice mismatch. This design flexibility offers a set of unique opportunities for the investigation and exploitation of quantum transport phenomena at the nanoscale. Since 2008, research efforts have focused on advanced single-electron systems based on InAs/InP NWs, on which now the NEST has a well-established expertise and a variety of national and international collaborations. More recently, activities have included the investigation of hybrid systems combining superconductive elements and semiconductor NWs for the investigation of coherent-transport phenomena and topological phase transitions

1. Quantum heterostructures

The quantum behavior of electrons in NWs can be controlled and tailored by designing suitable axial and/or radial heterostructures. Radial heterostructures offer a very promising research direction and have been used to implement bipolar nanodevices where an electron and hole system can coexist within a few nanometers. Historically, these systems have notoriously been rather hard to implement, but can be naturally obtained in a NW embedding a radial broken-gap InAs/GaSb heterojunction [5], as sketched in Fig.1a. We demonstrated NW architectures where the core and the shell can be separately contacted, as visible in the scanning electron microscope (SEM) picture in Fig.1b. In these devices, the voltage-dependent interband tunneling between InAs and GaSb gives rise to a marked negative differential resistance, see Fig. 2c. The achievement of closely spaced electron and hole systems in NWs also provides a very promising workbench for the investigation of interactions in low dimensions and of bipolar thermoelectric phenomena.

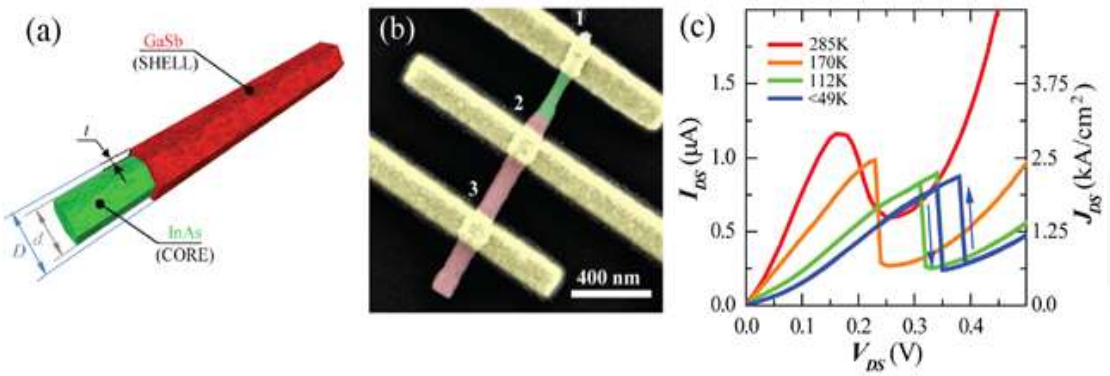

Figure 1. (a) Sketch of a radially heterostructured NW embedding a broken-gap GaSb/InAs junction. (b) Scanning electron micrograph of one of the studied devices, which integrate independent contacts to both the core (green) and shell (red) of the nanostructure. (c) Radial conduction displays a marked negative differential resistance, providing a clear fingerprint of bipolar transport through the broken gap heterojunction. From [5].

A different class of heterostructured NWs we studied includes axial InAs/InP systems, which are particularly promising for the creation of strongly confined quantum dot systems and clean tunnel barriers. Following the ground-breaking research carried out at NEST during the past years, recent activities focused on the adoption of these systems as active elements in different contexts such as microwave (MW) resonators [1], nanoscale thermoelectricity and electron tunneling spectroscopy.

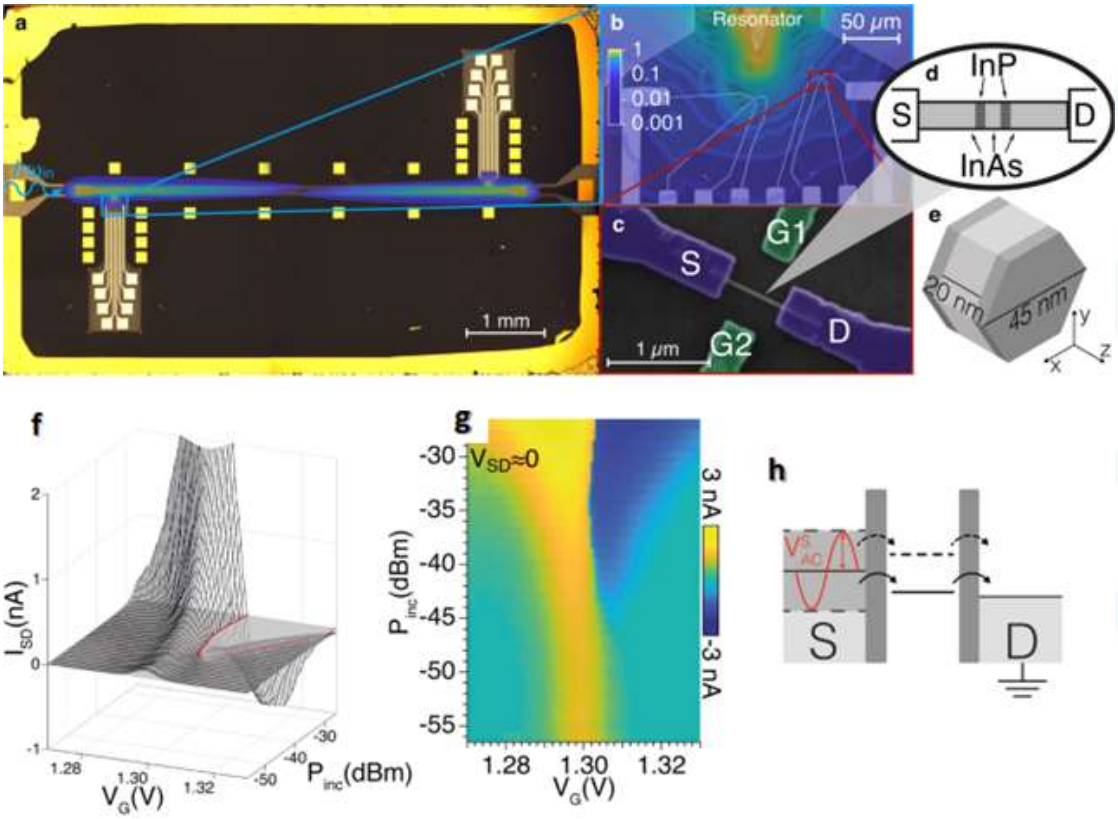

Figure 2. (a) Optical overview of the full device including InAs/InP NWs and an YBCO/sapphire coplanar resonator. (b) and (c) SEM close-up of the antenna tip and of the NW device. False colors in panels (a) and (b) represent the numerically simulated electric field strength of the fundamental resonator mode (normalized to the maximum value). (d) Schematic diagram of the InAs/InP NW QD. (e) Sketch of the NW QD showing InAs (light grey) and InP (dark grey) sections. (f) and (g) Evolution of the $I_{SD}(V_G)$ characteristics in the presence of a microwave drive of frequency ω_0 and increasing power P_{inc}. Three dimensional plots and maps are plotted for gate voltage around V_G=1.30 V at the temperature T = 2K. Solid lines indicate the contour of regions with negative I_{SD}. (h) Energy diagrams illustrating the MW-assisted tunneling through the dot levels ε′ and ε″.

2. Hybrid nanowire-based devices

The most common material choice in NW-based transport experiments is InAs, since this semiconductor material displays a favorable pinning of the Fermi energy at the surface of the nanostructure, leading to a natural electron population despite the very small dimension of the NW. For the same reason, NWs are very promising for the creation of hybrid devices where superconductive elements are coupled to the nanostructure via transparent tunnel junctions. An important part of NW transport activities focused on the investigation of Josephson coupling between NWs and different superconductors such as Al [6] and Pb [4], see Fig.3a and 3b. Activities targeted first of all the fundamental investigation of proximity effect in NWs, but highlighted potential applications of these systems in the context of topological quantum computation [6]. In view of this perspective, a crucial ingredient is spin-orbit interaction, which is rather strong in In-based nanowires. Selected activities have thus also targeted the study of the still not fully understood nature of spin-orbit interaction in InAs nanowires, and in particular of its dependence on external electric fields induced by field-effect electrodes [2], see Fig.3c-3h. A further crucial ingredient for the implementation of a reliable quantum technology is of course electron cooling. A very intriguing possibility consists in exploiting quantum phenomena such as tunneling between different

materials such as superconductors and semiconductors to directly cool electrons in the active region of a quantum device, as well-established in the case of metallic nanostructures and recently demonstrated by us in a set of experiments on tunnel-coupled Al-InAs NW devices [3].

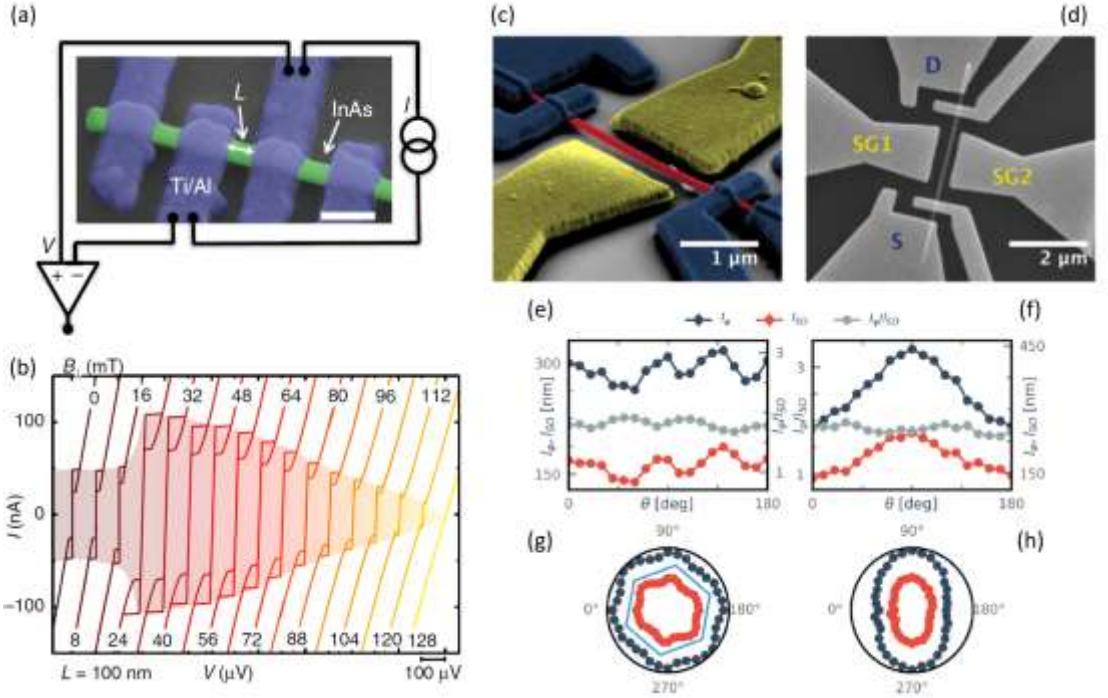

Figure 3. (a) Typical hybrid device for the investigation of proximity effects in InAs nanowires. (b) Magnetic field enhancement of the supercurrent through an Al-InAs-Al Josephson nanojunction. (c) and (d) Scanning electron micrograph of a suspended nanowire structure for the investigation of the field-effect dependence of spin-orbit interaction in InAs nanowires. Vectorial dependence of transport parameters extracted from weak localization/antilocalization data as a function of the orientation of the electric field applied to the suspended nanowire. From [2, 6].

References

[1] S. Cornia, F. Rossella, V. Demontis, V. Zannier, F. Beltram, L. Sorba, M. Affronte, A. Ghirri, *Microwave-Assisted Tunneling in Hard-Wall InAs/InP Nanowire Quantum Dots*, Scientific Reports **9**, 19523 (2019).

[2] A. Iorio, M. Rooci, L. Bours, M. Carrega, V. Zannier, L. Sorba, S. Roddaro, F. Giazotto, E. Strambini, *Vectorial Control of the Spin-Orbit Interaction in Suspended InAs Nanowires*, Nano Letters **19**, 652657 (2019).

[3] J. Mastomaki, S. Roddaro, M. Rocci, V. Zannier, D. Ercolani, L. Sorba, I.J. Maasilta, N. Ligato, A. Fornieri, E. Strambini, F. Giazotto, *InAs nanowire superconducting tunnel junctions: Quasiparticle spectroscopy, thermometry, and nanorefrigeration*, Nano Research **10**, 3468 (2017).

[4] J. Paajaste, M. Amado, S. Roddaro, F.S. Bergeret, D. Ercolani, L. Sorba, F. Giazotto, *Pb/InAs Nanowire Josephson Junction with High Critical Current and Magnetic Flux Focusing*, Nano Letters **15**, 1803 (2015).

[5] M. Rocci, F. Rossella, U.P. Gomes, V. Zannier, F. Rossi, D. Ercolani, L. Sorba, F. Beltram, S. Roddaro, *Tunable Esaki Effect in Catalyst-Free InAs/GaSb Core-Shell Nanowires*, Nano Letters **16**, 7950 (2016).

[6] J. Tiira, E. Strambini, M. Amado, S. Roddaro, P. San-Jose, R. Aguado, F.S. Bergeret, D. Ercolani, L. Sorba, F. Giazotto, *Magnetically-driven colossal supercurrent enhancement in InAs nanowire Josephson junctions*, Nature Communications **8**, 14984 (2017).

1.3.3 Subwavelength light control with semiconductor nanowires

Semiconductor nanostructures with large dielectric constant and high aspect ratio such as nanowires (NWs) represent a formidable playground for the study of the light-matter interaction as well as for nanophotonic, nano-optic and nanoplasmonic applications. The manipulation of light below the diffraction limit enabled by the use of semiconductor NWs attracts much attention owing to its potential impact on sensing and microscopy, as well as on computation and communication technologies. Here we report in brief our recent achievements in demonstrating semiconductor nanowire–based systems and devices for subwavelength light emission, scattering, guiding and reflection.

Building on our expertise in the InAs/InP NW growth technology we engineered InP-InAs-InP multi-shell NWs that behave as polychromatic emitters in the energy range from 0.7 to 1.6 eV [1]. The photoluminescence (PL) emission from these individual nanostructures displays different features ascribable to distinct emitting domains, including InAs quantum dot and quantum well, as well as crystal-phase quantum disks arising from the coexistence of InP zincblende (ZB) and wurtzite (WZ) segments in the same NW. These crystal-phase low-dimensional structures offer great potential for the implementation of photonic devices of interest for quantum information processing. In this context, we reported on the anisotropy of the g-factor tensor and diamagnetic coefficient in WZ/ZB crystal-phase quantum dots (QDs) realized in single InP nanowires (Fig. 1) [2]: the electron (hole) g-factor tensor and the exciton diamagnetic coefficients were determined through micro-PL measurements at 4.2 K with different magnetic field configurations, and rationalized by invoking the spin-correlated orbital current model. Overall, our single NW emitters can find applications as optically active components in nanodevices for quantum information and communication technologies.

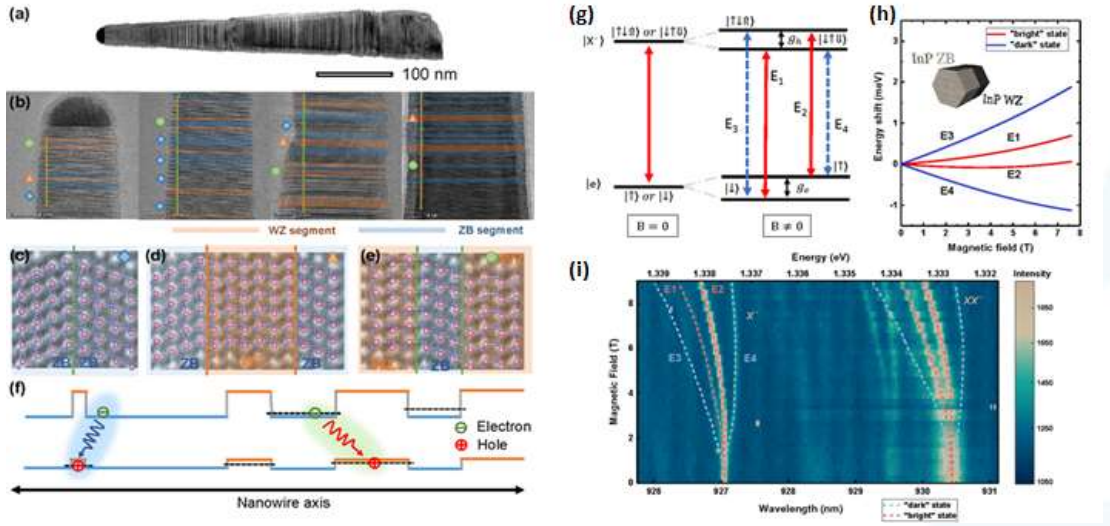

Figure 1. (a) Dark field STEM image of a mixed WZ/ZB InP NW. **(b)** STEM-HAADF images of different InP NW segments. Different symbols correspond to different structures depicted in Fig. **(c)-(e)**, where the ball-and-stick model of different segments and atomic resolution STEM images are reported. **(f)** Schematic energy level of the WZ/ZB sequence in the InP NW. **(g)** Energy diagram of the negatively-charged-exciton with B perpendicular to the growth axis. **(h)** Energy shift of the four possible transitions of charged exciton, as a function of B. **(i)** Magneto-PL spectra of X^- and XX^- with $B_{\text{out-of-plane}}$ from 0 to 9 T.

Besides, we engineered individual semiconductor nanowire devices that allowed us to demonstrate a novel technique for the realization of subwavelength light sources operating at 1 GHz [3]. Light sources with nanoscale emission spots are regarded as an alternative tool to aperture-based near-field optical systems for the implementation of microscopy techniques not subjected to the diffraction limit. We realized hybrid metal-GaAs nanowire devices by controlled thermal annealing of Ni/Au electrodes, and investigated the metallic phases observed in the nanostructure body. Devices were fabricated onto a SiN membrane compatible with transmission electron microscopy studies. Energy dispersive X-ray spectroscopy allowed us to show that the nanowire body includes two Ni-rich phases, that thanks to an innovative use of electron diffraction tomography were unambiguously identified as Ni3GaAs and Ni5As2 crystals [4]. Using the annealing technique, we prepared hybrid metal−GaAs nanowires embedding two sharp axial Schottky barriers acting as nanoscale point-sources of light. Visible-light electroluminescence was reported upon suitable voltage biasing of the junctions. We investigated the time-resolved emission properties of our devices and demonstrated an electrical modulation of light generation up to 1 GHz. We explored different drive configurations and discussed the intrinsic bottlenecks of the presented device architecture. Our results demonstrated a novel technique for the realization of fast subwavelength light sources, with possible applications in sensing and microscopy beyond the diffraction limit.

Another research activity focused on mesoscale and nanoscale systems with a topology characterized by bends or crossings - such as *V*-, *T*- or *Y*-shaped, crosswise or multi-armed structures – that provide a fascinating playground for the study of guiding and interference phenomena. We focused on individual multibranched SnO_2 nanostructures with "nodes" i.e. locations where two or more branches originate, and we studied how light propagates when a laser source is focused onto a node [5]. Combining scanning electron microscopy (SEM) and optical analysis along with Raman and Rayleigh scattering, we unveil the mechanism behind the light-coupling occurring at the node.
Moreover, we proved localization and field-effect control of the plasmonic resonance in semiconductor nanostructures with a spatial resolution of 20 nm. The coupling between light and collective electron density oscillations (plasmons) is exploited by nanoplasmonics to bypass the stringent limits imposed by diffraction, enabling confinement of light to subwavelength volumes. We demonstrated localization and field-effect control of the plasmon resonance in semiconductor NWs with a spatial resolution of 20 nm [6], using scattering-type scanning near-field optical microscopy in the mid-infrared region (Fig. 2). To this aim, we adopted InAs NWs embedding a graded doping profile to modulate the free carrier density along the axial direction. Our near-field measurements had a spatial resolution of 20 nm and demonstrated the presence of a local resonant feature whose position was controlled by a back-gate bias voltage. In our implementation, the field-effect induces a modulation of the free carrier density profile yielding a spatial shift of the plasmon resonance of the order of 100 nm. The relevance of our electrically tunable nanoplasmonic architectures was discussed in view of innovative optoelectronic devices concepts.

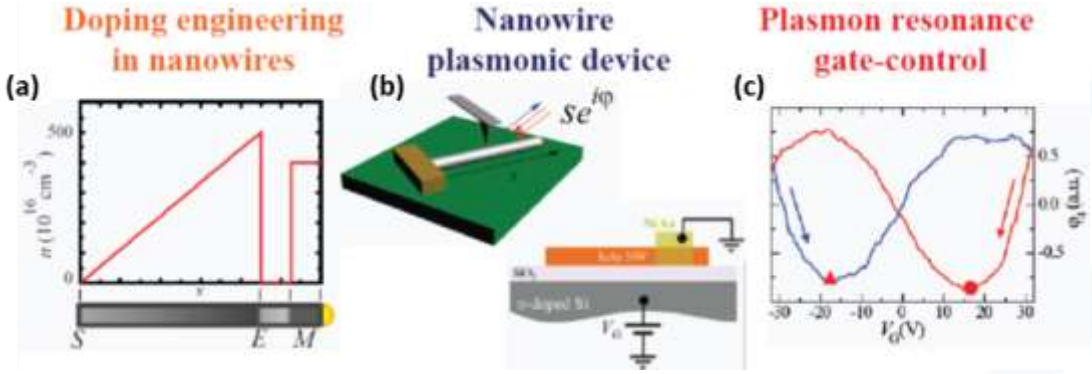

Figure 2. (a) We created a linear modulation of the carrier density profile *n(x)* as a function of the axial position *x* along an InAs nanowire. The induced density ranges from a nominally undoped value $n \approx 1 \times 10^{16}$ cm^{-3} (in the position labeled by the letter S) to a maximum doping $n \approx 5 \times 10^{18}$ cm^{-3} (in the position labeled by the letter E). An intermediate-doping segment was introduced in the growth sequence and used as marker (M) for the s-SNOM maps. The resulting graded-doping NW is sketched at the bottom of the diagram: the gray color modulation reflects the amount of doping in the NW body (with dark gray meaning high carrier concentration), while the yellow half sphere represents the metallic (Au) tip of the NW. **(b)** NWs were deposited on a SiO_2/Si substrate and contacted by a Ni/Au electrode. The bulk silicon was degenerately n-doped and thus can act as a back-gate upon application of a bias voltage, V_G (cross-sectional sketch), provided that a ground reference is set for the NW. A $\lambda = 10.5$ μm laser beam (red arrows) is focused on an s-SNOM tip oscillating at 250 kHz. The laser impinging on the tip was vertically polarized with the wave vector forming an angle of 30° with the surface of the NW. **(c)** The amplitude *s* and phase φ of the reflected beam (blue arrow) are detected using an interferometric pseudoheterodyne technique, demodulated at the fourth harmonic of the tip tapping frequency and used to reveal the local dielectric response of the NW. Phase modulation was achieved as a function of the gate voltage V_G. A strong hysteresis was observed by sweeping the gate voltage from low to high values (blue curve) and back (red curve).

Finally, we demonstrated that arrays of scatterers with subwavelength size and periodicity enable light manipulation and an extraordinary control of the light-matter interaction at the nanoscale. We proposed ensembles of subwavelength NWs – homogeneous as well as heterostructured - as an effective medium for light manipulation in reflection geometry [7,8]. We demonstrated that random assemblies of vertically aligned InAs NWs and core–shell GaAs–AlGaAs NWs display an optical response dominated by periodic modulations of the polarization-resolved reflected light as a function of the incident angle (Fig. 3). Numerical simulations clearly link the observed oscillatory effects to the semiconductor materials and the morphological features – e.g. the core and shell thickness and the tapering - of the nanostructures. Our results suggest the use of III-V NW arrays as optical meta-mirrors with perspective for sensing applications.

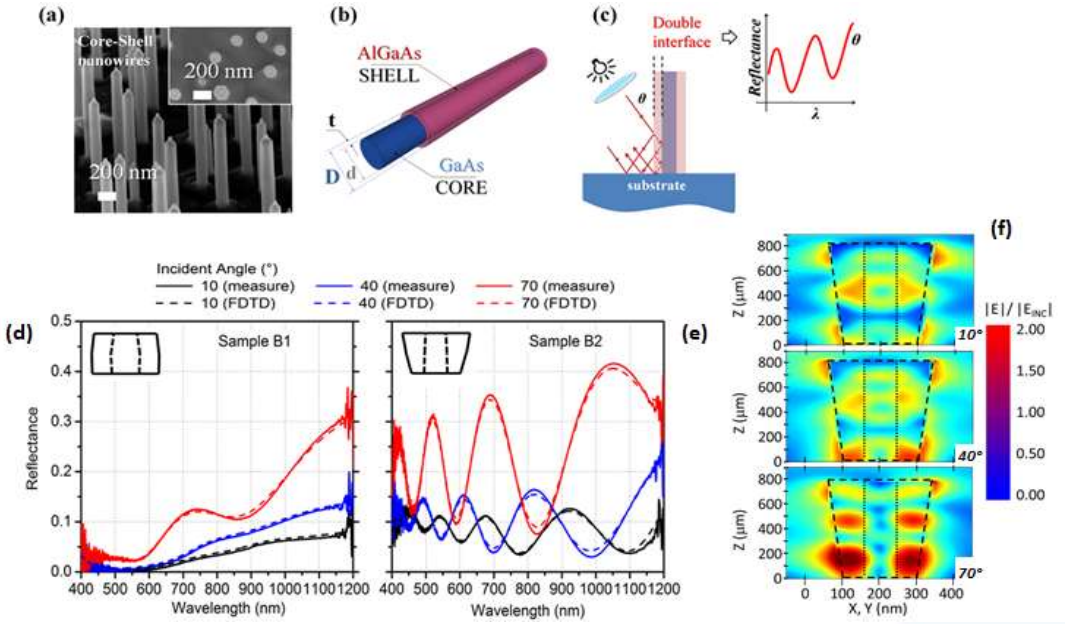

Figure 3. (a) 45° tilted SEM image of GaAs-AlGaAs core-shell (C-S) NWs. **(b)** Sketch of a C-S NW. **(c)** Shining light onto the lateral surface of a C-S NW. Measured (solid line) and simulated (dashed line) reflectance for a **(d)** non-tapered and **(e)** tapered C-S NW sample. **(f)** Near-field normalized electric field expansion for tapered C-S sample (incident angle is indicated).

References

[1] S. Battiato, S. Wu, V. Zannier, A. Bertoni, G. Goldoni, A. Li, S. Xiao, X.D. Han, F. Beltram, L. Sorba, X. Xu, F. Rossella, *Polychromatic emission in a wide energy range from InP-InAs-InP multi-shell nanowires*, Nanotechnology **30**, 194004 (2019).

[2] S. Wu, K. Peng, S. Battiato, V. Zannier, A. Bertoni, G. Goldoni, X. Xie, J. Yang, S. Xiao, C. Qian, F. Song, S. Sun, J. Dang, Y. Yu, F. Beltram, L. Sorba, A. Li, B. Li, F. Rossella, X. Xu, *Anisotropies of the g-factor tensor and diamagnetic coefficient in crystal-phase quantum dots in InP nanowires*, Nano Research **12**, 2842 (2019).

[3] F. Rossella, V. Piazza, M. Rocci, D. Ercolani, L. Sorba, F. Beltram, S. Roddaro, *GHz Electroluminescence Modulation in Nanoscale Subwavelength Emitters*, Nano Lett. **16**, 5521 (2016).

[4] J. David, F. Rossella, M. Rocci, D. Ercolani, L. Sorba, F. Beltram, M. Gemmi, S. Roddaro, *Crystal Phases in Hybrid Metal–Semiconductor Nanowire Devices*, Nano Lett. **17**, 2336 (2017).

[5] F. Rossella, V. Bellani, M. Tommasini, U. Gianazza, E. Comini, C. Soldano, *3D Multi-branched SnO2 semiconductor nanostructures as optical waveguides*, Materials **12**, 3148 (2019).

[6] A. Arcangeli, F. Rossella, A. Tomadin, J. Xu, D. Ercolani, L. Sorba, F. Beltram, A. Tredicucci, M. Polini, S. Roddaro, *Gate-Tunable Spatial Modulation of Localized Plasmon Resonances*, Nano Lett. **16**, 5688 (2016).

[7] F. Floris, L. Fornasari, A. Marini, V. Bellani, F. Banfi, S. Roddaro, D. Ercolani, M. Rocci, F. Beltram, M. Cecchini, L. Sorba, F. Rossella, *Self-Assembled InAs Nanowires as Optical Reflectors*, Nanomaterials **7**, 400 (2017).

[8] F. Floris, L. Fornasari, V. Bellani, A. Marini, F. Banfi, F. Marabelli, F. Beltram, D. Ercolani, S. Battiato, L. Sorba, F. Rossella, *Strong modulations of optical reflectance in tapered core-shell nanowires*, Materials **12**, 3572 (2019).

1.3.4 Quantum Hall effect in hybrid Josephson junctions

Quantum transport in two-dimensional electron systems was investigated at low temperatures and in high magnetic fields. Weak localization and the quantum Hall effect were studied in various material systems. Recently we also studied proximity effect in hybrid semiconductor-superconductor Josephson junctions, a powerful platform where intriguing topological properties can be investigated. Our findings demonstrate the potential of these hybrid devices to investigate the coexistence of superconductivity and quantum Hall effect and constitute the first step in the development of new device architectures hosting topological states of matter.

The study of two-dimensional (2D) electron systems represents a milestone in building solid-state nanodevices for applications in quantum technology. Starting from conventional semiconducting heterostructures, based on III-V compounds, an increasing number of novel 2D materials is investigated, both to explore fundamental physics and to develop new applications with potential impact on the future market. Mechanical exfoliation indeed allows for the fabrication of monolayer-thin devices ranging from a single 2D layer, like graphene and its van der Waals relatives, to multilayer systems with different and tunable properties while changing the number of layers. Although in all these systems electrons are confined in two spatial dimensions, very different properties can be observed, depending on the specific material and its band structure. Indeed, while in semiconducting heterostructures charge carriers behave as conventional electrons with parabolic bands, in graphene they obey a linear dispersion relation resembling the physics of relativistic Dirac fermions. Another emerging layered material, black phosphorus (bP), shares some aspects with graphene in the 2D monolayer configuration, but with important differences, that pave the way to new devices and potential applications. These differences stem from the peculiar and anisotropic shape of the bP band structure, which affects both its electronic and optical properties.

Low-temperature measurements allow investigating a large variety of quantum phenomena in these materials. For instance, quantum Hall physics emerges in the presence of a strong perpendicular magnetic field, with the formation of Landau levels (LLs) and the simultaneous coexistence of insulating bulk and metallic one-dimensional channels. The precise structure of LLs is influenced by the nature of the material hosting the 2D electron system, and the topologically protected edge states, chirally propagating along the border of the sample, inherit peculiar features.

Work at NEST aims at addressing the physics of novel 2D materials with special emphasis on new and intriguing quantum properties. To this end, we use state-of-the-art fabrication techniques and low-temperature magneto-transport measurements in combination with advanced microscopy techniques, such as scanning probe and scanning gate microscopy (SGM). These activities are supported by theoretical predictions and proper modelling of experimental data, and benefit from national and international collaborations. SGM represents a unique tool combining both high lateral resolution and quantum transport techniques, which allowed e.g. to unequivocally detect localized charged structures and their position with respect to quantum point contacts (QPCs)

properly patterned on the sample. This resulted in the unambiguous detection of the 0.7 anomaly, directly observed from SGM maps [1].

Moreover, by low-temperature magneto-transport experiments, weak localization was recently observed in graphene [2,3] and bP [4], in excellent agreement with theoretical predictions, from which characteristic scattering lengths could be inferred. The temperature dependence of the phase coherence length in bP decreases weaker than expected for two dimensions, with a power law closer to what expected for quasi-onedimensional systems like nanowires or carbon nanotubes. This peculiar character can be ascribed to the highly anisotropic nature of the puckered honeycomb crystal structure of bP [4,5]. We have as well observed the effects of the highly anisotropic structure of bP in the high-field longitudinal magnetoresistance, complemented by polarized Raman spectroscopy measurements [6].

Research also focused on innovative 2D materials and their combinations. We have reported the first experimental study of graphene transferred on β-Si_3N_4(0001) and provided a comprehensive quantitative understanding of the physics of ultrathin Si_3N_4 as a gate dielectric for graphene-based devices [7]. Furthermore, quantum transport data in single-crystal CVD graphene samples showed more than 12 flat and discernible half-integer quantum Hall plateaus on both the electron and hole sides of the Dirac point [3]. We have also reported on a buried split-gate architecture with this material. The control of the edge trajectories in these graphene-based devices is demonstrated by the observation of various fractional quantum resistances, as a result of a controllable inter-edge scattering [8]. These ideas have very recently found an application in quantum metrology as a programmable resistance standard based on a cascaded quantum Hall bisection scheme [9].

This architecture results particularly useful and unique in view of direct imaging via SGM, since graphene constitutes the topmost layer of the device [8,10]. As shown in Fig. 1, we found evidence of the backscattering of quantum Hall edge channels in a narrow graphene Hall bar, induced by the gating effect of the conducting tip of the SGM [10]. We demonstrated full control over the edge channels and were able, because of the spatial variation of the tip potential, to separate copropagating edge channels in the Hall bar, creating junctions between regions of different charge carrier density, that have not been observed before in devices based on top or split gates.

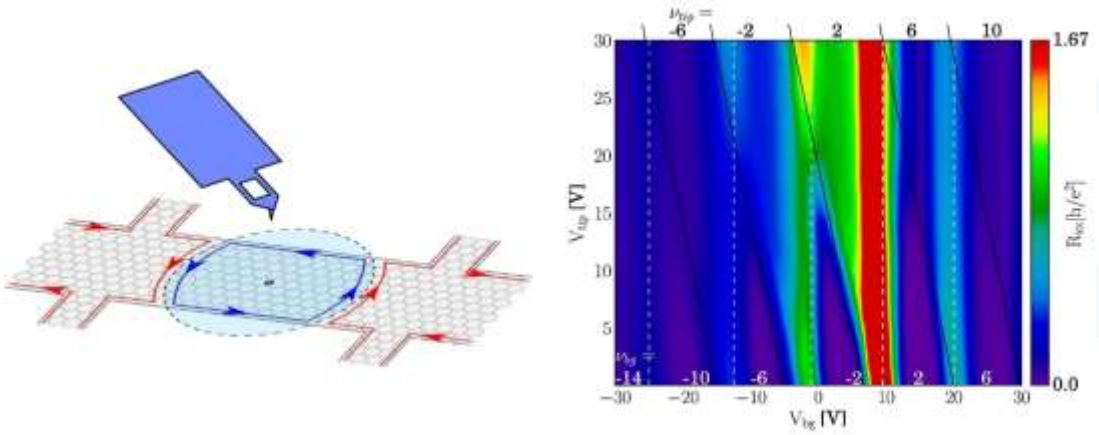

Figure 1. (a) A schematic representation of the SGM setup. By applying a voltage to the metallic tip, we can locally gate a region of choice. (b) A 2D map, showing the value of longitudinal resistance R_{xx} as a function of back-gate voltage V_{bg} and tip voltage V_{tip}. The data were collected at T = 4.2 K and B = 8 Tesla. The filling factors ν_{bg} and the filling factors underneath the SGM tip ν_{tip} are indicated. From Ref. [10].

Recent experimental and theoretical activities focused on hybrid semiconductor/superconductor systems, aiming at the emergence of new states of matter, exploiting the induced superconducting correlations in the 2D electron system thanks to the so-called proximity effect. Hybrid Josephson junctions formed by a high-quality InAs quantum-well placed between two Nb contacts have been thus realized and investigated, see Fig. 2(a). Transport measurements revealed critical temperature up to 8.1 K and high critical field, of the order of 3 Tesla. Modulation of supercurrent amplitude is achieved by side gates. Well-developed quantum Hall plateaus have been observed for magnetic fields below 3 Tesla, see Fig. 2(b), allowing for the coexistence of topological edge states and superconductivity [11,12].

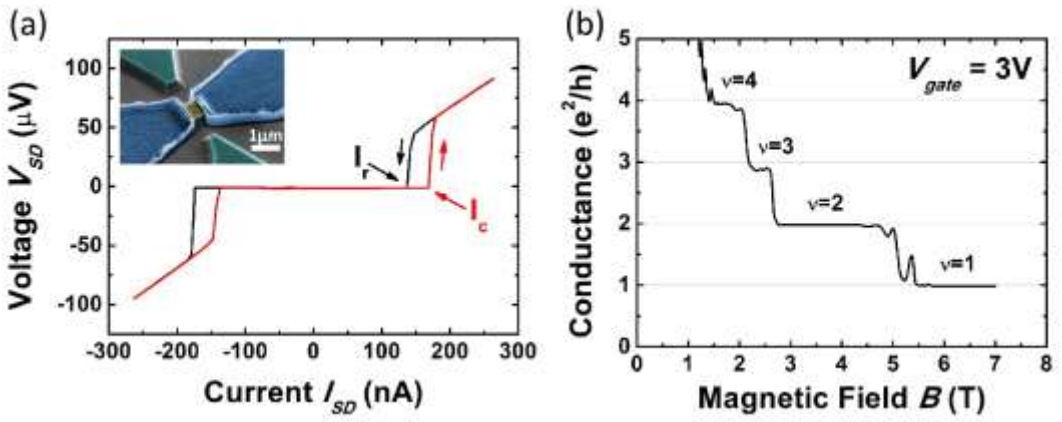

Figure 2. (a) Source-drain voltage V_{SD} vs. source-drain current I_{SD} of an InAs-based Josephson junction. The black (red) arrow shows the direction of the black (red) sweep. The inset shows a false color SEM image of the device. The mesa is yellow, side gates are green, Nb is blue. (b) Conductance (in units of e^2/h) as a function of magnetic field, showing well-developed quantum Hall plateaus already at 1.5 Tesla. From Ref. [11].

We have also fabricated and investigated a hybrid trenched Josephson junction where the width, area, and supercurrent of the two arms of a SQUID-like geometry

can be independently controlled with high precision. We have demonstrated a wide tunability of interference patterns by electrostatic means, from a superconducting quantum interference device with narrow arms to a Fraunhofer pattern in an extended Josephson junction [13]. In order to study similar effects in novel two-dimensional semiconductors, such as graphene or bP, many challenges have to be faced, especially for bP, since this material is very sensitive to air, with makes the device fabrication crucial. We studied possible stabilization mechanisms of bP [14], as well as local doping strategies, and we focused our attention on the optimization of the Ohmic contacts between metals and bP [15], since the interface transparency is crucial for Cooper pair injection. Currently we are studying some prototypical superconductor/bP devices (see Fig. 3).

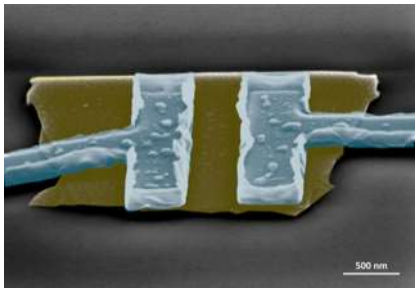

Figure 3. Tilted false color SEM image of a black phosphorus Josephson junction with Ti/Nb contacts. The black phosphorus flake is marked in yellow and the Ti/Nb contacts in blue.

These results pave the way for new device architectures with potential applications in the field of quantum computation and information. Indeed, the coexistence of quantum Hall physics and superconductivity is one of the key ingredients for the emergence of new topological states of matter, like Majorana fermions or even more exotic parafermions. The latter are predicted to form and localize at the interface between a superconductor and fractional quantum Hall edge states. Their possible realization and detection will constitute an unprecedented breakthrough, paving the way for the first development of topologically protected quantum computation architectures. The great flexibility offered by SGM, combined with low-temperature quantum transport measurements, represents a unique playground able to directly image and detect such exotic quasiparticles.

References

[1] A. Iagallo, N. Paradiso, S. Roddaro, C. Reichl, W. Wegscheider, G. Biasiol, L. Sorba, F. Beltram, S. Heun, *Scanning gate imaging of quantum point contacts and the origin of the 0.7 anomaly*, Nano Research **8**, 948 (2015).

[2] A. Iagallo, S. Tanabe, S. Roddaro, M. Takamura, H. Hibino, S. Heun, *Tuning of quantum interference in top-gated graphene on SiC*, Phys. Rev. B **88**, 235406 (2013).

[3] S. Xiang, V. Miseikis, L. Planat, S. Guiducci, S. Roddaro, C. Coletti, F. Beltram, S. Heun, *Low-temperature quantum transport in CVD-grown single crystal graphene*, Nano Research **9**, 1823 (2016).

[4] N. Hemsworth, V. Tayari, F. Telesio, S. Xiang, S. Roddaro, M. Caporali, A. Ienco, M. Serrano-Ruiz, M. Peruzzini, G. Gervais, T. Szkopek, S. Heun, *Dephasing in strongly anisotropic black phosphorus*, Phys. Rev. B **94**, 245404 (2016).

[5] A. Kumar, F. Telesio, S. Forti, A. Al-Temimy, C. Coletti, M. Serrano-Ruiz, M. Caporali, M. Peruzzini, F. Beltram, S. Heun, *STM study of exfoliated few layer black phosphorus annealed in ultrahigh vacuum*, 2D Mater. **6**, 015005 (2019).

[6] F. Telesio, N. Hemsworth, W. Dickerson, M. Petrescu, V. Tayari, O. Yu, D. Graf, M. Serrano-Ruiz, M. Caporali, M. Peruzzini, M. Carrega, T. Szkopek, S. Heun, G. Gervais, *Nonclassical*

longitudinal magnetoresistance in anisotropic black phosphorus, Phys. Status Solidi RRL **14**, 1900347 (2020).

[7] S. Salimian, S. Xiang, S. Colonna, F. Ronci, M. Fosca, F. Rossella, F. Beltram, R. Flammini, S. Heun, *Morphology and magneto-transport in exfoliated graphene on ultrathin crystalline β-Si_3N_4(0001)/Si(111)*, Adv. Mater. Interfaces **7**, 1902175 (2020).

[8] S. Xiang, A. Mrenca-Kolasinska, V. Miseikis, S. Guiducci, K. Kolasinski, C. Coletti, B. Szafran, F. Beltram, S. Roddaro, S. Heun, *Interedge backscattering in buried split-gate-defined graphene quantum point contacts*, Phys. Rev. B **94**, 155446 (2016).

[9] Z.S. Momtaz, S. Heun, G. Biasiol, S. Roddaro, *Cascaded Quantum Hall Bisection and Applications to Quantum Metrology*, Phys. Rev. Appl. **14**, 024059 (2020).

[10] L. Bours, S. Guiducci, A. Mrenca-Kolasinska, B. Szafran, J. C. Maan, S. Heun, *Manipulating quantum Hall edge channels in graphene through scanning gate microscopy*, Phys. Rev. B **96**, 195423 (2017).

[11] S. Guiducci, M. Carrega, G. Biasiol, L. Sorba, F. Beltram, S. Heun, *Toward quantum Hall effect in a Josephson junction*, Phys. Status Solidi RRL **13**,1800222 (2019).

[12] M. Carrega, S. Guiducci, A. Iorio, L. Bours, E. Strambini, G. Biasiol, M. Rocci, V. Zannier, L. Sorba, F. Beltram, S. Roddaro, F. Giazotto, S. Heun, *Investigation of InAs-based devices for topological applications*, Proc. of SPIE **11090**, 110903Z-1 (2019).

[13] S. Guiducci, M. Carrega, F. Taddei, G. Biasiol, H. Courtois, F. Beltram, S. Heun, *Full electrostatic control of quantum interference in an extended trenched Josephson junction*, Phys. Rev. B **99**, 235419 (2019).

[14] M. Caporali, M. Serrano-Ruiz, F. Telesio, S. Heun, A. Verdini, A. Cossaro, M. Dalmiglio, A. Goldoni, M. Peruzzini, *Enhanced ambient stability of exfoliated black phosphorus by passivation with nickel nanoparticles*, Nanotechnology **31**, 275708 (2020).

[15] F. Telesio, G. Le Gal, M. Serrano-Ruiz, F. Prescimone, S. Toffanin, M. Peruzzini, S. Heun, *Ohmic contact engineering in few-layer black phosphorus: approaching the quantum limit*, Nanotechnology **31**, 334002 (2020).

1.3.5 Coherent manipulation of electronic heat currents in superconducting hybrid devices

The ability to master heat currents at the nanoscale has become an essential request in many fields of nanoscience, including solid-state cooling, radiation detection and quantum information. Phase-coherent caloritronics takes advantage of long-range phase coherence in superconducting condensates to manipulate heat currents in solid-state mesoscopic circuits. The fundamental idea is to exploit suitable physical effects that depend on the superconducting phase difference φ, in order to control the electronic heat flow between two thermal reservoirs at different temperatures. Research activities at NEST led to the realization of many different nanodevices such as hybrid thermal diodes, thermal routers, a 0–π phase-controllable thermal Josephson junction (JJ). We proposed and theoretically demonstrated heat logic and memory architectures that may be operated also at GHz regimes. The aim is to realize unconventional tools for thermal management and/or thermal logic which may be beneficial for the field of quantum technologies.

The evolution of modern electronics has been boosted by the introduction of non-linear elements like interferometers, diodes and transistors. In the last 5 years, we demonstrated that superconducting hybrid structures at cryogenic temperatures represent an ideal platform to realize the thermal counterpart of these non-linear devices.

Thermal diode. In order to realize a thermal diode, i.e. a device that allows heat to flow preferentially in one direction we proposed normal metal-insulator-superconductor (NIS) junction (see Fig. 1a) [1]. It offers a sizeable asymmetry in the thermal transport due to the temperature dependence of the energy gap in the superconducting density of states.

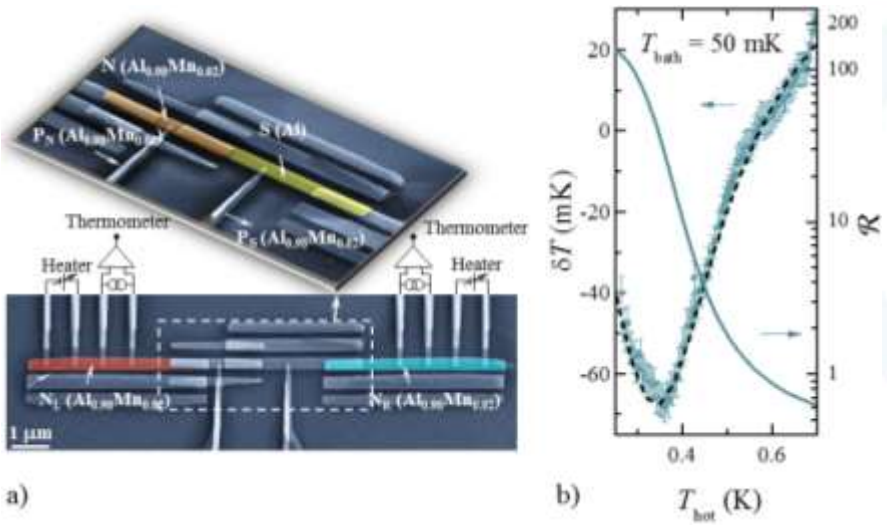

Figure 1. a) False-color scanning electron micrograph of the hybrid thermal diode. Top: NIS junction, where N stands for a normal metal (orange), I for a thin insulating layer and S for a superconductor (yellow). The probe P_N acts as a cold finger for the N electrode. Bottom: the NIS junction is inserted between two right and left N electrodes (red and blue), which act as thermal reservoirs and are connected to heaters and thermometers. b) Experimental output temperature difference δT between the forward and reverse configurations versus the bias temperature T_{hot} (left axes) measured at a bath temperature of 50 mK. Black dashed lines are the theoretical results for the device. The solid line is the thermal rectification coefficient R (right axes).

This asymmetry can be increased by connecting the N electrode to a thermalizing cold finger providing a highly efficient thermal rectification of at least one order of magnitude between the heat
current transmitted in the forward (J_{fw}) and reversal (J_{rev}) direction leading to R = J_{fw}/J_{rev} ≫1 or ≪ 1. Notably in previous experiments, a maximum R ≈ 1.4 was reported in phononic devices but our structure showed a maximum difference of more than 60 mK between the output temperatures in the forward and reverse configurations, corresponding to a heat rectification factor R ≈ 140 @50 mK (see Fig. 1b).

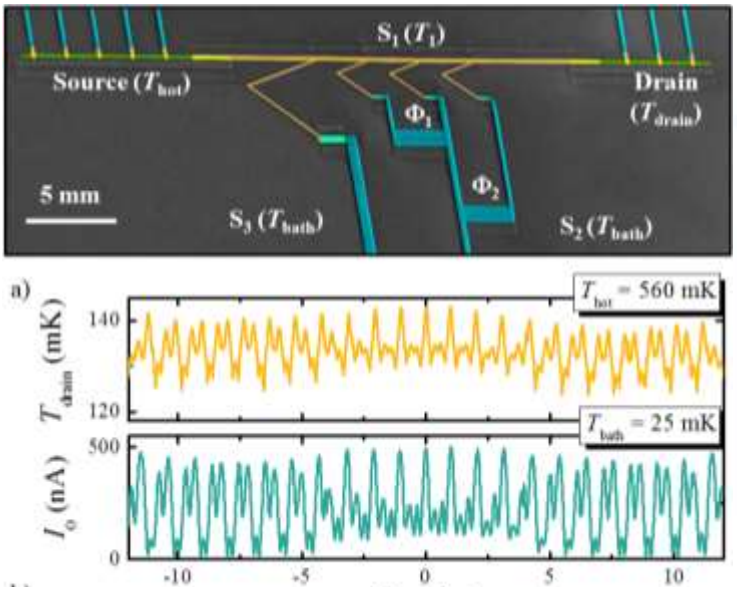

Figure 2. a) False-color scanning electron micrograph of the double-loop Josephson heat modulator. Source and drain N electrodes, depicted in green, are connected to the superconducting island S_1 (represented in orange) and to a set of heaters or thermometers (dark cyan). S_1 is tunnel-coupled to the superconducting lead S_2 (dark cyan) by means of three parallel JJs forming the double-loop SQUID and to a superconducting probe S_3 (dark cyan). b) Top: output drain temperature T_{drain} versus magnetic flux Φ_1 for a bias temperature T_{hot} = 560 mK. Bottom: magnetic flux modulation of the SQUID critical current I_0. Both curves were measured at a bath temperature of 25 mK.

Phase controlled Josephson modulator. On the other hand, it has been shown that the heat current flowing through a temperature-biased Josephson junction (JJ) has a coherent component that depends on the phase difference of the macroscopic condensates in the superconductors. This component can be manipulated at will by using a double-loop superconducting quantum interference device (SQUID) with three JJs in parallel (see Fig. 2a) [2]. Such heat modulator proved to be robust against unavoidable structure asymmetries showing exotic interference patterns of the output temperature, with large oscillation amplitude (reaching a maximum of 40 mK) and enhanced sensitivities to variations of the magnetic flux threading the loops (up to 200 mK per flux quantum). Foremost, the interferometer demonstrated the perfect correspondence between charge and heat currents (see Fig. 2b), breaking ground for advanced caloritronic nanodevices such as thermal splitters, heat pumps and time-dependent electronic engines.

Coherent caloritronics. The last experimental achievement [3] in coherent caloritronics brought us to the realization of a 0-π phase-controllable thermal JJ [4]. The latter is embedded in a superconducting quantum interference device (SQUID) containing three JJs (Fig. 3a), one of which (j) supports a lower Josephson critical current than the others (a and b).

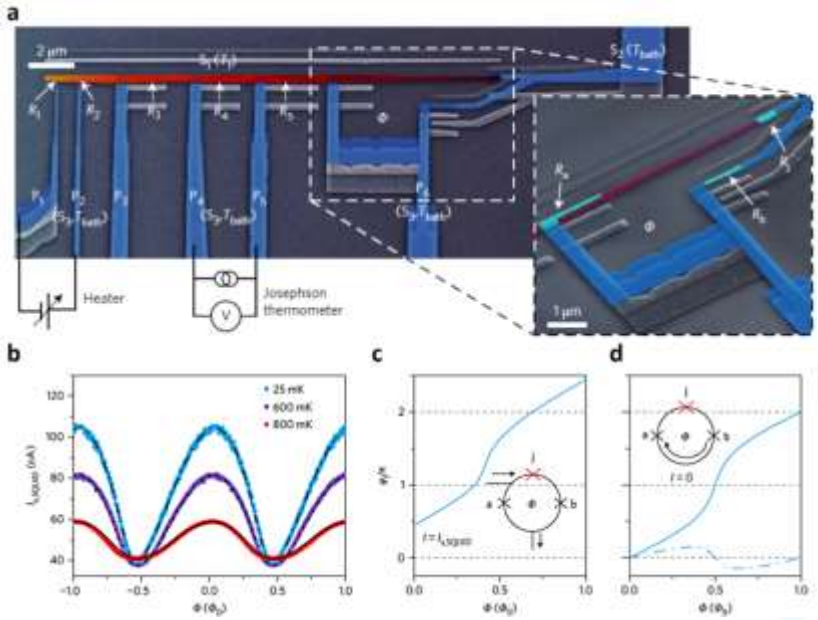

Figure 3. a) Pseudo-color scanning electron micrograph of the 0-π Josephson junction. The S_1 electrode, depicted in a yellow–red gradient, is coupled to five superconducting probes P_i (i =1,2,..,5) and to the lower branch of the SQUID P_6 (S_3, represented in blue). On the right side, S_1 is connected to the superconductor S_2 (also in blue). P_1 and P_2 are used as Joule heaters, whereas P_3, P_4, and P_5 are used to measure the electrical properties of the interferometer and to probe the electronic temperature of S_1. Inset: enlarged image of the SQUID, composed of three JJs.(b) SQUID total switching current $I_{s,SQUID}$ versus magnetic flux φ piercing the loop of the interferometer for selected values of the bath temperature T_{bath}. The filled circles are experimental values, and the black lines are the theoretical fits. (c) Calculated behavior of φ_j versus φ for the supercurrent $I=I_{s,SQUID}$ flowing through the interferometer at T_{bath}=25mK.(d) Calculated φj versus φ for I=0 and for the same parameters used in b. Dash-dotted line represents the calculated φ_a for the same parameters.

This configuration enables the phase-biasing of (j). When the magnetic flux threading the SQUID ring is varied from 0 to $\Phi_0/2$, φ_j ranges from 0 to π, namely, a result achieved for the first time in a coherent caloritronic device. As a consequence, unprecedented temperature-modulation amplitudes (~100mK at T_{bath}=25mK, see Fig. 3b), high magnetic sensitivities, and a remarkably high operational temperature up to 800mK are obtained.

Phase tunable thermal amplifiers. The advent of heat transistors and thermal memories could pave the way to a new field called thermal logic, where information is transferred, processed, and stored in the form of thermal energy.
We theoretically demonstrated the first fully-thermal caloritronic device based on an efficient thermoelectric hybrid junction coupled to a proximity heat valve: a very efficient temperature amplifier (Fig. 4a) [5]. When the input temperature $T_{in}>T_{bath}$, a thermoelectric current flows through a closed circuit including a superconducting coil, whose flux controls the thermal current across the heat valve. While maximum and minimum values of the output temperature T_{out}

depend on T_{bath} and T_{supply}, the value of T_{in} corresponding to the maximum T_{out} decreases as the inductive coupling is raised (see Fig. 4b). This device can provide T_{out} values in the same range as T_{in}, thus representing a crucial element for the realization of thermal logic gates.

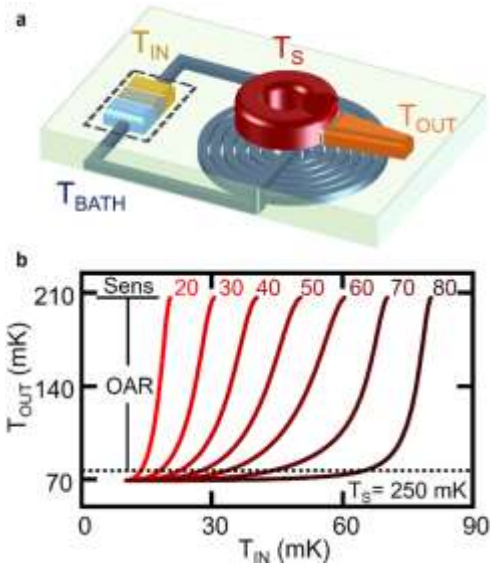

Figure 4. (a) Schematic representation of the temperature amplifier: the thermoelectric element highlighted with the dashed rectangle is constituted of a metal (yellow), a ferromagnetic insulator (gray) and a superconductor (turquoise). The turquoise depicts the superconducting coil. The SQUIPT (red) is composed of a superconducting ring interspersed by a normal metal wire and a tunnel-coupled metal probe (orange) through a thin insulator (dark gray). (b) Output temperature T_{OUT} as a function of T_{IN} calculated for T_S=250mK and for different values of Sens. The black dotted line represents the minimum value of active output T_{OUTMIN}. The output active range (OAR) is shown.

Thermal logic, routers and memories We envisioned novel unconventional thermal gates and logic [6] and realized thermal routers [7]. We also theoretically discussed other fundamental block required for a thermal logic: a superconducting thermal memory that exploits the thermal hysteresis in a flux-controlled, temperature-biased SQUID with a non-negligible inductance of the superconducting ring [8]. This system reveals a temperature bistability, which can be used to define two distinct logic states [9].

References

[1] M.J. Martínez-Pérez, A. Fornieri, F. Giazotto, *Rectification of electronic heat current by a hybrid thermal diode*, Nat. Nanotechnol. **10**, 303 (2015).

[2] A. Fornieri, C. Blanc, R. Bosisio, S. D'Ambrosio, F. Giazotto, *Nanoscale phase-engineering of thermal transport with a Josephson heat modulator*, Nat. Nanotechnol. **11**, 258 (2016).

[3] A. Fornieri, F. Giazotto, *Towards phase-coherent caloritronics in superconducting circuits*, Nat Nanotechnol. **12**, 944 (2017).

[4] A. Fornieri, G. Timossi, P. Virtanen, P. Solinas, F. Giazotto, *0–π phase-controllable thermal Josephson junction*, Nat Nanotechnol. **12**, 425 (2017).

[5] F. Paolucci, G. Marchegiani, E. Strambini, F. Giazotto, *Phase-tunable temperature amplifier*, Eur. Phys. Lett. **118**, 68004 (2017).

[6] F. Paolucci, G. Marchegiani, E. Strambini, F. Giazotto, *Phase-tunable thermal logic: computation with heat*, Phys. Rev. Applied **10**, 024003 (2018).

[7] G.F. Timossi, A. Fornieri, F. Paolucci, C. Puglia, F. Giazotto, *Phase-tunable Josephson thermal router*, Nano letters **18**, 1764 (2018).

[8] C. Guarcello, P. Solinas, M. Di Ventra, F. Giazotto, *Hysteretic Superconducting Heat-Flux Quantum Modulator*, Phys. Rev. Applied **7**, 044021 (2017).

[9] C. Guarcello, P. Solinas, A. Braggio, M. Di Ventra, F. Giazotto, *Josephson Thermal Memory*, Phys. Rev. Applied **9**, 014021 (2018).

1.3.6 Thermal transport, thermoelectricity and quantum thermodynamics in nanostructures

Thermoelectricity has recently received mich attention owing to the constant demand for new effective ways of energy conversion. Increasing the efficiency of thermoelectric materials, heat engines and refrigerators at the nanoscale is one of the main challenges for several different technological applications. Moreover, improving thermal management at low temperatures is crucial for nanoscale quantum technologies.

One of the keys to success in this field is the ability to modulate, control, and route heat and charge currents, ideally achieving their separate control. This is however by no means obvious as the charge and (the electronic contribution to) the heat are transported by the same carriers. In two-terminal systems, within the linear response regime, electrical and thermal currents are strictly interrelated, as manifested by the emergence at low enough temperatures of the Wiedemann-Franz (WF) law. In this respect, multi-terminal devices, so far poorly investigated, offer the possibility to 'decouple' energy and charge flows, and improve thermoelectric efficiency.
In this context we have developed a general formalism for linear-response multi-terminal thermoelectric transport. In particular, we have worked out analytical expressions for the efficiency at maximum power in the three-terminal case. By means of two simple quantum-dot-based non-interacting models, we have shown that a third terminal can be useful to improve the thermoelectric performance of a system with respect to the two-terminal case [1].

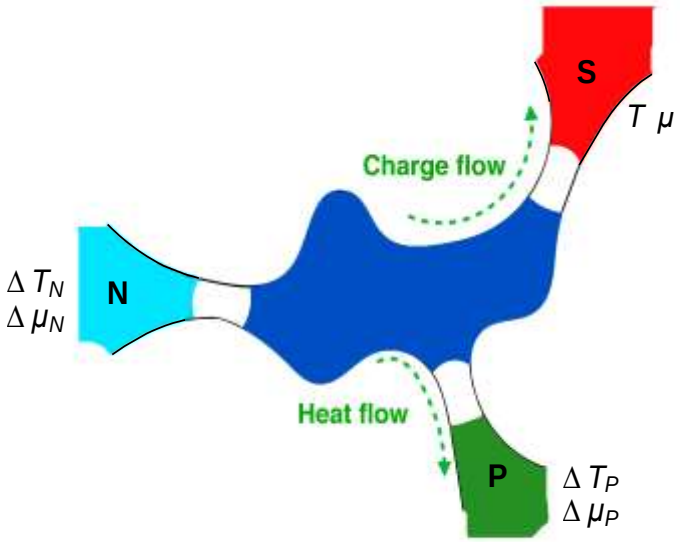

Figure 1. The heat-charge current separation scheme. A generic conductor is connected to three reservoirs labelled by the letters S (superconducting lead), P (voltage probe), and N (normal metal lead). The reservoir S is the reference for the temperature T and the chemical potential μ. A temperature (chemical potential) difference ΔT_N and ΔT_P ($\Delta\mu_N$ and $\Delta\mu_P$) is present in reservoir N and P, respectively. As indicated by the arrows, only charge flows inside lead S whereas only heat flows inside lead P.

Furthermore, we have analyzed the performance of a thermal machine that allows for the spatial separation between heat and charge currents. It is realized by connecting a conductor to a superconducting lead, a voltage probe, and a normal lead (see Fig. 1). We have shown that in the low temperature limit such system violates the WF law and allows, to some extent, an independent control of electrical conductance, thermal conductance, and thermopower [2]. We have thus shown, on statistical grounds, that the system exhibits much larger values of the power factor Q and of the figure of merit ZT (one order of magnitude), with respect to the two-terminal counterpart (see Fig. 2).

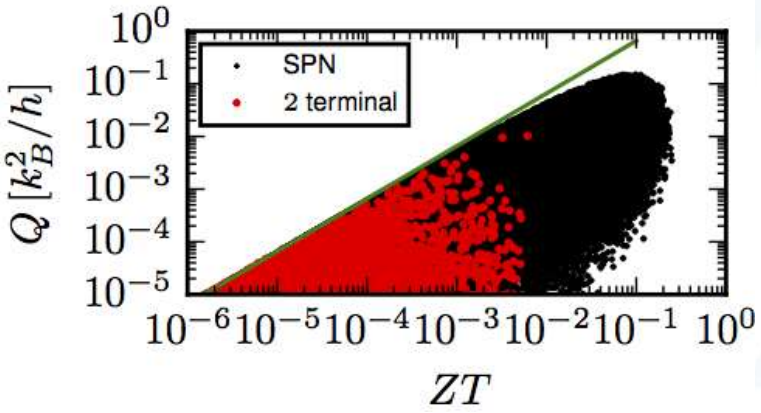

Figure 2. Correlation between the power factor Q and the figure of merit ZT relative to systems consisting of three quantum dots for the SPN setup (black points) and the two-terminal setup (red points). The green curve corresponds to the bound given by the unitarity of the scattering matrix, and sets a maximum value for Q as a function of ZT. The plot shows that for the SPN setup both Q and ZT are one order of magnitude larger with respect to the corresponding values for the two-terminal system. The plot refers to 10^5 Hamiltonian realizations, taking the couplings with the reservoirs P and N equal to $10^3\ k_BT$.

Heat-to-work conversion based on thermoelectricity promises an enhanced efficiency as a consequence of the reduction of the phonon contribution to thermal conductance in disordered nanostructures and of the "energy filtering" effect that can result from confinement and quantum effects. A heat engine composed of a quantum dot (QD) is a paradigmatic example, since it is characterized by a spectrum of discrete levels which maximizes energy filtering. In this context, we have theoretically studied the thermoelectric properties and heat-to-work conversion performance of a multilevel QD in a multi-terminal configuration within the Coulomb blockade regime [4]. In the linear response and for low temperatures, we have derived analytical expressions for all transport coefficients, for the power factor Q and for the figure of merit ZT (which controls the maximum efficiency and the efficiency at maximum power). We have found the specific values of the gate voltage, which only depend on temperature, for which Q and ZT are simultaneously maximized (see Fig. 3). The regime beyond the linear response has been analyzed numerically. In this case, the efficiency at maximum power develops peaks which approach the Carnot efficiency for large temperature differences. Remarkably, the maximum power, normalized to its peak value, only slightly depends on the temperature bias and can be well approximated by the analytic expression obtained for the linear response regime. Moreover, we have found that efficiency at maximum power and maximum power take approximately their peak values simultaneously, under the same conditions found for the linear response.

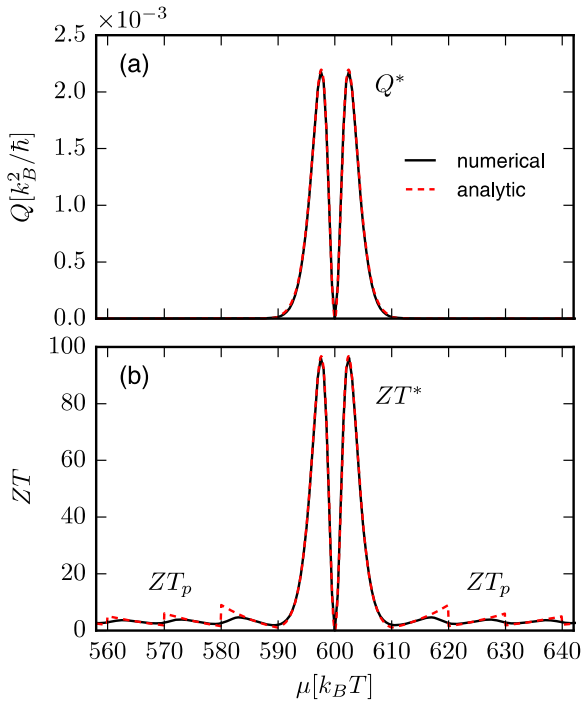

Figure 3. Power factor Q (a) and figure of merit ZT (b) are plotted as a function of the electrochemical potential μ (gate voltage) for a multi-level QD. For both quantities, the analytical quantum limit is plotted as a red dashed curve, while the numerically calculated result is plotted as a black solid curve. All curves are calculated for a charging energy $\boldsymbol{E_C = 50\, k_B T}$, level spacing $\boldsymbol{\Delta E = 10\, k_B T}$, and coupling energy of the tunnel barriers defining the QD given by $\boldsymbol{\hbar\Gamma = 0.01\, k_B T}$, $\boldsymbol{T}$ being the reference temperature. $\boldsymbol{Q^* \simeq 0.22 \frac{\Gamma k_B}{T}}$ is the peak value of $\boldsymbol{Q}$, $\boldsymbol{ZT^* \simeq 0.44 \frac{exp(\frac{\Delta E}{k_B T})}{(\frac{\Delta E}{k_B T})^2}}$ is the figure of merit peak value, and $\boldsymbol{ZT_p = 3}$ (for large $\boldsymbol{p}$) is the value of $\boldsymbol{ZT}$ of the secondary peaks.

In conclusion, we have found that Coulomb interactions dramatically increase ZT (by strongly suppressing the thermal conductance) and the non-linear-response efficiency at maximum power (pushing it above the Curzon-Alhborn limit).

More recently we have considered electronic thermal transport in systems composed of two metallic islands (MIs) or quantum dots (QDs) that are electrically isolated (but capacitively coupled) and placed in the two circuits (the drive and the drag) of a three- or four-electrode setup. In the latter setup we study the thermal drag effect when the system is biased, for example by a temperature ΔT, on the drive circuit, while no biases are present on the drag circuit [5]. The three-electrode setup is analyzed as a simple implementation of an autonomous refrigerator, a system that uses heat as a resource to achieve refrigeration [6]. We have also applied our theoretical approach to model three different experiments, the first regarding the measurement of thermovoltage in MIs [7], the second one regarding the occurrence of an apparent violation of the second law of thermodynamics in the statistics of work extraction from a MI [8] (see Fig. 4), and the third one regarding the thermoelectric response of a QD fabricated using the technology of heterostuctured nanowires. In the latter, a precise measurement of the Seebeck coefficient was obtained and – thanks to modelling – a precise estimate of the thermal transport and conversion efficiency was achieved (with a figure of merit up to ZT=35 at 30K).

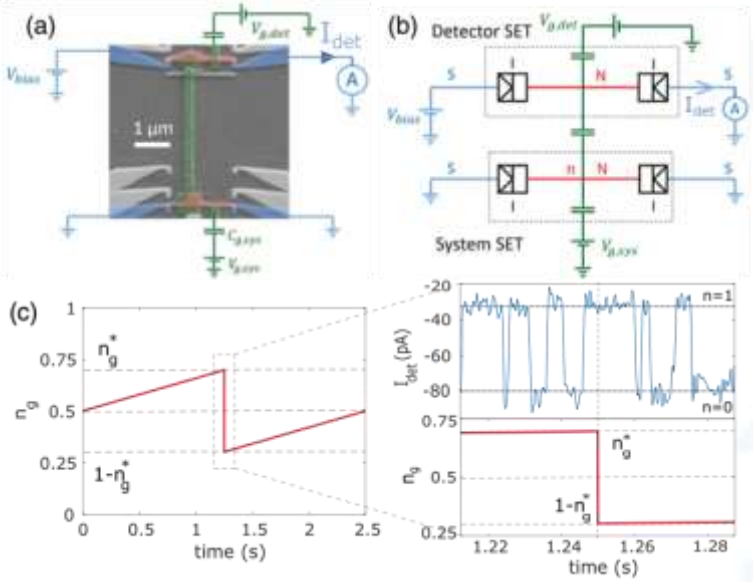

Figure 4. (a) Scanning electron micrograph of the single-electron transistor (SET) capacitively coupled to a voltage-biased detector SET. Leads (blue) made of superconducting aluminum are coupled through oxide (tunnel) barriers to the copper (red) island. (b) Electrical circuit representation. (c) Protocol used to maximize work extraction, with a zoom on the detector SET output current under system driving, around the quench event.

Finally, we have investigated nonlocal thermoelectricity in a hybrid superconducting nanosystem, such as the Cooper pair splitter (CPS), implemented using a double quantum dot in a nanowire system coupled to a superconductor (see Fig. 5a) [9]. Fig. 5b shows the thermodynamic efficiency of the nonlocal Seebeck (blue curve) and Peltier (red curve) effect. We have found that the nonlocal thermoelectric response is a direct consequence of the nonlocal splitting of the Cooper pair into the two quantum dots.

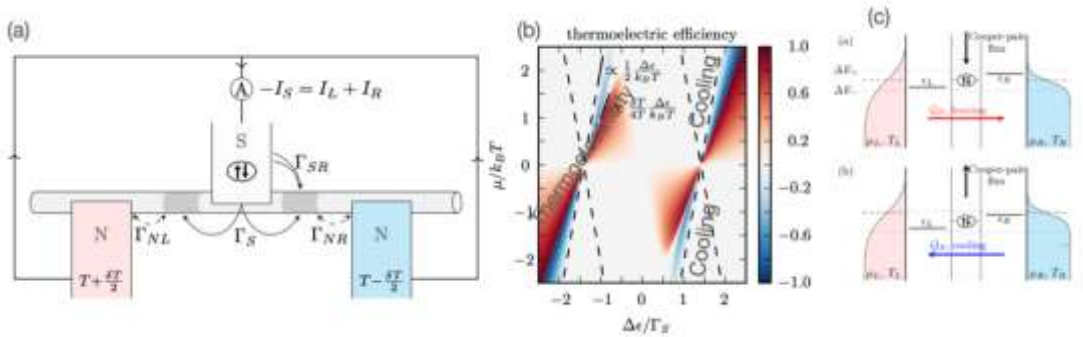

Figure 5. (a) Nanowire-based CPS to investigate nonlocal thermoelectric effects. The thermal gradient is applied to the normal metal leads N and the current is collected in the superconducting terminal. (b) Themoelectrical efficiency of the CPS in the plane of the level detuning and bias potential applied to the normal metal leads. In blue and red are shown the thermodynamical efficiency and the COP respectively for the nonlocal Seebeck and Peltier effect. (c) Energy scheme for the nonlocal heat pump (upper panel) and cooler (lower panel), depending on the direction of the driving current in the superconductor. The direction of the heat flows depends only on the gate configuration in the double quantum dots, thus realizing an electrically controlled nonlocal thermal router.

References

[1] F. Mazza, R. Bosisio, G. Benenti, V. Giovannetti, R. Fazio, F. Taddei, *Thermoelectric efficiency of three-terminal quantum thermal machines*, New J. Phys. **16**, 085001 (2014).

[2] F. Mazza, S. Valentini, R. Bosisio, G. Benenti, V. Giovannetti, R. Fazio, F. Taddei, *Separation of heat and charge currents for boosted thermoelectric conversion*, Phys. Rev. B **91**, 245435 (2015).

[3] R. Bosisio, S. Valentini, F. Mazza, G. Benenti, R. Fazio, V. Giovannetti, F. Taddei, *Magnetic thermal switch for heat management at the nanoscale*, Phys. Rev. B **91**, 205420 (2015).

[4] P.A. Erdman, F. Mazza, R. Bosisio, G. Benenti, R. Fazio, F. Taddei, *Thermoelectric properties of an interacting quantum dot based heat engine*, Phys. Rev. B **95**, 245432 (2017).

[5] B. Bhandari, G. Chiriacò, P.A. Erdman, R. Fazio, F. Taddei, *Thermal drag in electronic conductors*, Phys. Rev. B **98**, 35415 (2018).

[6] P.A. Erdman, B. Bhandari, R. Fazio, J. P. Pekola, F. Taddei, *Absorption refrigerators based on Coulomb-coupled single-electron systems*, Phys. Rev. B **98**, 45433 (2018).

[7] P.A. Erdman, J.T. Peltonen, B. Bhandari, B. Dutta, H. Courtois, R. Fazio, F. Taddei, J.P. Pekola, *Nonlinear thermovoltage in a single-electron transistor*, Phys. Rev. B **99**, 165405 (2019).

[8] O. Maillet, P.A. Erdman, V. Cavina, B. Bhandari, E.T. Mannila, J.T. Peltonen, A. Mari, F. Taddei, C. Jarzynski, V. Giovannetti, J.P. Pekola, *Optimal probabilistic work extraction beyond the free energy difference with a single-electron device*, Phys. Rev. Lett. **122**, 150604 (2019).

[9] R. Hussein, M. Governale, S. Kohler, W. Belzig, F. Giazotto, A. Braggio, *Nonlocal thermoelectricity in a Cooper-pair splitter*, Phys. Rev. B **99**, 075429 (2019).

1.3.7 Thermoelectrics and thermo-mechanics of individual nanostructures

Classical and quantum transport phenomena together with ultrafast optical response were investigated at the level of individual nano-objects focusing on the study of the combined heat-charge-energy conversion mechanisms and of their applications in the fields of nanoscale thermoelectrics and thermo-mechanics. Nano-objects display peculiar physical properties (e.g. electronic, thermal and mechanical ones) that are intimately related to their composition, structure, morphology, and to the environment. Unveiling the correlation between the morphological and physical properties of nano-objects would boost the engineering of nano-systems with tailored properties, and promote metrology protocols for their characterization, alternative to high-resolution imaging techniques. Recent results on the investigation of the thermoelectric and thermos-mechanical properties of individual nanostructures –semiconductor nanowires and metallic nanodisks - are summarized hereafter.

The advent of nanostructures has opened new perspectives for the creation of innovative thermoelectric (TE) materials that outperform the currently available solid-state converters. We demonstrate high-temperature thermoelectric conversion in InAs/InP nanowire (NW) quantum dots (QDs) by taking advantage of their strong electronic confinement (Fig. 1) [1]. The electrical conductance G and the thermopower S are obtained from charge transport measurements and accurately reproduced with a theoretical model accounting for the multilevel structure of the quantum dot. Notably, our analysis does not rely on the estimate of cotunneling contributions, since electronic thermal transport is dominated by multilevel heat transport. By taking into account two spin-degenerate energy levels we evaluate the electronic thermal conductance k and we investigate the evolution of the electronic figure of merit ZT as a function of the quantum dot configuration, demonstrating $ZT \approx 35$ at 30 K, corresponding to an electronic efficiency at maximum power close to the Curzon–Ahlborn limit.

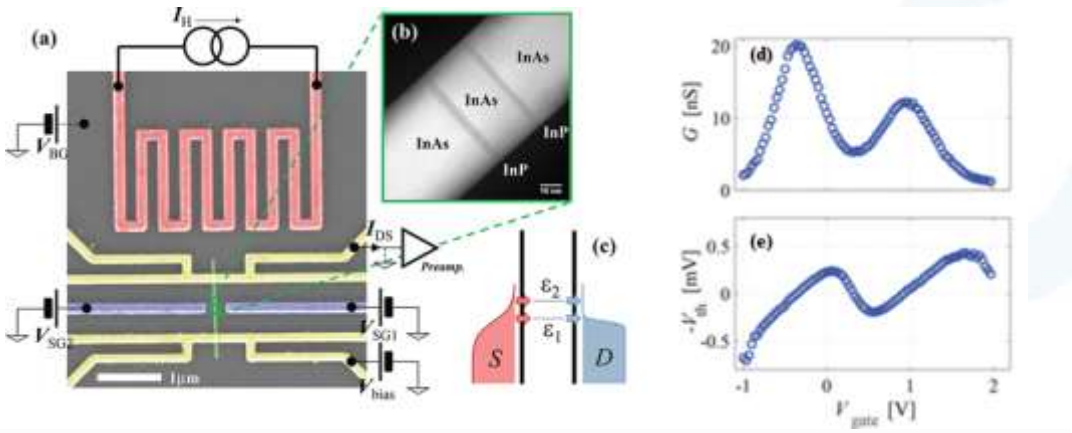

Figure 1. **(a)** SEM of a prototypical device. A local heater (red) is used to establish a temperature difference ΔT between the two ends of the NW (green) embedding an InAs/InP heterostructured QD. The device is fabricated on top of a degenerately doped SiO_2/Si p++ substrate (gray), and a set of Ti/Au electrodes (yellow) can be used both as electrical contacts to the NW and as local resistive thermometers. The QD electronic configuration can be controlled with a pair of side gates (purple) or using the conductive substrate as a backgate electrode. **(b)** TEM of the heterostructured QDs. **(c)** Sketch of the energetics scheme: the QD implements a multilevel system that can mediate heat and charge transport between the source (S) and drain (D), in the presence of thermal and electric bias. Two spin-degenerate levels ε_1 and ε_2 ($\Delta\varepsilon = \varepsilon_2 - \varepsilon_1$) play a relevant role in the regime studied in the experiment. **(d)** Extrapolated conductance G and **(e)** thermovoltage $-V_{th}$ as a function of the applied gate voltage V_{gate} for the first degenerate energy level for an average temperature T_{avg} = 24.9 K and for I_H = 10 mA current feeding the heating serpentine, when the system is in a T_{bath} = 4.2 K thermal bath.

A share of the experimental activities focuses on the development of reliable methods to precisely assess the TE properties of individual nanostructures [2,3]. We exploit noise measurements as an advanced thermometry tool to shine light on diffusive electronic transport in NW-based field effect transistors (FETs) [4,5] in presence of a thermal bias. We also demonstrate an all-electrical platform to measure the thermal conductivity *k* in suspended NW devices [6], using the so-called 3ω-method that relies on self-heating in the presence of an AC current modulation at frequency *ω*. Besides, we combine electrical and Raman measurements to achieve the full figure of merit of single NWs [7]. It is worth to mention that both the latter techniques – 3ω and Raman - can be exploited in combination with new outstanding methods for the field effect control of semiconductors at the micro- and nano-scale, based on the concept of electric double layer field effect transistor. Here, electric fields exceeding 30 MV/cm are built up at the interface between a semiconductor and a layer of tightly packed charged molecules (ions) conformally distributed around the surface of the semiconductor.

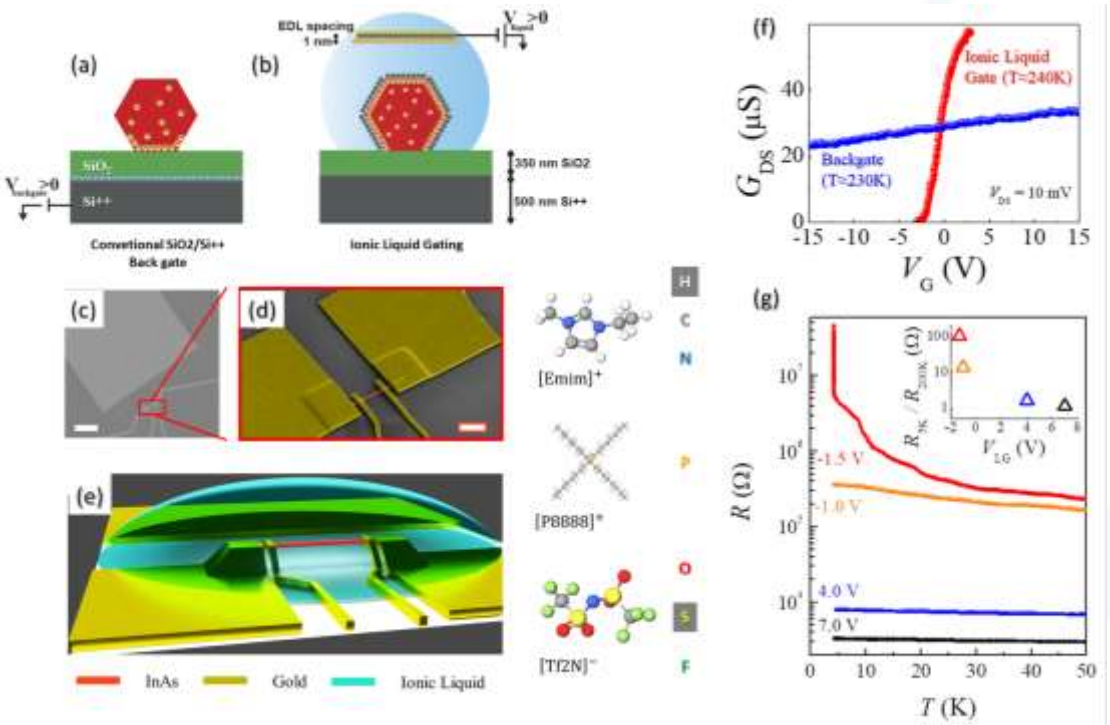

Figure 2. **(a)** Conventional back-gate method compared to **(b)** ionic liquid gating: the latter is conformal and allows to achieve outstanding charge carrier concentration. **(c-d)** scanning electron micrograph of device architecture where an individual NW (red colored) suspended onto a substrate is electrically contacted by four Ohmic contacts and equipped with a large counter-electrode used to polarize the ionic liquid (not shown in the image). **(e)** Pictorial view of the suspended NW-based device surrounded by an ionic liquid droplet used to enable electric double layer transistor operation. The ionic liquid may have a thermal conductivity up to 100 times smaller with respect to the one of the NW and the substrate. **(f)** Red (blue) transconductance corresponds to ionic-liquid gating (back-gating) operation of the NW transistor. **(g)** Temperature dependence of the device electrical resistance indicates the onset of a transition from a semiconducting to a quasi-metallic state.

In this approach, gate media typically consist of a soft-matter system such as a polymer functionalized with mobile ions or an ionic liquid (a salt melt at 300 K).

In this frame, we have demonstrated the operation of a FET based on a single InAs NW gated by an ionic liquid, reporting very efficient carrier modulation with a transconductance value up to 50 times larger with respect to conventional back-gating implemented via the SiO_2/Si++ substrate (Fig. 2).
This opens the way to the exploitation of ionic-liquid gating in nanodevices based on III–V semiconductor NWs [8,9]. Notably, soft-matter systems used as dielectric gate can be properly engineered in order to: (i) be transparent to a wide light wavelength range, thus being compatible with optical techniques; (ii) display a thermal conductivity two orders of magnitude smaller with respect to the one characteristic of solid-state semiconductors (Si, III-V compounds) and insulators (SiO_2), thus being compatible with *k* measurement using the 3ω-technique. This allows the simultaneous measurements of the electrical and thermal properties of the same nanostructure, and can stimulate novel investigations in the field of nanoscale thermoelectrics.
On the side of thermal-to-mechanical energy conversion at the nanoscale, we have investigated the mechanical vibrations of individual gold nanodots or nanodisks - nanopatterned on a sapphire substrate - using ultrafast time-resolved optical spectroscopy (Fig. 3) [10,11].

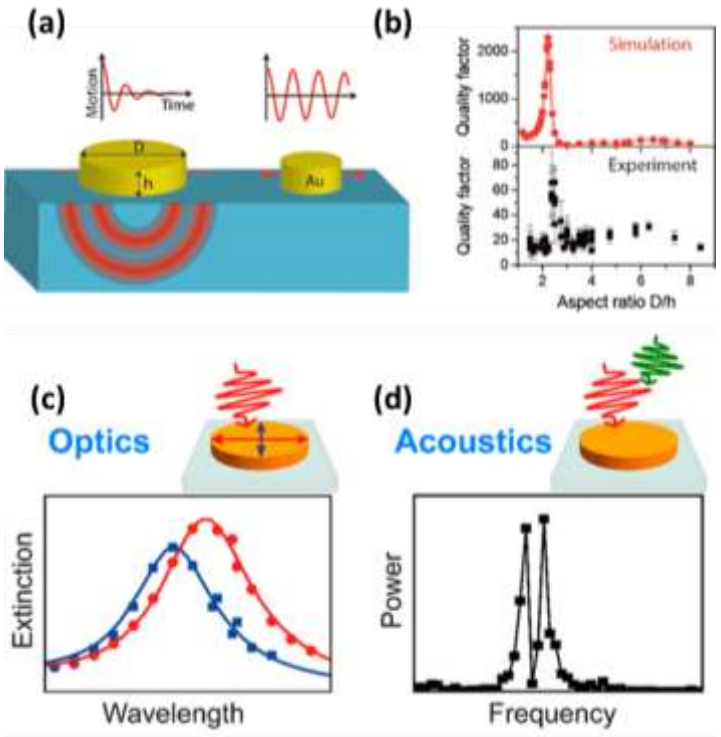

Figure 3. (a) Gold nanodisks are lithographically defined onto a sapphire substrate: the aspect ratio strongly affects the mechanical vibrations upon thermal excitation induced by a laser pulse. (b) Highest quality factor of experimentally detected vibrational modes for different nanodisks aspect ratio. The nanodisks may display circular section or noncircular one, and the presence of a major and a minor axes has an impact on the optical as well as acoustical response: (c) extinction spectra for the two orthogonal polarization directions are shifted in energy, and (d) the Fourier transform of the oscillating part of the time-resolved signal reveals two different resonances.

The number and characteristics of the detected acoustic modes are found to vary with nanodisk geometry. In particular, their quality factors strongly depend on nanodisk aspect ratio (i.e., diameter over height ratio), reaching a maximal value of ≈70, higher than those previously measured for substrate-supported nano-objects. The peculiarities of the detected acoustic vibrations are confirmed by finite-element simulations, and interpreted as the result of substrate-induced hybridization between the vibrational modes of a nanodisk. Moreover, using spatial modulation and pump–probe optical spectroscopies, we have identified the signatures of small morphological anisotropies in the plasmonic and vibrational responses of our nanostructures. In fact, the features of the measured extinction spectra and time-resolved signals are highly sensitive to faint deviations of the nanodisk morphology from a perfectly cylindrical one. An elliptical nanodisk section, as compared to a circular one, lifts the degeneracy of the two nanodisk in-plane dipolar surface plasmon resonances, which can be selectively excited by controlling the polarization of the incident light. This splitting effect, whose amplitude increases with nanodisk ellipticity, correlates with the detection of additional vibrational modes in the context of time-resolved spectroscopy. The analysis of the measurements is performed through the combination of optical and acoustic numerical models. This allowed us first to estimate the dimensions of the investigated nanodisks from their plasmonic response and then to compare the measured and computed frequencies of their detectable vibrational modes, which are found to be in excellent agreement. The results of our studies demonstrate novel possibilities for engineering the vibrational modes of nano-objects, and show that single-particle optical spectroscopies are able to provide access to fine morphological characteristics, representing in this case a valuable alternative to traditional techniques aimed at post-fabrication inspection of subwavelength nanodevice morphology.

References

[1] D. Prete, P. Erdman, V. Demontis, V. Zannier, D. Ercolani, L. Sorba, F. Rossella, F. Taddei, S. Roddaro, *Thermoelectric response at high temperature in nanowire quantum dots*, Nano Lett. **19**, 3033 (2019).

[2] F. Rossella, F. Pennelli, S. Roddaro, *Measurement of the Thermoelectric Properties of Individual Nanostructures*, Semiconductors and Semimetals **98**, 409 (2018).

[3] E. Dimaggio, F. Rossella, G. Pennelli, *Management of the output electrical power in thermoelectric generators*, Electronics **8**, 1514 (2019).

[4] E.S. Tikhonov, D.V. Shovkun, D. Ercolani, F. Rossella, M. Rocci, L. Sorba, S. Roddaro, V.S. Khrapai, *Local noise in a diffusive conductor*, Scientific Report **6**, 30621 (2016).

[5] E.S. Tikhonov, D.V. Shovkun, V.S. Khrapai, D. Ercolani, F. Rossella, M. Rocci, L. Sorba, S. Roddaro, *Noise thermometry applied to thermoelectric measurements in InAs nanowires*, Semicond. Sci. Technol. **31**, 104001 (2016).

[6] M. Rocci, V. Demontis, D. Prete, D. Ercolani, L. Sorba, F. Beltram, G. Pennelli, S. Roddaro, S. Rossella, *Suspended InAs Nanowire-Based Devices for Thermal Conductivity Measurement Using the 3ω-method*, Jour. Mat. Eng. and Perf. **27**, 6299 (2018).

[7] S. Yazji, E. Hoffman, D. Ercolani, F. Rossella, A. Pitanti, A. Cavalli, S. Roddaro, G. Abstreiter, L. Sorba, I. Zardo, *Complete thermoelectric benchmarking of individual InSb nanowires by combined micro-Raman and electrical transport analysis*, Nano Research **8**, 4048 (2015).

[8] J. Lieb, V. Demontis, D. Prete, D. Ercolani, V. Zannier, L. Sorba, S. Ono, F. Beltram, B. Sacepe, F. Rossella, *Ionic liquid gating of InAs nanowire-based field effect transistors*, Adv. Funct. Mater. **29**,1804378 (2019).

[9] D. Prete, J. Lieb, V. Demontis, L. Bellucci, V. Tozzini, D. Ercolani, V. Zannier, L. Sorba, S. Ono, F. Beltram, B. Sacépé, F. Rossella, *III-V semicondutor nanostructures and iontronics: InAs*

nanowire-based electric double layer field effect transistors, AIP Conference Proceedings **2145**, 020003 (2019).

[10] F. Medeghini, A. Crut, M. Gandolfi, F. Rossella, P. Maioli, F. Vallée, F. Banfi, N. Del Fatti, *Controlling the Quality Factor of a Single Acoustic Nanoresonator by Tuning its Morphology*, Nano Letters **18**, 5159 (2018).

[11] F. Medeghini, R. Rouxel, A. Crut, P. Maioli, F. Rossella, F. Banfi, F. Vallée, N. Del Fatti, *Signatures of Small Morphological Anisotropies in the Plasmonic and Vibrational Responses of Individual Nano-objects*, J. Phys. Chem. Lett. **10 (18)**, 5372 (2019).

1.3.8 Quantum Thermodynamics: from Quantum Thermal Machines to Quantum Batteries

Quantum thermodynamics [1,2] has emerged both as a field of fundamental interest, and as a potential candidate to improve the performance of thermal machines. Our activities span from theoretical characterization of the thermodynamics processes at the quantum level, to the development of control techniques to improve the performance of thermal processes (thermalization, cooling, etc), to the analysis of nanodevices for the storage of energy (quantum-battery models).

In Ref. [3] two different models of optomechanical systems where a temperature gradient between two radiation baths is exploited for inducing self-sustained coherent oscillations of a mechanical resonator was studied. Viewed from a thermodynamic perspective, such systems represent quantum instances of self-contained thermal machines converting heat into a periodic mechanical motion and thus they can be interpreted as nano-scale analogues of macroscopic piston engines. Our models are potentially suitable for testing fundamental aspects of quantum thermodynamics in the laboratory and for applications in energy efficient nanotechnology.

In Ref. [6] we studied the dynamics of heat flux in the thermalization process of a pair of identical quantum system that interact dissipatively with a reservoir in a *cascaded* fashion. Despite the open dynamics of the bipartite system is globally Lindbladian, one of the subsystems "sees" the reservoir in a state modified by the interaction with the other subsystem and hence it undergoes a non-Markovian dynamics.

The use of quantum control techniques to improve the performances of thermal machines has been studied in a series of papers. Specifically, in Ref. [4] we consider the problem of time optimal control of a continuous bosonic quantum system subject to the action of a Markovian dissipation. In Ref. [7] optimal control strategies were analyzed to optimize the relaxation rate towards the fixed point of a quantum system in the presence of a non-Markovian dissipative bath. Contrary to naive expectations that suggest that memory effects might be exploited to improve optimal control effectiveness, non-Markovian effects influence the optimal strategy in a non-trivial way: we presented a necessary condition to be satisfied so that the effectiveness of optimal control is enhanced by non-Markovianity subject to suitable unitary controls. For illustration, we specialize our findings for the case of the dynamics of single qubit amplitude damping channels. The optimal control strategy presented here can be used to implement optimal cooling processes in quantum technologies and may have implications in quantum thermodynamics when assessing the efficiency of thermal micro-machines. In Ref. [11] an optimal process for probabilistic work extraction beyond the second law was introduced and in Ref. [12] an experimental verification of the scheme was produced with single-electron devices. In Ref. [20] we studied how to achieve the ultimate power in the simplest, yet non-trivial, model of a thermal machine, namely a two-level quantum system coupled to two thermal baths. Without making any prior assumption on the protocol, via optimal control we show that, regardless of the microscopic details and of the operating mode of the thermal machine, the maximum power is universally achieved by a fast Otto-cycle like structure in which the controls are rapidly switched between two extremal

values. A closed formula for the maximum power is derived, and finite-speed effects are discussed. We also analyzed the associated efficiency at maximum power (EMP) showing that, contrary to universal results derived in the slow-driving regime, it can approach Carnot's efficiency, no other universal bounds being allowed. In Ref. [21] non-Markovian effect on the efficiency of thermal machines were analyzed.

In Refs. [13] we developed a perturbation theory of quantum (and classical) master equations with slowly varying parameters, applicable to systems which are externally controlled on a time scale much longer than their characteristic relaxation time. This technique was used to study finite-time isothermal processes in which, differently from quasi-static transformations, the state of the system is not able to continuously relax to the equilibrium ensemble. Within first order in the perturbation expansion, we identify a general formula for the efficiency at maximum power of a finite-time Carnot engine. We also clarify under which assumptions and in which limit one can recover previous phenomenological results as, for example, the Curzon-Ahlborn efficiency. In Ref. [14] instead we applied advanced methods of control theory to open quantum systems and we determine finite-time processes which are optimal with respect to thermodynamic performances. General properties and necessary conditions characterizing optimal drivings were derived, obtaining bang-bang type solutions corresponding to control strategies switching between adiabatic and isothermal transformations. A direct application of these results is the maximization of the work produced by a generic quantum heat engine, where we show that the maximum power is directly linked to a particular conserved quantity naturally emerging from the control problem. Finally, we used our general approach to the specific case of a two level system, which can be put in contact with two different baths at fixed temperatures, identifying the processes which minimize heat dissipation. Moreover, we explicitly solved the optimization problem for a cyclic two-level heat engine driven beyond the linear-response regime, determining the corresponding optimal cycle, the maximum power, and the efficiency at maximum power. In Ref. [14] we generalize the previous approach to derive a variational approach to optimal control that can be applied to coherently driven, open quantum dynamical systems.

In Ref. [5] we studied the thermopower of a three-terminal setup composed of a quantum dot attached to three electrodes, one of which is a topological superconductor. We compared the results for s-wave (trivial) and p-wave (topological) superconductors and observed that for small temperatures the thermopower has different sign in the two cases. This behavior is strongly dependent on temperature and we estimate an energy scale that controls the sign in the p-wave case, which results proportional to the square root of the gap and the coupling to superconductor. In Ref. [8] instead we introduce and analyze a class of multi-terminal devices where (electronic) heat and charge currents can follow different paths. We demonstrated that this regime allows to control independently heat and charge flows and to greatly enhance thermoelectric performances at low temperatures. We analyzed in details a three-terminal setup involving a superconducting lead, a normal lead and a voltage probe, showing that in the regime of heat-charge current separation both the power factor and the

figure of merit ZT are highly increased with respect to a standard two-terminal system. Building up from these effects a magnetic thermal switch for heat management at the nanoscale was then presented in Ref. [9], see Fig. 1.

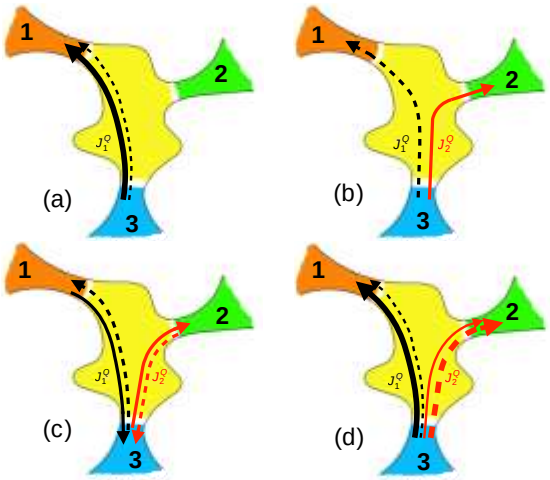

Figure 1. Schematic of the operational principle of the magnetic thermal switch discussed in Ref. [9] – figure taken from such article. 1,2, and 3, represent the contact of the models, while the arrows the heat currents that can be activated by properly changing the external magnetic field.

The Eigenstate Thermalization Hypothesis (ETH), quantum-quenched systems equilibrate towards canonical, thermal ensembles. While at first glance the ETH might seem a very strong hypothesis in Ref. [10] we showed that it is indeed not only sufficient but also necessary for thermalization. More specifically, we considered systems coupled to baths with well-defined macroscopic temperature and show that whenever all product states thermalize then the ETH must hold. Our result definitively settles the question of determining whether a quantum system has a thermal behavior, reducing it to checking whether its Hamiltonian satisfies the ETH.

In Ref. [15] we presented geometrical bounds for the irreversibility of open quantum system in the presence of thermal bath. Entropy production and thermalization effects were discuss in Ref. [16] while in Ref. [22] we consider control through instantaneous Gaussian unitary operations on the ubiquitous lossy channel, and find locally optimal conditions for the cooling and heating of a multimode Gaussian state subject to losses and possibly thermal noise.

In Ref. [17] we investigated a quantum battery made of N two-level systems, which is charged by an optical mode via an energy-conserving interaction. We quantified the fraction E(N) of energy stored in the battery that can be extracted in order to perform thermodynamic work demonstrating that E(N) is highly reduced by the presence of correlations between the charger and the battery or between the two-level systems composing the battery. We then showed that the correlation-induced suppression of extractable energy, however, can be mitigated by preparing the charger in a coherent optical state. We concluded by proving that the charger-battery system is asymptotically free of such locking correlations in the limit of large N. In Ref. [18] the energy charging of a quantum battery was analyzed in an open quantum setting, where the interaction between the battery element and the external power source is mediated by an ancilla system (the quantum charger) that acts as a controllable switch – see Fig. 2. In Ref. [19] a comparison between quantum and classical battery models was proposed.

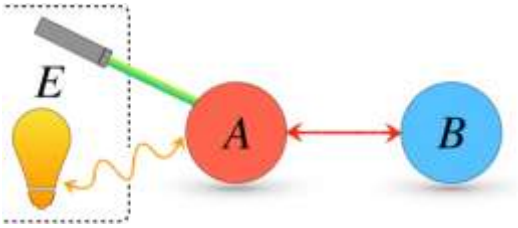

Figure 2. Schematic of the charger-mediated energy transfer model for quantum battery discussed in Ref. [18]- figure taken from the article. Here B is the battery, A the charger, and E the external energy source.

References

[1] R. Alicki, R. Kosloff, *Introduction to quantum thermodynamics: history and prospects. Thermodynamics in the Quantum Regime: Fundamental Aspects and New Directions*, Berlin, Springer (2019).

[2] J. Goold, M. Huber, A. Riera, L. del Rio, P. Skrzypczyk, *The role of quantum information in thermodynamics-a topical review*, J. Phys. A: Math. Theor. **49**, 143001 (2016).

[3] A. Mari, A. Farace, V. Giovannetti, *Quantum optomechanical piston engines powered by heat*, Journal of Physics B: Atomic, Molecular and Optical Physics **48 (17)**, 175501 (2015).

[4] A. Carlini, A. Mari, V. Giovannetti, *Time-optimal thermalization of single-mode Gaussian states*, Phys. Rev. A **90**, 052324 (2014).

[5] S. Valentini, R. Fazio, V. Giovannetti, F. Taddei, *Thermopower of three-terminal topological superconducting systems*, Phys. Rev. B **91**, 045430 (2015).

[6] S. Lorenzo et al., *Heat flux and quantum correlations in dissipative cascaded systems*, Phys. Rev. A **91**, 022121 (2015).

[7] V. Mukherjee et al., *Efficiency of quantum controlled non-Markovianthermalization*, New J. Phys. **17**, 063031(2015).

[8] F. Mazza et al., *Separation of heat and charge currents for boosted thermoelectric conversion*, Phys. Rev. B **91**, 245435 (2015).

[9] R. Bosisio et al., *Magnetic thermal switch for heat management at the nanoscale*, Phys. Rev. B **91**, 205420 (2015).

[10] G. De Palma et al., *Necessity of Eigenstate Thermalization*, Phys. Rev. Lett. **115**, 220401 (2015).

[11] V. Cavina, A. Mari, V. Giovannetti, *Optimal processes for probabilistic work extraction beyond the second law*, Scientific Reports **6**, 29282 (2016).

[12] O. Maillet et al., *Optimal Probabilistic Work Extraction beyond the Free Energy Difference with a Single-Electron Device*, Phys. Rev. Lett. **122**, 150604 (2019).

[13] V. Cavina, A. Mari, V. Giovannetti, *Slow Dynamics and Thermodynamics of Open Quantum Systems*, Phys. Rev. Lett. **119**, 050601 (2017).

[14] V. Cavina, A. Mari, A. Carlini, V. Giovannetti, *Optimal thermodynamic control in open quantum systems*, Phys. Rev. A **98**, 012139 (2018).

[15] L. Mancino et al., *Geometrical Bounds on Irreversibility in Open Quantum Systems*, Phys. Rev. Lett. **121**, 160602 (2018).

[16] S. Cusumano et al., *Entropy production and asymptotic factorization via thermalization: A collisional model approach*, Phys. Rev. A **98**, 032119 (2018).

[17] G.M. Andolina et al., *Extractable Work, the Role of Correlations, and Asymptotic Freedom in Quantum Batteries*, Phys. Rev. Lett. **122**, 047702 (2019).

[18] D. Farina et al., *Charger-mediated energy transfer for quantum batteries: An open-system approach*, Phys. Rev. B **99**, 035421 (2019).

[19] G.M. Andolina et al., *Quantum versus classical many-body batteries*, Phys. Rev. B **99**, 205437 (2019).

[20] P. A. Erdman et al., *Maximum power and corresponding efficiency fortwo-level heat engines and refrigerators: optimalityof fast cycles*, New J. Phys. **21**, 103049 (2019).

[21] P. Abiuso, V. Giovannetti, *Non-Markov enhancement of maximum power for quantum thermal machines*, Phys. Rev. A **99**, 052106 (2019).

[22] U. Shackerley-Bennett et al., *Locally optimal symplectic control of multimode Gaussian states*, Quantum Sci. Technol. **2**, 044014 (2017).

1.3.9 Topology in hybrid and multi-terminal Josephson junctions

Topologically protected systems have an large potential impact on quantum technologies, especially for quantum-computation purposes. Much attention was devoted to topological superconductivity and Majorana bound states (MBS) that are generated in hybrid platforms comprising semiconductors and superconductors with broken time-reversal symmetry. We explored both experimentally and theoretically possible signatures of topological transitions in these systems. Moreover, we investigated an alternative route to encode the topological protection in superconducting multiterminal Josephson-junction nanodevices. From tunneling conductance experiments we probed these new topological states that we proposed as an optimal platform to encode topologically-protected quantum-computation protocols.

Phase-controlled topological transitions

Hybrid devices based on superconducting proximity effect in multiterminal configurations offer also another opportunity to engineer topological non-trivial quantum states. We have realized the first double-loop Josephson interferometer [1] with three terminals (Fig. 1a) based on a proximized weak link and probed its characteristics via tunneling spectroscopy.

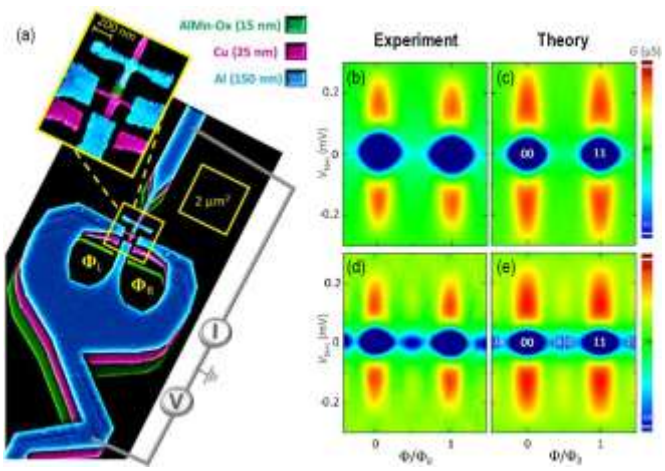

Figure 1. (a) The ω-SQUIPT, three-terminal double-loop Josephson interferometer based on the proximity effect. False-color tilted scanning electron micrograph. The inset highlights the core of the interferometer: a nanosized T-shaped proximized Cu weak link (magenta) in a clean metallic contact with two Al superconducting loops (blue). Loop area is around 2 μm². (b)-(e) Comparison between the tunneling conductance G vs V_{bias} measured at 30 mk (left panels) with theory (right panels) for symmetric (b and c) and asymmetric (d and e) length of the arm.

This structure promotes an additional phase control and allows an exotic phase-engineering of the weak-link topology which manifests in the peculiar behavior of the interferometer conductance.

Varying the phase differences between the three arms of the interferometer we observe transitions between gapped (insulating) and gapless (conducting) regions. The topological numbers characterizing such gapped states are given by superconducting phase windings over the two loops forming the Josephson interferometer. Since these gapped states cannot be transformed to one another continuously without passing through a gapless condition, they are topologically protected, demonstrating their non-trivial nature. The density of state of the three-terminal devices is accessed through a metallic tip tunnel-coupled to the weak link. Transitions between gapless and gapped regions are revealed by measurements of the tunneling conductance as a function of voltage bias and magnetic flux (Fig. 1b and Fig. 1d). Comparison with theoretical calculations fully confirms the mentioned scenario (Fig. 1c and Fig. 1e).

Topological nanodevices

We have recently proposed and theoretically examined a device based on a topological Josephson junction where the helical edge states of a two-dimensional (2D) topological insulator are in close proximity to two superconducting leads. The presence of a magnetic flux through the junction leads to a Doppler shift in the spectrum of Andreev bound states, and affects the quantum interference between proximized edge states. Such systems have been envisioned for several interesting applications, such as highly sensitive magnetometers [2], thermal switches and rectifiers [3]. Hybrid superconducting nanodevices are an ideal platform also to manipulate the entanglement in solid-state systems. Indeed, hybrid structures with topological insulators also show unique possibilities to manipulate the spin-symmetry of the entanglement by using external gates and easily addressed with measurement of the critical current [4].

References

[1] E. Strambini, S. D'Ambrosio, F. Vischi, F.S. Bergeret, Yu.V. Nazarov, F. Giazotto, *The ω-SQUIPT as a tool to phase-engineer Josephson topological materials*, Nature Nanotech. **11**, 1055 (2016).

[2] L. Bours, B. Sothmann, M. Carrega, E. Strambini, E. M. Hankiewicz, L. W. Molenkamp, F. Giazotto, *Topological SQUIPT Based on Helical Edge States in Proximity to Superconductors*, Phys. Rev. Applied **10**, 014027 (2018).

[3] L. Bours, B. Sothmann, M. Carrega, E. Strambini, A. Braggio, E.M. Hankiewicz, L.W. Molenkamp, F. Giazotto, *Phase-tunable thermal rectification in the topological SQUIPT*, Phys. Rev. Applied **11**, 044073 (2019).

[4] G. Blasi, F. Taddei, V. Giovannetti, A. Braggio, *Manipulation of Cooper pair entanglement in hybrid topological Josephson junctions*, Phys. Rev. B **99**, 064514 (2019).

1.3.10 Strain engineering in two-dimensional materials

Two-dimensional (2D) materials constitute a large family of one-atom-thick crystals offering a broad range of transport and optoelectronic properties. A key peculiarity of 2D materials is that the electron system is readily accessible at the surface of the crystal and can be easily tuned by the proximity of different materials as well as by other perturbations including, in particular, local mechanical deformations that can have a profound influence on the electron-system behavior.

The control of mechanical deformations in 2D materials, such as graphene, transition metal dichalcogenides, or even their Van der Waals heterostructures, opens exciting perspectives for the engineering of the electronic states and of the optoelectronic response. These include the possibility to create/tune the local bandgap, the creation of gauge field and strain-induced quantization and in general the modulation of the band dispersion and electron properties. While many of these concepts have been ideally validated in artificial-lattice studies, their actual implementation using true atomic lattices remains today largely elusive. In the past few years, we have developed a set of methods to controllably induce and measure strain in 2D crystals using different actuation strategies.

1. Measurement of local strain. The precise quantification of strain is an obvious key prerequisite to strain engineering, but it is also very important in view of the application of 2D crystals in the context of nanomechanical devices, such as nanoresonators (see Fig.1a). The current fabrication procedures are indeed typically based on delicate transfer schemes and thus prone to the creation of uncontrolled strain profiles in suspended membranes, which can have a detrimental/unknown effect on the final device behavior. The most common method to map strain in graphene and other 2D materials is micro Raman spectroscopy, whose resolution in the far field is limited by diffraction (typical laser excitation has a wavelength of 532nm). Near-field techniques can go beyond this limit and we have developed a method to precisely quantify the local mechanical properties by atomic force microscopy, thanks to a new procedure to deconvolve the complex combination of effects that determine the mechanical response of the membrane [4].

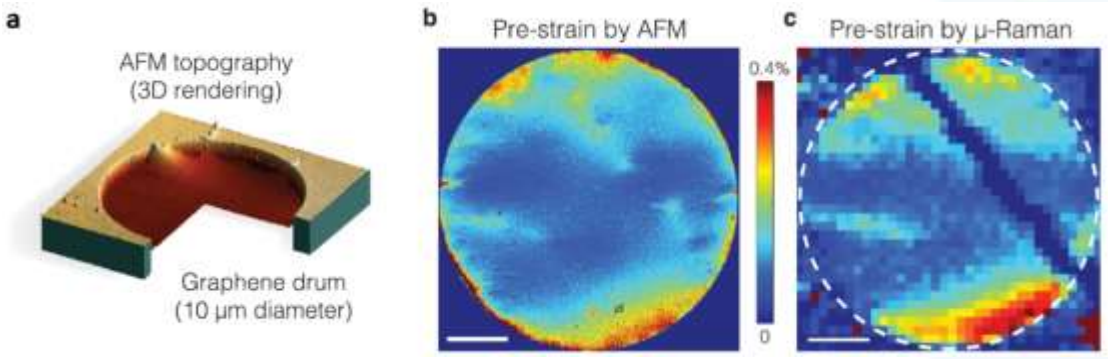

Figure 1. (a) Atomic force microscope (AFM) topography of a suspended graphene membrane. (b) Strain profile caused by fabrication, obtained based on AFM force spectroscopy. (c) Strain profile of the same membrane, obtained using conventional micro Raman. From [4].

2. Deterministic creation of custom strain profiles. A well-known method to strain a 2D material consists in creating a circular membrane and subject it to a

differential pressure, creating an approximately homogeneous strain profile. A first method we explored to induce custom strain profiles on graphene thus focused on the study of pressurized membranes with different shapes, since the *shape* of the membrane boundary has a direct effect on the induced *strain profile*. In particular, we have demonstrated how the application of a differential pressure to an elliptical membrane can be exploited to induce an anisotropic strain, depending on the orientation of the major and minor axes of the ellipse [6]. This simple approach has a limited flexibility with respect to the possibility to create true local strain actuators. For this reason, we demonstrated a novel method based polymeric actuators that can be nanopatterned with a great freedom by electron-beam nanolithography [2], see Fig.2a-c. In particular, strong local anisotropic strain could be demonstrated, as visible in Fig.2d and 2e, and the deterministic creation of nanowrinkles was reported in the suspended membrane. The method provides an ideal platform to induce custom strain profiles, which would be very challenging to obtain using more conventional techniques reported in the literature, and it can be easily combined with a variety of imaging and spectroscopic techniques including in particular scanning electron microscopy, atomic force microscopy and micro Raman and micro photoluminescence [3, 4]. All these techniques are in fact crucial to measure and understand the mechanical configuration of the material.

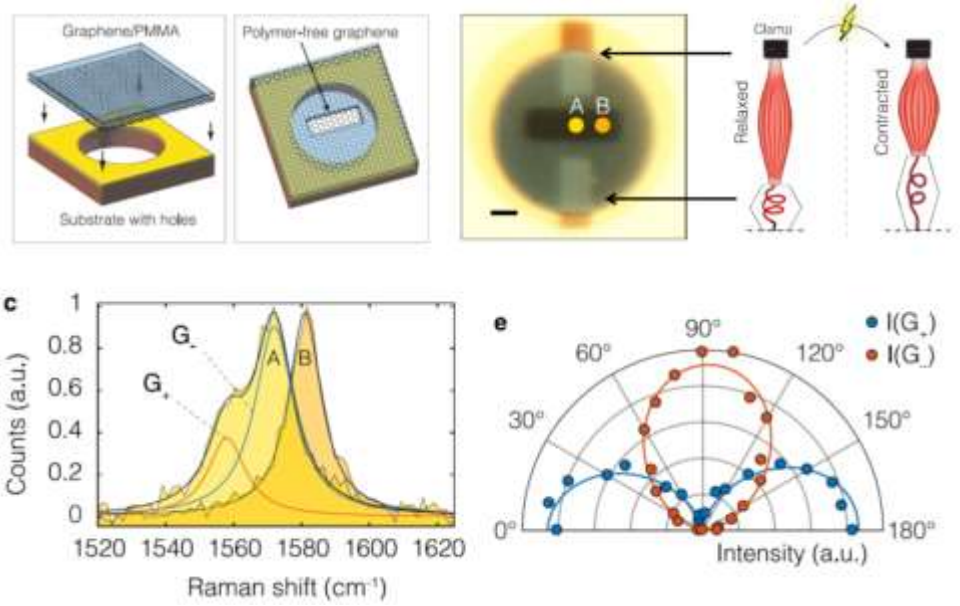

Figure 2. (a) Sketch of a suspended graphene membrane structure, including polymeric layers suitable for the creation of local strain actuators. (b) Optical image of one of the studied devices: the dark circular region corresponds to the suspended part of the membrane; shaded rectangles are the polymeric actuators. (c) Raman G-peak at position A and B of the membrane, see (b): no strain is detected in B while a strongly anisotropic strain is detected in the pulled region A. (d) Polarization-dependent measurements in position A highlights the oscillatory behavior of the amplitudes of the G+ and G- peaks; the effect can be used to directly determine the orientation of the crystal axes in the membrane. From [2].

3. Multilayer systems. A unique option of 2D materials is that they can be relatively easily stacked on different substrates [1] or in VdW heterostructures [4]. VdW systems are particularly promising in the context of the control of mechanical deformations, since the friction between the stacked layers can be very low. In this case, in our activities we studied the deformation of WS_2 on top

of graphene, using its impact on the position of the local photoluminescence (PL) response of the dichalcogenide monolayer as a probe of the local induced strain, see Fig. 3. The same approach can be applied to the many possible combinations of 2D materials that are currently studied within the scientific community and we expect it to be relevant for the creation of deterministic wrinkle structures and to control the relative mechanical configuration of the stacked layers, which is known to have a strong influence on the electronic states.

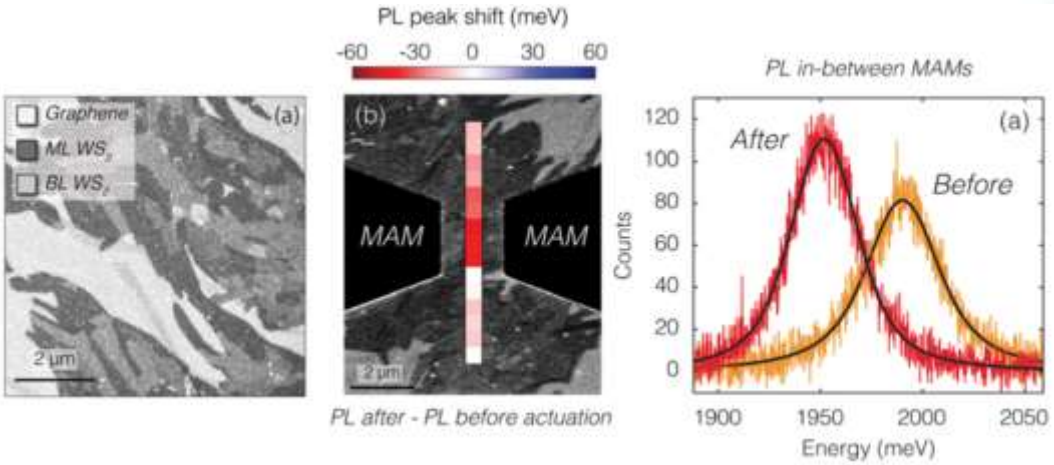

Figure 3. (a) Scanning electron micrograph of one of the WS2-graphene heterostructures obtained by chemical vapor deposition of WS2 on top of bilayer graphene obtained by thermal decomposition of SiC. (b) Typical device structure, including two polymeric actuators (micrometric artificial muscles, MAMs) pulling the WS2 in the horizontal direction; in overlay, averaged shift of the photoluminescence (PL) position. (c) Comparison between the PL of the pristine WS2 crystal and after the strain actuation. From [3].

References

[1] I. Aliaj, A. Sambri, V. Miseikis, D. Stornaiuolo, E. Di Gennaro, C. Coletti, V. Pellegrini, F.M. Granozio, S. Roddaro, *Probing charge transfer during metal-insulator transitions in graphene-LaAlO3/SrTiO3 systems*, APL Materials **6**, 066103 (2018).

[2] F. Colangelo, A. Pitanti, V. Miseikis, C. Coletti, P. Pingue, D. Pisignano, F. Beltran, A. Tredicucci, S. Roddaro, *Controlling local deformation in graphene using micrometric polymeric actuators*, 2D Materials **5**, 045032 (2018).

[3] F. Colangelo, A. Morandi, S. Forti, F. Fabbri, C. Coletti, F.V. Di Girolamo, A. Di Lieto, M. Tonelli, A. Tredicucci, A. Pitanti, S. Roddaro, *Local tuning of WS2 photoluminescence using polymeric micro-actuators in a monolithic van der Waals heterostructure*, Applied Physics Letters **115**, 183101 (2019).

[4] F. Colangelo, P. Pingue, V. Miseikis, C. Coletti, F. Beltram, S. Roddaro, *Mapping the mechanical properties of a graphene drum at the nanoscale*, 2D Materials **6**, 025005 (2019).

[5] F.V. Di Girolamo, A. Di Lieto, A. Sottile, S. Roddaro, M. Tonelli, A. Tredicucci, *Microphotoluminescence (uPL) measurements of bidimensional materials in a custom-made setup*, Journal of Physics **1226**, 012008 (2019).

[6] F.F. Settembini, F. Colangelo, A. Pitanti, V. Miseikis, C. Coletti, G. Menichetti, R. Colle, G. Grosso, A. Tredicucci, S. Roddaro, *Anisotropic straining of graphene using micropatterned SiN membranes*, APL Materials **4**, 116107 (2016).

1.3.11 Hydrogen storage in functionalized graphene

Owing to its large surface-to-mass ratio, graphene is a promising candidate for hydrogen storage. However, hydrogen is weakly physisorbed by graphene so that useful storage densities can be achieved only at low temperature/high pressure. Conversely, chemisorption leads to stable loading at room temperature, but with slow kinetics. We have investigated both physi- and chemisorption of hydrogen on functionalized graphene in the perspective of improving its performance for applications.

All amazing properties of graphene – high carrier mobility, robustness and flexibility, broadband transmittance, large surface to mass ratio, lubricity – rely on its being a perfect 2D hexagonal crystal. However, this brings also some drawbacks, such as zero density of states at the Dirac point, weak interactions and reactivity, limiting its potential both in nanoelectronics and in storage applications. These, in addition, require functionalization or building 3D graphene-based scaffolds. We combine Density Functional Theory (DFT), classical Molecular Dynamics (MD), Scanning Tunneling Microscopy (STM), Low Energy Electron Diffraction (LEED), and nanocalorimetry to the aim of functionalizing and morphing graphene for energy applications. To these aims, graphene imperfections acquire a new significance: the crystal symmetry breaking through chemical defects, structural deformations, or other types of disorder creates electron density inhomogeneities with an enhancement of reactivity and new interaction capabilities.

Our work focuses mainly on epitaxial monolayer graphene grown on SiC. Both the buffer layer on SiC [1,2], obtained by Si evaporation and partially covalently bound to the substrate, and quasi free-standing monolayer graphene (QFMLG) [2-5], obtained by metal [6] or H intercalation [2,5], show possible "hot spots" of chemical reactivity located on nanosized super lattices, which could be exploited for chemical nanopatterning. On the other hand, grain boundaries of supported nanocrystalline graphene are shown to pin Ti clusters more efficiently than single-crystalline graphene [7].

In the last years we have performed combined Density Functional Theory (DFT) and Scanning Tunneling Microscopy (STM) studies of graphene with different kinds of irregularities. Starting from carbon layers epitaxially grown on silicon carbide (SiC) by Si evaporation, the covalently bond buffer layer (BL) can be viewed as extremely distorted graphene, because its structures includes a large portion of sp^3 hybridized sites, organized on a nanosized superlattice. Our DFT studies [1] reveal the space-resolved electronic structure of the system as well as the location and shape of localized states, and give indications on the reactivity of the different sites to additive or substitutive reactions, which could be exploited for controlled nanopatterning. Conversely, quasi free-standing monolayer graphene QFMLG, formed by hydrogen intercalation under the BL, is completely sp^2 hybridized, but the regularity of the electronic structure is disrupted by the presence of localized states in correspondence to H vacancies. By means of a combined STM-DFT [3,4] study we have completely characterized these states, which appear to locate on a regular nanosized super lattice [5] and have various shapes and tunable energy depending on their size, opening opportunities in optoelectronics and controlled chemical nanopatterning (Fig. 1) [8].

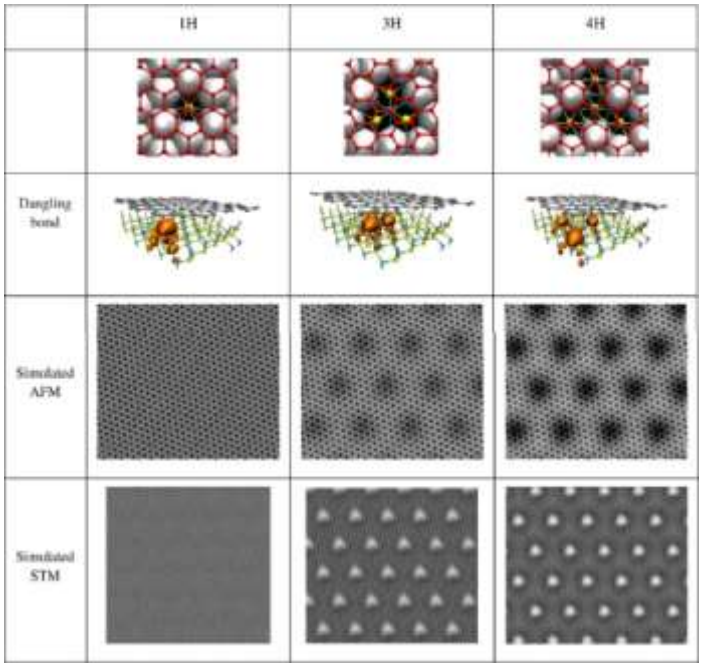

Figure 1. Theoretical analysis of the structure of vacancies with one, three, and four missing H atoms (columns 1H, 3H, 4H). The fully relaxed structure models of the vacancies are represented in the first row, where the graphene lattice, Si, and substrate C atoms are colored red, yellow, and cyan, respectively. H atoms are represented by white spheres. Second and third row are the simulated AFM and STM images, respectively. From Ref. [4].

The graphene functionalization with Ti has been widely investigated in several samples: epitaxial monolayer graphene (EMLG) [9-11], CVD grown graphene [12], and nanocrystalline graphene grown on Ge(110) [7]. Corrugation and other kinds of structural defects can favor the adhesion of metal clusters (e.g. Ti) [11]. We showed that grain boundaries of nanocrystalline graphene are attractors for Ti clusters [7], which form a larger amount of smaller Ti islands on it than on monocrystalline graphene. The hydrogen uptake has been investigated as a function of Ti coverage up to about 1 ML [9]. Hydrogen is capable of different kinds of binding modes with the Ti clusters, both in atomic and molecular form [10]. In other words, hydrogen exploits both physisorption and chemisorption on such samples, but physisorption can be observed at low temperatures only. The physisorption of H_2 on functionalized graphene has been studied by thermal desorption spectroscopy (TDS), utilizing epitaxial monolayer graphene (EMLG) [10] and nanocrystalline graphene (Fig. 2) [7]. In both cases, however, the main feature that has been observed is related to chemisorption. Indeed, the nanocrystalline samples show a lower chemisorption yield than the EMLG samples. This effect is related to the strong bonds between Ti and the defects on the surface, which influences the electronic structure of the Ti clusters.

A particular effort has been made to study the energetics of the hydrogen storage process. Therefore, beside the well-established TDS evaluation of the H_2 binding energy, an original calorimetric technique has been developed [12]. The technique allowed, for the first time, both to measure the heat released during the hydrogenation process in real time and the non-destructive quantification of the hydrogen stored, with an extremely high sensitivity (5 μJ and 0.2 ng). Our

nanocalorimeter is based on a gold film thermometer as detector. The thermometer has been upgraded recently utilizing a mica substrate, which allows for a better performance and has an atomically flat surface, suitable for STM analysis [13].

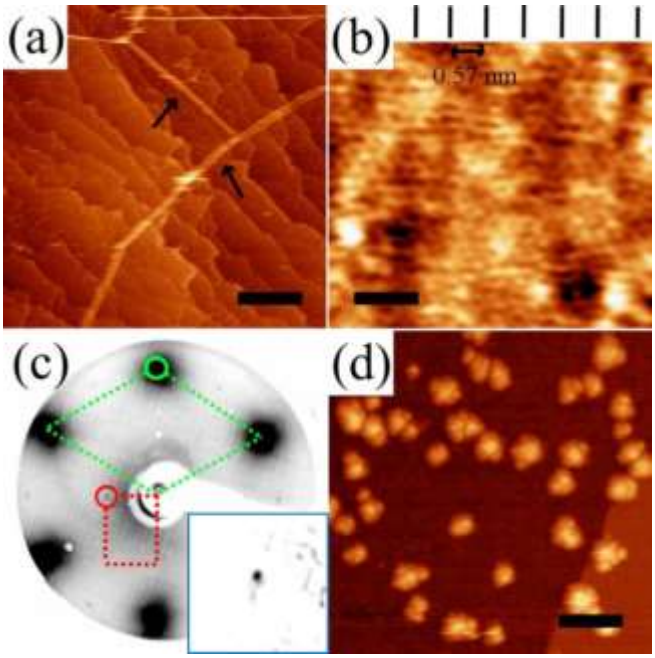

Figure 2. Ti on nanocrystalline graphene. (a) STM image, scan size 1000 nm x 1000 nm. (b) STM image, scan size 5 nm x 5 nm. Vertical lines indicate the periodicity of the Ge(110)-[110] lattice. (c) LEED pattern with electron energy 75 eV. (d) STM image after Ti deposition of 0.55 ML, scan size 100 nm x 100 nm. From Ref. [7].

Hydrogen chemisorption has been widely investigated in structurally deformed graphene [14]. Our idea is to exploit the natural corrugation of graphene grown on SiC to enhance one or more of the mentioned features. The moiré pattern of corrugation is multi-stable and can be manipulated by changing environmental conditions (e.g. temperature, external fields). This in turn opens the possibility of manipulating reactivity, which is shown to be larger on convexities. This increases the adhesion of hydrogen in atomic form (Fig. 3). Besides, electric [15] or electrochemically driven functionalization is shown to be a viable route to control H adhesion, and is enhanced by the presence of structural defects such as epoxy or hydroxyl groups produced by oxidation so to allow the combination of H-storage with water splitting for new concept devices in the clean energy field.

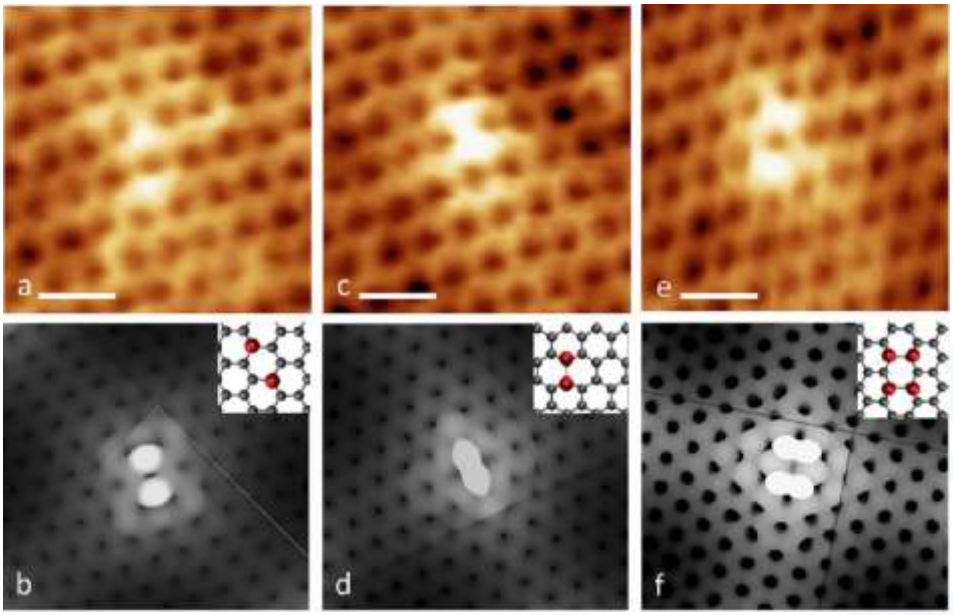

Figure 3. (a) A para dimer observed by STM on EMLG after a dose of 5 s of atomic hydrogen. (b) Simulated STM image by DFT calculation. (c) STM image of an ortho dimer and (d) corresponding simulation. (e) STM image of a tetramer and (f) corresponding simulation. Scale bar in (a), (c), (e) is 0.4 nm. From Ref. [14].

References

[1] T. Cavallucci, V. Tozzini, *Intrinsic structural and electronic properties of the Buffer Layer on Silicon Carbide unraveled by Density Functional Theory*, Sci. Rep. **8**, 13097 (2018).

[2] S. Goler, C. Coletti, V. Piazza, P. Pingue, F. Colangelo, V. Pellegrini, K.E. Emtsev, S. Forti, U. Starke, F. Beltram, S. Heun, *Revealing the atomic structure of the buffer layer between SiC(0001) and epitaxial graphene*, Carbon **51**, 249 (2013).

[3] T. Cavallucci, Y. Murata, M. Takamura, H. Hibino, S. Heun, V. Tozzini, *Unraveling localized states in quasi free standing monolayer graphene by means of Density Functional Theory*, Carbon **130**, 466 (2018).

[4] Y. Murata, T. Cavallucci, V. Tozzini, N. Pavliček, L. Gross, G. Meyer, M. Takamura, H. Hibino, F. Beltram, S Heun, *Atomic and Electronic Structure of Si Dangling Bonds in Quasi-Free-Standing Monolayer Graphene*, Nano Res. **11**, 864 (2018).

[5] Y. Murata, T. Mashoff, M. Takamura, S. Tanabe, H. Hibino, F. Beltram, S. Heun, *Correlation between morphology and transport properties of quasi-free-standing monolayer graphene*, Appl. Phys. Lett. **105**, 221604 (2014).

[6] S. Fiori, Y. Murata, S. Veronesi, A. Rossi, C. Coletti, S. Heun, *Li-intercalated graphene on SiC(0001): An STM study*, Phys. Rev. B **96**, 125429 (2017).

[7] Y. Murata, S. Veronesi, D. Whang, S Heun, *Morphology of Ti on Monolayer Nanocrystalline Graphene and Its Unexpectedly Low Hydrogen Adsorption*, J. Phys. Chem. C **123**, 1572 (2019).

[8] L. Bellucci, T. Cavallucci, V. Tozzini, *From the buffer layer to graphene on silicon carbide: exploring morphologies by computer modeling*, Front. in Mater. **6**, 198 (2019).

[9] T. Mashoff, M. Takamura, S. Tanabe, H. Hibino, F. Beltram, S. Heun, *Hydrogen storage with titanium-functionalized graphene*, Appl. Phys. Lett. **103**, 013903 (2013).

[10] K. Takahashi, S. Isobe, K. Omori, T. Mashoff, D. Convertino, V. Miseikis, C. Coletti, V. Tozzini, S. Heun, *Revealing the multibonding state between hydrogen and graphene-supported Ti clusters*, J. Phys. Chem. C **120**, 12974 (2016).

[11] T. Mashoff, D. Convertino, V. Miseikis, C. Coletti, V. Piazza, V. Tozzini, F. Beltram, S. Heun, *Increasing the active surface of titanium islands on graphene by nitrogen sputtering*, Appl. Phys. Lett. **106**, 083901 (2015).

[12] L. Basta, S. Veronesi, Y. Murata, Z. Dubois, N. Mishra, F. Fabbri, C. Coletti, S. Heun, *A sensitive calorimetric technique to study energy (heat) exchange at the nano-scale*, Nanoscale **10**, 10079 (2018).

[13] S. Veronesi, T. Papa, Y. Murata, S. Heun, *An atomically flat single-crystalline gold film thermometer on mica to study energy (heat) exchange at the nano-scale*, Appl. Surf. Sci. **512**, 145658 (2020).
[14] S. Goler, C. Coletti, V. Tozzini, V. Piazza, T. Mashoff, F. Beltram, V. Pellegrini, S. Heun, *Influence of graphene curvature on hydrogen adsorption: toward hydrogen storage devices*, J. Phys. Chem. C **117**, 11506 (2013).
[15] Y. Murata, A. Calzolari, S. Heun, *Tuning hydrogen adsorption on graphene by gate voltage*, J. Phys. Chem. C **122**, 11591 (2018).

1.3.12 Scalable high-mobility graphene for photonics and biomedicine

Often mentioned as the "wonder material", graphene, has shown a cornucopia of new physics and potential novel applications. Years after its discovery, although basic science is definitely still not exhausted, there is a great possibility to demonstrate technologically viable high-tech applications in fields such as photonics and biomedicine. For most of these applications scalable high-mobility graphene is necessary. Here, we demonstrate different approaches that yield wafer scale production of graphene with qualities comparable to those of flakes obtained via mechanical exfoliation. We report high-performance photonic devices and possible biomedical applications.

Photonics is an extremely promising realm of applications for graphene, whose lack of bandgap strongly hinders its use in conventional digital logic devices. The same lack of bandgap makes graphene a unique broadband absorption material that further presents electro-absorption and electro-refraction for modulators and switches and photo-thermoelectric effect for detectors. Also, graphene holds the potential to overcome the present limitations of optical interconnects in Datacom and Telecom communications by providing integrated optical components with superior performances, reduced cost, minimal power consumption and footprint. This potential could be however unfulfilled if high-carrier mobilities (above 10 000 cm^2/Vs @ 10^{12} cm^{-2} at room temperature (RT)) are not demonstrated over wafer-scale and on technologically relevant substrates, thus ensuring competitive modulation, detection and switching performances. Graphene exfoliated flakes present an extraordinary mobility thanks to their high crystallinity and only when devices are fabricated in ideal conditions (i.e., flakes are suspended or encapsulated in extremely flat, clean and low-interacting materials) so that carrier transport is not disrupted. In 2014 there was still no viable approach in literature to obtain high mobility graphene over wafer-scale because fundamental issues in the growth, transfer and interface control of graphene needed to be solved. At NEST, we have demonstrated in the last years the synthesis of wafer-scale graphene with carrier mobilities comparable to those of exfoliated flakes and that this mobility can be preserved in devices by finely engineering graphene interface with bulk substrates and overlayers.

In first instance, we perfectioned the synthesis [1-3] and investigated the photonic performance of graphene synthesized via different approaches on silicon carbide (SiC) [4-6]. In 2014, this synthetic approach was the most promising to obtain graphene with high carrier mobilities on a scalable substrate. The observation of THz saturable absorption [4, 6] and THz detection [5] further stimulated our efforts to find alternative ways to synthesize scalable graphene for photonic applications. Indeed, SiC is an expensive substrate and considered a niche material for technological applications.

We hence started to perfect growth of graphene on copper (Cu) foil, a substrate that allowed at the time to obtain polycrystalline graphene that could be transferred to any target substrate. We first demonstrated the synthesis of large single-crystals of graphene (up to 4 mm in size) on Cu foil via chemical vapor deposition (CVD) by carefully controlling the substrate chemistry and growth conditions [7]. On these single-crystals, high performing devices with notable electrical performance could be obtained [8]. We subsequently demonstrated a novel approach which led to the first report of deterministically grown single-crystal graphene arrays with dimensions suitable for the realization of photonic devices (i.e., each crystal being hundreds of micrometers) (see Fig. 1) [9]. Such

seeded growth approach allows one to obtain high-mobility single-crystal graphene exactly where is needed (i.e., seed deposition is implemented according to the design and placement of the final devices). We presented a protocol to deterministically transfer the arrays to the target substrate, where photonic components can be realized each on a single crystal. Graphene RT mobilities approach 10 000 cm^2/Vs on conventional SiO_2/Si substrates and are above 20 000 cm^2/Vs on hBN [9].

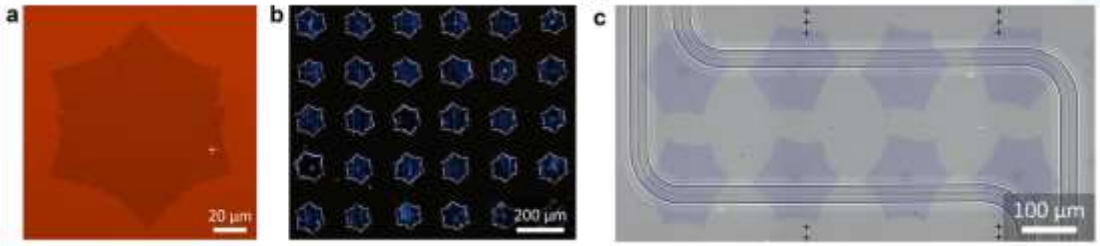

Figure 1. (a) Optical image of a typical single-crystal deterministically grown within an array on Cu foil and transferred on 285 nm SiO_2. (b) Dark-field microscopy image of a graphene array. (c) False color optical image of an array transferred on top of two adjacent waveguides.

By using these graphene matrixes, we have demonstrated high-performance photonics building-blocks such as modulators and detectors [10-12]. In particular, in collaboration with commercial partners such as Nokia and Thales, we have demonstrated ultrafast electro-absorption modulators (working at 50 Gb/s) [10] and photodetectors (with a flat band response up to 67 GHz) [12] integrated on silicon passive waveguides. To preserve graphene mobility during device fabrication we proposed different solutions: adopting a polymeric top dielectric (whose deposition does not damage graphene) [12] or a sacrificial 2D layer prior to dielectric deposition [10]. Several other novel photonic geometries and devices have been demonstrated by adopting graphene synthesized on copper [13-15]. We have also recently demonstrated that the electronic properties of the graphene single-crystals are entirely equivalent to those of exfoliated flakes [16]. We have shown that, in hBN-encapsulated CVD-graphene single-crystals, mobilities exceed 140 000 cm^2/Vs at RT (600 000 cm2/Vs at low temperature) and that signatures of electronic correlation, including the fractional quantum Hall effect are observed under magnetic fields [16].

Although graphene matrixes grown on Cu hold great potential for photonics, the back-end-of-line (BEOL) integration of this material might encounter problems if the amount of Cu contamination is above the allowed limits. To overcome this hurdle, we recently proposed and demonstrated an elegant solution that makes graphene a fab-compatible material while maintaining satisfying electronic performances over wafer-scale. In Ref. [17] we demonstrate for the first time the metal-free growth of monolayer graphene on 4-inch and 6-inch sapphire wafers and identified the sapphire surface reconstruction $(\sqrt{31}\times\sqrt{31})R9°$ as crucial to obtain high-quality epitaxial graphene. To broaden the applicative range of the grown material, we demonstrated that entire wafers of graphene can be transferred to any target substrate with a metal-free polymeric lamination approach. A high degree of uniformity and consistency, which is crucial for any industrial process, was observed in all produced graphene wafers (Fig. 2) and the

measured metal contamination levels was found to fully satisfy BEOL integration requirements.

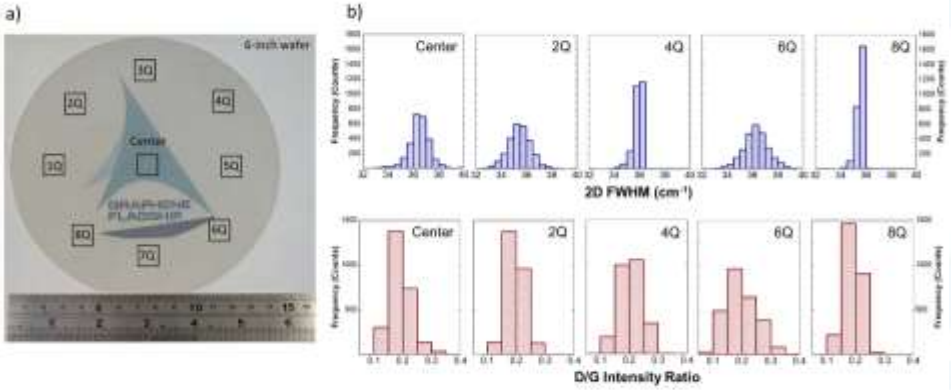

Figure 2. Characterization of graphene grown on 6-inch sapphire wafer. (a) Optical image of the grown wafer, with squares indicating the approximate locations where Raman measurements were performed. (b) Raman analysis of graphene grown on a 6-inch sapphire wafer, measured at 5 different places.

Graphene could also become a central material in biomedicine, due to its exceptional electrical, optical and tribological properties. On this regard, its biocompatibility, transparency and high electrical conductivity make it an interesting candidate for the development of biosensors. On this topic, we have patented a platform for the isolation from biological fluids and characterization by optical and biological assays of exosomes, which are early-stage cancer markers [17]. Also, we have investigated graphene potential for the development of novel neural conduit for regenerative medicine. In Ref. [18], we reported increased elongation and differentiation of peripheral neuronal cells grown on graphene. However, to date, the molecular mechanism driving axon elongation had remained elusive. Hence, we studied the axonal transport of nerve growth factor (NGF), the neurotrophin supporting development of peripheral neurons, as a key player in the time course of axonal elongation of dorsal root ganglion neurons on graphene [19]. We found that graphene drastically reduces the number of retrogradely transported NGF vesicles in favor of a stalled population in the first 2 days of culture, in which the boost of axon elongation was observed. Targeted spectroscopic, ultrastructural and electrophysiological studies indicate that both electrophysiological and structural effects account for graphene action on neuron development [19].

References

[1] C. Coletti, S. Forti, A. Principi, K.V. Emtsev, A.A. Zakharov, K.M. Daniels, B.K. Daas, M.V.S. Chandrashekhar, A.H. MacDonald, M. Polini, U. Starke, *The ABC of trilayer graphene*, MRS proceedings **1693** (2014).

[2] D. Convertino, A. Rossi, V. Miseikis, V. Piazza, C. Coletti, *Thermal decomposition and chemical vapor deposition: a comparative study of multi-layer growth of graphene on SiC(000-1)*, MRS Advances **1 (55)**, 3667 (2016).

[3] A. Candini, N. Richter, D. Convertino, C. Coletti, F. Balestro, W. Wernsdorfer, M. Kläui, M. Affronte, *Electroburning of few-layer graphene flakes, epitaxial graphene, and turbostratic graphene discs in air and under vacuum*, Beilstein J. Nanotechnol. **6**, 711 (2015).

[4] F. Bianco, V. Miseikis, D. Convertino, J.-H. Xu, F. Castellano, H.E. Beere, D.A. Ritchie, M.S. Vitiello, A. Tredicucci, C. Coletti, *THz saturable absorption in turbostratic multilayer graphene on silicon carbide*, Optics Express **23 (9)**, 11632 (2015).
[5] F. Bianco, D. Perenzoni, D. Convertino, S.L. De Bonis, D. Spirito, M. Perenzoni, C. Coletti, M.S. Vitiello, A. Tredicucci, *Terahertz detection by epitaxial-graphene field-effect-transistors on silicon carbide*, Applied Physics Letters **107 (13)**, 131104 (2015).
[6] F. Meng, M.D. Thomson, F. Bianco, A. Rossi, D. Convertino, A. Tredicucci, C. Coletti, H.G. Roskos, *Saturable absorption of femtosecond optical pulses in multilayer turbostratic graphene*, Optics Express **24 (14)**, 15261 (2016).
[7] V. Miseikis, D. Convertino, N. Mishra, M. Gemmi, T. Mashoff, S. Heun, N. Haghighian, F. Bisio, M. Canepa, V. Piazza, C. Coletti, *Rapid CVD growth of millimetre-sized single crystal graphene using a cold-wall reactor*, 2D Materials **2 (1)**, 014006 (2015).
[8] S. Xiang, V. Miseikis, L. Planat, S. Guiducci, S. Roddaro, C. Coletti, F. Beltram, S. Heun, *Low-temperature quantum transport in CVD-grown single crystal graphene*, Nano Research **9 (6)**, 1823 (2016).
[9] V. Miseikis, F. Bianco, J. David, M. Gemmi, V. Pellegrini, M. Romagnoli, C. Coletti, *Deterministic patterned growth of high-mobility large-crystal graphene: a path towards wafer scale integration*, 2D Materials **4 (2)**, 021004 (2017).
[10] M.A. Giambra, V. Sorianello, V. Miseikis, S. Marconi, A. Montanaro, P. Galli, S. Pezzini, C. Coletti, M. Romagnoli, *High-speed double layer graphene electro-absorption modulator on SOI waveguide*, Optics express **27 (15)**, 20145 (2019).
[11] J.E. Muench, A. Ruocco, M.A. Giambra, V. Miseikis, D. Zhang, J. Wang, H.F.Y. Watson, G.C. Park, S. Akhavan, V. Sorianello, M. Midrio, A. Tomadin, C. Coletti, M. Romagnoli, A.C. Ferrari, I. Goykhman, *Waveguide-integrated, plasmonic enhanced graphene photodetectors*, Nano Letters **19 (11)**, 7632 (2019).
[12] V. Miseikis, S. Marconi, M.A. Giambra, A. Montanaro, L. Martini, F. Fabbri, S. Pezzini, G. Piccinini, S. Forti, B. Terrés, I. Goykhman, L. Hamidouche, P. Legagneux, V. Sorianello, F. Koppens, A.C. Ferrari, M. Romagnoli, C. Coletti, *Ultrafast, Zero-Bias, Graphene Photodetectors with Polymeric Gate Dielectric on Passive Photonic Waveguides*, ACS Nano (accepted).
[13] S. Zanotto, C. Lange, A. Pitanti, V. Miseikis, C. Coletti, R. Degl'Innocenti, L. Baldacci, R. Huber, A. Tredicucci, *Magneto-optic transmittance modulation observed in a hybrid graphene-split ring resonator terahertz metasurface*, Applied Physics Letters **107 (12)**, 121104 (2015).
[14] S. Zanotto, F. Bianco, V. Miseikis, D. Convertino, C. Coletti, A. Tredicucci, *Coherent absorption of light by graphene and other optically conducting surfaces in realistic on-substrate configurations*, APL Photonics **2 (1)**, 019901 (2017).
[15] A. Candini, L. Martini, Z. Chen, N. Mishra, D. Convertino, C. Coletti, A. Narita, X. Feng, K. Müllen, M. Affronte, *High Photoresponsivity in Graphene Nanoribbon Field-Effect Transistor Devices Contacted with Graphene Electrodes*, The Journal of Physical Chemistry C **121 (19)**, 10620 (2017).
[16] S. Pezzini, V. Mišeikis, S. Pace, F. Rossella, K. Watanabe, T. Taniguchi, C. Coletti, *High-quality electrical transport using scalable CVD graphene*, 2D Materials **7**, 041003 (2020).
[17] V. Voliani, C. Coletti, G. Signore, S. Luin, V. Piazza, F. Beltram, *Biosensore grafenico per l'analisi di esosomi in fluidi biologici, suoi procedimenti di preparazione e relativi usi, (Device with electronic or optical readout for the recognition of Exosomes from human fluids - EGVC test)*, Italian Patent Application TO2014A001005 - PT140236 (2014).
[18] D. Convertino, S. Luin, L. Marchetti, C. Coletti, *Peripheral neuron survival and outgrowth on graphene*, Frontiers in neuroscience **12**, 1 (2018).
[19] D. Convertino, F. Fabbri, N. Mishra, M. Mainardi, V. Cappello, G. Testa, S. Capsoni, L. Albertazzi, S. Luin, L. Marchetti, C. Coletti, *Graphene promotes axon elongation through local stall of Nerve Growth Factor signaling endosomes*, Nano Letters **20 (5)**, 3633 (2020).

1.3.13 Synthesis and properties of van der Waals heterostructures

Van der Waals heterostructures (vdWh) are "designer heterostructures" made by assembling two-dimensional (2D) sheets in a precisely chosen sequence. They are a playground for fundamental studies with the potential to reveal unusual properties and new phenomena. Before 2014, vdWh presented limited lateral dimensions, being obtained via mechanical exfoliation of bulk crystals and a cumbersome process of mechanical assembly. This hindered not only the technological prospects of vdWh, but also their accessibility to a number of techniques of interest for fundamental studies. We demonstrated that it is possible to synthesize a large number of high-quality and scalable vdWh via chemical vapor deposition (CVD) and that these materials host enticing optical, electronic and nanomechanical properties and significant applicative prospects.

In the last years we have demonstrated the synthesis and investigated the properties and applicative prospects of different vdWh that can be grouped as follows: (i) vdWh based on 2D transition metal dichalcogenides (TMDs); (ii) vdWh based on uncharted 2D materials; (iii) twisted vdWh with controlled azimuthal angles.

(i) By 2014, a large plethora of 2D materials beyond graphene had been isolated via mechanical exfoliation. Among them, 2D semiconducting TMDs displayed strong appeal for fundamental studies (e.g. direct bandgap transition, extraordinary photoluminescence, giant exciton binding energies, sizable spin-splitting, valley degree of freedom) and great applicative potential in optoelectronics and spintronics. The combination in a vertical structure of semimetallic graphene and 2D TMDs was identified as a largely uncharted and extremely exciting playground to realize and to investigate. The first results in this direction were published in Ref. [1], where we demonstrated a critical step in the scalable CVD synthesis of vdWh by reporting for the first time the direct growth of a continuous atomic-thick layer of tungsten disulfide (WS_2) on different 2D materials such as hexagonal boron nitride (hBN) and graphene. In view of applications where the transduction of quantum information is crucial (e.g., electro-optical transducers), this work showed that the synthesized heterostacks present a remarkable conservation of polarization peaking at 74%. Furthermore, we presented an approach for the bottom-up fabrication of photoconductive and photoemitting patterns in WS_2 on epitaxial graphene on silicon carbide (SiC), where the quantum-optical properties of WS_2 can be combined with the outstanding ballistic transport properties of graphene [1]. Among the heterostacks demonstrated in Ref. [1], we selected that of WS_2 on epitaxial graphene on SiC as the ideal one to further adopt for fundamental investigations because of its extreme cleanliness. Microscopic and spectroscopic characterization by using in-house and synchrotron facilities demonstrated a 0° azimuthal alignment of graphene and WS_2 as well as the largest reported spin-orbit splitting for monolayer WS_2 (i.e., 462 meV) [2]. With tailored nanotribological studies, we also demonstrated superlubric sliding of WS_2 on graphene on SiC induced by scanning microscopy techniques [3]. We interpreted the reported experimental results by means of classical molecular dynamics simulations which indicated that an ultra-low friction motion is triggered by the tip-sample interaction. Further experiments presented in the paper demonstrated that our growth approach led to an atomically sharp WS_2/graphene interface, which is ideal for nanotribology investigations. The aging of monolayer WS_2 synthesized on epitaxial graphene was thoroughly studied and the effect of defects

in accelerating the aging process assessed and modeled [4]. Spectroscopic ellipsometry was used to investigate the complex dielectric function of WS_2 flakes on epitaxial graphene [5]. Also, we recently reported the direct evidence for efficient ultrafast charge separation in WS_2/graphene heterostructures by performing time- and angle-resolved photoemission spectroscopy (tr-ARPES) investigations [6]. After having explored the optical, electronic, chemical and nanotribological properties of this heterostack [1-6], we tested its application in the field of optoelectronics. In Refs. [7] and [8], we reported original approaches for the fabrication of optoelectronic devices on up to 4 inches wafers. Thanks to these approaches, low contact resistance, band alignment control, and ultimately high-performing devices could be achieved. In Ref. [7], a wavelength dependent persistent photocurrent (PPC) was observed, making this system interesting for the implementation of 2D-based data storage devices. As SiC is often considered a niche substrate for device fabrication, we recently demonstrated the possibility to obtain WS_2/graphene arrays (that behave as unipolar optoelectronic component) on the technologically relevant substrate SiO_2/Si [9]. Also, we reported on the possibility of using TMD/graphene stacks for realizing low-voltage field-effect-transistors (FETs) for digital and analog electronics [10].

(ii) In Ref. [11] and [12], we realized novel 2D materials by intercalating a single layer of copper and gold atoms, respectively, in between SiC and graphene. In particular, in Ref. [12] we were the first to report on the synthesis and properties of 2D gold (2D-Au). We demonstrated that graphene imposes a crystalline order on the gold layer, thereby allowing its electronic properties to unravel. ARPES studies showed that 2D-Au is remarkably a semiconductor with the valence band maximum 50 meV below the Fermi level, significant spin-orbit splitting, and a saddle point at −400 meV, meaning that the van Hove singularity (vHS) in the density of states is at an energy at reach for electronic measurements (Fig. 1). This makes this system an appealing platform for the exploration of collective phenomena at low temperatures and non-linear optics effects.

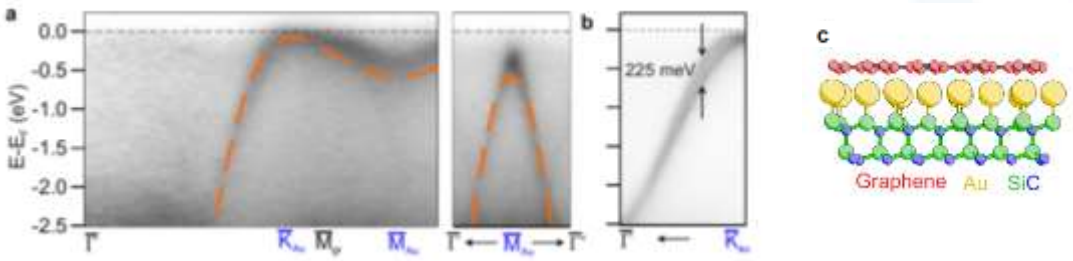

Figure 1. Electronic band structure of 2D-Au. (a) ARPES cut along k_y showing the Au bands dispersion (left panel) and spectrum cuts along k_x direction (right panel). The orange dashed lines superimposed to the data are tight-binding bands. (b) Au bands dispersion along the ky direction highlighting their spin-orbit splitting. Photon energy is 95 eV. (c) Ball-stick model of the gold atoms intercalated between graphene and SiC(0001).

(iii) Twisted heterostructures of layered 2D materials are currently a central topic in science, boosting research efforts at the intersection of condensed-matter physics and nanotechnology. Despite the exciting results recently achieved by the community, the relative orientation of the individual layers typically relies on the researchers' manual crafts, which is unavoidably limited in control and

reproducibility. With our work we have demonstrated that CVD can be used to obtain large-scale heterostructures with controlled angles. In Ref. [12], we investigated the properties of graphene grown on hBN with different rotation angle by Raman spectroscopy. Recently, in collaboration with Harvard University, we took the challenge of controlling the twist angle of graphene bilayers during their growth by CVD, focusing on the case of the incommensurate dodecagonal quasicrystals formed at 30° (30TBLG). We concentrated on this system because of recent reports of multiplication of the Dirac cones revealed by photoemission experiments, indicating important modification of the low-energy electronic structure. We were the first to report on the low-temperature transport and magnetotransport properties of 30TBLG. We obtained samples with excellent crystalline quality and carrier mobilities up to 10^5 cm^2/Vs, indicating low disorder, and found that the graphene quasicrystals effectively behave as uncoupled layers, showing 8-fold degenerate quantum Hall states (Fig. 2) [13]. With this result we could provide an answer to the debate whether the Dirac cones replica detected by previous photo-emission experiments could contribute to the electrical transport.

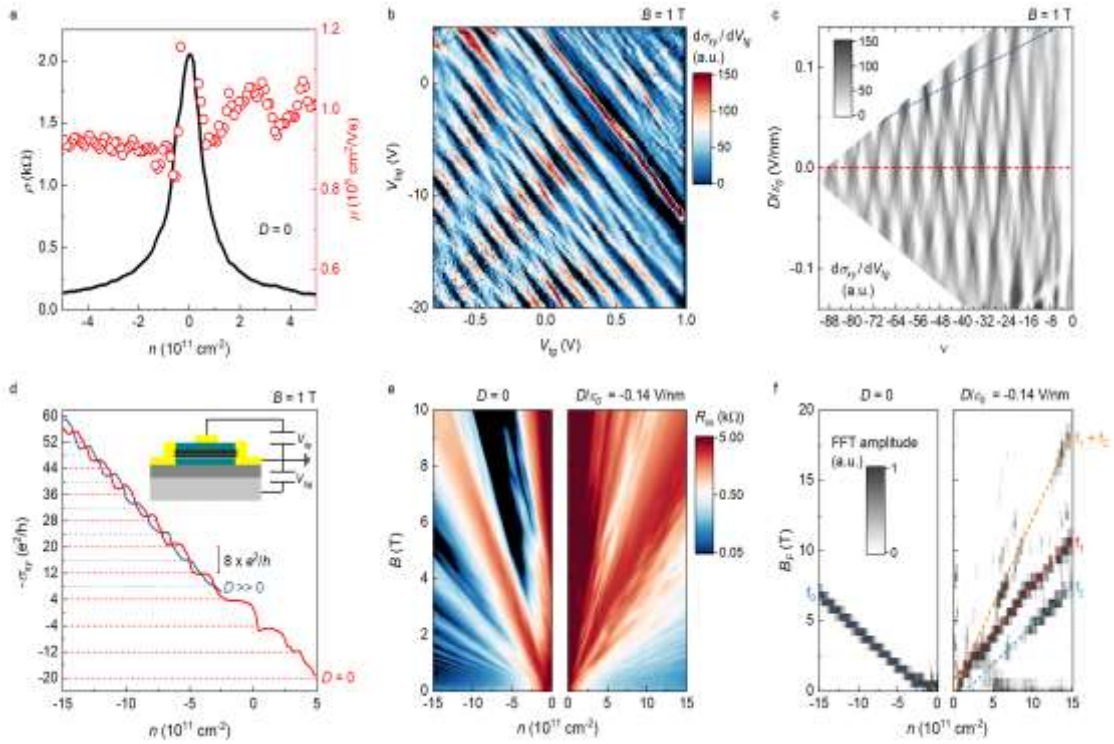

Figure 2. (a) Resistivity (black line) and carrier mobility (red circles) of 30TBLG as a function of carrier density n, at zero displacement field D. (b) First derivative of the Hall conductivity σ_{xy} as a function of V_{tg} and V_{bg}, at B = 1 T. (c) Same data of (b) as a function of ν and D/ε_0. The red dashed line marks D = 0. (d) Hall conductivity as a function of carrier density at B = 1 T, for D = 0 (red line) and D >> 0 (blue line). The inset shows a schematic cross section of the devices studied (light grey = Si; dark grey = SiO_2; black = graphene; dark cyan = hBN; yellow = Cr/Au). (e) Longitudinal resistance as a function of carrier density for zero (left panel) and finite (right) displacement field. (f) Fast Fourier transform (FFT) of the oscillatory component of the resistance data in (e). The dashed lines $f_{0,1,2}$ are fits of the main peaks in the FFT spectra as a function of n, while f_1+f_2 is the sum of the fits to the two split components. All the data were acquired at T = 4.2 K.

References

[1] A. Rossi, H. Büch, C. Di Rienzo, V. Miseikis, D. Convertino, A. Al-Temimy, V. Voliani, M. Gemmi, V. Piazza, C. Coletti, *Scalable synthesis of WS2 on graphene and h-BN: An all-2D platform for light-matter transduction*, 2D Materials **3 (3)**, 031013 (2016).

[2] S. Forti, A. Rossi, H. Buech, T. Cavallucci, F. Bisio, A. Sala, T.O. Mentes, A. Locatelli, M. Magnozzi, M. Canepa, K. Mueller, S. Link, U. Starke, V. Tozzini, C. Coletti, *Electronic properties of single-layer tungsten disulfide on epitaxial graphene on silicon carbide*, Nanoscale **9 (42)**, 16412 (2017).

[3] H. Büch, A. Rossi, S. Forti, D. Convertino, V. Tozzini, C. Coletti, *Superlubricity of epitaxial monolayer WS2 on graphene*, Nano Research **11 (11)**, 5946 (2018).

[4] F. Fabbri, F. Dinelli, S. Forti, L. Sementa, S. Pace, G. Piccinini, A. Fortunelli, C. Coletti, P. Pingue, *Edge Defects Promoted Oxidation of Monolayer WS2 Synthesized on Epitaxial Graphene*, The Journal of Physical Chemistry C **124 (16)**, 9035, (2020).

[5] M. Magnozzi, M. Ferrera, G. Piccinini, S. Pace, S. Forti, F. Fabbri, C. Coletti, F. Bisio, M. Canepa, *Optical dielectric function of two-dimensional WS2 on epitaxial graphene*, 2D Materials **7 (2)**, 025024 (2020).

[6] S. Aeschlimann, A. Rossi, M. Chávez-Cervantes, R. Krause, B. Arnoldi, B. Stadtmüller, M. Aeschlimann, S. Forti, F. Fabbri, C. Coletti, I. Gierz, *Direct evidence for efficient ultrafast charge separation in epitaxial WS2/graphene heterostructures*, Science Advances **6 (20)**, eaay0761 (2020).

[7] A. Rossi, D. Spirito, F. Bianco, S. Forti, F. Fabbri, H. Büch, A. Tredicucci, R. Krahne, C. Coletti, *Patterned tungsten disulfide/graphene heterostructures for efficient multifunctional optoelectronic devices*, Nanoscale **10 (9)**, 4332 (2018).

[8] A.T. Hoang, A.K. Katiyar, H. Shin, N. Mishra, S. Forti, C. Coletti, J-H. Ahn, *Epitaxial Growth of Wafer-scale Molybdenum Disulfide/Graphene Heterostructures by Metalorganic Vapor-phase Epitaxy and Its Application to Photodetectors*, ACS Appl. Mater. Interfaces **12 (39)**, 44335 (2020).

[9] G. Piccinini, S. Forti, L. Martini, S. Pezzini, V. Miseikis, U. Starke, F. Fabbri, C. Coletti, *Deterministic direct growth of WS2 on CVD graphene arrays*, 2D Materials **7**, 0140 02 (2019).

[10] S. Conti, L. Pimpolari, G. Calabrese, R. Worsley, S. Majee, D.K. Polyushkin, M. Paur, S. Pace, D.H. Keum, F. Fabbri, G. Iannaccone, M. Macucci, C. Coletti, T. Mueller, C. Casiraghi, G. Fiori, *Low-voltage 2D materials-based printed field-effect transistors for integrated digital and analog electronics on paper*, Nature communications **11**, 3566 (2020).

[11] S. Forti, A. Stöhr, A.A. Zakharov, C. Coletti, K.V. Emtsev, U. Starke, *Mini-Dirac cones in the band structure of a copper intercalated epitaxial graphene superlattice*, 2D Materials **3 (3)**, 035003 (2016).

[12] S. Forti, S. Link, A. Stöhr, Y. Niu, A.A. Zakharov, C. Coletti, U. Starke, *Semiconductor to metal transition in two-dimensional gold and its van der Waals heterostack with graphene*, Nature Communications **11 (1)**, 1 (2020).

[13] N. Mishra, V. Miseikis, D. Convertino, M. Gemmi, V. Piazza, C. Coletti, *Rapid and catalyst-free van der Waals epitaxy of graphene on hexagonal boron nitride*, Carbon **96**, 497 (2016).

[14] S. Pezzini, V. Miseikis, G. Piccinini, S. Forti, S. Pace, R. Engelke, F. Rossella, K. Watanabe, T. Taniguchi, P. Kim, C. Coletti, *30°-twisted bilayer graphene quasicrystals from chemical vapor deposition*, Nano Letters **20 (5)**, 3313 (2020).

1.3.14 Light-matter interaction in metamaterials and opto-mechanical systems

The use of artificial photonic materials and micromechanical elements allows the ultimate degree of control of light, which can be finely tuned to achieve peculiar regimes (time-reverse lasing), dynamically modulated for fast and arbitrary operations or used to reach complex nonlinear mechanical and optical states.

The possibility of precisely controlling the parameters of electromagnetic waves (intensity, phase, polarization) is becoming the cornerstone of light-based technologies, which find broad and diverse applications in areas ranging from telecommunications to high-precision measurements and quantum/classical computation. Most successful approaches to light control originate from the field of artificial materials, where the first results in reproducing the optical properties of natural materials through nano-structuration quickly led to their recognition as powerful elements for photonic applications. A different approach sees the combination of light-based devices with nano-mechanical elements; the ability of integrating phonon resonators and photonic crystals inaugurated a new era where mechanics is used to control light and vice-versa, leading to unprecedented levels of mass, velocity, acceleration sensitivity, to the observation of quantum effects in macroscopic systems and to new avenues for hybrid systems which use vibrations as connecting elements [1].

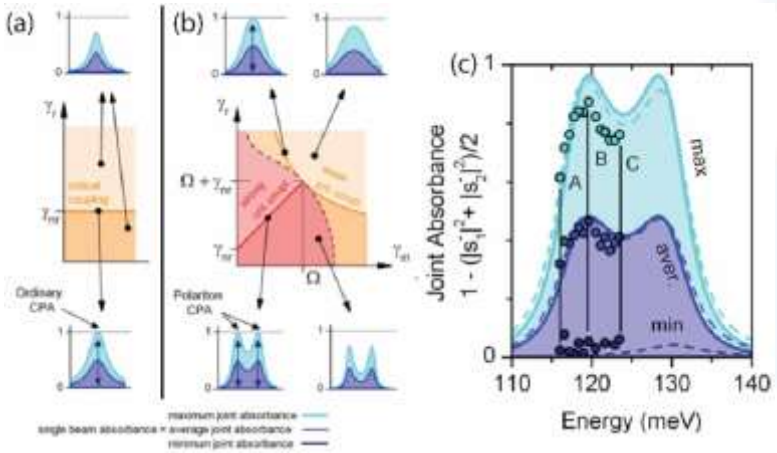

Figure 1. (a): Multi-beam coupling in a simple cavity system, where only the radiative loss rate (γ_r) can be controlled. (b): Multi-beam coupling in a polaritonic system, where also the light-matter coupling can be tuned. (c): Experimental realization of CPA in a polaritonic system.

Our activities explore different topics in this vast field, with interest in both fundamental and applied research.

A first front of investigation deals with the possibility of tuning the material absorbance through multi-beam interference. As recently demonstrated, it is possible to achieve perfect energy feeding into a lossy system (CPA – Coherent Perfect Absorption) or perfect Transparence (CPT) by controlling the relative phase of two light beams impinging on the device [2]. We extended this concept to strongly-coupled resonant systems, showing that also polaritonic excitations [3-5] can be "perfectly fed" from the outside free-space (Fig. 1) [6]. Furthermore, we investigated coherent absorption in 2D systems exploiting multilayer graphene

grown on silicon carbide [7]. For a proper interpretation of such experimental results, a general theory of CPA in linear two-port systems has been constructed, without any symmetry requirements except for reciprocity [2]; this model has also allowed defining fundamental limits to the operation of interferential light-light switches [8].

A different approach to light control uses mechanical elements combined with photonic devices. Light can be modulated by mechanical vibrations; conversely, light can exert (back) action on the mechanics via radiation pressure or thermal forces. These simple concepts have led to the field of optomechanics, where we have been showing novel schemes for hybrid opto-electro-mechanical systems [9,10] and devices based on silicon nonlinearities to achieve ~GHz coherent phonon emission at room temperature [11]. In particular, we used this basic element to investigate nonlinear mechanical effects such as chaos and synchronization [12], with the future goal of creating nonlinear networks of optomechanical devices. While most optomechanical systems rely on exploiting light intensity and phase to achieve the desired effects, a different avenue aims at exploiting all the degrees of freedom of electromagnetic waves for novel results and applications. Our contribution in this direction sees the combination of chiral metasurfaces with mechanical elements to create novel polarization modulators.

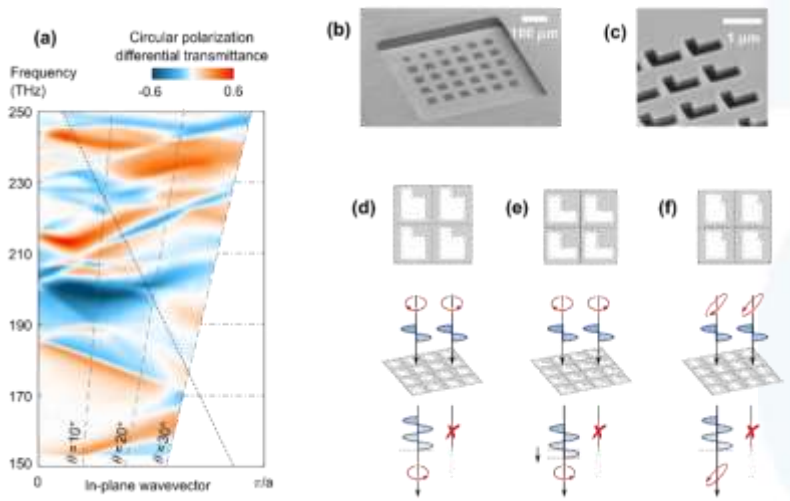

Figure 2. (a) Circular polarization differential transmittance (i.e., circular dichroism for transmitted intensities) measured at oblique incidence. The sample is a dielectric membrane metasurface (b), patterned with L-shaped holes (c). By means of an inverse-design technique we have shown that general wave operations can be performed by design (d-f).

Chiral metasurfaces offer advanced control on the polarization state of near infrared light; our minimal metasurfaces are composed by patterned single GaAs layers (see Fig. 2 (b)). By defining a chiral geometry, as a simple "L-shape" (Fig. 2 (c)), we obtain strong linear and circular dichroisms, as shown by the differential transmittance reported in Fig. 2 (a) [13]. The polarization, intensity and phase of the reflected and transmitted waves can be arbitrarily controlled by changing the shape of the holes, as demonstrated by numerical simulations based on inverse-design of which special cases are reported in Fig. 2 (d)-(f). A further tuning knob of the metasurface properties can be added considering the tunability given by mechanical actuation of the suspended membrane that hosts the chiral pattern.

Thanks to the high phase sensitivity of the metasurface and to the underlying substrate, tiny displacements from the equilibrium position lead to strong modifications of the state of the transmitted/reflected waves, see Fig. 3 (a). Using the ~350 kHz fundamental membrane mode (Fig. 3 (b)), we can obtain a fast, dynamic modulation along non-trivial paths on the Poincaré sphere, as shown by the colored lines in Fig. 3 (c), which represent different laser wavelengths and are superimposed on the static metasurface response (dotted line) [14]. Exploiting the back-action of light on the mechanics induced through thermal effects (Fig. 3 (d)), we can use the same device as a fast polarimeter, where we can uniquely associate to each input polarization state an amplitude and frequency of the mechanical resonance (the latter shown in Fig. 3 (e)) [15].

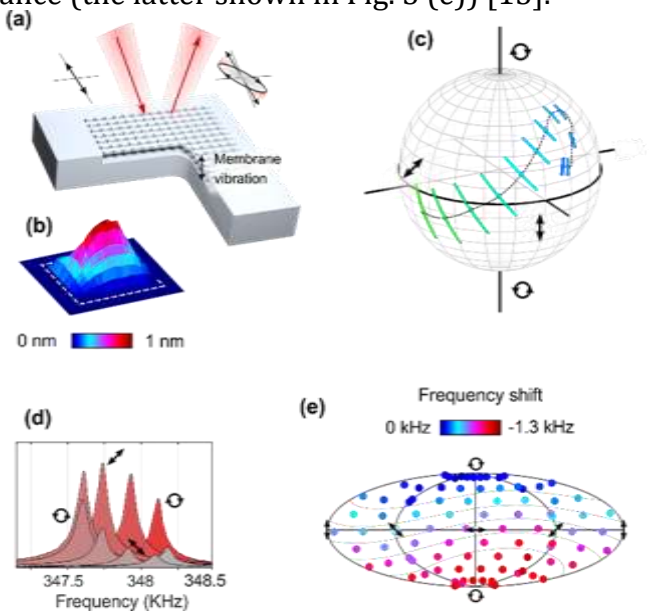

Figure 3. (a): sketch of the investigated device. (b): interferometric measurement of the fundamental drum-like mode. (c): Static (dotted line) and dynamic polarization modulation paths on the Poincaré sphere. If the structure is illuminated with different polarizations, the mechanical resonance frequency and transduction amplitude are affected (d); this effect has a peculiar fingerprint when plotted on the projected Poincaré sphere (e).

The potential of increasing the operating frequencies exploiting overdamped resonances makes our system particularly appealing for fast light modulation technology. Surface acoustic waves (SAW) could be also used to activate ~GHz mechanical modes defined by the same lattice generating the photonic resonances, naturally exploiting the GaAs natural piezoelectricity. First encouraging results of SAW coupled into a silicon nanostring [17] offer interesting insights for RF control of optomechanical systems, with spillovers in fields such as microwave photonics. Similar concepts such as the ones employed in the near infrared can be extended to the more challenging THz spectral range. Adding external or internal mechanical degrees of freedom to quantum cascade lasers would offer additional tuning knobs to control the device emission, mode locking and high-frequency wavelength sweeping, for novel and powerful spectroscopic sources. The route we followed for achieving THz optomechanics starts by coupling silicon nitride trampoline membranes with external lasers, from NIR laser diodes to THz QCLs via self-mixing interferometry [18,19]. After first experiments detecting the membrane motion via the feed voltage oscillations, next steps will see the linking of more lasers in a master-slave configuration via a commonly coupled membrane

resonator. In a different approach, we imagined to embed an oscillating string within a QCL cavity itself. To this end, we designed and demonstrated new designs based on a "LC" approach, which show impressive performance in terms of device footprints, CW emitted power and focused far-field emission [20]. Leveraging on the already existing suspended element, next steps will see the full investigation of optomechanical features in the laser emission characteristic.

References

[1] M. Aspelmeyer, T.J. Kippenberg, F. Marquardt, *Cavity optomechanics*, Rev. Mod. Phys. **86**, 1391 (2014).

[2] L. Baldacci, S. Zanotto, G. Biasiol, L. Sorba, A. Tredicucci, *Interferometric control of absorption in thin plasmonic metamaterials: general two port theory and broadband operation*, Opt. Express **23 (7)**, 9202 (2015).

[3] J.-M. Manceau, S. Zanotto, T. Ongarello, L. Sorba, A. Tredicucci, G. Biasiol, R. Colombelli, *Mid-infrared intersubband polaritons in dispersive metal-insulator-metal resonators*, Appl. Phys. Lett. **105**, 081105 (2014).

[4] S. Zanotto, F. Bianco, L. Sorba, G. Biasiol, A. Tredicucci, *Saturation and bistability of defect-mode intersubband polaritons*, Phys. Rev. B **91**, 085308 (2015).

[5] J. Raab, C. Lange, J.L. Boland, I. Laepple, M. Furthmeier, E. Dardanis, N. Dessmann, L. Li, E.H. Linfield, A.G. Davies, M.S. Vitiello, R. Huber, *Ultrafast two-dimensional field spectroscopy of terahertz intersubband saturable absorbers*, Opt. Express **27**, 2248 (2016).

[6] S. Zanotto, F.P. Mezzapesa, F. Bianco, G. Biasiol, L. Baldacci, M.S. Vitiello, L. Sorba, R. Colombelli, A. Tredicucci, *Perfect energy-feeding into strongly coupled systems and interferometric control of polariton absorption*, Nat. Phys. **10 (11)**, 830 (2014).

[7] S. Zanotto, F. Bianco, V. Miseikis, D. Convertino, C. Coletti, A. Tredicucci, *Coherent absorption of light by graphene and other optically conducting surfaces in realistic on-substrate configurations*, APL Photonics **2 (1)**, 016101 (2017).

[8] S. Zanotto, G.C. La Rocca, A. Tredicucci, *Understanding and overcoming fundamental limits of asymmetric light-light switches*, Opt. Express **26 (3)**, 3618 (2018).

[9] A. Pitanti, J.M. Fink, A.H. Safavi-Naeini, J.T. Hill, C.U. Lei, A. Tredicucci, O. Painter, *Strong opto-electro-mechanical coupling in a silicon photonic crystal cavity*, Opt. Express **23 (3)**, 3196 (2015).

[10] J.M. Fink, M. Kalaee, A. Pitanti, R. Norte, L. Heinzle, M. Davanço, K. Srinivasan, O. Painter, *Quantum electromechanics on silicon nitride nanomembranes*, Nat. Commun. **7**, 12396 (2016).

[11] D. Navarro-Urrios, N.E. Capuj, J. Gomis-Bresco, F. Alzina, A. Pitanti, A. Griol, A. Martínez, C. M. Sotomayor Torres, *A self-stabilized coherent phonon source driven by optical forces*, Sci. Rep. **5**, 15733 (2015).

[12] M.F. Colombano, G. Arregui, N.E. Capuj, A. Pitanti, J. Maire, A. Griol, B. Garrido, A. Martinez, C.M. Sotomayor-Torres, D. Navarro-Urrios, *Synchronization of Optomechanical Nanobeams by Mechanical Interaction*, Phys. Rev. Lett. **123**, 017402 (2019).

[13] S. Zanotto, G. Mazzamuto, F. Riboli, G. Biasiol, G.C. La Rocca, A. Tredicucci, A. Pitanti, *Photonic bands, superchirality, and inverse design of a chiral minimal metasurface*, Nanophotonics **8**, 2291 (2019).

[14] S. Zanotto, A. Pitanti, *Optomechanical modulators*, Patent Pending.

[15] S. Zanotto, A. Tredicucci, D. Navarro Urrios, M. Cecchini, G. Biasiol, D. Mencarelli, L. Pierantoni, A. Pitanti, *Optomechanics of Chiral Dielectric Metasurfaces*, Adv. Opt. Mater. **8**, 1901507 (2020).

[16] S. Zanotto, M. Colombano, D. Navarro-Urrios, G. Biasiol, C.M. Sotomayor-Torres, A. Tredicucci, A. Pitanti, *Broadband Dynamic Polarization Conversion in Optomechanical Metasurfaces*, Front. Phys. **7**, 231 (2020).

[17] A. Pitanti, T. Makkonen, M.F. Colombano, S. Zanotto, L. Vicarelli, M. Cecchini, A. Griol, D. Navarro-Urrios, C. Sotomayor-Torres, A. Martinez, J. Ahopelto, *High frequency mechanical excitation of a silicon nanostring with piezoelectric aluminum nitride layers*, Phys. Rev. Appl. **14**, 014054 (2020).

[18] L. Baldacci, A. Pitanti, L. Masini, A. Arcangeli, F. Colangelo, D. Navarro-Urrios, A. Tredicucci,

Thermal noise and optomechanical features in the emission of a membrane-coupled compound cavity laser diode, Sci. Rep. **6**, 31489 (2016).

[19] A. Ottomaniello, J. Keeley, P. Rubino, L. Li, M. Cecchini, E.H. Linfield, A.G. Davies, P. Dean, A. Pitanti, A. Tredicucci, *Optomechanical response with nanometer resolution in the self-mixing signal of a terahertz quantum cascade laser*, Opt. Lett. **44 (23)**, 5663 (2019).

[20] L. Masini, A. Pitanti, L. Baldacci, M.S. Vitiello, R. Degl'Innocenti, H.E. Beere, D.A. Ritchie, A. Tredicucci, *Continuous-wave laser operation of a dipole antenna terahertz microresonator*, Light Sci. Appl. **6**, e17054 (2017).

1.3.15 Near-field nanoscopy

Near-field imaging with terahertz (THz) waves is emerging as a powerful technique for fundamental research in photonics and across physical and life sciences. Spatial resolution beyond the diffraction limit can be achieved either by collecting THz waves from an object through a small aperture placed in the near-field or via scattering in a near-field optical microscopy set up. However, both approaches suffer from severe limitations in the far infrared. Here we report on near-field THz nanoscopy in both detectorless and ultrafast architectures and discuss intriguing applications in plasmonics and ultrafast polaritonics.

Light transmission through a sub-wavelength size aperture is fundamentally limited by the wave nature of light. To overcome the above limit, we conceived a novel architecture that exploits the inherently strong evanescent THz field arising within the aperture to mitigate the problem of vanishing transmission. The sub-wavelength aperture is originally coupled to asymmetric electrodes, which activate the thermo-electric THz detection mechanism in a transistor channel made of flakes of black-phosphorus or InAs nanowires (Fig. 1a). The proposed novel THz near-field probes enable room-temperature sub-wavelength resolution coherent imaging with a 3.4 THz quantum cascade laser, paving the way to compact and versatile THz imaging systems and promising to bridge the gap in spatial resolution from the nanoscale to the diffraction limit (Fig. 1b).

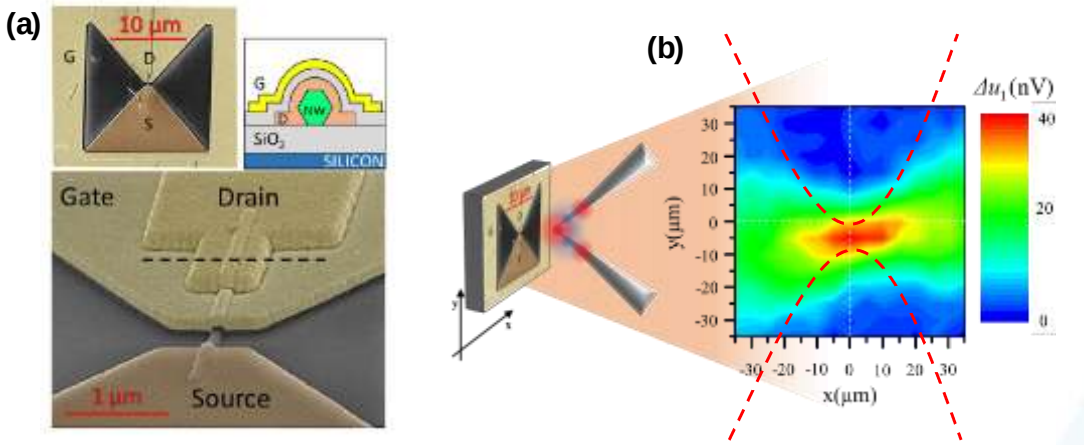

Figure 1. (a) Upper left and lower left: Scanning electron microscope (SEM) images of the near-field probe with an embedded FET-based THz nanodetector (view angles of 0° and 70°). A top gate contact (G) defines the aperture; the aperture size is 18 µm × 18 µm; the InAs nanowire detector is at the aperture center; and the source (S) and drain (D) contacts are isolated from the gate with a layer of SiO_2. (upper right) Schematic diagram of the cross-sectional view of the device. **(b)** Left: schematics of two needles employed for focusing the THz beam to a sub-wavelength spot. The needles are placed in front of the NW nanodetector probe. Right: spatial distribution of the near-field probe photovoltage; the red dotted lines mark the simulated confinement provided by the drain and gate contact.

At THz frequencies, scattering-type scanning near-field optical microscopy (s-SNOM), that is the alternative near field configuration, mostly relies on cryogenic and bulky detectors, which represents a major constraint for its practical application. Amplitude- and phase–resolved near-field imaging is particularly appealing to enable access to the spatial variation of complex-valued dielectric responses of THz frequency resonant 2D materials, heterostructures and low dimensional systems.

We devised the first THz s-SNOM system that provides both amplitude and phase contrast, and achieves nanoscale (60-70nm) in-plane spatial resolution. It features a quantum cascade laser that simultaneously emits THz frequency light and senses the backscattered optical field through a voltage modulation induced inherently through the self-mixing technique (Fig. 2a). We demonstrated its performance by probing a phonon-polariton-resonant CsBr crystal, doped black phosphorus flakes, ink jet printed graphene and propagation of THz acoustic plasmons in graphene (Fig. 2b).

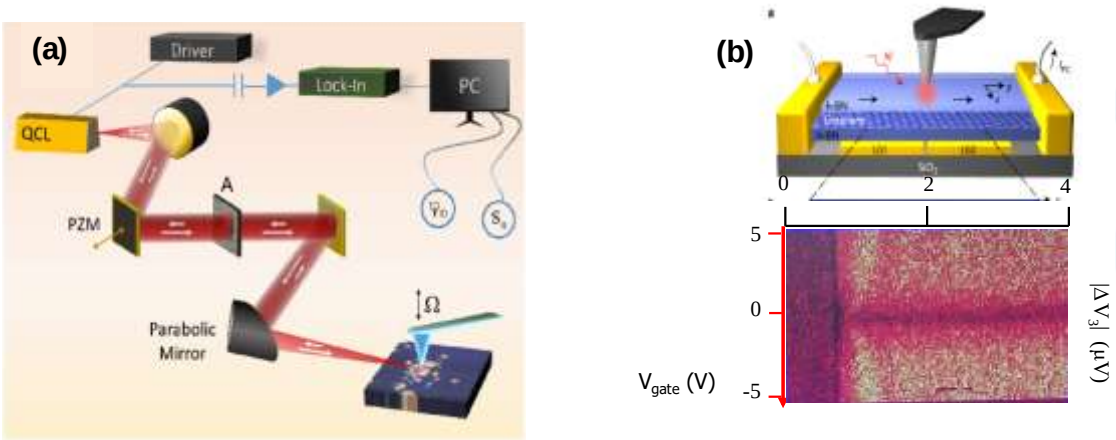

Figure 2. (a) Self-detection scattering type near field optical microscope with nanometer resolution at terahertz frequencies: schematic diagram showing the experimental arrangements; (**b)** Propagating THz acoustic plasmons in graphene. Upper: Schematics of the employed device; bottom: third harmonic self-mixing near field signal collected as a function of the gate voltage (V_{gate}).

Furthermore, we devised lightning-fast switch for electron waves in the far-infrared based on black phosphorus (BP) heterostructures, in which interface polaritons can be activated by photo-induced interband excitation within 50 fs, with switching times on the femtosecond scale (Fig. 3), many orders of magnitude faster than the fastest existing transistors.

The possibility of hybridizing collective electronic motion with mid-infrared light to form surface polaritons has made van der Waals layered materials a versatile platform for extreme light confinement and tailored nanophotonics.

We design a SiO_2/black phosphorus/SiO_2 heterostructure in which the surface phonon modes of the SiO_2 layers hybridize with surface plasmon modes in black phosphorus that can be activated by photo-induced interband excitation. Within the reststrahlen band of SiO_2, the hybrid interface polariton assumes surface-phonon-like properties, with a well-defined frequency and momentum and excellent coherence. During the lifetime of the photogenerated electron–hole plasma, coherent hybrid polariton waves can be launched by a broadband mid-infrared pulse, coupled to the tip of a scattering type scanning near-field optical microscopy set-up. The scattered radiation allows us to trace the new hybrid mode in time, energy and space.

The excellent switching contrast and switching speed, the coherence properties and the constant wavelength of this transient mode make it a promising candidate for ultrafast nanophotonic devices.

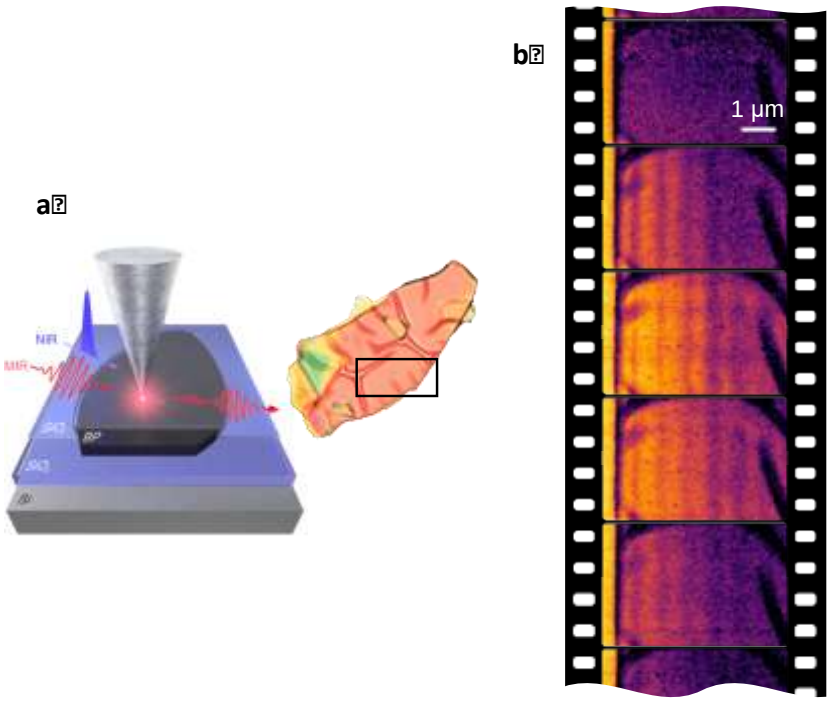

Figure 3. (a) Schematic of set-up. An ultrafast near-infrared pump pulse is focused onto a heterostructure of SiO_2 and BP on a SiO_2-capped Si wafer. The sample is probed in the near field with a mid-infrared pulse coupled to a sharp metallic tip. Right side: optical image of a single BP flake capped with SiO_2; **(b)** Scattered near-field intensity images of the SiO_2/BP/SiO_2 heterostructure, plotted for different delay times between the pump and probe pulses.

Ultrabroadband electrooptic sampling of few-cycle field transients can even reveal novel dynamics that occur faster than a single oscillation cycle of light. However, conventional terahertz spectroscopy is intrinsically restricted to ensemble measurements by the diffraction limit. As a result, it measures dielectric functions averaged over the size, structure, orientation and density of nanoparticles, nano-crystals or nano-domains. We extended ultra-broadband time-resolved THz spectroscopy to the sub-nanoparticle scale (10 nm) by combining subcycle, field-resolved detection (10 fs) with scattering-type near-field scanning optical microscopy (s-NSOM). We trace the time-dependent dielectric function at the surface of a single photoexcited InAs nanowire in all three spatial dimensions and reveal the ultrafast (<50 fs) formation of a local carrier depletion layer.

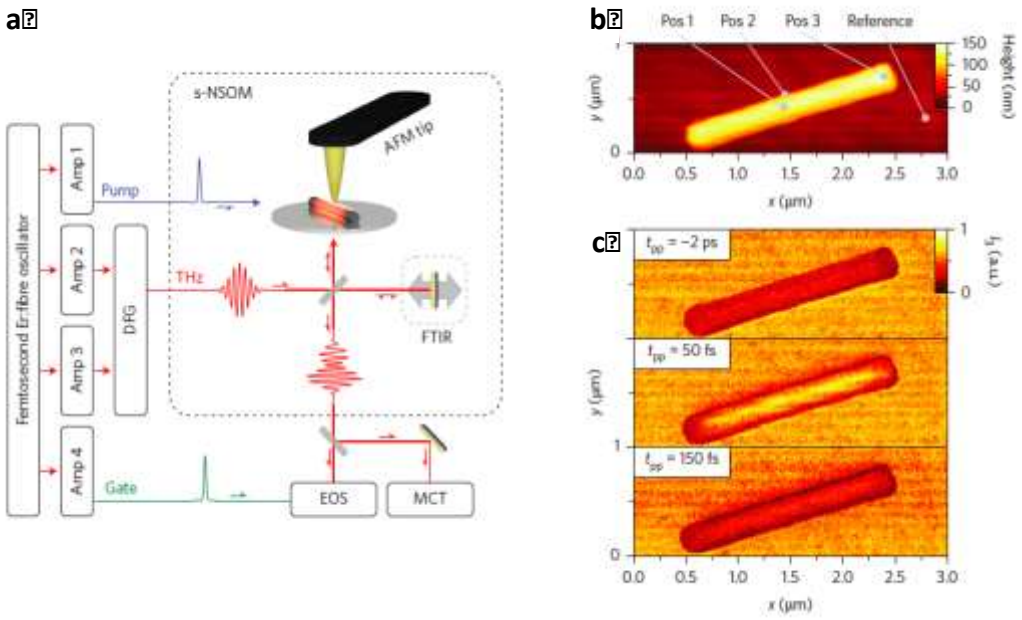

Figure 4. (a) Schematic of the experimental set-up. A femtosecond Er: fiber oscillator seeds four separate Er:fiber amplifiers, which are used to produce the near-infrared (1.56 μm) pump pulses (Amp 1), near-infrared (1.3 μm) electro-optic gate pulses (Amp 4) and phase-stable multi-terahertz probe pulses (Amp 2 and Amp 3) via difference frequency generation (DFG). The THz transients are focused onto the atomic force microscope (AFM) tip of an s-NSOM and the scattered electric near field is detected by electro-optic sampling (EOS) with sub-cycle temporal resolution. Alternatively, a mercury cadmium telluride (MCT) photodiode records the time integrated scattered intensity and enables Fourier transform infrared (FTIR) spectroscopy (>60 fs time resolution). **(b)** Topography of the InAs nanowire (on diamond) studied in the experiments, measured by AFM. (**c)** Ultrafast terahertz nano-movie frames of nanowire photoexcitation. Free carriers are photoinjected into the InAs nanowire by near-infrared pump pulses and time-resolved near-field terahertz intensity images are measured as a function of pump–probe delay time tpp. The pump fluence is 1.0 mJ cm^{-2} and the tapping amplitude is 130 nm.

References

[1] M.C. Giordano, S. Mastel, C. Liewald, L.L. Columbo, M. Brambilla, L. Viti, A. Politano, K. Zhang, L. Li, A.G. Davies, E.H. Linfield, R. Hillenbrand, F. Keilmann, G. Scamarcio, M. S. Vitiello, *Phase-resolved terahertz self-detection near-field microscopy*, Optics Express **26**, 18423 (2018).

[2] M.C. Giordano, L. Viti, O. Mitrofanov, M.S. Vitiello, *Phase-sensitive terahertz imaging using room-temperature near-field nanodetectors*, Optica **5**, 651 (2018).

[3] O. Mitrofanov, L. Viti, E. Dardanis, M. Caterina Giordano, D. Ercolani, A. Politano, L. Sorba, M.S. Vitiello, *Near-field terahertz probes with room-temperature nanodetectors for subwavelength resolution imaging*, Nature Scientific Reports **7**, 44240 (2018).

[4] M.A. Huber, F. Mooshammer, M. Plankl, L. Viti, F. Sandner, L.Z. Kastner, T. Frank, J. Fabian, M.S. Vitiello, T.L. Cocker, R. Huber, *Femtosecond photo-switching of interface polaritons in black phosphorus heterostructures*, Nature Nanotechnology **12**, 207 (2017).

[5] M. Eisele, T.L. Cocker, M.A. Huber, M. Plankl, L. Viti, D. Ercolani, L. Sorba, M.S. Vitiello, R. Huber, *Ultrafast multi-terahertz nano-spectroscopy with sub-cycle temporal resolution*, Nature Photonics **8**, 841 (2014).

[6] L. Masini, S. Meucci, J. Xu, R. Degl'Innocenti, F. Castellano, H.E. Beere, D. Ritchie, D. Balduzzi, R. Puglisi, A. Galli, F. Beltram, M.S. Vitiello, M. Cecchini, A. Tredicucci, *Terahertz probe of individual subwavelength objects in a water environment*, Laser & Photonics Reviews **8**, 734 (2014).

1.3.16 THz nanophotonic devices with 2D materials and 1D nanostructures

Bi-dimensional nano-materials and related heterostructures are establishing themselves as new photonic and electronic materials for the development of innovative devices, with huge potential in a variety of applications, ranging from saturable absorbers to optical modulators, from optical communication modules to spintronics, from near-field components to high-resolution sensing and fast tomography. Their peculiar band-structure and electron transport characteristics, which can be easily manipulated via layer-thickness control, suggest they could also form the basis for a new generation of high-performance devices operating in the Terahertz frequency range (1-10 THz) of the electromagnetic spectrum. We here review our latest achievements in THz nano-photonics and nano-electronics based on 2D nano-materials and combined heterostructures

The ability to convert light into an electrical signal with high efficiencies and controllable dynamics is a major need in photonics and optoelectronics. In the Terahertz (THz) frequency range, with its exceptional application possibilities in high-data-rate wireless communications, security, night-vision, biomedical or video-imaging and gas sensing, detection technologies providing efficiency and sensitivity performances that can be "engineered" from scratch, remain elusive. These key priorities prompted, in the last decade, a major surge of interdisciplinary research, encompassing the investigation of different technologies in-between optics and microwave electronics, different physical mechanisms and a large variety of material systems offering ad-hoc properties to target the expected performance and functionalities.

By exploiting the inherent electrical and thermal in-plane anisotropy of a flexible thin flake of black-phosphorus (BP), we recently devised plasma-wave, thermoelectric and bolometric nano-detectors with a selective, switchable and controllable operating mechanism. All devices operate at room-temperature at 0.3 THz and are integrated on-chip with planar nano-antennas, which provide remarkable efficiencies through light-harvesting in the strongly sub-wavelength device channel. The achieved selective detection (5-8 V/W responsivity) and sensitivity performances (signal-to-noise ratio of 500), are exploited to demonstrate the first concrete application of a phosphorus-based active THz device, for pharmaceutical and quality control imaging of macroscopic samples, in real-time and in a realistic setting.

Artificial semiconductor heterostructures played a pivotal role in modern electronic and photonic technologies, providing a highly effective means for the manipulation and control of carriers, from the visible to THz frequency range. Despite the exceptional versatility, they commonly require challenging epitaxial growth procedures, due to the need of clean and abrupt interfaces, which proved to be a major obstacle for the realization of room temperature (RT), high efficiency photonic devices, like sources, detectors or modulators, especially in the far-infrared. Inspired by the artificial semiconductor heterostructure architecture and the fascinating capabilities of van der Waals (vdW) heterostructures, we embedded a BP flake within a natural semiconductor heterostructure formed by multilayered hexagonal boron nitride (hBN) crystals to devise hBN/BP/hBN heterostructured THz photodetectors having high optical response, and an extremely good time-dependent electrical stability. The achieved selective detection (40 V/W responsivity) and sensitivity performances (signal-to-noise ratio of 10000), has been exploited for real-time THz imaging of biological samples in a realistic setting and for application of process and quality control.

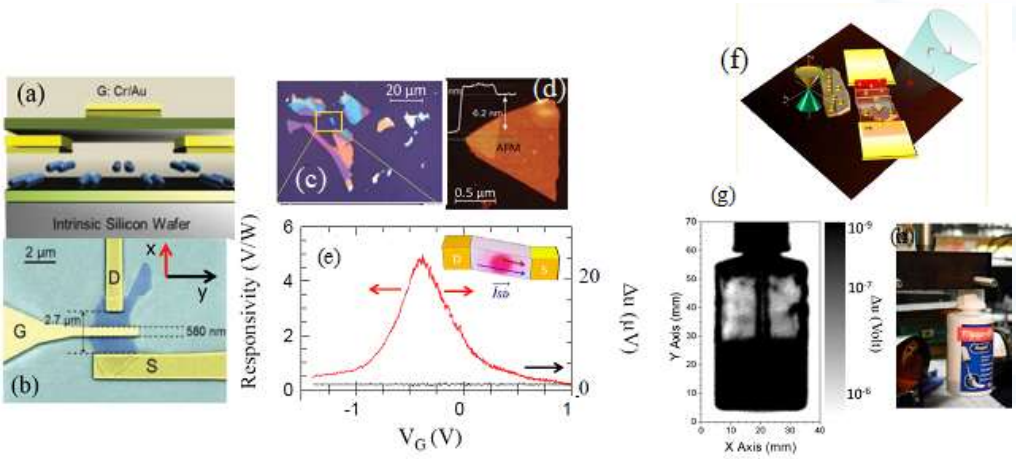

Figure 1. (a) Sketch of a black phosphorus (BP) photodetector device structure (vertical section). **(b)** False colors SEM image of the BP-based FET. The channel length (Lc) is 2.7 μm, the gate length (Lg) is 530 nm. **(c)** Optical image of exfoliated flakes of BP. **(d)** Atomic force microscopy topographic image of an individual BP flake with thickness 6.2 nm. A topographic line profile, acquired along the dashed green line is shown. **(e)** Gate bias dependence of the experimental room temperature responsivity. The red line was measured by impinging the THz beam on the detector surface; the black line was measured while blanking the beam with an absorber (considering unaltered the incident power). Inset: schematics of the over-damped plasma-wave dynamics. **(f)** Schematic sketch of a THz detection process mediated by topological insulator surface states. **(g)** Room temperature, large area THz imaging obtained while impinging the 332.6 GHz radiation a topological insulator THz detector, mounted on a XY stage, with an acquisition time of 20 ms/pixel. For visible light illumination the contents cannot be seen, either by naked eye or by the CCD camera used to take the picture. The detection of THz transmitted radiation gives information about the jar content. **(h)** Photograph of the glue jar.

As a very intriguing alternative, we explored topological insulators (TIs), which represent a novel quantum state of matter, characterized by edge or surface-states, showing up on the topological character of the bulk wave-functions. Allowing electrons to move along their surface, but not through their inside, they emerged as an intriguing material platform for the exploration of exotic physical phenomena, somehow resembling the graphene Dirac-cone physics, as well as for exciting applications in optoelectronics, spintronics, nanoscience, low-power electronics and quantum computing. Investigation of topological surface states (TSS) is conventionally hindered by the fact that, in most of experimental conditions, the TSS properties is mixed up with those of bulk-states. We devised a novel tool to unveil TSS and to probe related plasmonic effects. By engineering $Bi_2Te_{(3-x)}Se_x$ stoichiometry, and by gating the surface of nanoscale field-effect-transistors, exploiting thin flakes of $Bi_2Te_{2.2}Se_{0.8}$ or Bi_2Se_3, we recently provided the first demonstration of room-temperature THz detection mediated by over-damped plasma-wave oscillations on the "activated" TSS of a $Bi_2Te_{2.2}Se_{0.8}$ flake.

Uncooled THz photodetectors (PDs) combining such a high sensitivity (noise equivalent power (NEP) < $nW/Hz^{1/2}$) with fast response times, over a broad (0.1-10 THz) frequency range are needed for applications in high-resolution spectroscopy (precisions of 10^{-11}), metrology, quantum information, security, imaging, optical communications. However, present THz receivers cannot provide

the required balance between sensitivity, speed, operation temperature and frequency range.

To address this goal, we developed THz-frequency detectors exploiting hBN/graphene/hBN heterostructures that exploit the photo-thermoelectric effect. The core structure relies on a novel architecture that employs a dual-gated, dipolar antenna with a gap of 100 nm. We demonstrate that this new detector has excellent sensitivity, with a noise-equivalent power of 80 pW/Hz$^{1/2}$ at room temperature, a response time below 30 ns (setup-limited), a high dynamic range (linear power dependence over more than 3 orders of magnitude) and broadband operation (measured range 1.8 - 4.2 THz, antenna-limited), which fulfills a combination that is currently missing in the state of the art (Figs 2a-b).

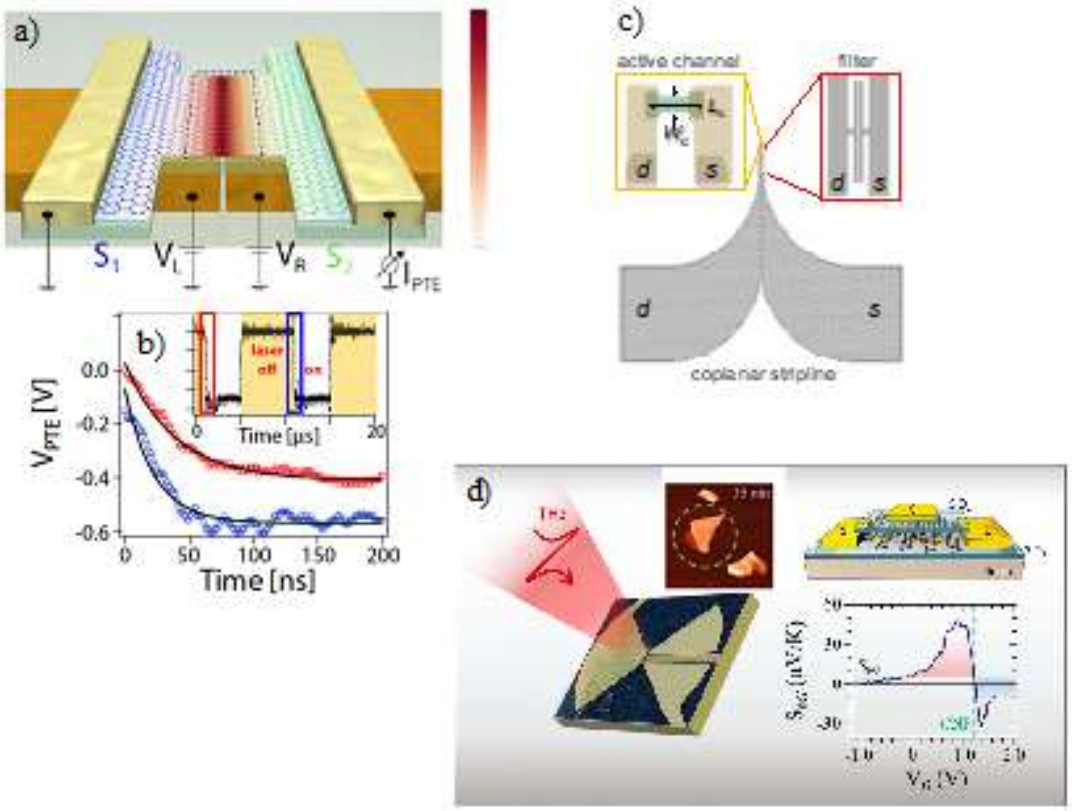

Figure 2. (a) Schematic representation (right; not to scale) of the antenna-integrated pn-junction graphene photodetector; **(b)** Results of the pulsed laser experiment, where the photocurrent was amplified by a fast current pre-amplifier (Femto) and the data were acquired with a fast oscilloscope. The inset shows how the photovoltage VPTE follows the switching of the pulsed laser; **(c)** On-chip RF components. The S and D electrodes are shaped in a CPS geometry. Inset (left): the shape of the active LMH channel (green area) guarantees a lower contact resistance with respect to a rectangular geometry. The S and D contacts have a thickness of 45 nm in vicinity proximity of the GFET channel (yellow areas) and a thickness of 140 nm far from the GFET channel. Inset (right): planar low-pass filter, with cut-off frequency 300 GHz; **(d)** Terahertz detection activated by photo-thermoelectric effect in selenium-doped thin (35 nm) black phosphorus flakes.

We also demonstrate that by integrating our RT THz nano-receivers with lithographically patterned high-bandwidth (~100 GHz) chips, we can further improve the detection speed to hundred ps response times, preserving the high sensitivity (Fig. 2c). Remarkably, this can be achieved with various antenna and

transistor architectures (single gate, dual gate) for any frequency in the 0.1-10 THz range, thus paving the way for the design of ultrafast graphene arrays in the far infrared, opening concrete perspective for targeting the aforementioned applications

If graphene can be an interesting material system for THz oriented applications due to its high mobility and gapless nature, the inherent in-plane anisotropy of BP, combined with the tunable bandgap, makes it an appealing and intriguing alternative for many applications in the far-infrared. We therefore exploited the intrinsic chemical stability of thin flakes of Se-doped BP, combined with the strong electrical and thermal anisotropy and the possibility to control, via its thickness, the energy gap to develop highly sensitive room-temperature photodetectors at high frequencies (3.4 THz) with state-of-the-art performances and different layer thicknesses (Fig.2d).
We also pioneered the use semiconductor nanowires (NW) as building block for implementing rectifying diodes or detectors that could be well operated into the THz, thanks to their typical achievable attofarad-order capacitance. We therefore devised 1D InAs or InAs/InSb NW-based field effect transistors (FETs) exploiting novel morphologies and/or material combinations effective for addressing the goal of a semiconductor plasma-wave THz detector array technology. We demonstrated room-temperature operation in the 0.3-3 THz range with over 100V/W responsivity and < 1nW/Hz$^{1/2}$ noise equivalent powers.

In parallel, we also worked on the development of novel passive and active optical components. THz saturable absorbers (SA) can be extremely appealing in combination with QCLs to passively mode-lock these micro-sources. We developed flexible THz SAs by transfer coating and inkjet printing single and few-layer graphene films prepared by liquid phase exfoliation of graphite, achieving a record transparency modulation of 80% at 3 THz (Fig. 3), almost one order of magnitude larger than that reported to date at THz frequencies.

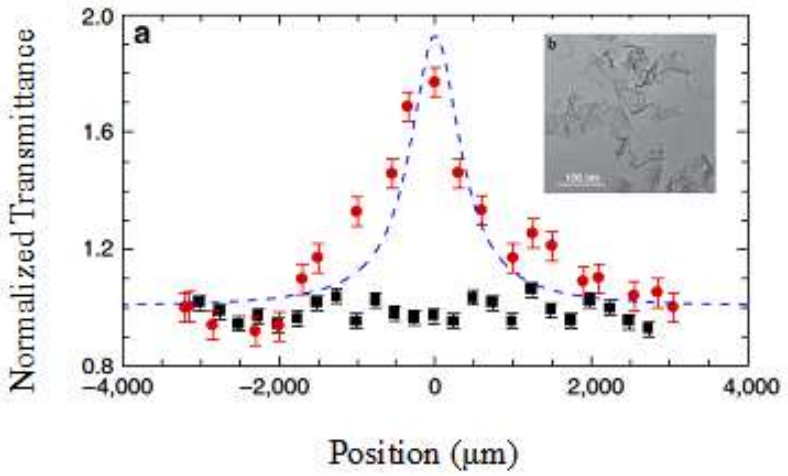

Figure 3. (a) z-scan normalized transmittance of a water-based graphene saturable absorber probed with a 3.4 TH QCL
(b) Transmission electron microscopy images of few-layer graphene flakes from water based inks.

References

[1] M.S. Vitiello, *Nanodevices at terahertz frequency based on 2D materials*, Journal of Physics: Materials **3 (1)**, 014008 (2019).
[2] S. Castilla, B. Terrés, M. Autore, L. Viti, J. Li, A.Y. Nikitin, I. Vangelidis, K. Watanabe, T.

Taniguchi, E. Lidorikis, M.S. Vitiello, R. Hillenbrand, K.-J. Tielrooij, F.H.L. Koppens, *Fast and sensitive terahertz detection using an antenna-integrated graphene pn junction*, Nano Letters **19**, 2765 (2019).

[3] L. Viti, A. Politano, K. Zhang, M.S. Vitiello, *Thermoelectric terahertz photodetectors based on selenium-doped black phosphorus flakes*, Nanoscale **11**, 1995 (2019).

[4] A. Agarwal, M.S. Vitiello, L. Viti, A. Cupolillo, A. Politano, *Plasmonics with two-dimensional semiconductors: from basic research to technological applications*, Nanoscale **10**, 8938 (2018).

[5] C. Liu, L. Wang, X. Chen, A. Politano, D. Wei, G. Chen, W. Tang, W. Lu, A. Tredicucci, *Hot-Carrier-Driven Photodetection: Room-Temperature High-Gain Long-Wavelength Photodetector via Optical-Electrical Controlling of Hot Carriers in Graphene*, Advanced Optical Materials **6**, 1870093 (2018).

[6] V. Bianchi, T. Carey, L. Viti, L. Li, E.H. Linfield, A.G. Davies, A. Tredicucci, D. Yoon, P.G. Karagiannidis, L. Lombardi, F. Tomarchio, A.C. Ferrari, F. Torrisi, M.S. Vitiello, *Terahertz saturable absorbers from liquid phase exfoliation of graphite*, Nature Communications **8**, 1 (2017).

[7] L. Viti, A. Politano, M.S. Vitiello, *Black phosphorus nanodevices at terahertz frequencies: Photodetectors and future challenges*, APL Materials **5**, 035602 (2017).

[8] A. Politano, L. Viti, M.S. Vitiello, *Optoelectronic devices, plasmonics, and photonics with topological insulators*, APL Materials **5 (3)**, 035504 (2017).

[9] A. Politano, M.S. Vitiello, L. Viti, D.W. Boukhvalov, G. Chiarello, *The role of surface chemical reactivity in the stability of electronic nanodevices based on two-dimensional materials "beyond graphene" and topological insulators*, Flat Chem **1**, 60 (2017).

[10] A. Politano, M.S. Vitiello, L. Viti, J. Hu, Z. Mao, J. Wei, G. Chiarello, D.W. Boukhvalov, *Unusually strong lateral interaction in the CO overlayer in phosphorene-based systems*, Nano Research **9**, 2598 (2017).

[11] L. Viti, J. Hu, D. Coquillat, A. Politano, C. Consejo, W. Knap, M.S. Vitiello, *Heterostructured hBN-BP-hBN Nanodetectors at Terahertz Frequencies,* Advanced Materials **28**, 7390 (2016).

[12] A.M. Kadykov, C. Consejo, M. Marcinkiewicz, L. Viti, M.S. Vitiello, S.S. Krishtopenko, S. Ruffenach, S.V. Morozov, W. Desrat, N. Dyakonova, W. Knap, V.I. Gavrilenko, N.N. Mikhailov, S.A. Dvoretsky, F. Teppe, *Observation of topological phase transition by terahertz photoconductivity in HgTe based transistors*, Physica Status Solidi C **13 (7-9)**, 534 (2016).

[13] L. Viti, J. Hu, D. Coquillat, A. Politano, W. Knap, M.S. Vitiello, *Efficient Terahertz detection in black-phosphorus nano-transistors with selective and controllable plasma-wave, bolometric and thermoelectric response*, Nature Scientific Reports **6**, 20474 (2016).

[14] L. Viti, D. Coquillat, A. Politano, K.A. Kokh, Z.S. Aliev, M.B. Babanly, O.E. Tereshchenko, W. Knap, E.V. Chulkov, M.S. Vitiello, *Plasma-wave terahertz detection mediated by topological insulators surface states*, Nano Letters **16 (1)**, 80 (2016).

[15] A. Politano, V.M. Silkin, I.A. Nechaev, M.S. Vitiello, L. Viti, Z.S. Aliev, M.B. Babanly, G. Chiarello, P.M. Echenique, E.V. Chulkov, *Interplay of Surface and Dirac Plasmons in Topological Insulators: The Case of Bi2Se3*, Physical Review Letters **115**, 216802 (2015).

[16] A.M. Kadykov, F. Teppe, C. Consejo, L. Viti, M.S. Vitiello, S.S. Krishtopenko, S. Ruffenach, S.V. Morozov, M. Marcinkiewicz, W. Desrat, N. Dyakonova, W. Knap, V.I. Gavrilenko, N.N. Mikhailov, S.A. Dvoretsky, *Terahertz detection of magnetic field-driven topological phase transition in HgTe-based transistors*, Applied Physics Letters **107**, 152101 (2015).

[17] L. Viti, J. Hu, D. Coquillat, W. Knap, A. Tredicucci, A. Politano, M.S. Vitiello, *Black phosphorus terahertz photodetectors*, Advanced Materials **27**, 5567 (2015).

[18] F. Bianco, D. Perenzoni, D. Convertino, S.L. De Bonis, D. Spirito, M. Perenzoni, C. Coletti, M.S. Vitiello, A. Tredicucci, *Terahertz detection by epitaxial-graphene field-effect-transistors on silicon carbide*, Applied Physics Letters **107**, 131104 (2015).

[19] F. Bianco, V. Miseikis, D. Convertino, J.-H. Xu, F. Castellano, H.E. Beere, D.A. Ritchie, M.S. Vitiello, A. Tredicucci, C. Coletti, *THz saturable absorption in turbostratic multilayer graphene on silicon carbide*, Optics Express **23**, 11632 (2015).

[20] M.S. Vitiello, L. Viti, D. Coquillat, W. Knap, D. Ercolani, L. Sorba, *One dimensional semiconductor nanostructures: An effective active-material for terahertz detection*, APL Materials **3 (2)**, 026104 (2015).

[21] L. Romeo, D. Coquillat, E. Husanu, D. Ercolani, A. Tredicucci, F. Beltram, L. Sorba, W. Knap, M.S. Vitiello, *Terahertz photodetectors based on tapered semiconductor nanowires*, Applied Physics Letters **105 (23)**, 231112 (2014).

[22] F.H.L. Koppens, T. Mueller, P. Avouris, A.C. Ferrari, M.S. Vitiello, M. Polini, *Photodetectors based on graphene, other two-dimensional materials and hybrid systems*, Nature Nanotechnology **9**, 780 (2014).
[23] L. Viti, D. Coquillat, D. Ercolani, L. Sorba, W. Knap, M.S. Vitiello, *Nanowire Terahertz detectors with a resonant four-leaf-clover-shaped antenna*, Optics Express **22**, 8996 (2014).
[24] M. Ravaro, M. Locatelli, L. Viti, D. Ercolani, L. Consolino, S. Bartalini, L. Sorba, M.S. Vitiello, P. De Natale, *Detection of a 2.8 THz quantum cascade laser with a semiconductor nanowire field-effect transistor coupled to a bow-tie antenna*, Applied Physics Letters **104 (8)**, 083116 (2014).
[25] D. Spirito, D. Coquillat, S.L. De Bonis, A. Lombardo, M. Bruna, A.C. Ferrari, V. Pellegrini, A. Tredicucci, W. Knap, M.S. Vitiello, *High performance bilayer-graphene terahertz detectors*, Applied Physics Letters **104**, 061111 (2014).

1.3.17 Quantum engineering of THz quantum cascade lasers and applications to quantum metrology

Quantum cascade lasers (QCLs) represent a fascinating accomplishment of quantum engineering and enable the direct generation of terahertz (THz) frequency radiation from an electrically-biased semiconductor heterostructure. Their large spectral bandwidth, high output powers and quantum-limited linewidths have facilitated the realization of THz pulses by active mode-locking and passive generation of optical frequency combs (FCs) through intracavity four-wave-mixing. Here we present recent results in the implementation of THz QCLs into advanced photonic structures and report on state-of-the-art applications in quantum-metrology and high-resolution spectroscopy.

The development of modern nanofabrication technologies, combined with new laser resonator concepts, has recently enabled the control and confinement of electron and photon paths, in optoelectronic devices, with an unprecedented degree of control. For example, microcavities, photonic crystals, and both pseudo-random and random photonic structures, can manipulate and confine light in small volumes, and at targeted frequencies. This has further expanded the functionality of the THz QCL, allowing operation at a single emission frequency or over a broad (0.5 THz) frequency bandwidth, with designed directional beam patterns.

We demonstrated double-metal waveguided distributed feedback THz quantum cascade wire lasers, exploiting an innovative approach in which feedback is provided by a lateral sinusoidal ridge corrugation, while light extraction is separately controlled by a hole array in the top metallization. In this case, the periodicity of the array of surface holes is not an integer multiple of the lateral corrugation controlling the feedback. The feedback grating selects the lasing frequencies and allows robust single mode emission, exploiting the inherently high spectral purity of THz QCLs, while the extraction array is finely tuned to optimize the radiation outcoupling (Fig.1a). This new architecture, extendable to a broad range of far-infrared frequencies, has led to the achievement of low-divergent beams (10°), single-mode emission, high slope efficiencies (250 mW/A), and stable CW operation.

By exploiting a broadband heterostructure, we furthermore developed the first one-dimensional quasi-crystal distributed feedback laser by lithographically patterning a series of air slits of different widths, following the Octonacci sequence, on the top metal layer of a THz QCL. We tuned the emission from single-mode to multi-mode over a 530 GHz bandwidth, achieving a maximum peak optical power of 240 mW (190 mW) in multimode (single-mode) lasers with record slope efficiencies up to ≈570 mW/A at 78 K and ≈700 mW/A at 20 K, wall-plug efficiencies of $\eta \approx 1\%$ and low divergent emission (Fig. 1b).

To push the concept of disordered resonators further, we also developed the first electrically pumped CW random laser (Fig. 1c). By combining this concept with the QCL gain media we obtain a highly collimated vertical emission at ~3 THz, with a 430 GHz bandwidth, device operation up to 110 K, peak (pulsed) power of 21 mW, CW emission of 1.7 mW and continuous frequency tuning over 11 GHz.

The same broadband heterostructure can be also exploited to develop miniaturized frequency comb (FC) sources across hard-to-access spectral regions, as the far-infrared. Four-wave-mixing based QCL-combs are ideal candidates, in this respect, due to the unique possibility to tailor their spectral emission by proper nanoscale design of the quantum wells. We demonstrate full-phase-

stabilization of record dynamic range, high power QCL-comb against the primary frequency standard, proving independent and simultaneous control of the two comb degrees of freedom (modes spacing and frequency offset) at a metrological level (Fig.1d). Each emitted mode exhibits sub-Hz relative frequency stability, while a correlation analysis on the modal phases confirms the high degree of coherence in the device emission, proving that this technology is mature for metrological-grade uses, as well as for an increasing number of scientific and technological applications.
Also, by integrating an on-chip tightly coupled mirror with the QCL cavity (Gires Tournois interferometer) we demonstrate tunable, lithographically independent, control of the free-running coherence properties of THz QCL FCs.

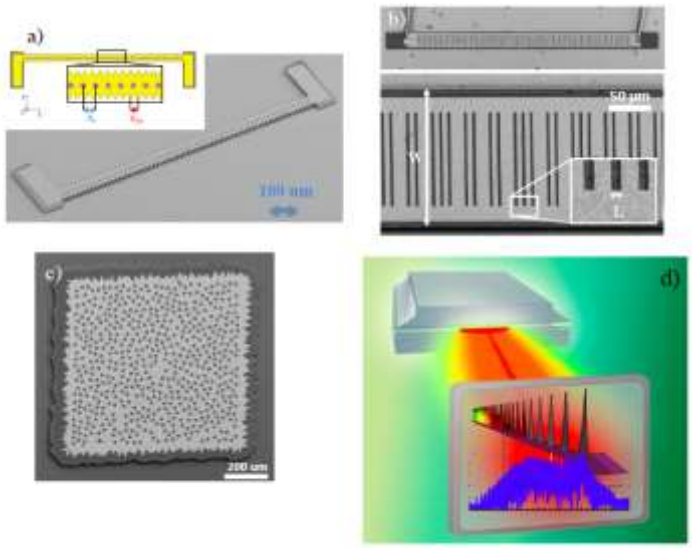

Figure 1. (a) Schematic diagram of the laterally corrugated wire laser and related SEM picture; (**b)** SEM image of an Octonacci quasi crystal THz laser; (**c)** SEM image of a random 2D THz QCL resonator; (**d)** Quantum cascade laser emitting a discrete set of equally spaced modes, each corresponding to the tooth of an optical frequency comb. The semiconductor heterostructure embedded in the QCL active core is schematically shown as a sequence of striped lines.

Tunable oscillators are a key component of almost all electronic and photonic systems. Yet, a technology capable of operating in the terahertz (THz)-frequency range and fully suitable for widescale implementation is still lacking. This issue is significantly limiting potential THz applications in gas sensing, high-resolution spectroscopy, hyper-spectral imaging and optical communications. The THz QCL is arguably the most promising solution in terms of output power and spectral purity. In order to achieve reliable, repeatable and broad tuneability, we exploited the strong coupling between two different cavity mode concepts: a distributed feedback one-dimensional photonic resonator (providing gain), and a mechanically actuated wavelength-size microcavity (providing tuning). The result is a continuously tunable, single-mode emitter covering a 162 GHz spectral range, centered on 3.2 THz with a few tens of MHz resolution and an unprecedented compact and simple architecture (Fig. 2a-b).
In parallel, we also developed a novel approach to couple THz radiation from a double-metal QCL into an on-chip hollow rectangular waveguide feeding a triangular horn, with the specific aim of optimizing the optical beam divergence. The conceived novel extractor is composed of three parts: a series of slits

patterned at the end of the laser top contact (slit coupler), a metallic waveguide section (feeder) assembled on top of the laser itself, and an adiabatic expansion of the feeder, forming a horn that radiates into an optical fiber or, alternatively, into free space (Fig. 2c-e). The developed waveguide component is capable of efficiently shaping the output beam profile from a double-metal THz QCL simultaneously reducing the facet reflectivity opening the way to the realization of more complex systems such as QCL amplifiers or external cavity tuners for multi-spectroscopy applications, injection seeding and metrological approaches across the far-infrared.

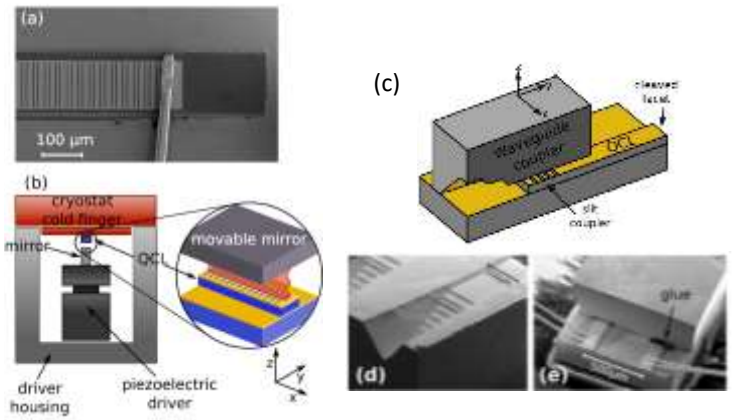

Figure 2. (a) Scanning electron microscope (SEM) image of a dual-slit DFB QCL. The absorbing boundary is visible around the grating. **(b)** Schematic diagram of the external cavity arrangement. The movable mirror was milled from an aluminum block and was then laid on top of the piezoelectric actuator. **(c)** Device schematics: yellow areas indicate metallized surfaces, gray corresponds to GaAs **(d)** SEM image of the cleaved chip containing two waveguide couplers; **(e)** SEM image of the final assembly, taken from the cleaved facet side.

We also pioneered a novel approach to optimize extraction efficiency and collimation of the output radiation of single-mode THz QCLs by developing quasi-crystalline resonators in which the distinction between symmetric (vertically radiative, but low-quality factor, Q) and antisymmetric (non-radiative, high-Q) modes is fully overcome, therefore elegantly circumventing any power cancellation issue in the far-field. Our 2D photonic quasi-crystal THz QCLs based on a Penrose P2 (kite and dart) tiling with a five-fold rotational symmetry, reached 0.1-0.2% wall-plug efficiencies and 65mW peak output powers with characteristic surface-emitting conical beam profiles, result of the rich quasi-crystal Fourier spectrum (Fig. 3a-b).

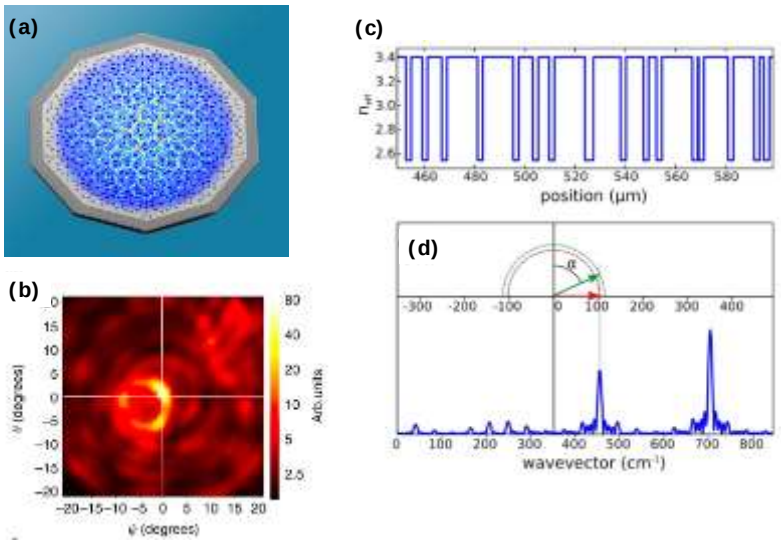

Figure 3. (a) SEM image of a prototype quasi-crystal resonator device. The lattice spatial length scale a was lithographically designed at each vertex of a Penrose pattern and imprinted into the top Cr/Au metallization of the THz QCL (see inset). The computed 2D spatial profiles of the electric field modulus for the higher quality factor optical mode is shown on the top of the SEM picture **(b)** Far-field measured from the device with a=21 μm; **(c)** Spatial dependence of the effective refractive index of a bi-periodic DFB THz QCL. **(d)** Spatial spectra of the grating of panel (c). Two light cones (dashed lines) are drawn, corresponding to the two bandgap modes of a first order grating with spatial periodicity of 712 cm^{-1}. The two modes are predicted to be at 3.1 THz (red, inner circle) and 3.35 THz (green, outer circle), and to radiate at different angles, as indicated by the arrows.

We then worked on photonic engineering solutions to control the emission frequency and the output beam direction of one-dimensional DFB THz QCLs, independently. The spatial refractive index modulation of the gratings necessary to provide optical feedback at a fixed frequency and, simultaneously, a far-field emission pattern centered at controlled angles, was designed through use of an appropriate wavevector scattering model (Fig. 3c-d). Single-mode THz emission at angles tuned by design between 0° and 50° was realized, leading to an original phase-matching approach, lithographically independent, for highly collimated THz QCLs.

We then developed intriguing application systems based on the described THz QCL resonators.

We demonstrate real-time digital holography (DH) at THz frequencies exploiting the high spectral purity and the mW output power of a QCL combined with the high sensitivity and resolution of a microbolometric array. We show that, in a one-shot exposure, phase and amplitude information of whole samples, either in reflection or in transmission, can be recorded. Furthermore, a 200 times reduced sensitivity to mechanical vibrations and a significantly enlarged field of view are observed, as compared to DH in the visible range. These properties of THz DH enable unprecedented holographic recording of real-world dynamic scenes.

We demonstrate a metrological-grade THz spectroscopy system based on the combination of a free space THz frequency-comb synthesizer (FCS) and a THz QCL. The QCL is phase locked to the free-space THz FCS, and its frequency is swept across a methanol transition by tuning the comb repetition rate, which is ultimately disciplined by the Cs primary frequency standard. The absolute frequency scale provides an uncertainty of a few parts in 10^{-11} on the laser

frequency and 10^{-9} on the line-center determination, ranking this technique among the most precise ever developed in the THz range.

References

[1] L. Consolino, M. Nafa, F. Cappelli, K. Garrasi, F.P. Mezzapesa, L. Li, A.G. Davies, E.H. Linfield, M.S. Vitiello, P. De Natale, S. Bartalini, *Fully phase-stabilized quantum cascade laser frequency comb*, Nature Communications **10**, 2938 (2019).

[2] S. Biasco, H.E. Beere, D.A. Ritchie, L. Li, A.G. Davies, E.H. Linfield, M.S. Vitiello, *Frequency-tunable continuous-wave random lasers at terahertz frequencies*, Nature Light: Science & Applications **8 (1)** (2019).

[3] F.P. Mezzapesa, V. Pistore, K. Garrasi, L. Li, A.G. Davies, E.H. Linfield, S. Dhillon, M.S. Vitiello, *Tunable and compact dispersion compensation of broadband THz quantum cascade laser frequency combs*, Optics Express **27 (15)**, 20231 (2019).

[4] L. Consolino, A. Campa, D. Mazzotti, M.S. Vitiello, P. De Natale, S. Bartalini, *Bow-tie cavity for terahertz radiation*, Photonics **6 (1)** (2019).

[5] K. Garrasi, F.P. Mezzapesa, L. Salemi, L. Li, L. Consolino, S. Bartalini, P. De Natale, A.G. Davies, E.H. Linfield, M.S. Vitiello, *High dynamic range, heterogeneous, terahertz quantum cascade lasers featuring thermally tunable frequency comb operation over a broad current range*, ACS Photonics **6**, 73 (2019).

[6] L.H. Li, K. Garrasi, I. Kundu, Y.J. Han, M. Salih, M.S. Vitiello, A.G. Davies, E.H. Linfield, *Broadband heterogeneous terahertz frequency quantum cascade laser*, Electronics Letters **54**, 1229 (2018).

[7] S. Biasco, K. Garrasi, F. Castellano, L. Li, H.E. Beere, D.A. Ritchie, E.H. Linfield, A.G. Davies, M.S. Vitiello, *Continuous-wave highly-efficient low-divergence terahertz wire lasers*, Nature Communications **9**, 1 (2018).

[8] L. Consolino, S. Jung, A. Campa, M. De Regis, S. Pal, J.H. Kim, K. Fujita, A. Ito, M. Hitaka, S. Bartalini, P. De Natale, M.A. Belkin, M.S. Vitiello, *Spectral purity and tunability of terahertz quantum cascade laser sources based on intracavity difference-frequency generation*, Science Advances **3**, e1603317 (2017).

[9] S.S. Dhillon, M.S. Vitiello et al., *The 2017 terahertz science and technology roadmap*, Journal of Physics D: Applied Physics **50 (4)**, 043001 (2017).

[10] S. Biasco, L. Li, E.H. Linfield, A.G. Davies, M.S. Vitiello, *Multimode, aperiodic terahertz surface-emitting laser resonators*, Photonics **3 (2)**, 32 (2016).

[11] A. Sampaolo, P. Patimisco, M. Giglio, M.S. Vitiello, H.E. Beere, D.A. Ritchie, G. Scamarcio, F.K. Tittel, V. Spagnolo, *Improved tuning fork for terahertz quartz-enhanced photoacoustic spectroscopy*, Sensors **16**, 439 (2016).

[12] F. Castellano, L. Li, E.H. Linfield, A.G. Davies, M.S. Vitiello, *Frequency and amplitude modulation of ultra-compact terahertz quantum cascade lasers using an integrated avalanche diode oscillator*, Scientific Reports **6**, 23053 (2016).

[13] R. Degl'Innocenti, Y.D. Shah, L. Masini, A. Ronzani, A. Pitanti, Y. Ren, D.S. Jessop, A. Tredicucci, H.E. Beere, D.A. Ritchie, *Hyperuniform disordered terahertz quantum cascade laser*, Scientific Reports **6**, 193225 (2016).

[14] F.P. Mezzapesa, L.L. Columbo, C. Rizza, M. Brambilla, A. Ciattoni, M. Dabbicco, M.S. Vitiello, G. Scamarcio, *Photo-generated metamaterials induce modulation of CW terahertz quantum cascade lasers*, Scientific Reports **5**, 16207 (2015).

[15] F. Castellano, V. Bianchi, L. Li, J. Zhu, A. Tredicucci, E.H. Linfield, A.G. Davies, M.S. Vitiello, *Tuning a microcavity-coupled terahertz laser*, Applied Physics Letters **107**, 261108 (2015).

[16] M. Locatelli, M. Ravaro, S. Bartalini, L. Consolino, M.S. Vitiello, R. Cicchi, F. Pavone, P. De Natale, *Real-time terahertz digital holography with a quantum cascade laser*, Scientific Reports **5**, 13566 (2015).

[17] V. Spagnolo, P. Patimisco, R. Pennetta, A. Sampaolo, G. Scamarcio, M.S. Vitiello, F.K. Tittel, *THz Quartz-enhanced photoacoustic sensor for H2S trace gas detection*, Optics Express **23**, 7574 (2015).

[18] F. Castellano, L. Li, E.H. Linfield, A.G. Davies, H.E. Beere, D.A. Ritchie, M.S. Vitiello, *THz waveguide adapters for efficient radiation out-coupling from double metal THz QCLs*, Optics Express **23**, 5190 (2015).

[19] M.S. Vitiello, G. Scalari, B. Williams, P. De Natale, *Quantum cascade lasers: 20 years of challenges*, Optics Express **23 (4)**, 5167 (2015).
[20] A. Campa, L. Consolino, M. Ravaro, D. Mazzotti, M.S. Vitiello, S. Bartalini, P. De Natale, *High-Q resonant cavities for terahertz quantum cascade lasers*, Optics Express **23**, 3751 (2015).
[21] L. Consolino, A. Campa, M. Ravaro, D. Mazzotti, M.S. Vitiello, S. Bartalini, P. De Natale, *Saturated absorption in a rotational molecular transition at 2.5 THz using a quantum cascade laser*, Applied Physics Letters **106**, 021108 (2015).
[22] F. Castellano, S. Zanotto, L.H. Li, A. Pitanti, A. Tredicucci, E.H. Linfield, A.G. Davies, M.S. Vitiello, *Distributed feedback terahertz frequency quantum cascade lasers with dual periodicity gratings*, Applied Physics Letters **106**, 011103 (2015).
[23] M.S. Vitiello, M. Nobile, A. Ronzani, A. Tredicucci, F. Castellano, V. Talora, L. Li, E.H. Linfield, A.G. Davies, *Photonic quasi-crystal terahertz lasers*, Nature Communications **5 (1)**, 1 (2014).
[24] F. Mezzapesa, M. Petruzzella, M. Dabbicco, H. Beere, D. Ritchie, M.S. Vitiello, G. Scamarcio, *Continuous-wave reflection imaging using optical feedback interferometry in terahertz and mid-infrared quantum cascade lasers*, IEEE Transactions on Terahertz Science and Technology **4**, 631 (2014).
[25] S. Bartalini, L. Consolino, P. Cancio, P. De Natale, P. Bartolini, A. Taschin, M. De Pas, H. Beere, D. Ritchie, M.S. Vitiello, R. Torre, *Frequency-comb-assisted terahertz quantum cascade laser spectroscopy*, Physical Review X **4**, 021006 (2014).
[26] F.P. Mezzapesa, L.L. Columbo, M. Brambilla, M. Dabbicco, M.S. Vitiello, G. Scamarcio, *Imaging of free carriers in semiconductors via optical feedback in terahertz quantum cascade lasers*, Applied Physics Letters **104**, 041112 (2014).
[27] P. Patimisco, S. Borri, A. Sampaolo, H.E. Beere, D.A. Ritchie, M.S. Vitiello, G. Scamarcio, V. Spagnolo, *A quartz enhanced photo-acoustic gas sensor based on a custom tuning fork and a terahertz quantum cascade laser*, Analyst **139**, 2079 (2014).

1.3.18 Nanotechnologies for the nervous system

The nervous system (NS) is in some ways the most complex and fascinating organ of the human body. Unfortunately, NS pathologies that lead to tissue loss are dramatically difficult to treat because of the negligible regenerative potential of the central nervous system (CNS) on one side, and of the very slow and ineffective repair mechanisms of peripheral nervous system (PNS) on the other. The interest of our research activity in this field is to develop biocompatible nanostructured materials to help the heal of the PNS and cure and study CNS diseases. In particular, at the moment our attention is focused on nanoparticles for Globoid Cell Leukodystrophy (or Krabbe disease; OMIM #245200), on textured surfaces for helping nerve regeneration and on nanotechnological methods for studying Ube3A-related neurodevelopmental disorders (e.g. Angelman Syndrome, OMIM #105830).

Brain-targeted enzyme-loaded nanoparticles: A breach through the blood-brain barrier for enzyme replacement therapy in Krabbe disease

Lysosomal storage disorders (LSDs) result from an enzyme deficiency within lysosomes. The systemic administration of the missing enzyme, however, is not effective in the case of LSDs with central nervous system (CNS)-involvement. An enzyme delivery system based on the encapsulation of cross-linked enzyme aggregates (CLEAs) into poly-(lactide-co-glycolide) (PLGA) nanoparticles (NPs) functionalized with brain targeting peptides (Ang2, g7 or Tf2) has been demonstrated for Krabbe disease, a neurodegenerative LSD caused by galactosylceramidase (GALC) deficiency [1]. We first synthesized and characterized Ang2-, g7- and Tf2-targeted GALC CLEA NPs. We studied NP cell trafficking and capability to reinstate enzymatic activity in vitro (Fig. 1a,b). Then, we successfully test our formulations in the twitcher mouse. We reported enzymatic activity measurements in the nervous system and in accumulation districts upon intraperitoneal injections, demonstrating activity recovery in the brain up to the unaffected mice level (Fig. 1c). Together, these results open new therapeutic perspectives for all LSDs with major CNS-involvement.

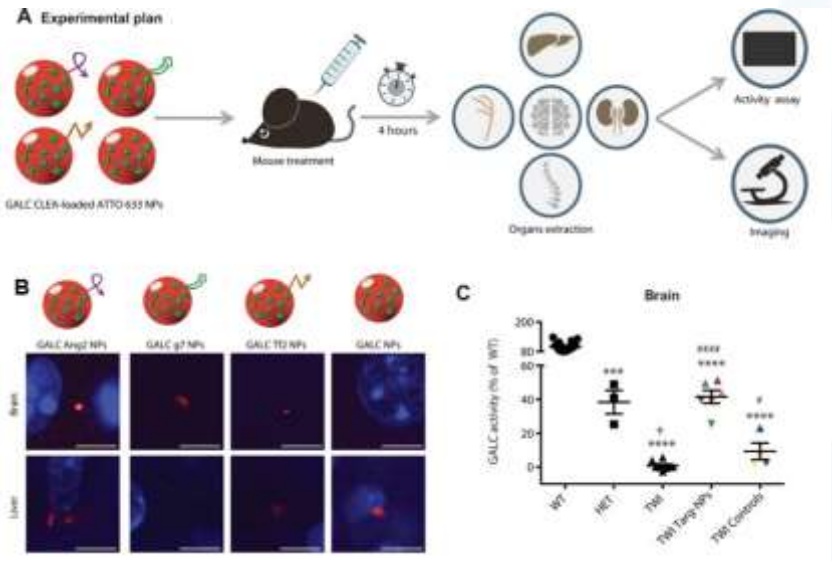

Figure 1. Brain-targeted enzyme-loaded nanoparticles for Krabbe disease

Schwann cell contact guidance versus boundary interaction in functional wound healing along nano and micro-structured membranes

Peripheral nerve transection is often encountered after trauma and can lead to long-term/permanent loss of sensor/motor functionality. The effect of pure contact interaction of several nano/micro-structured substrates on glial Schwann cells (SCs) was previously studied in view of their possible use for nerve-repair applications, for example anisotropic hierarchical rippled nanotopographies [2]. Recently we tested the ability of grating (GR)-patterned elastomeric membranes (i.e. grooved substrates) to control and direct SC shaping and migration, with the aim to evaluate these geometries for nerve-regeneration applications [3]. Poly(dimethylsiloxane) (PDMS) GRs were developed with different lateral periods (ranging from 1 to 20 μm) and depths (from 0.35 to 2.5 μm) (Fig. 2, left), leading to two distinct cell-substrate interaction regimes: contact guidance (GR period < cell body diameter, for T1, T4) and boundary guidance (GR period ≥ cell body diameter, for T20). We examined the response of primary SCs to GRs in terms of cell morphology, actin cytoskeleton organization, single and collective migration, and cell-cell interaction. Specifically, T20 performed best among all tested GRs, showing the best SC elongation and alignment, actin organization and single-cell directional migration. Conversely, wound-healing experiments demonstrated that contact-guidance can be more effective in driving collective SC migration than boundary guidance and indeed only T4 could significantly improve wound-closure speed (Fig. 2, center).

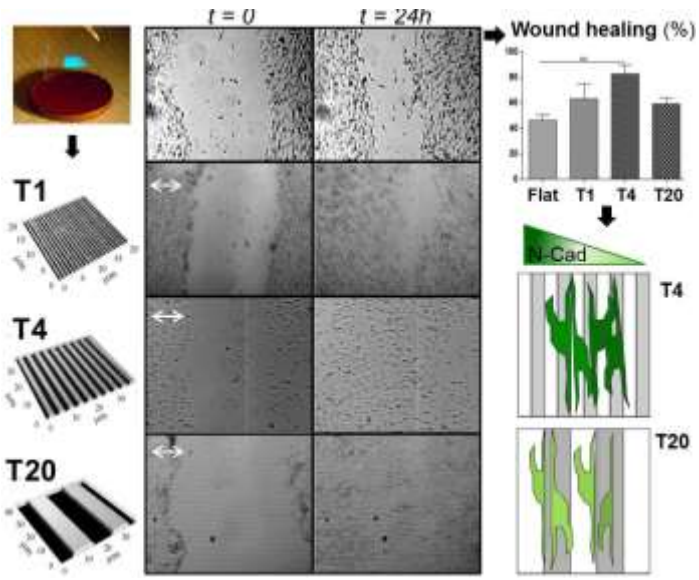

Figure 2. *left)* PDMS micro-grooved membranes were developed with lateral period of 1 (T1), 4 (T4) and 20 (T20) μm; z -scales are 350 nm,850 nm, and 2.5 μm, respectively. *center)* Bright-field images of SC collective migration on the substrates, immediately after the scratch (t = 0) and at t = 24 h; white arrows = GR direction, 200 μm. *right)* Wound closure (%) at t = 24 h: ** P<0.01 T4 vs. FLAT, Dunnett's' test. The collective migration performances are linked to the properties of the SC monolayers generated on the different GRs: SCs on large-period GRs (T20) are characterized by the downregulation of N-Cadherin, a protein that mediates cell-cell adhesion.

We linked this behavior to the properties of the SC monolayers generated on the different GRs by studying the expression of the neural cell-adhesion molecule cadherin (N-cadherin), a protein that mediates cell-cell adhesion, and triggers intracellular signaling cascades to promote migration. SCs on large-period GRs are

characterized by N-cadherin downregulation and enhanced single-cell scattering with respect to SCs on small-period GRs, indicating a less compact monolayer in the boundary guidance regime (Fig. 2, right). Overall T4 (4 μm period, 0.85 μm depth) emerged as the most effective topography in tuning SC directional orientation and migration. Our results provide information of the impact of specific topographical elements that can be exploited for tissue engineering applications and for the production of new devices enhancing peripheral-nerve regeneration.

The role of ubiquitin ligase E3A in polarized contact guidance and rescue strategies in UBE3A-deficient hippocampal neurons

Although neuronal extracellular sensing is emerging as crucial for brain wiring and therefore plasticity, little is known about these processes in neurodevelopmental disorders. Ubiquitin protein ligase E3A (UBE3A) plays a key role in neurodevelopment. Lack of UBE3A leads to Angelman Syndrome (AS), while its increase is among the most prevalent genetic causes of autism (e.g. Dup15q syndrome). By using microgrooved substrates that can induce specific directional stimuli in cells, we previously found deficient topographical contact guidance in AS neurons, which was linked to a dysregulated activation of the focal adhesion pathway [4].

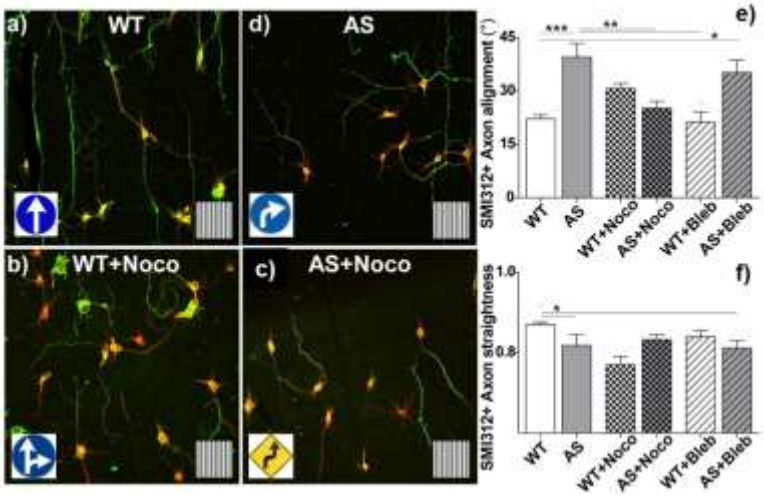

Figure 3. Confocal images of WT (**a-b**) and AS (**c-d**) neurons (div4), untreated (**a**, **d**) or treated from early div2 with nocodazole 40 nM (**b**, **c**); GRs pattern side= 60μm. **e-f**) Axonal morphological parameters of WT (*white*) and AS (*grey*) neurons on GRs in the presence of Noco (*squared*) and Blebbistatin 25μM (*striped*): axon alignment (**e**), and straightness (**f**). */*** Bonferroni test; n ≥ 3, at least 15 neurons/sample.

Here, we studied axon and dendrite contact guidance of Wild-Type, AS and UBE3A-overexpressing neurons (Dup15q autism model) on micrograting (GRs) substrates, with the aim to clarify the role of UBE3A in neuronal guidance [5]. We found that loss of axonal contact guidance is specific for AS neurons while UBE3A overexpression does not affect neuronal directional polarization along GRs. Deficits at the level of axonal branching, growth cone orientation and actin fiber content, focal adhesion effectors and proteins were observed in AS neurons. We tested different rescue strategies for restoring correct topographical guidance in

AS neurons on GRs, by either UBE3A protein re-expression or by pharmacological treatments acting on cytoskeleton contractility. Nocodazole, a drug that depolymerizes microtubules and increases cell contractility, rescued AS axonal alignment to the gratings by partially restoring focal adhesion pathway activation. Surprisingly, UBE3A re-expression only resulted in partial rescue of the phenotype. Overall, cytoskeleton dynamics emerge as important partners in UBE3A-mediated guidance responses. These results support the view that UBE3A-related deficits in early neuronal morphogenesis may lead to defective neuronal connectivity and plasticity.

References

[1] A. Del Grosso, M. Galliani, L. Angella, M. Santi, I. Tonazzini, G. Parlanti, G. Signore, M. Cecchini, *Brain-targeted enzyme loaded nanoparticles: a breach through the blood brain barrier for enzyme replacement therapy in Krabbe disease*, Science Advances **11,** eaax7462 (2019).

[2] C. Masciullo, R. Dell'Anna, I. Tonazzini, R. Böttger, G. Pepponi, M. Cecchini, *Hierarchical thermoplastic rippled nanostructures regulate Schwann cell adhesion, morphology and spatial organization*, Nanoscale **9**, 14861 (2017).

[3] I. Tonazzini, E. Jacchetti, S. Meucci, F. Beltram, M. Cecchini, *Schwann cell contact guidance versus boundary interaction in functional wound healing along nano and micro-structured membranes*, Adv. Healthc. Mat. **4,** 1849 (2015).

[4] I. Tonazzini, S. Meucci, G.M. Van Woerden, Y. Elgersma, M. Cecchini, *Impaired neurite contact guidance in Ubiquitin ligase E3a (Ube3a)-deficient hippocampal neurons on nanostructured substrates*, Adv. Healthcare Mat. **5**, 850 (2016).

[5] I. Tonazzini, G. Van Woerden, C. Masciullo, E. Mientjes, Y. Elgersma, M. Cecchini, *The role of ubiquitin ligase E3A in polarized contact guidance and rescue strategies in UBE3A-deficient hip neurons*, Mol. Autism. **10**, 41 (2019).

1.3.19 Surface-acoustic-wave biosensors and microfluidics

Surface acoustic waves (SAWs) are acoustic waves that travel on the surface of an elastic material, with an amplitude that typically decays exponentially with depth into the substrate. Given their very superficial nature, SAWs are highly sensitive to surface perturbations of the substrate along which they propagate. For example, they can interact with liquid droplets or streams inducing macroscopic fluid manipulations or, in a different configuration, be exploited for sensing applications. The interest of our research in this field is to explore and study novel SAW-driven microfluidic phenomena, and apply this new knowledge to the fields of biosensing and cell biology.

A Rayleigh surface acoustic wave (R-SAW) resonator biosensor based on positive and negative reflectors with sub-nanomolar limit of detection

A label-free sub-nanomolar Rayleigh surface acoustic wave (R-SAW)-based resonator biosensor has been demonstrated for biomolecular detection in liquid after drying [1]. The biosensor comprises two interdigital transducers for R-SAW generation and two positive and negative reflectors to confine the acoustic energy in the sensitive area. We benchmark this biosensor against biotin-streptavidin binding, which is a standard, well-known model for a variety of biosensing processes. The experiments demonstrate a limit of detection of 104 pM and a normalized sensitivity of −296 m^2 kg^{-1}. As a comparison with similar acoustic-wave based systems, both sensitivity and limit of detection are better than that of standard commercial gravimetric sensors (i.e., quartz-crystal-microbalances) and generally better than that of more common Love-SAW biosensors. Our biosensor has a dynamic range potentially comparable with several healthy and safety-related assays, among all cancer biomarker detection.

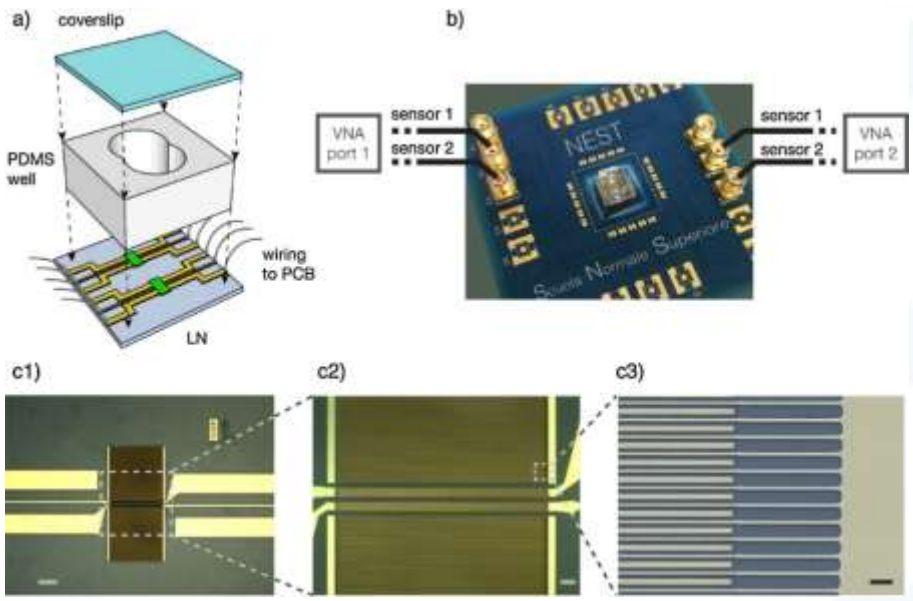

Figure 1. Chip and experimental setup. a) Exploded scheme of the biosensor chip. b) Photo of the mounted biosensor chip with external connections for electrical measurements. c1) and c2) Representative optical microscope images of a resonator. Scale bars are 200 µm (c1) and 40 µm (c2). c3) Representative scanning electron microscopy detail of a PNR (scale bar is 2 µm).

Full-SAW Microfluidics-Based Lab-on-a-Chip for Biosensing

Many approaches to diagnostic testing remain decades old. Well-established biosensing technologies (e.g., enzyme linked immunosorbent assays, radio-

immunoassays) typically cannot fulfill the requirements of portability and ease of use necessary for point-of-care purposes. Several alternatives have been proposed (e.g., quartz-crystal-microbalances, electrochemical sensors, cantilevers, surface-plasmon-resonance sensors) but often lack high performance or still necessitate bulk ancillary instruments to operate. Here we present a highly sensitive, versatile and easily integrable microfluidic lab-on-a-chip (LoC) for biosensing, fully based on surface acoustic waves (SAWs) [2]. By using ultra-high-frequency resonator-biosensors, we show that it is possible to perform highly sensitive assays in complex media. This all-electrical readout platform is benchmarked with the biotin-streptavidin binding in presence of non-specific binding proteins (serum albumin) at physiological concentration. The benchmark experiments were performed with the idea of mimicking a biological fluid, in which other molecular species at high concentration are present together with the analytes.

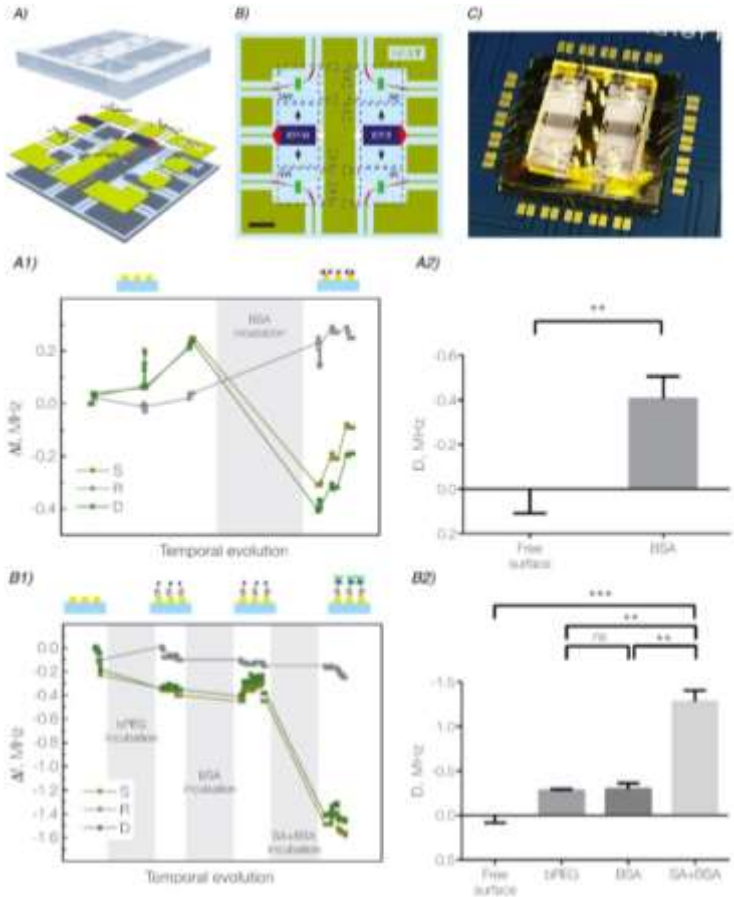

Figure 2. A-C) Chip and experimental setup. A1-2; B1-2) Biosensing measurements of biotin-streptavidin binding in presence of non-specific binding proteins (bovine serum albumin, BSA).

We demonstrate that this LoC can detect sub-nanomolar concentrations of analytes in complex media. As a comparison with similar acoustic-wave based systems, this full-SAW platform outperforms the standard commercial gravimetric sensors (i.e., quartz-crystal-microbalances) and the more common Love-SAW biosensors. This full-SAW LoC could be further developed for the detection of biomarkers in biological fluids.

References

[1] M. Agostini, G. Greco, M. Cecchini, *A Rayleigh surface acoustic wave (R-SAW) resonator biosensor based on positive and negative reflectors with sub-nanomolar limit of detection*, Sensors and Actuators B: Chemical **254**, 1 (2018).

[2] M. Agostini, G. Greco, M. Cecchini, *Full-SAW Microfluidics-Based Lab-on-a-Chip for Biosensing*, IEEE Access **7**, 70901 (2019).

1.3.20 *In vivo* brain physiology: molecules and brain disease

The clinical manifestations of the pathological brain include epilepsy, cognitive deficits and impairment of superior functions. We are gradually realizing that this variety of signs arises from defects at the molecular level that impair cortical-circuit formation and function. We study the biophysical basis of brain disease by applying a variety of techniques for the i- vivo study of cortical processing. To this end we are also developing several tools useful for the study of intracellular signaling and for the creation of mouse models of brain diseases.

Biophysics of the neuronal negative feedback by means of in vivo two photon non-linear microscopy and spectroscopy

Proper brain computation requires a fine equilibrium between excitatory connections, necessary to recruit large neuronal ensembles responsible for computation and behavioral responses, and the negative feedback that maintains activity within the rather limited dynamic range available to neurons. The inhibitory feedback is provided by the activity of a specific set of inhibitory synapses permeable to chloride. The direction of chloride flux determines the extent of neuronal inhibition and these currents depend critically on the intracellular concentration of chloride. In a set of studies, we have achieved methodological and basic-science advancements in this important field.

The excitation/inhibition equilibrium is a dynamic process in continuous evolution during daily activity and during sleep. The key effector of inhibition is a class of inhibitory neurons that uses gamma amino butyric acid (GABA) as a neurotransmitter. When GABA is released at the synapse a chloride channel opens and, if intracellular chloride is low enough, the entrance of negative charges renders the neuron more negative thus opposing the effects of excitation (Fig. 1A). A correct operation of this feedback is essential for proper brain computation as demonstrated by the fact that disruptions of this system leads unavoidably to some form of brain pathology. Given that inhibitory currents are mostly carried by chloride, its intracellular concentration ($[Cl]_i$) dictates the direction of these currents and the result of their action: low $[Cl]_i$ leading to inhibition and high $[Cl]_i$ leading to depolarization. The regulation of $[Cl]_i$ exerts wide-ranging effects on synaptic signaling and plasticity and on development and disorders of the brain. In the last few years, we developed a technique for the measurement of $[Cl\text{-}]_i$ by means of two photon imaging and spectroscopy. Our genetically encoded fluorescent sensor includes a spectroscopic reference (Fig. 1) and we were able to perform parallel measurements of $[Cl]_i$ and pH at the single-cell level in the mouse cortex in vivo.

With this too we have demonstrated for the first time the developmental change of intracellular chloride in the cortex [8] and how this process is altered in a mouse model of cognitive impairment.

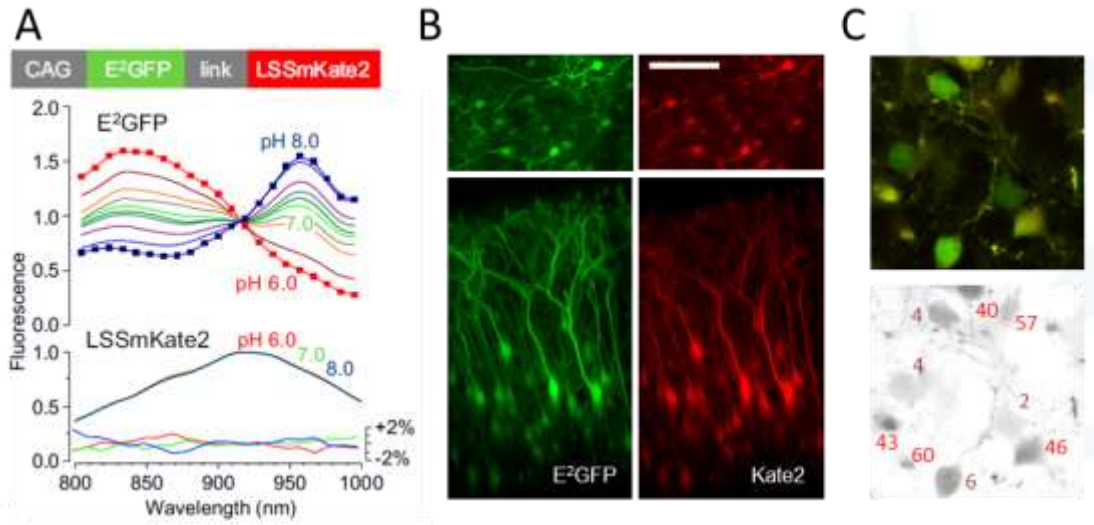

Figure 1. A) The chloride/pH sensor is formed by the fusion of the Cl sensitive element E²GFP with the insensitive spectral reference LSSmKate2. E²GFP is sensitive to both intracellular pH and $[Cl]_i$. Changes in pH are reported with a shift of the 2-photon excitation spectra. Chloride interacts with the chromophore by collisional quenching, therefore increasing $[Cl]_i$ is reported as a decrement of the green fluorescence in comparison with the red reference. The plot shows the two-photon excitation spectra of E²GFP and LSSmKate2 at different levels of pH. The non-labeled spectra of E²GFP have been obtained at pH 6.4, 6.8, 6.9, 7.1, 7.2, 7.4, and 7.6. The excitation spectrum of LSSmKate2 is pH-insensitive: the lower panel shows the normalized difference between the spectra obtained at pH values of 6, 7, and 8, with the mean spectrum averaged for all pH values. B) Expression and spectra of LSSmClopHensor in vivo after transfection by in utero electroporation. The field depicted lies in the superficial layers of the visual cortex. Calibration bar 100 μm. C) Measurement of intracellular Chloride in the mouse cortex: different cells display different hues from green to orange, with low chloride cells appearing green. Numbers in the lower panel report the computed concentrations.

ddGCaMP: a new tool for long term imaging of intracellular calcium

Calcium imaging is a powerful tool for the study of intracellular signaling and for the single neuron level analysis of neuronal computation. The main tool of the trade is a family of Ca-sensors formed by proteins that are almost non-fluorescent at resting state and that undergo a large increase in fluorescence upon Ca binding. Therefore, neuronal activity, which causes the influx of calcium ions, is signaled by a transient fluorescence increase. Despite the importance of this tool, its biocompatibility is far from optimal, since the sensor is a Ca binding protein and its prolonged expression leads to an epileptic phenotype, possibly because of altered Ca homeostasis. In this work we have fused GCaMP6 with a destabilization domain that causes the rapid degradation of the protein. This domain can be neutralized by a ligand that crosses the blood brain barrier and rapidly suppresses protein degradation. In this way, we can target the cortex early in development with widespread GCaMP transfection but the protein levels are so low that do not cause any side effect. One hour before of the imaging session, the ligand is provided to the sensor by simple intraperitoneal injection, the degradation stops and the sensor builds up in the cortex (Fig. 2) to return to basal level after a few hours. This tool will allow long term chronic recording of Ca activity during development without any of the side effects due to the constitutive expression of GCaMP. The data shown in Fig 2 are collected with a wide field microscope that we have developed for wide field imaging of the entire brain.

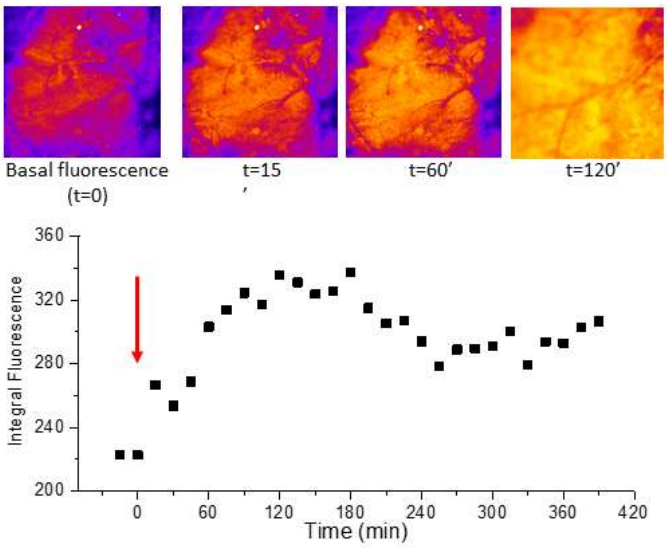

Figure 2. Wide field imaging of the resting state fluorescence of ddGCaMP in basal conditions and after activation (red arrow). The basal florescence is mostly due to background fluorescence and increases rapidly after the blockage of protein degradation (red arrow in the lower plot). The field is about 4 mm wide.

The analysis of wide field imaging data requires specific software tools that can extract the fluorescence fluctuations caused by Calcium transient from the background noise. To this effect, we have developed a novel quantitative method for the concurrent analysis of electrophysiological and 2-photon imaging data. We show how the statistics of the time series provided by the recordings of LFP and Ca^{2+} imaging can be used to classify epileptic activity in the entire zebrafish brain. Then, we demonstrate that by cross correlating the time series originating from Ca^{2+} imaging with the LFP recordings it is possible to pinpoint the specific regional sources of epileptiform activity [13].

Modelling genetic mosaicism

Genetic mosaicism refers to the presence of genetically distinct cellular populations within the same individual. This condition originates from DNA mutations, either monogenic or genome-wide, that may occur through different biological mechanisms (X-chromosome inactivation for X-linked genes or somatic mutations). A pathophysiological role for mosaicism has been initially identified for X-linked disorders (for example Rett syndrome or Xfragile) and then for disorders associated to somatic mutations, leading to focal cortical dysplasia. As our capacity of detecting somatic mosaicism in human patients improved, it gradually emerged that somatic mosaicism plays an important role in brain pathology, where even low frequency of mutation can lead to cognitive disorders and epilepsy. To underline the importance of this mechanism, recent whole exomes studies on genetic samples from families including one ASD offspring have detected the presence of somatic mosaicism in 3-5% of the analyzed samples. The creation of mosaicism requires the use of conditional transgenic mice where the target gene is normally expressed but it can be excised by the presence of the bacterial enzyme CRE recombinase. The transfection of a random set of cells with CRE recombinase therefore creates a mosaic of expression for the specific gene. This approach has a severe drawback due to the lack of control of the mosaicism

degree. Furthermore, the genetic identity of the cells in the transfected area is unknown. To answer these criticalities, at NEST we have generated Beatrix, a new Cre-reporting architecture capable of amplifying and preserving weak or transient Cre events with a tenfold increase in sensitivity compared to canonical reporter structures. Beatrix is a reliable reporter of Cre-mediated recombination and it allows the creation of genetic mosaics of arbitrary degree that are amenable to be imaged in vivo by two-photon microscopy. As a proof of principle of the methodology, we created a mosaic of expression of the autism-related gene PTEN, a constitutive inhibitor of the mTOR pathway, and we describe the anatomical phenotype of this mosaic in the mouse cortex and olfactory bulb (Fig. 3). Finally, we demonstrate that the cortical mosaic is characterized by impaired network activity and by transient episodes of hyperexcitability strongly reminiscent of the electrophysiological signature of the human disease.

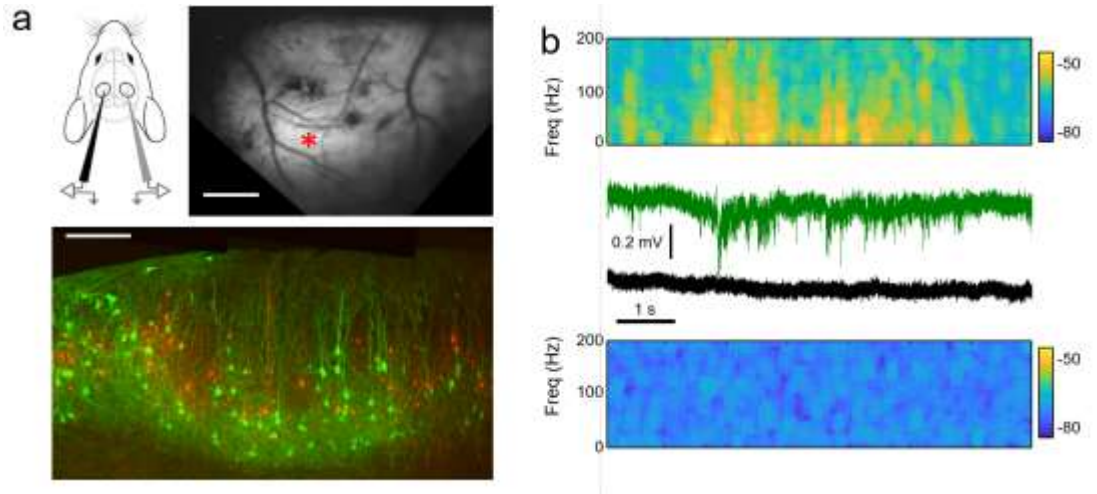

Figure 3. Mosaicism for the gene PTEN leads to an epileptic phenotype. A) double recordings from the focal mutation site and from the opposite, control, hemisphere. The wide field image shows the recording site in correspondence of a fluorescent patch (bar 1 mm). The lower panel shows a coronal section of the brain fixed after the recordings that shows a mosaic of normal neurons (red) and neurons lacking PTEN (green). B) recordings from the focus (green trace) shows characteristics hypersynchronous bursts, while the other hemisphere is silent (black trace).

References

[1] M. Sessolo, I. Marcon, S. Bovetti, G. Losi, M. Cammarota, G.M. Ratto, T. Fellin, G. Carmignoto, *Parvalbumin-Positive Inhibitory Interneurons Oppose Propagation but Favor Generation of Focal Epileptiform Activity*, J. Neurosci. **35 (26)**, 9544 (2015).

[2] G. Della Sala, E. Putignano, G. Chelini, R. Melani, E. Calcagno, G.M. Ratto, E. Amendola, C.T. Gross, M. Giustetto, T. Pizzorusso, *Dendritic Spine Instability in a Mouse Model of CDKL5 Disorder Is Rescued by Insulin-like Growth Factor 1*, Biol. Psychiatry **80 (4)**, 302 (2016).

[3] F. Pederzoli, B. Ruozi, E. Pracucci, G. Signore, M. Zapparoli, F. Forni, M.A. Vandelli, G.M. Ratto, G. Tosi, *Nanoimaging: photophysical and pharmaceutical characterization of poly-lactide-co-glycolide nanoparticles engineered with quantum dots*, Nanotechnology **27 (1)**, 015704 (2015).

[4] J. Szczurkowska, A.W. Cwetsch, M. Dal Maschio, D. Ghezzi, G.M. Ratto, L. Cancedda, *Targeted in vivo genetic manipulation of the mouse or rat brain by in utero electroporation with a triple-electrode probe*, Nature Protoc. **11 (3)**, 399 (2016).

[5] P. Artoni, S. Landi, S.S. Sato, S. Luin, G.M. Ratto, *Arduino Due based tool to facilitate in vivo two-photon excitation microscopy*, Biomed. Opt. Express **7 (4),** 1604 (2016).

[6] J.M. Paredes, A.I. Idilli, L. Mariotti, G. Losi, L.R. Arslanbaeva, S.S. Sato, P. Artoni, J. Szczurkowska, L. Cancedda, G.M. Ratto, G. Carmignoto, D. Arosio, *Synchronous Bioimaging of Intracellular pH and Chloride Based on LSS Fluorescent Protein*, ACS Chem. Biol. **11 (6)**, 1652 (2016).

[7] L. Petrucco, E. Pracucci, M. Brondi, G.M. Ratto, S. Landi, *Epileptiform activity in the mouse visual cortex interferes with cortical processing in connected areas*, Sci. Rep. **7**, 40054 (2017).

[8] S.S. Sato, P. Artoni, S. Landi, O. Cozzolino, R. Parra, E. Pracucci, F. Trovato, J. Szczurkowska, S. Luin, D. Arosio, F. Beltram, L. Cancedda, K. Kaila, G.M. Ratto, *Simultaneous two-photon imaging of intracellular chloride concentration and pH in cortical pyramidal neurons in vivo*, Proc. Natl. Acad. Sci. USA **114 (41)**, E8770 (2017).

[9] A. Giorgi, S. Migliarini, A. Galbusera, G. Maddaloni, M. Mereu, G. Margiani, M. Gritti, S. Landi, F. Trovato, S.M. Bertozzi, A. Armirotti, G.M. Ratto, M.A. De Luca, R. Tonini, A. Gozzi, M. Pasqualetti, *Brain-wide Mapping of Endogenous Serotonergic Transmission via Chemogenetic fMRI*, Cell Rep. **21 (4),** 910 (2017).

[10] O. Cozzolino, M. Marchese, F. Trovato, E. Pracucci, G.M. Ratto, M.G. Buzzi, F. Sicca, F.M. Santorelli, *Understanding Spreading Depression from Headache to Sudden Unexpected Death*, Front. Neurol. **9 (19)** (2018).

[11] G. Faini, A. Aguirre, S. Landi, D. Lamers, T. Pizzorusso, G.M. Ratto, C. Deleuze, A. Bacci, *Perineuronal nets control visual input via thalamic recruitment of cortical PV interneurons*, eLife **7**, e41520 (2018).

[12] S. Landi, L. Petrucco, F. Sicca, G.M. Ratto, *Transient Cognitive Impairment in Epilepsy*, Front Mol. Neurosci. **11,** 458 (2019).

[13] O. Cozzolino, F. Sicca, E. Paoli, F. Trovato, F.M. Santorelli, G.M. Ratto, M. Marchese, *Evolution of Epileptiform Activity in Zebrafish by Statistical-Based Integration of Electrophysiology and 2-Photon Ca2+ Imaging*, Cells **9 (3)**, 769 (2020).

1.3.21 Biosensors for functional imaging of cells and diagnostic applications at the nanoscale

Fluorescence offers the unique opportunity to combine high detection sensitivity (down to single molecule detection) and spatial imaging resolution, with an optical signal responsive to nanoscale changes of environmental physicochemical properties. Here, we shall show how the rational design of the chemical structure transforms organic dyes into efficient biosensors of dielectric and viscosity properties with confocal spatial resolution (200 nm) at intracellular level. These environmental biosensors were effectively applied to image physicochemical properties of intracellular organelles, shedding light on several biomedically-relevant phenomena including drug-delivery mechanisms and chromatin compaction upon nuclear-lamina misassembly in the Hutchinson-Guilford progeria syndrome.

Intracellular polarity and viscosity play regulative roles irrespective of the specific nature of any biochemical reaction. Accordingly, intensive research has been recently devoted to polarity/viscosity fluorescent sensors for high-resolution fluorescent microscopy. Usually, polarity affects the energy of emission, whereas viscosity effectively modulates the fluorescent lifetime.

By a combined computational and experimental approach, we developed fluorescent "molecular rotors" able to monitor independently intracellular polarity and viscosity [1]. These probes provided quantitative measurements of polarity and viscosity of the endosomal membrane. Real time monitoring of polarity and viscosity allowed for validating engineered drug delivery peptides able to disrupt the lipid bilayer once internalized, thus providing a novel assay of drug delivery efficacy (Fig. 1).

As an alternative approach, we focused on a peculiar fluorescent "molecular rotor", whose excited state is unaffected by local polarity [2]. According to a strategy previously established by us, we followed the lifetime-viscosity dependence by the phasor approach to fluorescence lifetime imaging, a fit-free graphical method based on the frequency-domain analysis of the fluorescence decay. Our probe highlighted that cells characterized by a genetically-encoded misassembly of lamin A, as observed in Hutchinson-Gilford progeria syndrome (HGPS) [2], are associated with a reduced nucleoplasm viscosity (Fig. 2), supporting a strict correlation between HGPS and chromatin compaction and regulation.

Complementary to these approaches, a coumarine derivative was demonstrated to possess two concomitantly emitting excited states with different energies, breaking the so-called Kasha's rule. On account of its unique photophysics, this probe was applied to cell imaging to report both the dielectric constant and the water content of subcellular regions.

In conclusion, on account of the exquisite sensitivity of fluorescence, we developed a toolbox of intracellular sensors to monitor polarity and viscosity of nano-environments, in view of diagnostic applications.

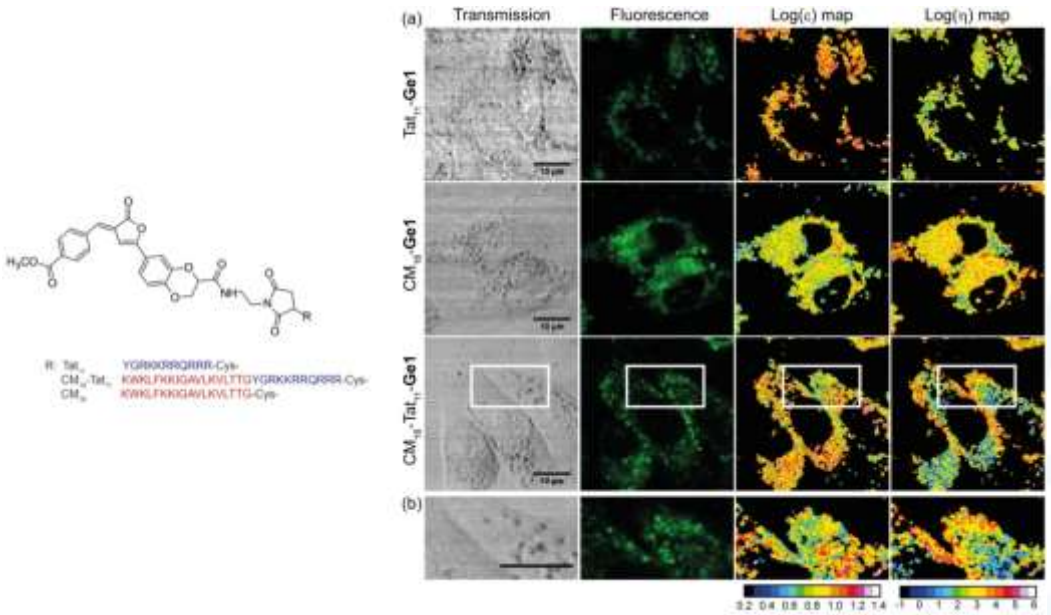

Figure 1. Left panel: molecular structure of the dual polarity (dielectric constant,) / viscosity ( ) fluorescent sensor Ge1 conjugated to the membrane-active peptides Tat_{11} and/or CM_{18}. Right panel: administration of conjugated Ge1 to Hamster Ovary Cells. (a) Transmission, Fluorescence, Log(ε) and Log(η) maps of cells treated with CM_{18}-Ge1 (upper panels), CM_{18}-Tat_{11}-Ge1 (medium panels) and Tat_{11}-Ge1 (lower panels). (b) Zoomed region (white squares in panel a) of CM_{18}-Tat_{11}-Ge1 treated cells. Polarity and viscosity data clearly show that mono-substituted Tat_{11}-Ge1 and CM_{18}-Ge1 remain entrapped inside the endosomal membranes; conversely, the fusion construct CM_{18}-Tat_{11}-Ge1 disrupt the lipid bilayer, as witnessed by the much lower viscosity and higher polarity, and allows for cargo release to the cytoplasm.

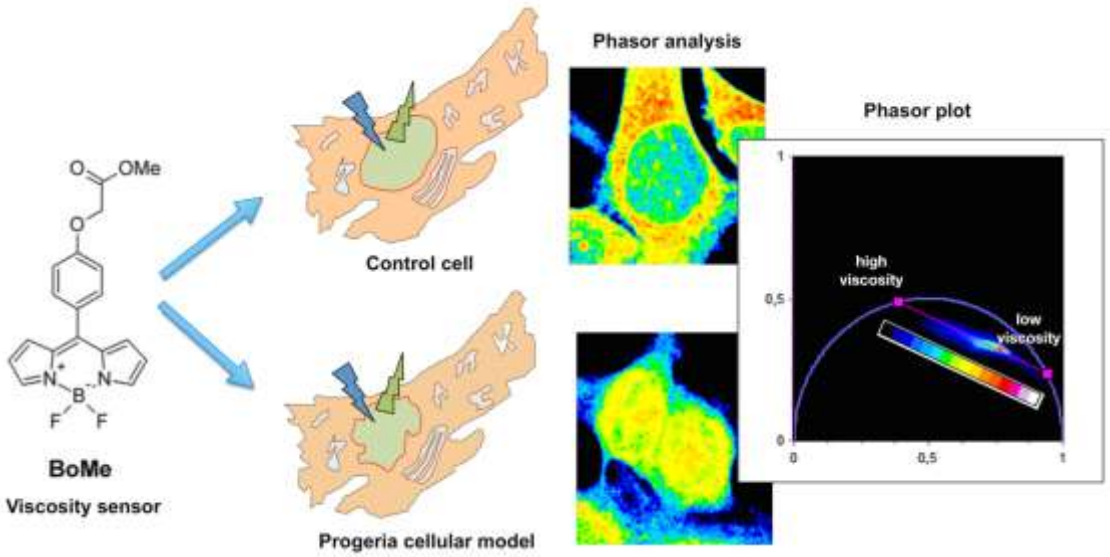

Figure 2. Left panel: molecular structure of the polarity-independent viscosity-dependent fluorescent sensor BoMe. Middle panels: BoMe was administered to both health and HGPS-affected human osteosarcoma cells 2 (U2OS), which displayed different structure of nuclear lamina (round and smooth: healthy cells; irregular and blebbed: HGPS cells). BoMe binds to chromatin and reports on the local viscosity. Right panel: phasor plot of frequency-domain lifetime response of BoMe: different positions on the phasor plot indicate different viscosity values, and are color codified according to cell images in the middle panel. Color distribution clearly shows lower chromatin viscosity for HGPS cells.

References

[1] M. Koenig, B. Storti, R. Bizzarri, D.M. Guldi, G. Brancato, G. Bottari, *A fluorescent molecular rotor showing vapochromism, aggregation-induced emission, and environmental sensing in living cells*, J. Mater. Chem. C **4**, 3018 (2016).

[2] G. Ferri, L. Nucara, T. Biver, A. Battisti, G. Signore, R. Bizzarri, *Organization of inner cellular components as reported by a viscosity-sensitive fluorescent Bodipy probe suitable for phasor approach to FLIM*, Biophys. Chem. **208**, 17 (2016).

1.3.22 Multiscale simulations of peptide-bilayer interactions

As highlighted by increasing scientific evidence, the crossing of biological membrane by cell penetrating peptides (CPPs) is governed by their self-association. We report a combined experimental and computational study showing that Tat_{11}, a CPP, is able to form dimers despite its sizeable positive charge. By extensive MD simulations, we unraveled the structural motives of Tat_{11} self-association, providing the basis to understand the membrane penetration mechanisms. Computational modeling of the peptide-aggregate interaction with the membrane can be greatly facilitated by using simplified coarse grain (CG) models. Here we also describe a strategy to build and optimize statistics-based analytical CG force fields, particularly suited to account for the common interaction motives between biopolymers.

Molecular dynamics (MD) simulations of aggregation phenomena become particularly challenging when dealing with intrinsically disordered proteins, such as the highly charged Tat_{11} peptide. The complexity of aggregation *per se* is compounded with the requirement of exhaustively sampling the numerous peptide conformations. Notwithstanding this complexity, the topic is of broad interest given its recurrence in several biological phenomena. One example is the mechanism of Tat_{11} internalization (across the biological membrane), being concentration dependent in a way that mirrors the aggregation state of the peptide in solution. Light scattering and NMR measurements of the diffusion coefficient (Fig. 1a) provide a picture suggesting the presence of a dimeric aggregate. These observations prompted us to investigate putative structure of Tat_{11} dimer by MD all-atom simulations. Starting configurations were obtained by maximizing the inter-peptide contacts by metadynamics, and unrestrained MD simulations at the μs timescale. The dimer structures were shown to be highly flexible with the inter-peptide interactions taking place mostly between the C-termini. In this arrangement the negatively charged carboxylic groups (COO^-) engages in salt bridges with the several charged side chains (see Fig. 1b). A notable feature is the presence of stacking between two or more Arg guanidinium groups close to the C-termini. Albeit keeping two positively charged groups in close contact, this motif optimized the geometry for the interaction with COO^- (Fig. 1b). The question whether this stacking is functional to the peptide interaction with the membrane will be the topic of further studies.

In spite of their increasing use, Coarse Grained (CG) models for biopolymers are still far from reaching the level of standard and validation currently available for all-atom models. This depends in part on the fact that the parameterization strategies are various and most often adjusted on the specific cases. We tried to design a general strategy to aid building and optimization of statistics based analytical force fields which we implemented in the software AsParaGS (Assisted Parameterization platform for Coarse Grained models, www.muscade-lab.it/project/asparags). The method relies on the exploration of the parameters space of the analytical interaction potential by combining different algorithms (i.e., relative entropy driven stochastic exploration and iterative Boltzmann inversion) and searching for optimal parameters set with respect to given score function, e.g., depending on the distance between the simulation and the experimental distribution of structural variables.

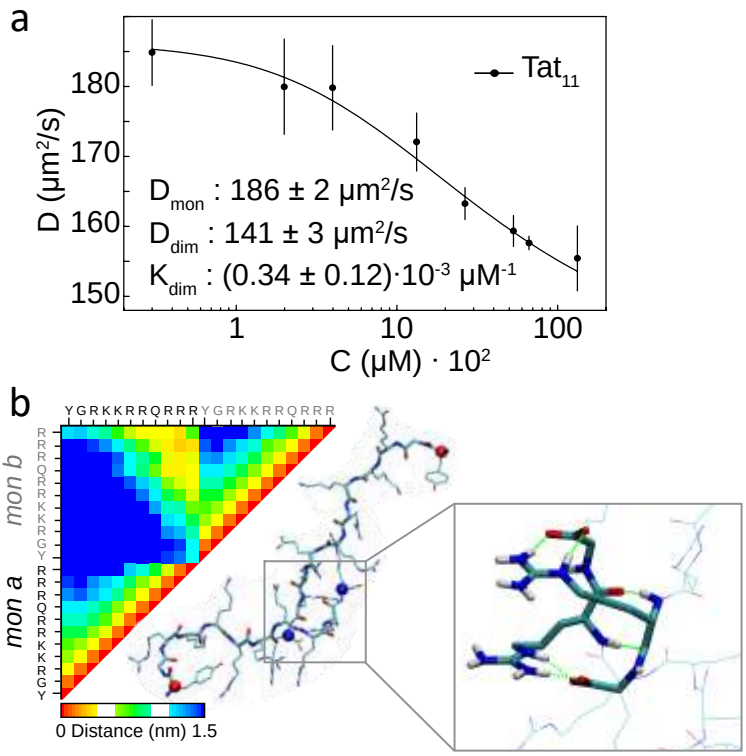

Figure 1. Panel a): Diffusion coefficients obtained by NMR DOSY experiments for increasing peptide concentrations. Monomer and dimer diffusion coefficients (D_{mon} and D_{dim}, respectively) with dimerization constant (K_{dim}) are obtained by fitting. Panel b): Tat_{11} inter and intra peptide contact map averaged during the simulation, and dimer representative structure. Single letter amino acids are indicated for each monomer. The inset shows the Arg-Arg stacking motif with salt bridges between C-termini and Arg side chains.

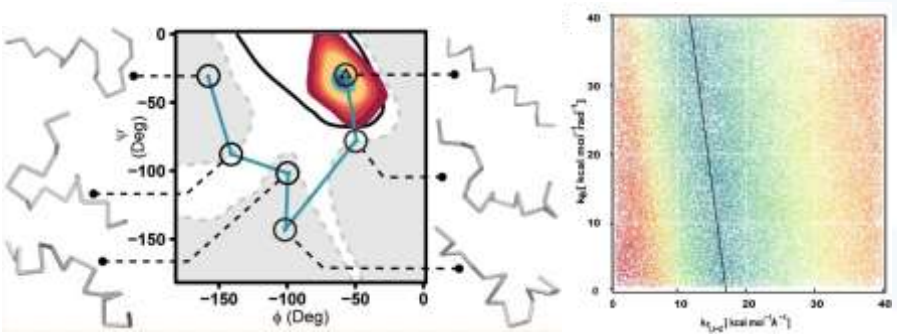

Figure 2. Illustration of the AsParaGS method on a test case (helical polypeptide). On the left: the parameters space is explored until the helical-stabilizing parameterization is reached, as shown in the Ramachandran Map. On the right: the methods reveal correlations between parameters: if two terms in the force filed are correlated (e.g., the bond angle and 1-3 interaction term), areas with similarly high scores appear in the parameters space (blue color), indicating that any combination of the two terms lying on the correlation line will give similarly good force fields.

References

[1] S. Macchi, R. Nifosì, G. Signore, S. Di Pietro, C. Boccardi, F. D'Autilia, F. Beltram, F. Cardarelli, *Self-aggregation propensity of the Tat peptide revealed by UV-Vis, NMR and MD analyses*, Phys. Chem. Chem. Phys. (Communication) **19**, 23910 (2017).

[2] P. Mereghetti, G. Maccari, G.L.B. Spampinato, V. Tozzini, *Optimization of Analytical Potentials for Coarse-Grained Biopolymers Models*, J. Phys. Chem. B **120**, 8571 (2016).

1.3.23 Advanced microscopy and single-particle tracking: applications to neuroscience

We exploited, optimized, and developed various techniques in light-based microscopy for analyzing living matter at cellular and molecular levels. In particular, we developed a toolbox for single particle tracking (SPT) of membrane receptors and their ligands, suitable also for relatively fast single-pass membrane receptors; this is based on chemical tagging of recombinant proteins, TIRF microscopy, and automatized analyses of single-particle trajectories. We are now extending it to simultaneous visualization and analysis of two moieties.
The superresolved localization of this technique allowed analyzing dynamics, functions, interactions and stoichiometry of (pro)neurotrophin receptors p75^{NTR} and TrkA and of their ligands in living cells.

Techniques in light-based microscopy continue to be central tools for analyzing organization, function and interactions of and within cells from the tissue down to the molecular levels. In particular, the methods of reconstruction of single-particle trajectories (single-particle tracking - SPT) are allowing the study of dynamics and transient interactions of molecules at excellent space-time resolutions, up to the order of (tens of) nanometers and milliseconds, and multicolor methods allow to analyze interactions between different objects in living cells [2]. Moreover, the SPT techniques are intrinsically super-resolved, and allow to obtain a distribution of the parameters of interest on the population; among these, the average lifetime of homo- and hetero-dimers, the constants of association and dissociation, their type of motion and, in case, their diffusivity [2].
We developed procedures for labeling, visualization and tracking of relatively fast-moving membrane receptors and their ligands, and methods to maximize the effectiveness of SPT data analysis, especially for the two-color analysis we are implementing. Proteins of interest are modified with peptidic tags and labelled by enzymatic reactions; we implemented and optimized short versions of this kind of tags that could also be functionalized orthogonally with different fluorophores [1, 5]. The possibility to label only receptors on the membrane with virtually any tag (e.g. fluorophores, quantum dots) is useful in various experiments [12]. Moreover, if needed, we can tune protein expression using inducible lentiviral vectors [1,8]. The movement of the receptors in the membrane and/or of the ligands within vesicles are then captured by (multi-channel) TIRF or epifluorescence microscopy.
Research on nervous system and neural cells is pivotal in our laboratory [6,7,10], and we applied also the SPT toolbox to the study of neurotrophins and their receptors [1-5,8,9]. Neurotrophic signaling is regulated through a complex interplay of different ligands and receptors, whose detailed network of interactions is still a source of debate. Superresolved SPT of receptors or ligands can help solving these issues, e.g. by counting the molecules in complexes while inspecting their dynamics and interactions in the membrane of living cells at low expression levels.
We studied dynamics, stoichiometry, and signaling of TrkA and p75^{NTR} neurotrophic receptors (and some mutants of them) on the membrane of various cell lines and primary neurons or astrocytes (Fig. 1). This analysis, also after treatments with ligands or drugs, unraveled their mode of action in the first steps of sundry signaling pathways; indeed, the molecular basis for initiating signaling pathways can be very different, even if the same receptor and the same or similar ligands are involved. Moreover, we found puzzling results on commonly used control mutants [8, 9].

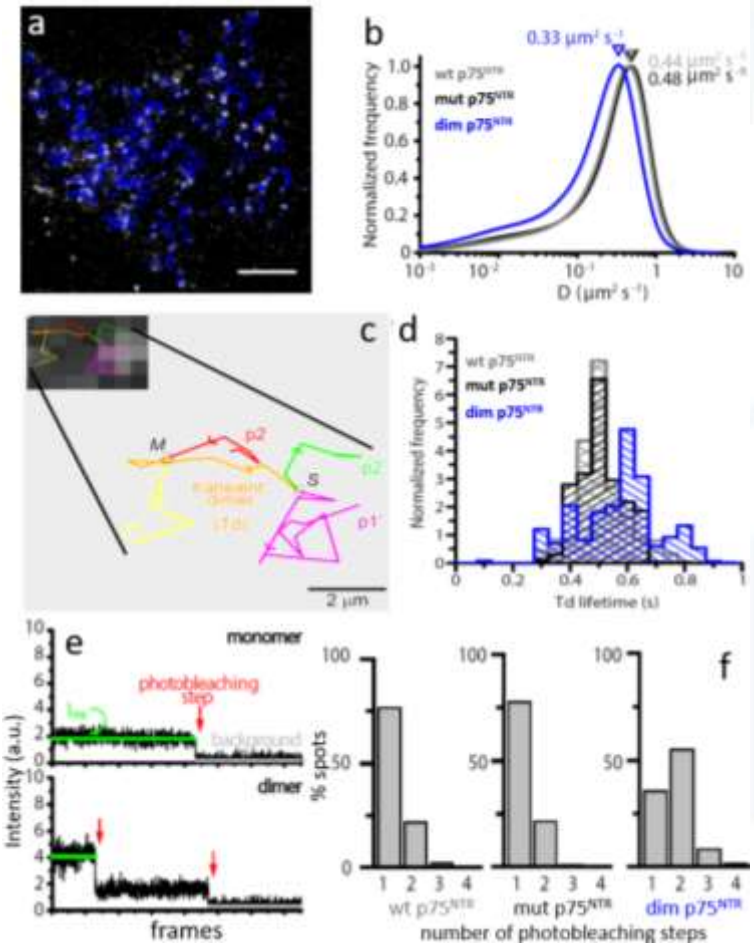

Figure 1. Examples of possible results from single particle tracking (SPT): application to neurotrophin receptors. **a-f)** Membrane p75^{NTR} moves as a monomer with at most transient interactions: membrane located wild type (wt) p75^{NTR}, a monomeric (mut p75^{NTR}) and a dimeric (dim p75^{NTR}) controls where labeled with Abberior635P exploiting a peptidic tag and imaged with TIRF microscopy. **a)** Reconstructed single receptor trajectories (blue) superimposed on a TIRF movie frame. Scale bar: 5 μm. **b)** Distribution of diffusion coefficient D for the constructs. **c-d)** Analysis of transient dimerization: **c)** transient dimer (Td) trajectory superimposed on a region of a TIRF movie frame and enlarged on bottom (M: merge, S: split events); **d)** distribution of the cell-average duration of Td trajectories for wt (gray), mut (black) and dim (blue) p75^{NTR} constructs. All data are from cells with [0.18-0.36] spots/μm^2. **e)** Examples of intensity profile traces of monomers and dimers. I_{PRE}: particle average intensity before the first bleaching step; red arrows: counted single photobleaching steps. **f)** Histograms of the number of photobleaching steps per trace for wt, mut and dim p75^{NTR}.

In particular, we contributed to solve some controversial results on stoichiometry and activation mechanisms for different signaling pathways of P75^{NTR} in the membrane of living cells (Fig. 2). We showed that, at densities of 0.2-0.5 receptors/μm^2, most receptors are fast diffusing monomers (D~1 μm^2/s in neurons), not substantially altered by (pro)neurotrophins administration. We found different signaling mechanisms for apoptosis and axon growth-cone collapse, and demonstrated that, in leaving cells at low expression levels, P75^{NTR} and a mutant developed as a monomeric control (mut P75^{NTR}) have the same stoichiometry in membrane, but a different partitioning into cholesterol-rich membrane regions upon NGF stimulation [8]. In a recent work, we studied

different TrkA kinase-dead mutants that were previously used for various work; we found that they can have different membrane trafficking and functions (among themselves and with respect to the wild type counterpart), and found that some of these differences are caused by different molecular structures; moreover, we demonstrated the existence of at least two distinct membrane immobilization modes, linked or not to NGF stimulation [9].

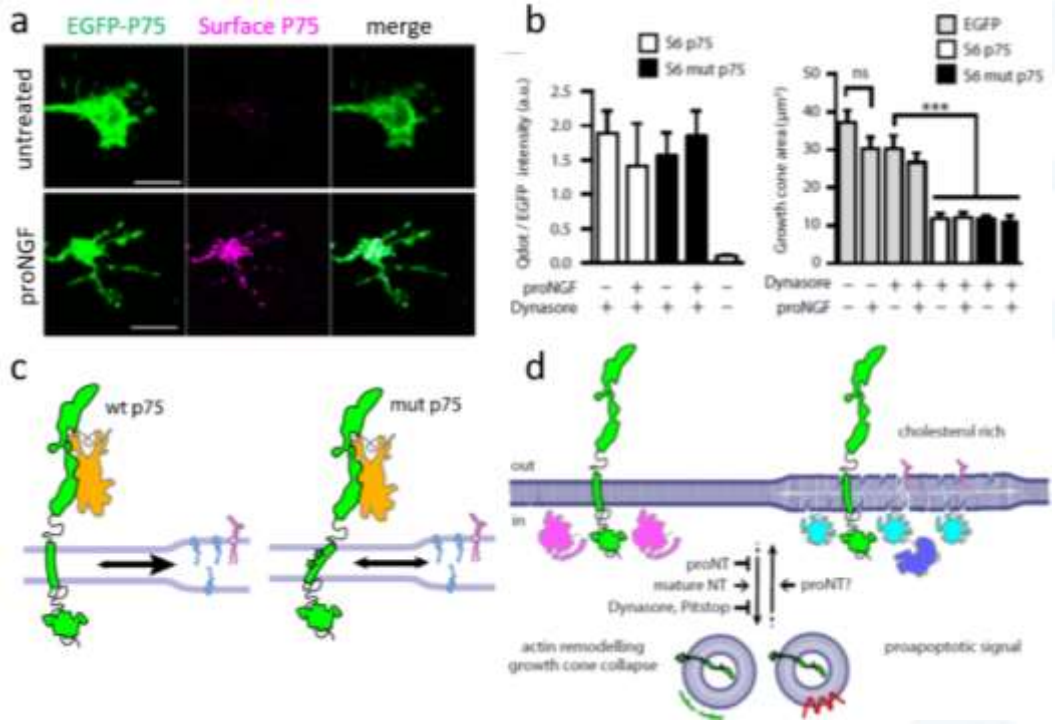

Figure 2. a-b) P75^{NTR} was fused with a fluorescent protein (EGFP), and only the receptors on the membrane were functionalized with biotin using a short peptidic tag (S6) and labeled with streptavidinated quantum dots (Qdot); the Qdot to EGFP ratio is a measure of surface p75NTR-EGFP fraction. **a)** Representative confocal images of growth cones of wt hippocampal neurons, transfected with S6-tagged p75^{NTR}-EGFP constructs, untreated (top) or incubated with proNGF for 30' (bottom). Total (green) and surface (magenta) receptor pools are shown. EGFP channel levels in the left panels are linearly scaled to highlight cone dimensions. Scale bar, 5μm. **b)** Left: both wt and mut p75^{NTR} are enriched on the plasma membrane after 30' proNGF treatment or by treatment with Dynasore (an inhibitor for dynamin-dependent internalization). Right: retention on the membrane is sufficient for both wt and mut p75^{NTR} to cause growth cone collapse. ***p<0.001, ns: not significant at the 0.05 level in a one-way ANOVA test with Tuckey's multiple comparisons. Bars are mean±sem. **c-d)** Proposed model for cholesterol-dependent p75^{NTR} signaling on the plasma membrane. **c)** Schematic view of the membrane partitioning of wt p75^{NTR} (green, left) or mut p75^{NTR} mutant (green, right), upon NGF (orange) binding. Cholesterol-rich, signaling-competent regions have increased membrane thickness and contain cholesterol and gangliosides. Partitioning is highlighted by the arrows in opposite directions. **d)** Schematic view of p75^{NTR} signaling at the membrane and downstream internalization. Signaling can occur from cholesterol-poor or cholesterol-rich membrane regions resulting in receptor internalization within clathrin-positive (green) or caveolin-positive (red) endosomes. In our model, interactors of surface-retained p75^{NTR} (magenta), involved in actin-remodeling and growth cone collapse, are more abundant in non-raft regions and indeed this pathway is not impaired by the mutations introduced in mut p75^{NTR}. Conversely, apoptotic signaling effectors (blue) are enriched in raft platforms and therefore efficiently activated only by NGF-bound wt p75^{NTR}. Differently from mature NTs, proNTs at the growth cones cause surface accumulation of p75^{NTR}, which is sufficient for causing growth cone collapse.

We addressed also dynamics and stoichiometry of NGF and proNGF in vesicles moving within neuron axons [3-5,11] (Fig. 3), demonstrating, *e.g.*, that local stall of signaling endosomes containing nerve growth factor (NGF) is responsible for an increased axon elongation for neurons cultured on top of a graphene layer [11]. Moreover, the algorithms and techniques implemented for SPT can be used for analyzing the motion of vesicles imaged with any tool, *e.g.* by confocal fluorescence microscopy [13].

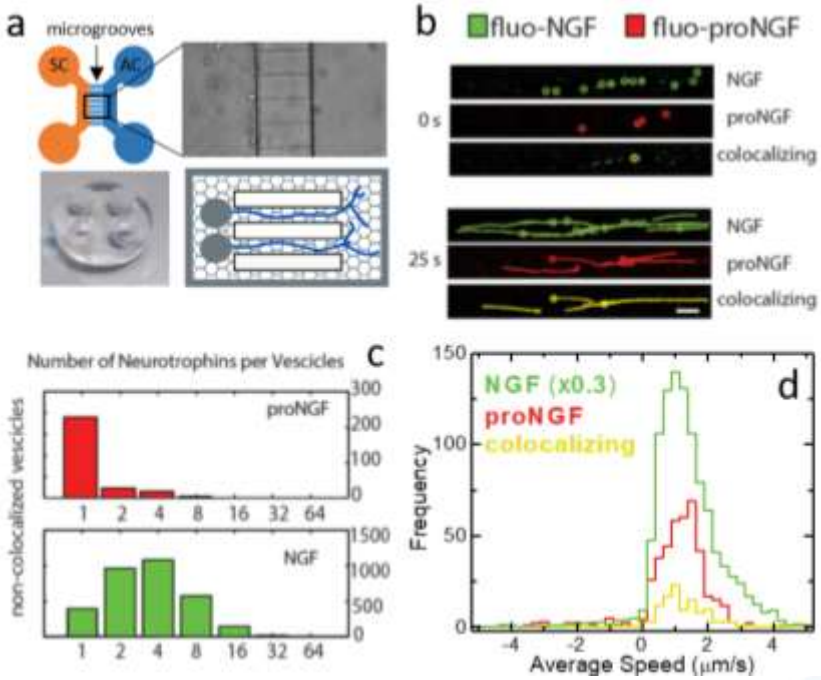

Figure 3. Example of single-vesicle tracking for the transport of fluorescent NGF and proNGF in neuronal axons. **a)** Schemes and images of a microfluidic compartmentalized chamber used to align the axons of neurons grown inside it. **b)** Examples of reconstructed trajectories. **c)** Histograms of the number of fluo-proNGF and fluo-NGF molecules inside moving vesicles. **d)** Example of histogram of average velocities of moving vesicles.

References

[1] L. Marchetti, T. De Nadai, F. Bonsignore, M. Calvello, G. Signore, A. Viegi, F. Beltram, S. Luin, A. Cattaneo, *Site-specific labeling of neurotrophins and their receptors via short and versatile peptide tags*, PLoS one **9 (11)**, e113708 (2014).

[2] L. Marchetti, S. Luin, F. Bonsignore, T. De Nadai, F. Beltram, A. Cattaneo, *Ligand-Induced Dynamics of Neurotrophin Receptors Investigated by Single-Molecule Imaging Approaches*, International journal of molecular sciences **16 (1)**, 1949 (2015).

[3] T. De Nadai, L. Marchetti, C. Di Rienzo, M. Calvello, G. Signore, P. Di Matteo, F. Gobbo, S. Turturro, S. Meucci, A. Viegi, F. Beltram, S. Luin, A. Cattaneo, *Precursor and mature NGF live tracking: one versus many at a time in the axons*, Scientific Reports **6**, 20272 (2016).

[4] L. Marchetti, T. De Nadai, R. Amodeo, C. Di Rienzo, F. Bonsignore, F. Gobbo, F. Beltram, S. Luin, A. Cattaneo, *Single Molecule Imaging and Tracking of Neurotrophins and their Receptors in Living Neuronal Cells*, Biophysical Journal **110**, 371a (2016).

[5] P. Di Matteo, M. Calvello, S. Luin, L. Marchetti, A. Cattaneo, *An Optimized Procedure for the Site-Directed Labeling of NGF and proNGF for Imaging Purposes*, Frontiers in Molecular Biosciences **4**, 4 (2017).

[6] F. Gobbo, L. Marchetti, A. Jacob, B. Pinto, N. Binini, F.P. Bisogni, C. Alia, S. Luin, M. Caleo, T. Fellin, L. Cancedda, A. Cattaneo, *Activity-dependent expression of Channelrhodopsin at neuronal synapses*, Nature Communications **8 (1)**, 1629 (2017).

[7] D. Convertino, S. Luin, L. Marchetti, C. Coletti, *Peripheral neuron survival and outgrowth on graphene*, Front Neurosci. **12**, 1 (2018).
[8] L. Marchetti, F. Bonsignore, F. Gobbo, R. Amodeo, M. Calvello, A. Jacob, G. Signore, C. Schirripa Spagnolo, D. Porciani, M. Mainardi, F. Beltram, S. Luin, A. Cattaneo, *Fast-diffusing p75NTR monomers support apoptosis and growth cone collapse by neurotrophin ligands*, Proc. Natl. Acad. Sci. **116**, 21563 (2019).
[9] R. Amodeo, R. Nifosì, C. Giacomelli, C. Ravelli, L. La Rosa, A. Callegari, M.L. Trincavelli, S. Mitola, S. Luin, L. Marchetti, *Molecular insight on the altered membrane trafficking of TrkA kinase dead mutants*, Biochimica et Biophysica Acta (BBA) - Molecular Cell Research **1867 (2)**, 118614 (2019).
[10] G. De Vito, P. Parlanti, R. Cecchi, S. Luin, V. Cappello, I. Tonazzini, V. Piazza, *Effects of fixatives on myelin molecular order probed with RP-CARS microscopy*, Appl. Opt. **59**, 1756 (2020).
[11] D. Convertino, F. Fabbri, N. Mishra, M. Mainardi, V. Cappello, G. Testa, S. Capsoni, L. Albertazzi, S. Luin, L. Marchetti, C. Coletti, *Graphene promotes axon elongation through local stall of Nerve Growth Factor signaling endosomes*, Nano Lett. **20 (5)**, 3633 (2020).
[12] R. Amodeo, D. Convertino, M. Calvello, L. Ceccarelli, F. Bonsignore, C. Ravelli, A. Cattaneo, C. Martini, S. Luin, S. Mitola, G. Signore, L. Marchetti, *Fluorolabelling of the PPTase-related chemical tags: comparative study of different membrane receptors and different fluorophores in the labelling reactions*, Front. Mol. Biosci. **7**, 195 (2020).
[13] W. Durso, M. Martins, L. Marchetti, F. Cremisi, S. Luin, F. Cardarelli, *Lysosome Dynamic Properties during Neuronal Stem Cell Differentiation Studied by Spatiotemporal Fluctuation Spectroscopy and Organelle Tracking*, Int. J. Mol. Sci. **21 (9)**, 3397 (2020).

1.3.24 Plant molecular physiology

Molecular and post-genomic approaches to plant physiology provides indications of the mechanisms that drive the plant response to environmental stress and endogenous stimuli. In the NEST laboratory, NanoPLANT has carried out studies on plant molecular physiology, developmental biology, synthetic biology and contributed to nanostructure application to the agrochemical compartment.

NEST research center guarantees the possibility to conduct scientific projects in plant physiology with advanced methodologies of molecular and cellular biology. Measurements with laser scanning confocal microscopy join the possibility to perform quantitative assays for analysis of processes at nanoscale on living cells. These methods are complementary to genomic, transcriptomic, proteomic and metabolomic methodologies that characterize the expertise of NanoPLANT. In this way, we offer a large qualitative and quantitative overview of biological processes that are under study. This approach has contributed substantially to deepen basic knowledge in the field of plant developmental biology, molecular physiology and synthetic biology. In parallel, new nanostructures developed at NEST were tested on plant systems available at NanoPLANT in order to develop new applications for industrial use.

Plant survival is greatly impaired when O_2 levels are limiting, such as during flooding or when anatomical constraints limit O_2 diffusion. O_2 sensing in *Arabidopsis thaliana* is mediated by Ethylene Responsive Factor (ERF)-VII transcription factors, which control a core set of hypoxia- and anoxia-responsive genes responsible for metabolic acclimation to low-O_2 conditions. Anoxic conditions also induce genes related to reactive oxygen species (ROS). Whether the O_2-sensing machinery coordinates ROS production under anoxia has remained unclear. Recently, we showed that a low-O_2-responsive universal stress protein (USP), Hypoxia Responsive Universal Stress Protein 1 (HRU1), is induced by RAP2.12 (Related to Apetala 2.12), an ERF-VII protein, and modulates ROS production in Arabidopsis [1, Fig. 1].

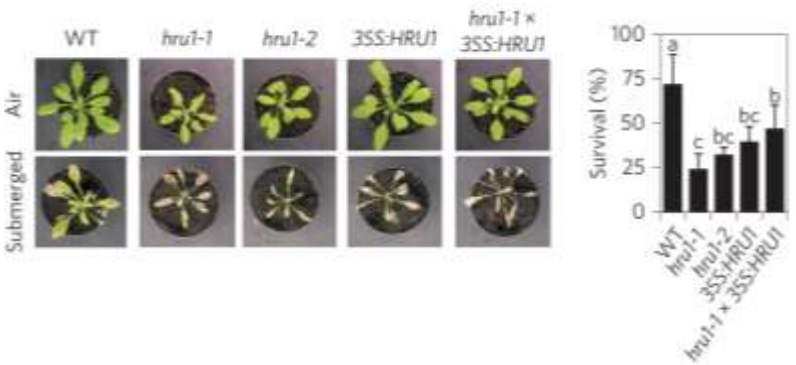

Figure 1. Effect of 4 days of submergence in the dark on the survival of Arabidopsis plants. The bar chart shows the percentage of surviving plants. Data and photographs were taken after 10 days of recovery in air. Letters indicate significantly different means (ANOVA, $p < 0.05$).

We found that HRU1 is strongly induced by submergence, but that this induction is abolished in plants lacking RAP2.12. Mutation of HRU1 through transfer DNA (T-DNA) insertion alters hydrogen peroxide production, and reduces tolerance to submergence and anoxia. Yeast two-hybrid and bimolecular fluorescence complementation (BiFC) analyses reveal that HRU1 interacts with proteins that induce ROS production, the GTPase ROP2 and the NADPH oxidase RbohD, pointing to the existence of a low-O_2-specific mechanism for the modulation of ROS levels.

We propose that HRU1 coordinates O_2 sensing with ROS signaling under anoxic conditions.

Our activities also focus on the characterization of molecular traits that promote plant tolerance to O_2 shortage and therefore may represent a major target for breeding purposes. In this context, following the identification of the calcineurin B-like interacting protein kinase 15 (CIPK15), which is a regulator of starch degradation in rice, the low O_2 signal elicited during rice germination under submergence has been linked to the sugar sensing cascade and calcium (Ca^{2+}) signaling. CIPK proteins are downstream effectors of calcineurin B-like proteins (CBLs), which act as Ca^{2+} sensors, whose role under low O_2 has yet to be established. We described CBL4 as a putative CIPK15 partner, transcriptionally activated under low O_2 in rice coleoptiles [2, Fig. 2]. The transactivation of the rice embryo CBL4 transcript and CBL4 promoter was influenced by the Ca^{2+} blocker ruthenium red (RR). The bimolecular fluorescence complementation (BiFC) assay associated to fluorescence recovery after photobleaching (FRAP) analysis confirmed that CBL4 interacts with CIPK15. The CBL4-CIPK15 complex is localized in the cytoplasm and the plasma-membrane. Experiments in protoplasts showed a dampening of α-amylase 3 (*RAMY3D*) expression after CBL4 silencing by artificial miRNA. Our results suggest that under low O_2, the Ca^{2+} sensor CBL4 interacts with CIPK15 to regulate RAMY3D expression in a Ca^{2+}-dependent manner.

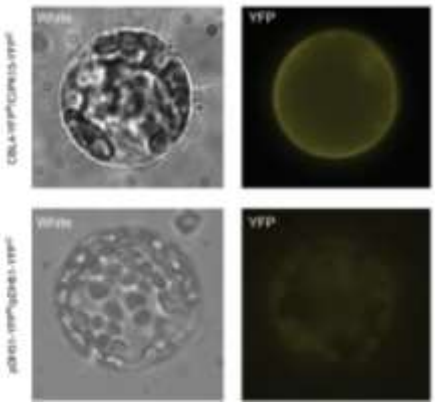

Figure 2. CBL4 interaction with CIPK15 in rice protoplasts. BiFC analysis of the protein–protein interaction between CBL4 with CIPK15. CBL4 was fused to the N-terminus of YFP (CBL4: YFPn), whereas CIPK15 was fused to the C-terminus of YFP (CIPK15:YFPc). The constructs were co-transformed into rice protoplasts. The pDH51-YFPn and pDH51-YFPc BiFC control plasmids were used as negative controls. The pictures are representative of four replicate experiments.

In mammals, the expression of hypoxia-response genes is controlled by the heterodimeric Hypoxia-Inducible Factor. The activity of this transcriptional regulator is linked mainly to the O_2-dependent hydroxylation of conserved proline residues in its α-subunit, carried out by prolyl-hydroxylases, and subsequent ubiquitination via the E3 ligase von Hippel-Lindau tumor suppressor, which targets Hypoxia-Inducible Factor-α to the proteasome. By exploiting bioengineered versions of this mammalian O_2 sensor, we designed and optimized a synthetic device that drives gene expression in an O_2-dependent fashion in plants, Fig. 3 [3].

Transient assays in Arabidopsis mesophyll protoplasts indicated that a combination of the yeast Gal4/upstream activating sequence system and the mammalian O_2 sensor machinery can be used effectively to engineer a modular, O_2-inducible transcriptional regulator. This synthetic device also was shown to be selectively controlled by O_2 in whole plants when its components were expressed

stably in Arabidopsis seedlings. We envision the exploitation of our genetically encoded controllers to generate plants able to switch gene expression selectively depending on O_2 availability, thereby providing a proof of concept for the potential of synthetic biology to assist agricultural practices in environments with variable O_2 provision.

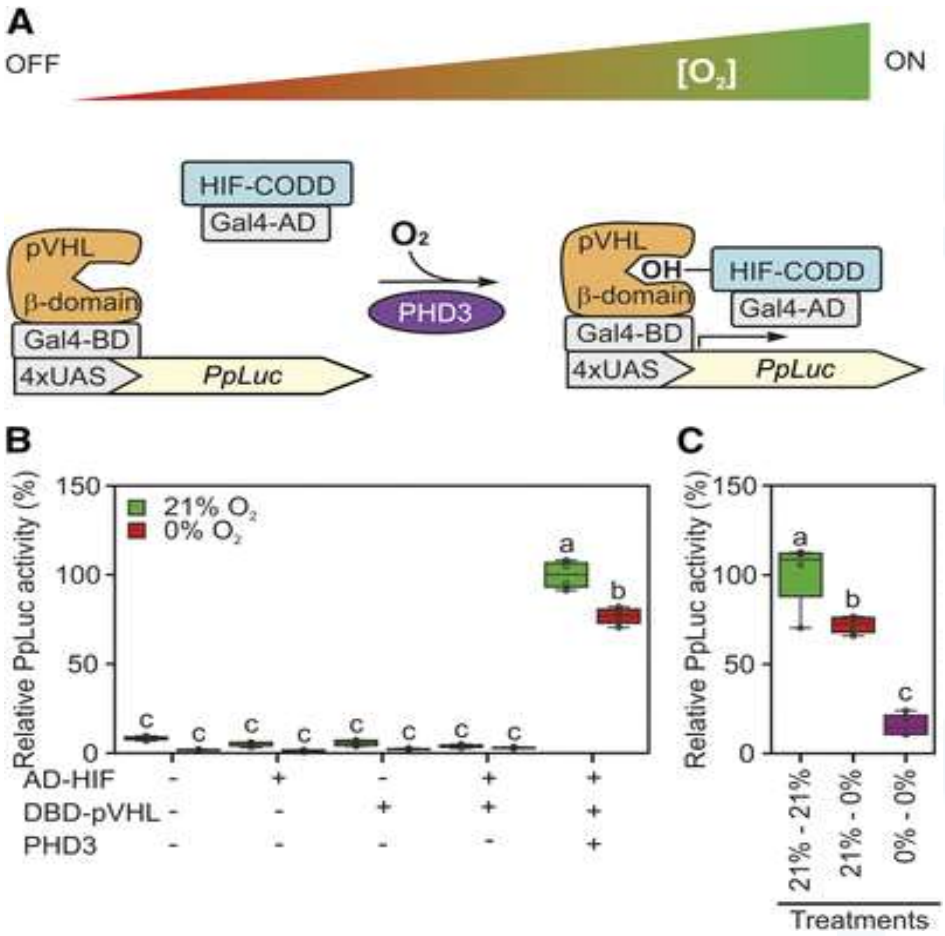

Figure 3. Schematization and testing of a synthetic O_2 sensor device based on the mammalian hypoxia sensing. A, Conceptual working mechanism of the device dependent on the environmental O_2 concentration. B, Sensor output in Arabidopsis protoplasts subjected to 18-h-long anoxia (0% O_2) or normoxia (21% [v/v] O_2) 12 h after transfection with plasmids bearing the modules depicted in A. C, Comparison of sensor responsiveness to an 18-h-long anoxic treatment applied either 12 h after protoplast transfection (21%–0%) or immediately after it (0%–0%).

While hypoxia is a detrimental and important component of flooding stress, we also found stable low O_2 conditions in plant meristems, the site of the plant stem cell pools. O_2 profiles in meristems were made using miniaturized O_2 electrodes or fluorescence-based microoptodes (Fig. 4a-b). Such conditions were confirmed at the NanoPLANT using laser scanning confocal microscopy by employing hypoxia biosensors. While low O_2 availability in stem cells may appear counterintuitive at first glance, such local hypoxic conditions were shown to play an important role in preventing differentiation and to regulate the rate at which new leaves are formed. A similar role for O_2 in directing pluripotency was also shown for several metazoan stem cells niches and different types of cancer, suggesting convergent evolution. Now we are further elucidating the molecular mechanism that acts to prevent differentiation in hypoxic environments and to

understand how low O_2 conditions are maintained at the meristems. To study this we are currently characterizing newly developed fluorescence based tools to measure O_2 levels at high spatial resolution in tissue (Fig. 4c-d). The most promising candidates of these rely on variable sensitivity to O_2 of specific fluorescent proteins. We also recently installed a microsensor multimeter setup, which aside from O_2, can also be used to measure H_2, H_2S, N_2O, NO, pH, Redox and Temperature.

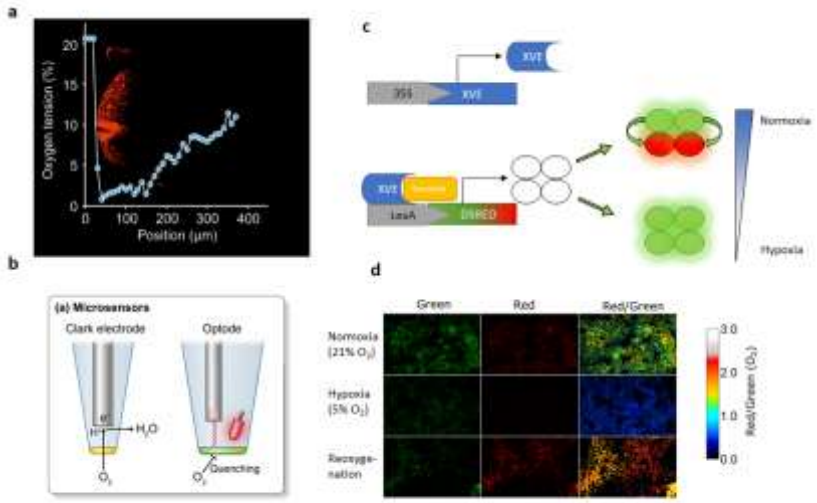

Figure 4. Role of O_2 in plant development. a) A representative O_2 profile through the shoot apical meristem showing that this stem cell pool is hypoxic. Confocal microscopy using FM4-64 membrane staining was used to detect the site of insertion of the O_2 microsensor. b) Representation of two types of O_2 microsensors: Clark type electrodes and phosphorescent based optodes. c) Schematic representation of the expression cassette of the DsRed FT based O_2 biosensor. A two-component inducible expression system employs a constitutively expressed XVE transcription factor, that upon binding to the steroid hormone estradiol activates expression of DsRed FT. The DsRed FT fluorophore can mature either to emit green or red fluorescence depending on the O_2 concentration. d) Green and red fluorescence of DsRed FT under different oxic conditions: normoxia, hypoxia and reoxyation. Normoxia permits green and red fluorescence, while hypoxia only shows green fluorescence.

References

[1] S. Gonzali, E. Loreti, F. Cardarelli, G. Novi, S. Parlanti, C. Pucciariello, L. Bassolino, V. Banti, F. Licausi, P. Perata, *Universal stress protein HRU1 mediates ROS homeostasis under anoxia*, Nature Plants **1**, 15151 (2015).

[2] V.T. Ho, A.N. Tran, F. Cardarelli, P. Perata, C. Pucciariello, *A calcineurin B-like protein paticipates in low O2 signalling in rice*, Functional Plant Biology **44**, 917 (2017).

[3] S. Iacopino, S. Jurinovich, L. Cupellini, L. Piccinini, F. Cardarelli, P. Perata, B. Mennucci, B. Giuntoli, F. Licausi, *A synthetic O2 sensor for plants based on animal hypoxia signalling*, Plant Physiol. **179**, 986 (2019).

1.3.25 Non-persistent plasmonic nanotherapeutics and 3D cancer models

Nanomaterials have attracted increasing interest for their potential to revolutionize the diagnosis and treatment of several diseases, especially neoplasms. Nowadays, despite the significant research efforts, less than 100 nanotherapeutics have progressed to the market since the acceptance of Doxil® during the 90's. Challenges in translation to the clinic are mainly due to: i) difficulties in industrialization of the synthesis processes (e.g., scalability, sterility, and homogeneity), ii) unsuitable pharmacokinetics with long retention in the body, and iii) toxicity. Actually, regulatory agencies have mostly approved soft (organic) nanomedicines designed to improve the availability of common drugs to the action site(s). In contrast, inorganic (especially plasmonic) nanomaterials, due to their size/shape-dependent optoelectronic behaviors, display advantageous properties that widen their utilization as, for instance, in combined hyperthermia, radiosensitization and medical imaging. This means that the full potential of nanomaterials in the clinical practice, and particularly in cancer management, is not yet reached. Here, we present recent advancements towards the development of non-persistent plasmonic nanomaterials for the treatment of oral malignancies and pulmonary infectious diseases, together with the progress on the composition of reliable 3D cancer models for the assessment of conventional and innovative therapeutics within the 3R's concept.

The lack of translation of noble metal nanomaterials (NPs) to clinics is mainly related to lack of industrially-compatible synthesis processes and NPs long-term retention in the body [1]. The persistence of NPs in organisms leads to possible interference with common medical diagnoses and can induce severe damages and gene expression alterations [2]. Regulatory agencies require a complete clearance from the body of the pharmaceuticals and their components in an acceptable timeframe [3]. The excretion is an essential biological process to eliminate materials from organisms, and can be accomplished by renal or hepatic pathways [1]. The renal pathway relies on glomerular filtration in kidneys, which size threshold is typically <8nm, denoting that only materials with ultrasmall hydrodynamic diameters (HD) can be efficiently eliminated through the urinary system [4]. Materials with HD >8 nm (as mostly of the NPs with intriguing behaviors for medical applications) are mainly captured by liver and spleen [5]. If the captured materials are biodegradable, the building blocks are then excreted by bile and feces, while if non-biodegradable, they result in long-term accumulation in the reticuloendothelial system (RES). As a first attempt to overcome the issue of persistence, the size of NPs has been reduced to ultrasmall range (<8nm, ultrasmall nanoparticles, USNPs) in order to enhance their renal clearance efficiency [6]. Due to this smart approach an interesting level of metal excretion was reached but commonly losing some key-features of NPs, among which physical and physiological behaviors [6].

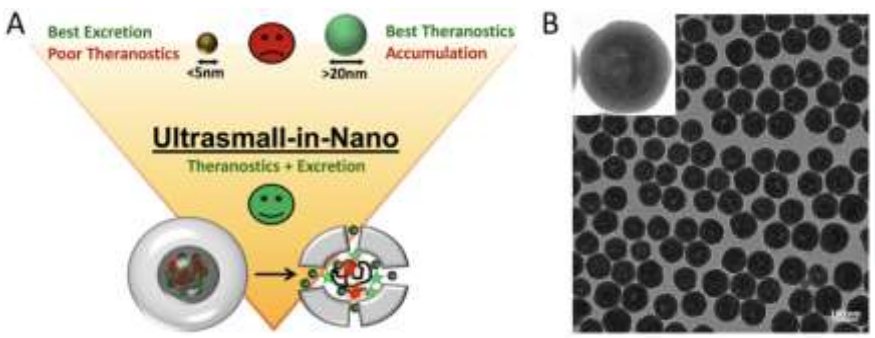

Figure 1. A) Cartoon explaining the groundbreaking nature of the ultrasmall-in-nano approach. B) Typical wide-area TEM image of NAs. Scalebar: 100 nm. Inset: zoom on one NAs.

In this context, we disclosed in 2015 the ultrasmall-in-nano approach (Fig. 1) for the reliable production of a family of non-persistent noble metal nano-architectures (NAs) that jointly combine the unique behaviors of plasmonic NPs with the body excretion [7]. NAs are composed by aggregates of plasmonic USNPs comprised in silica nanocapsules (Fig. 1) that biodegrade in <48h to the building blocks in several cell lines and biological fluids (Fig. 2) [8]. Briefly, the hollow silica shell is conceived as a shielding nanocapsule that: i) preserves the encapsulated materials until its degradation, ii) enhances ultrasound echo signals and iii) offers a straightforward modifiable surface [9,10]. Meanwhile, the gold USNPs promote light-matter interactions essential for photothermal effects or for radiosensitization, while the polymer can be modified with active molecules, such as drugs and dyes [11–13]. Biocompatibility and *in vivo* biokinetics investigations prior to *in vivo* efficacy tests are of particular interest in order to significantly reduce the number of required living models. Indeed, a number of metal nanomaterials have demonstrated intriguing features for theranostic applications, albeit without possible real applications because of persistence issue [2]. The whole-body toxicity of NAs has been investigated on zebrafish during their growth (Fig. 2), evaluating different toxicity end-points such as the survival rate, hatching rate, heart beat rate, malformations and cardiac effects [14]. Our findings indicate non-toxic effects according to the normative EU law and significantly highlight the biosafety of NAs at therapeutic concentrations [15]. The data collected on zebrafish have been also confirmed by histological investigations performed on healthy murine models i.v. injected with NAs up to the maximum amount of 150 mg/kg (Fig. 2) [16]. On these models, we also assessed the biokinetics of NAs. In particular, we have confirmed an interesting metal excretion profile by the renal pathway and a significant metal reduction in excretory system organs during 10 days [15]. It is worth to mention that, in agreement with ongoing investigations on lung diseases, we have explored the biokinetics of NAs administered to the models by inhalation [17]. Beyond accumulation in the lungs, translocation to secondary organs, and an almost completely excretion of NAs from the models, we observed a transient accumulation of NAs in the central nervous system [17].

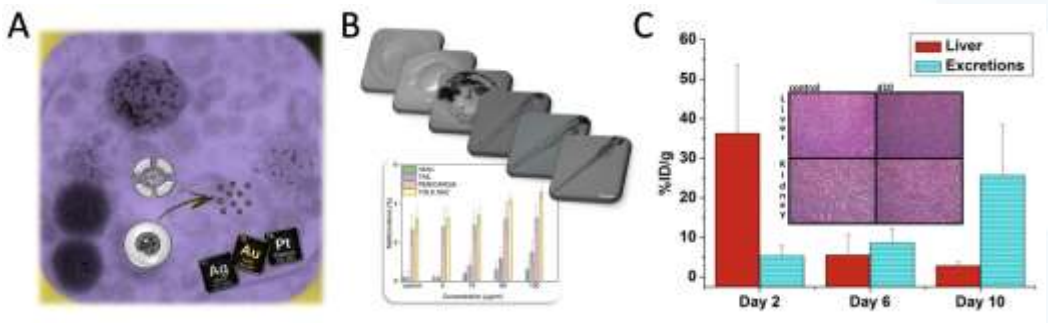

Figure 2. A) General biodegradation process of NAs in a cancer cell. The biodegradation process does not depend on the noble metal comprised in NAs. B) ICP-MS quantification of gold in liver and in excretions (cumulative) at the 3 time-points. Inset: Histological analysis of liver and kidney tissues from CD1-*Foxn1*^{nu} mice. C) Morphology of zebrafish treated with 100 µg/ml of NAs at the different time points investigated (4, 24, 48, 72, 96, 120 hpf). Scale bars= 500 µm. The graph reports the malformations rates vs NAs concentration in different larvae's parts at 96 hpf (head, tail, heart, yolk sac).

This work paves the way for the development of systemic or local pulmonary-delivered noble metal-based treatments for oncology and infectious diseases as well as for the investigation of the risks associated to the (in)voluntary inhalation of nanoparticles

During these years, some of the potential applications of NAs have been demonstrated (Fig. 3), pointing out that all the building blocks are pivotal. For example, we reported on the efficacy of NAs as a double-endogenously triggered drug delivery vehicles for a home-made cisplatin prodrug; a nanoplatform able to strongly reduce the side effects associated to cisplatin [8,13]. In 2019, we addressed two key hurdles that currently hinder the clinical translation of NPs-associated photothermal treatments: i) NIR-absorption occurs for NPs whose size is above the renal excretion threshold, and ii) anisotropic NPs undergo reshaping after PT transduction. On this regard, we demonstrate that narrow-NIR-responsive *thermo* NAs bear the optimal size for renal excretion and sustain repeated series of NIR light-to-heat transduction without losing their functionalities, avoiding metal sintering or reshaping [12]. Recently, the first multifunctional NAs for combined chemotherapy and photothermal therapy was synthesized and added to the list of NAs varieties, supporting the development of ultrasmall-in-nano multifunctional systems for combined therapeutic applications, such as photodynamic therapy-PTT and chemo-radiotherapy [18]. Beside therapeutic applications, NAs have been designed and investigated for diagnostic and imaging purposes.

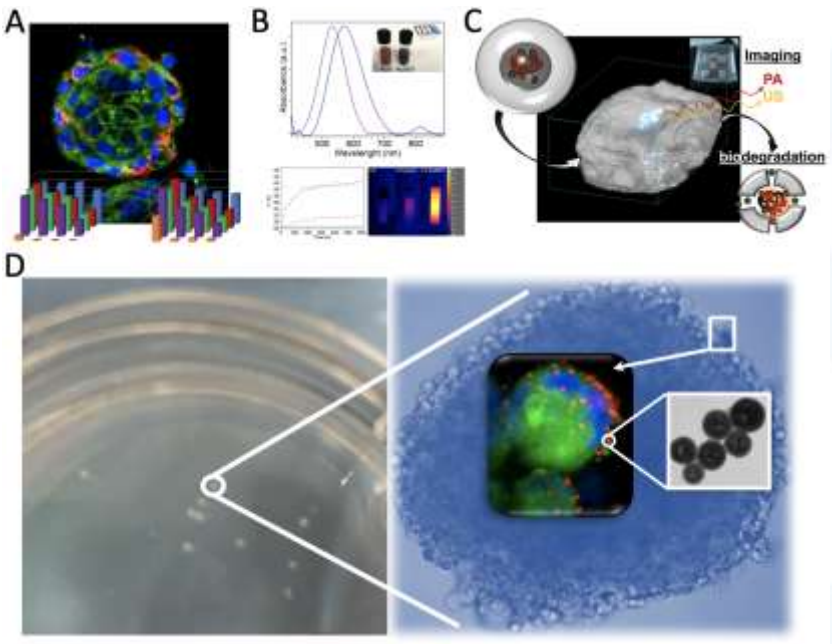

Figure 3. A) Combined image depicting the action of the double endogenous-controlled NAs platform as cisplatin prodrug carrier on cancer spheroids. B) UV/vis spectra of NAs and *thermo* NAs (upper panel) and the photothermal conversion during irradiation in the first biological window (bottom panel). C) Scheme depicting the *ex vivo* employment of NAs as dual photoacoustic/ultrasound (PAUS) contrast agents. D) Micrometastasis-like oral malignances (left panel) and optical/electronic zooms (right panel).

The design of NAs is a key-factor for their performances, among which are stability and high output signal. On this hand, we introduced a novel paradigm that exploits the synergistic interaction between commercial NIR-fluorophores and ultrasmall metal nanoparticles to produce a photoacoustic signal enhancement in the first biological window [11].

We have demonstrated that NAs are intrinsically bi-modal contrast agents for both photoacoustic and ultrasound imaging [10,11]. They can be exploited to jointly provide complementary information from both techniques, paving the way: i) for an enhanced diagnostic accuracy of neoplasms without employing ionizing radiation or ii) to follow and localize potential treatments [10].

Beyond metal persistence and bio-nano interactions, a major requirement for a successful scale-up and clinical translation of metal nanoplatforms are related to the production, which should be cost-effective and reproducible. In this direction, we have standardized and generalized the protocols for the production of NAs and the cascade characterization assay, reaching an high level of reproducibility and batch-by-batch homogeneity within samples [19,20]. Now, we are working on the semi-automatization of the procedures.

Finally, an important portion of our research at NEST is devoted to the development of 3D cancer models in order to perform investigations within the EU and local directives on animal models (Fig. 3) [21]. 3D tumor models act as a bridge between the investigations on cell monolayers and *in vivo* animal models. While both 2D cell culture and animal models cannot be completely avoided, the addition of 3D models in the research workflow provides robust and economical preclinical insights for the evaluation of conventional and nanomaterial-based treatments, as well as for the evaluation of nanomaterial features and nano-bio interactions. Moreover, they are employed to refine nanomaterials properties in order to reduce the use of animals for research. The accessibility of 3D tumor models can be extended to primary cell cultures, paving the way for personalized screenings. Ultimately, the full implementation of 3D tumor models in the pipeline of nanomaterials assessment will foster the advancement and translation of novel nanotechnology-based diagnostic and treatment systems to the clinical practice. On this hand, we employed 3D models in all our assessments and we have already standardized our procedures for their production and employment [22]. Our efforts are now aimed to the establishment of more complex 3D models that even better represent the neoplasms behaviors and environment.

References

[1] D. Bobo, K.J. Robinson, J. Islam, K.J. Thurecht, S.R. Corrie, *Nanoparticle-Based Medicines: A Review of FDA-Approved Materials and Clinical Trials to Date*, Pharm. Res. **33**, 2373 (2016).

[2] D. Cassano, S. Pocoví-Martínez, V. Voliani, *Ultrasmall-in-Nano Approach: Enabling the Translation of Metal Nanomaterials to Clinics*, Bioconjug. Chem. **29**, 4 (2018).

[3] V. Sainz, J. Conniot, A.I. Matos, C. Peres, E. Zupanǒiǒ, L. Moura, L.C. Silva, H.F. Florindo, R.S. Gaspar, *Regulatory aspects on nanomedicines*, Biochem. Biophys. Res. Commun. **468**, 504 (2015).

[4] J. Wang, G. Liu, *Imaging Nano-Bio Interactions in the Kidney: Toward a Better Understanding of Nanoparticle Clearance*, Angew. Chemie Int. Ed. **57**, 3008 (2018).

[5] K.M. Tsoi, S.A. Macparland, X.Z. Ma, V.N. Spetzler, J. Echeverri, B. Ouyang, S.M. Fadel, E.A. Sykes, N. Goldaracena, J.M. Kaths, et al., *Mechanism of hard-nanomaterial clearance by the liver*, Nat. Mater. **15**, 1212 (2016).
[6] K. Zarschler, L. Rocks, N. Licciardello, L. Boselli, E. Polo, K.P. Garcia, L. De Cola, H. Stephan, K.A. Dawson, *Ultrasmall inorganic nanoparticles: State-of-the-art and perspectives for biomedical applications*, Nanomedicine: Nanotechnology Biol. Med. **12**, 1663 (2016).
[7] D. Cassano, D. Rota Martir, G. Signore, V. Piazza, V. Voliani, *Biodegradable hollow silica nanospheres containing gold nanoparticle arrays*, Chem. Commun. **51**, 9939 (2015).
[8] D. Cassano, M. Santi, V. Cappello, S. Luin, G. Signore, V. Voliani, *Biodegradable Passion Fruit-Like Nano-Architectures as Carriers for Cisplatin Prodrug*, Part. Part. Syst. Charact. **33**, 818 (2016).
[9] A.K. Mapanao, M. Santi, P. Faraci, V. Cappello, D. Cassano, V. Voliani, *Endogenously Triggerable Ultrasmall-in-Nano Architectures: Targeting Assessment on 3D Pancreatic Carcinoma Spheroids*, ACS Omega **3**, 11796 (2018).
[10] P. Armanetti, S. Pocoví-Martínez, A. Flori, C. Avigo, D. Cassano, L. Menichetti, V. Voliani, *Dual photoacoustic/ultrasound multi-parametric imaging from passion fruit-like nano-architectures*, Nanomedicine: Nanotechnology Biol. Med. **14**, 1787 (2018).
[11] C. Avigo, D. Cassano, C. Kusmic, V. Voliani, L. Menichetti, *Enhanced Photoacoustic Signal of Passion Fruit-Like Nanoarchitectures in a Biological Environment*, J. Phys. Chem. C **121**, 6955 (2017).
[12] D. Cassano, M. Santi, F. D'Autilia, A.K. Mapanao, S. Luin, V. Voliani, *Photothermal effect by NIR-responsive excretable ultrasmall-in-nano architectures*, Mater. Horizons **6**, 531 (2019).
[13] M. Santi, A.K. Mapanao, D. Cassano, Y. Vlamidis, V. Cappello, V. Voliani, *Endogenously-Activated Ultrasmall-in-Nano Therapeutics: Assessment on 3D Head and Neck Squamous Cell Carcinomas*, Cancers (Basel) **12**, 1063 (2020).
[14] M. d'Amora, D. Cassano, S. Pocoví-Martínez, S. Giordani, V. Voliani, *Biodistribution and biocompatibility of passion fruit-like nano-architectures in zebrafish*, Nanotoxicology **12**, 914 (2018).
[15] D. Cassano, A.K. Mapanao, M. Summa, Y. Vlamidis, G. Giannone, M. Santi, E. Guzzolino, L. Pitto, L. Poliseno, R. Bertorelli, et al., *Biosafety and Biokinetics of Noble Metals: The Impact of Their Chemical Nature*, ACS Appl. Bio Mater. **2**, 4464 (2019).
[16] D. Cassano, M. Summa, S. Pocoví-Martínez, A.K. Mapanao, T. Catelani, R. Bertorelli, V. Voliani, *Biodegradable Ultrasmall-in-Nano Gold Architectures: Mid-Period In Vivo Distribution and Excretion Assessment*, Part. Part. Syst. Charact. **36**, 1800464 (2019).
[17] A.K. Mapanao, G. Giannone, M. Summa, M.L. Ermini, A. Zamborlin, M. Santi, D. Cassano, R. Bertorelli, V. Voliani, *Biokinetics and clearance of inhaled gold ultrasmall-in-nano architectures*, Nanoscale Adv. **2**, 3815 (2020).
[18] A.K. Mapanao, M. Santi, V. Voliani, *Combined chemo-photothermal treatment of three-dimensional head and neck squamous cell carcinomas by gold nano-architectures*, J. Colloid Interface Sci. **582 (Pt B),** 1003 (2020).
[19] D. Cassano, J. David, S. Luin, V. Voliani, *Passion fruit-like nano-architectures: a general synthesis route*, Sci. Rep. **7**, 43795 (2017).
[20] G. Giannone, M. Santi, M.L. Ermini, D. Cassano, V. Voliani, *A Cost-Effective Approach for Non-Persistent Gold Nano-Architectures Production*, Nanomaterials **10**, 1600 (2020).
[21] A.K. Mapanao, V. Voliani, *Three-dimensional tumor models: Promoting breakthroughs in nanotheranostics translational research*, Appl. Mater. Today **19**, 100552 (2020).
[22] M. Santi, A.K. Mapanao, V. Cappello, V. Voliani, *Production of 3D Tumor Models of Head and Neck Squamous Cell Carcinomas for Nanotheranostics Assessment*, ACS Biomater. Sci. Eng. **6 (9)**, 4862 (2020).

1.3.26 Targeted nanostructures tailored to *in vivo* delivery

Development of efficient nanostructures for drug delivery tailored to in vivo use requires careful engineering of different aspects (targeting unit, nanoparticle composition, encapsulation method) that must be optimized separately but synergistically to provide best performances. At NEST laboratory we focused both on development of innovative targeting sequences tackling the transferrin receptor pathway and on innovative formulation strategies to improve encapsulation efficiency of small molecules and proteins.

Development of nanostructured carriers for delivery of therapeutic payloads represents an assessed research line at NEST. The focus in this area is on the assembly of nanostructures that can perform efficient and targeted delivery of delicate therapeutic payloads (e.g. enzymes) without compromising the activity of the payload itself. Particular attention has been paid to the perspective use *in vivo* of these systems. This involved development of nanostructures able to avoid, or selectively interact with, serum proteins. The activity can be divided in two separate optimizations: design/evolution of targeting units, and engineering of the nanoparticle scaffold. These two activities are shortly described in the following.

Development of binding sequences for targeted delivery

Targeted delivery requires engineering of structures able to recognize biomolecules either critically involved in the pathologic process or playing a pivotal role in crossing of biologic barriers. Transferrin pathway is, in this sense, an extremely interesting target. In fact, transferrin receptor is overexpressed (up to 100 folds) in high-proliferating cells such as in tumors. Additionally, it is expressed on the surface of the blood brain barrier, where it constitutively delivers iron to the brain. These two features make it an ideal target for drug delivery in cancer treatment and in all those pathologies that involve the central nervous system.

Transferrin receptor is saturated, in physiologic conditions, by endogenous transferrin. Thus, therapies based on transferrin-mediated delivery have little chance of success. Recent advances in this field took in consideration alternative targeting molecules such as oligonucleotide and peptide aptamers. In the framework of the ongoing research activity in nanomedicine, a rational optimization of an oligonucleotide aptamer was performed on the basis of a previously published structure. This reported anti-TfR aptamer undergoes a series of conformational equilibria leading to the formation of a major, inactive conformer at physiologic temperature. Conformational equilibrium of the reported aptamer was evaluated in silico and confirmed experimentally at different temperatures; punctual mutations were performed to obtain a mutated form (DW4) which is completely stable at 37 °C, with nanomolar affinity towards human and murine transferrin receptor [1]. This aptamer is also able to promote internalization in cells of large nanoparticles, allowing selective delivery of liposome-encapsulated doxorubicin to living cells [2].

Capability of oligonucleotide aptamers to perform combined delivery of two therapeutic payloads in cells was evaluated (Fig. 1, A). To this end, an anti-transferrin receptor oligonucleotide aptamer was exploited in the selective co-delivery of two therapeutic agents: a small drug (Doxorubicin) and an oligonucleotide decoy against NF-kB (an anti-apoptotic protein activated in tumor

cells). This strategy allows performing two therapeutic actions at the same time, i.e. cytotoxic activity of the drug and inhibition –induced by the decoy- of natively constituted anti-apoptotic mechanisms. This construct shows high cytotoxicity (comparable with free doxorubicin) in target cells, with negligible off-target effect (Fig. 1, B) [3].

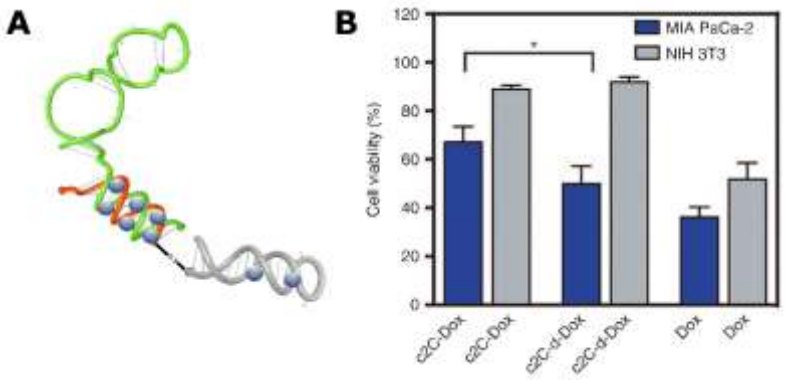

Figure 1. *A:* Scheme of aptamer-based nanostructure for co-delivery. The TfR aptamer (green) is partially hybridized with an antisense oligonucleotide (red) to provide anchor points for doxorubicin (blue dots). A disulphide bond connects this architecture to the NF-kB decoy (grey). The whole system readily disassembles during cell internalization leading to release of cytotoxic (doxorubicin) and antiapoptotic inhibitor (NF-kB decoy) agents. *B:* Combined effects of these molecules and selective uptake triggered by NF-kB leads to highly selective cytotoxic activity that does not affect control cells, while exerting an important effect on tumor cells *in vitro*.

An alternative approach to TfR targeting was developed by considering the complex environment represented by blood. It is accepted that immediate solvation of exogenous materials by serum proteins leads to a substantial change of surface properties of administered nanostructures. This translates in the shift from the "chemical identity", i.e. the surface functionalization obtained during nanoparticle synthesis and isolation, to the "biological identity", that is the nanoparticle solvated with one or more layers of serum proteins. This layer, which is at the interface between the nanoparticle and the organism, ultimately drive the fate of the nanoparticle itself. There are two not mutually exclusive strategies to overcome this effect: avoiding nonspecific adsorption by using antifouling coatings or exploiting surface functionalization to selectively bind a specific serum protein, which in turn can steer the destination of the nanoparticle.

This last approach was exploited by developing a peptide aptamer against transferrin. Unlike the classic aptamer selection process, which is exquisitely experimental and thus with unpredictable binding site on the protein, a combined modelling/evolutionary algorithm (Fig. 2) was adopted to rationally design a small peptide (Tf2).

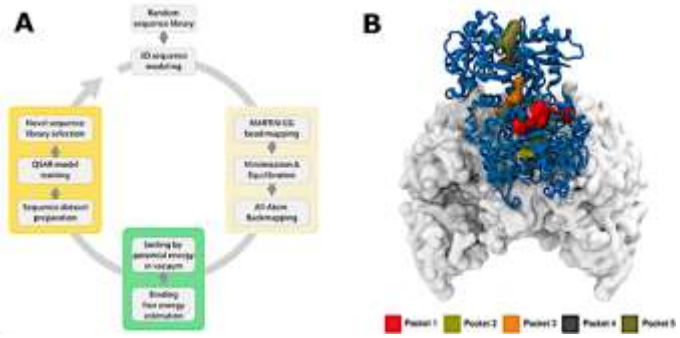

Figure 2. *A* Schematization of *in silico* selection process for Tf2. A suitable pocket is identified on the transferrin in a position which is not proximal to the binding site to either TfR or iron binding sites. An iterative evolutionary algorithm is performed, screening a random peptide library for binding energy in the pocket, introducing random mutations and selecting at each iteration the most affine candidates. Multivariate optimization allows identifying best candidates. *B In silico* identification of suitable pockets for aptamer selection (in this selection "Pocket 3", orange was chosen) on the docked transferrin-TfR complex.

This peptide recognizes transferrin in a pocket that does not interfere with transferrin binding to its receptor or iron ions. Other serum proteins interact only to a minimal level with Tf2, leading to selective protein adsorption on the surface of nanoparticles derivatized with Tf2 [4]. Controlled orientation of transferring on Tf2 functionalized nanoparticles leads to nearly 40-fold increase in cell uptake, compared with non-derivatized nanoparticles. Notably, the absolute amount of transferrin adsorbed on the surface of Tf2-derivatized and untargeted nanoparticles is similar, so the increased uptake is driven to a large extent by the proper orientation of transferrin adsorbed onTf2-derivatized nanoparticles. This strategy has also been validated using mesoporous silica nanoparticles with Tf2. The presence of this peptide significantly improves uptake in tumor organoids derived from MiaPaCa-2 cell line [5].

Development of nanodevices tailored to enzyme delivery in vivo

The identity of a nanoparticle scaffold significantly affects delivery efficiency of therapeutics. Design of a nanostructure for *in vitro* and *in vivo* delivery requires efficient encapsulation of the active principle, with minimal impact on conformation in the case of enzymatic payloads, whose activity is strictly connected with secondary and tertiary structure. Additionally, surface composition of the nanoparticle must be appropriately designed to modulate interaction with serum proteins. Finally, disassembly triggered by changes in physico-chemical properties of the surrounding environment (e.g. pH changes upon internalization) can be conferred by appropriate design of nanoparticle excipients. Nanoparticles were developed with the specific purpose of delivering delicate protein therapeutics across the blood brain barrier, addressing the complex issue of enzyme replacement therapy in lysosomal storage disorders.

Novel biomimetic, PEG-free scaffolds were engineered. These scaffolds are characterized by ultra-low protein adsorption and long residence time (>12h) in serum. The particles are based on a zwitterionic amino acid sequence (EKEKEKE) derivatized with a lipid tail to promote self-assembly and insertion in liposomes. These nanostructures outperform benchmark PEGylation reagents in terms of

protein interaction and can be conveniently modified with biorthogonal linkers for derivatization with targeting agents. Self-assembled particles loaded with doxorubicin and functionalized with DW4 aptamer efficiently internalize in cells demonstrating dose-dependent cytotoxicity Fig. 3 A), while nonspecific uptake of untargeted nanoparticles is completely negligible (Fig. 3 B) [2]. The same stealth architecture, modified with Tf2 transferrin-binding peptide, has been loaded with functional PPT1, and recently evaluated as a way to deliver protein palmitoyl thiotransferase (PPT1) enzyme *in vitro* to primary dermal fibroblasts derived from NCL-1 patients, leading to partial restore of biochemical (palmitoylation level) and proteomic parameters.

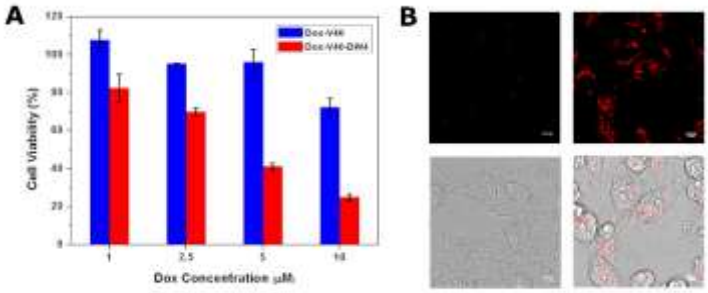

Figure 3. A Dose-response curve of doxorubicin encapsulated in untargeted (blue) and targeted (red) stealth liposomes administered to Mia PaCa2 cells. Untargeted liposomes are not internalized and hence show negligible cytotoxicity. *B* confocal fluorescence microscopy images of untargeted (left) and targeted (right) stealth liposomes to Mia PaCa2 cells.

Efficient loading of functional enzymes in nanoparticles is knowingly difficult, due to the harsh environment encountered by encapsulated proteins (very lipophilic, with important unbalance of saline content, ultimately leading to partial or complete enzyme denaturation). This leads to either poor encapsulation yield, or partial unfolding of the protein, often with almost complete loss of activity. Encapsulation in liposomes, which is usually obtaining by freeze-thaw or sonication, has a profound effect on both enzyme activity, that decreases by 30-40%, and on encapsulation yield, usually limited to less than 10-20%. These limitations can be circumvented by using chemically linked enzyme aggregates (CLEAs), produced by reaction of the enzyme with reversible chemical crosslinkers. This controlled aggregation makes the enzyme itself lipophilic and induces aggregation and precipitation from aqueous environment in small (<20nm) aggregates. These aggregates can be encapsulated by simple nanoprecipitation techniques in a matrix of PLGA, with excellent yields (>90%) and excellent activity retention (Fig. 4 A, B). Pristine enzyme can be easily restored by spontaneous hydrolysis of the crosslinker under mildly acidic aqueous conditions. At the same time, PLGA carrier easily decomposes leaving only enzyme. Overall, this approach represents an efficient strategy to perform delivery of lysosomal enzymes. PLGA-CLEAs nanoparticles functionalized with Tf2 transferrin binding peptide have been demonstrated to restore enzymatic activity in vitro with different enzymes, including GALC and PPT1 [6]. Appropriate modification of the nanoparticle design using proton sponges (polyethyleneimine, PEI) as nanoparticle excipients promote endosomal escape of the enzyme allowing cytoplasmic delivery of functional enzymes [7].

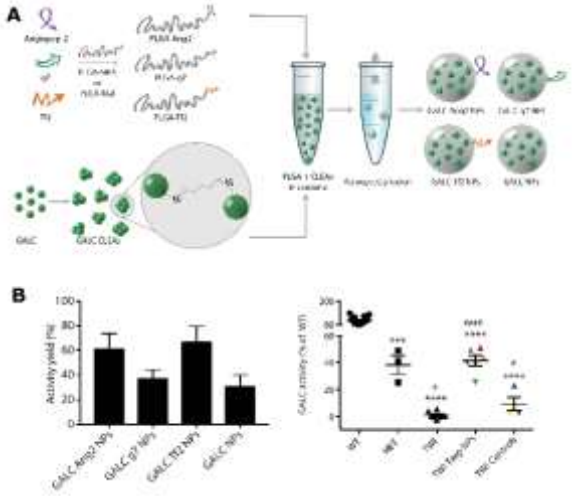

Figure 4. A Synthesis of targeted CLEAs PLGA nanoparticles. Enzyme aggregates are formed using glutaraldehyde and precipitate from water. After resuspension, CLEAs-PLGA nanoparticles are formed by conventional nanoprecipitation. Targeting sequences can be inserted by appropriate functionalization of PLGA. **B** Enzymatic activity (% respect to WT) of GALC after encapsulation (left) and at brain level (right) after intraperitoneal administration to Twitcher mice. Targeted nanoparticles (orange, green, magenta) lead to partial restore of enzymatic activity. Untargeted nanoparticles (yellow) and free enzyme (blue) fail to provide increase in enzyme activity.

CLEAs-PLGA nanoparticles loaded with GALC were functionalized with targeting sequences including: two peptides with reported capability to cross the blood brain barrier (Angiopep2 and glycosylated peptide g7), and the transferrin-binding Tf2 peptide for indirect targeting *in vivo* (Fig. 4 A). In all cases, intraperitoneal administration to mice restores physiologic enzymatic activity in the brain [8], demonstrating that Tf2-derivatized PLGA nanoparticles are effective in delivering functional, folded enzymes to the brain *in vivo* (Fig. 4 B).

References

[1] D. Porciani et al., *Two Interconvertible Folds Modulate the Activity of a DNA Aptamer Against Transferrin Receptor*, Mol. Ther. Acids **3**, e144 (2014).

[2] A. Ranalli et al., *Peptide-Based Stealth Nanoparticles for Targeted and pH-Triggered Delivery*, Bioconjug. Chem. **28**, 627 (2017).

[3] D. Porciani et al., *Aptamer-Mediated Codelivery of Doxorubicin and NF-κB Decoy Enhances Chemosensitivity of Pancreatic Tumor Cells*, Mol. Ther. - Nucleic Acids **4**, e235 (2015).

[4] M. Santi et al., *Rational Design of a Transferrin-Binding Peptide Sequence Tailored to Targeted Nanoparticle Internalization*, Bioconjug. Chem. **28**, 471 (2017).

[5] A.K. Mapanao et al., *Endogenously Triggerable Ultrasmall-in-Nano Architectures: Targeting Assessment on 3D Pancreatic Carcinoma Spheroids*, ACS Omega **3**, 11796 (2018).

[6] M. Galliani et al., *Cross Linked Enzyme Aggregates as Versatile Tool for Enzyme Delivery: Application to Polymeric Nanoparticles Cross Linked Enzyme Aggregates as Versatile Tool for Enzyme Delivery: Application to Polymeric Nanoparticles*, Bioconjug. Chem. **29(7)**, 2225 (2018).

[7] M. Galliani et al., *Nanocarriers for protein delivery to the cytosol: Assessing the endosomal escape of poly(lactide-co-Glycolide)-poly(ethylene Imine) nanoparticles*, Nanomaterials **9** (2019).

[8] A. Del Grosso et al., *Brain-targeted enzyme-loaded nanoparticles: A breach through the blood-brain barrier for enzyme replacement therapy in Krabbe disease*, Sci. Adv. **5** (2019).

1.3.27 New paradigms in nanoscale biophysics: looking at life (mis)regulation inside cells

Capturing life (mis)regulation at the nanoscale is a crucial challenge for present and future biophysics. At this scale, molecules are the main actors. To successfully tackle molecular behavior within living matter, two crucial requisites are typically needed: (i) nanometer spatial resolution, (ii) micro-to-millisecond temporal resolution. In this context, optical microscopy is a valuable methodological platform: by using fluorescence as readout, spatial and temporal details of molecular processes can be investigated directly within living matter.

We introduced/developed a number of methods, based on the statistical analysis of fluorescence fluctuations, in order to increase the quantitative information that can be extracted from time-resolved optical-microscopy experiments and provide further insight into dynamic molecular processes. In particular, new spatiotemporal variants of fluorescence correlation spectroscopy (FCS) were proposed which are able to resolve the dynamic behavior of molecules well below the nominal imaging resolution of the optical setup (e.g. the imaging derived Mean Squared Displacement analysis, or iMSD, is reported in Fig.1a-d) [1-5].

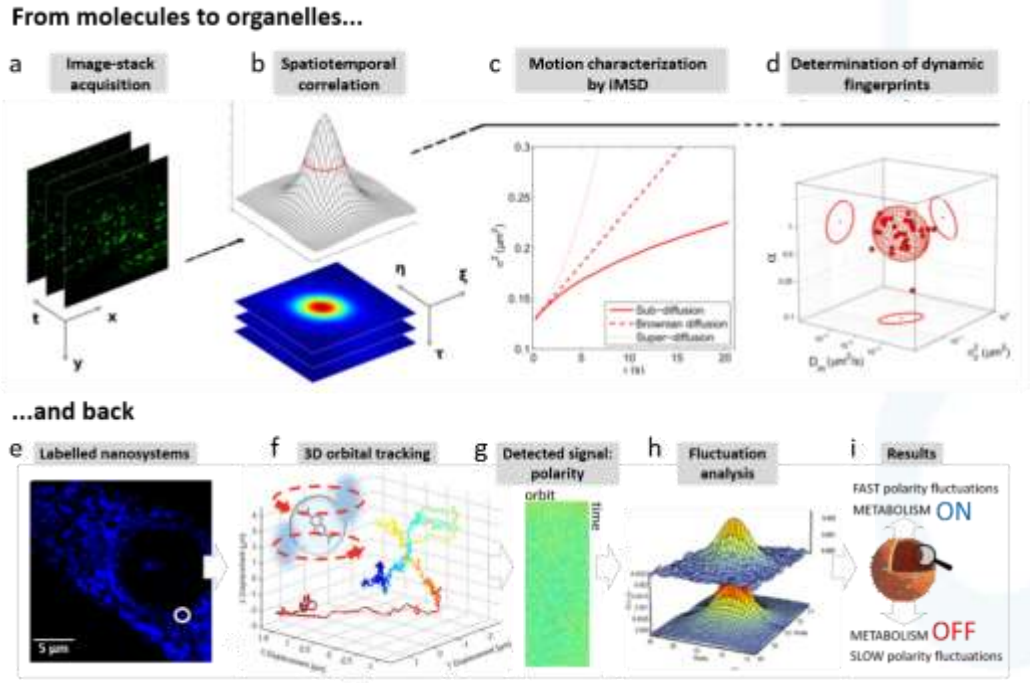

Figure 1. From molecules to organelles: Schematic representation of the iMSD-based dynamic fingerprint analysis. **a**) A stack of images of fluorescently-labelled intracellular structures is acquired by time-lapse confocal microscopy. **b**) Spatiotemporal correlation function is derived from image analysis by the iMSD algorithm (see Materials and Methods for equations). **c**) Gaussian fitting of correlation functions allows to extract the iMSD plot, which in turn depicts the average diffusion law of the structure of interest (exemplary cases are reported: super-diffusion, dotted red line; isotropic diffusion, dashed red line; sub-diffusion, solid red line). **d**) The short-range diffusion coefficient (D_m), the anomalous diffusion coefficient (α), and the y-axis intercept of the iMSD plot, indicating the average size of the diffusing structures. These three parameters are organized in a 3D plot, used to identify the 'dynamic fingerprint' of the diffusing structure. Adapted from Digiacomo et al. Scirep 2017 (Ref. 11). **From organelles to molecules:** Here, lysosome lumen is labelled by the polarity-sensitive 6-acetyl-2-dimethylaminonaphthalene (ACDAN) probe (**e**). 3D orbital tracking affords the trajectory of single organelles (**f**) while detecting luminal polarity (**g**). Fluctuation analysis finally yields the amplitude and timing of polarity fluctuations (**h**), which in turn are informative of lysosome metabolic status (**i**). Adapted from Ref. [13].

Methodological demonstrations were provided in a series of applications of relevant biological/biomedical interest, including: the spatiotemporal regulation of intracellular transport [6-9], the dynamics and oligomerization of membrane receptors and their ligands [10], the intracellular trafficking of drug-delivery vectors within subcellular nanostructures [11, 12].

For instance, the spatiotemporal dynamics of Transient Potential Vanilloid 1 (TRPV1) membrane receptors (implied in nociception and target of pain therapy) was addressed by combining for the first time the nanoscale resolution of Fluorescence Resonance Energy Transfer (FRET) with the iMSD analysis [10]. It was found that TRPV1 is split in three pools with distinct functional roles: i) TRPV1 trapped in caveolae, and implied in long-term receptor desensitization; ii) TRPV1 stabilized by microtubules, and organized in large supramolecular assemblies, and iii) TRPV1 a freely diffusing on the plasmamembrane and acting as a receptor reservoir [10].

In spite of these technological achievements, molecular details of life regulation are still destined to remain elusive within subcellular, membrane-enclosed, nanosystems such as vesicles, organelles, or even entire subcellular protrusions. At this scale, in fact, the molecular actors are part of a reference nanosystem that is endlessly changing position in space and time in the complex 3D cellular environment. This condition imposes a third requisite to be concomitantly met in the same experiment, large volume sampling to localize the target nanosystem. Unfortunately, no method has the capability to subtract the 3D evolution of the entire nanosystem while preserving the temporal resolution needed to probe molecular details on it. We tackled this bottleneck by sending the excitation beam in a periodic orbit around the nanostructure of interest, with the recorded signal (e.g. fluorescence or scattered light) used as feedback to localize the nanostructure position with unprecedented spatial and temporal resolution. At this point, state-of-the-art imaging/analytical approaches (e.g. fast spatiotemporal correlation spectroscopy) can be used along the orbit to push biophysics to an entirely new level: molecular analysis on a moving, nanoscopic, reference system. The potential of this strategy have been recently demonstrated in a paradigmatic application in which metabolism-dependent solvent polarity fluctuations were measured in the lumen of a 3D-trafficking lysosome (as reported in Fig. 1e-i) [13]. Overall, by such a toolbox of techniques we propose a paradigm shift in the way we address the natural physiopathology of living matter at the sub-cellular scale, where molecular information is still hidden behind a plethora of dynamic intracellular nanostructures. The direct involvement of these latter in the processing of drug-delivery vectors suggests them as a due target for a new era of *theranostic* strategies using engineered nanoarchitectures. Preliminary studies are actively carried out, also in collaboration with external biomedical research units and medical clinics. If successful, this research activity is expected to open new perspectives in biophysics and related fields, nanomedicine above all.

References

[1] C. Di Rienzo, F. Cardarelli, M. Di Luca, F. Beltram, E. Gratton, *Diffusion Tensor Analysis by Two-Dimensional Pair Correlation of Fluorescence Fluctuations in Cells*, Biophysical Journal **111 (4)**, 841 (2016).

[2] C. Di Rienzo, E. Gratton, F. Beltram, F. Cardarelli, *From Fast Fluorescence Imaging to*

Molecular Diffusion Law on Live Cell Membranes in a Commercial Microscope, JoVE **92**, 51994 (2014).

[3] L. Malacrida, P.N. Hedde, S. Ranjit, F. Cardarelli, E. Gratton, *Visualization of Barriers and Obstacles to Molecular Diffusion in Live Cells by Spatial Pair-Cross-Correlation in Two Dimensions*, Biomed. Opt. Express **9 (1)** 303 (2018).

[4] C. Di Rienzo, E. Gratton, F. Beltram, F. Cardarelli, *Spatiotemporal Fluctuation Analysis: A Powerful Tool for the Future Nanoscopy of Molecular Processes*, Biophysical Journal **111 (4)**, 679 (2016).

[5] G. Ferri, L. Digiacomo, F. D'Autilia, W. Durso, G. Caracciolo, F. Cardarelli, *Time-Lapse Confocal Imaging Datasets to Assess Structural and Dynamic Properties of Subcellular Nanostructures*, Sci. Data **5 (1)**, 180191 (2018).

[6] C. Di Rienzo, V. Piazza, E. Gratton, F. Beltram, F. Cardarelli, *Probing Short-Range Protein Brownian Motion in the Cytoplasm of Living Cells*, Nat. Commun. **5 (1)**, 5891 (2014).

[7] P. Bianchini, F. Cardarelli, M.D. Luca, A. Diaspro, R. Bizzarri, *Nanoscale Protein Diffusion by STED-Based Pair Correlation Analysis*, PLoS ONE **9 (6)**, e99619 (2014).

[8] L. Lanzanò, L. Scipioni, M. Di Bona, P. Bianchini, R. Bizzarri, F. Cardarelli, A. Diaspro, G. Vicidomini, *Measurement of Nanoscale Three-Dimensional Diffusion in the Interior of Living Cells by STED-FCS*, Nat. Commun. **8 (1)**, 65 (2017).

[9] E. Hinde, F. Cardarelli, E. Gratton, *Spatiotemporal Regulation of Heterochromatin Protein 1-Alpha Oligomerization and Dynamics in Live Cells*, Sci. Rep. **5 (1)**, 12001 (2015).

[10] B. Storti, C. Di Rienzo, F. Cardarelli, R. Bizzarri, F. Beltram, *Unveiling TRPV1 Spatio-Temporal Organization in Live Cell Membranes*, PLoS ONE **10 (3)**, e0116900 (2015).

[11] L. Digiacomo, F. D'Autilia, W. Durso, P.M. Tentori, G. Caracciolo, F. Cardarelli, *Dynamic Fingerprinting of Sub-Cellular Nanostructures by Image Mean Square Displacement Analysis*, Sci. Rep. **7 (1)**, 14836 (2017).

[12] G. Ferri, L. Digiacomo, Z. Lavagnino, M. Occhipinti, M. Bugliani, V. Cappello, G. Caracciolo, P. Marchetti, D.W. Piston, F. Cardarelli, *Insulin Secretory Granules Labelled with Phogrin-Fluorescent Proteins Show Alterations in Size, Mobility and Responsiveness to Glucose Stimulation in Living β-Cells*, Sci. Rep. **9 (1)**, 2890 (2019).

[13] F. Begarani, F. D'Autilia, G. Signore, A. Del Grosso, M. Cecchini, E. Gratton, F. Beltram, F. Cardarelli, *Capturing Metabolism-Dependent Solvent Dynamics in the Lumen of a Trafficking Lysosome*, ACS Nano **13 (2)**, 1670 (2019).

1.3.28 Nanostructuring soft matter for targeted delivery at the cellular and sub-cellular scale

A significant body of knowledge was acquired at NEST on how soft-matter building blocks can be nanostructured in order to develop novel carriers tailored to therapeutic/diagnostic applications. Nanocarriers with a variety of synthetic identities and functions were developed and tested in in-vitro cellular models.

A variety of soft-matter building blocks were engineered to *either* target specific endocytic routes, *or* promote endosomal escaping *or* even avoid trapping and promote direct delivery of payloads into the cytoplasm. For instance, using small aminoacidic sequences (peptides) as platform, we demonstrated that vesicle-mediated transport (i.e. endocytosis) mediates their entry into cells at relatively low concentrations (i.e. nano- to micromolar), while direct translocation across the plasma membrane comes into play at higher concentrations (i.e. micro- to millimolar) [1]. In more detail, by a combination of UV-Vis analyses, NMR-based diffusion measurements and MD simulations it was demonstrated for the first time that the HIV-1 Tat arginine-rich peptide (Tat_{11}) is able to self-aggregate into dimers in a concentration-dependent manner (Fig. 1).

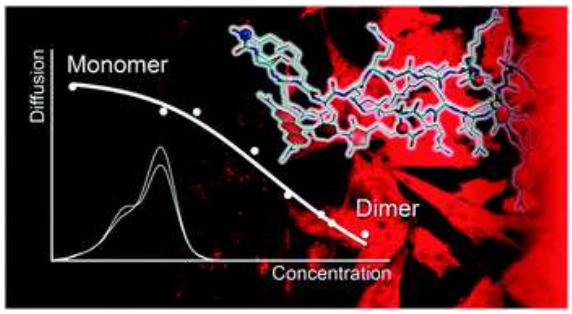

Figure 1. HIV-1 Tat arginine-rich peptide (Tat_{11}) is able to self-aggregate into dimers in both its fluorescently labeled and unlabeled variants (taken from Ref. [1])

The dimeric form is able to induce local perturbations of the plasma-membrane composition and/or integrity and favor peptide direct translocation. Experimental and *in-silico* data support the enhanced capability of peptide dimers in comparison to monomers to stabilize membrane pores [1, 2]. Worthy of mention, data also show how organic fluorophores (typically used for peptide labelling) have overall negligible kinetic and energetic effects on peptide transduction, yet they promote the process indirectly by favoring peptide aggregation. Similar conclusions were extended to either other cationic cell penetrating peptides (CPPs), such as Antennapedia (Ant) and nona-arginine (R9), and to amphipathic spontaneous membrane-translocating peptides [3].
To avoid trapping into endocytic vesicles at low peptide concentrations, it was demonstrated that the addition of the Tat-peptide module to well-established antimicrobial sequences (e.g. Cecropin-Melittin, or CM_{18}) is able to trigger a concentration-dependent detergent-like disruption of the vesicle membrane and massive release of the cargo into the cell cytoplasm [4]. The peptide concentration needed to produce an effect can be drastically reduced by the synergistic use of nanosecond electric pulses (NPs): by this approach, a nontoxic, high-yield, gene delivery system based on stable nanopore formation within vesicle membranes

followed by DNA release can be obtained, with no detectable perturbation of the plasma membrane [5].

There are selected cases in which the endocytic route cannot be avoided. For instance, it was demonstrated that the standard carriers used for lipid-mediated gene/drug delivery (i.e. liposomes) are invariably taken up by vesicle-mediated endocytosis, typically fluid-phase micropinocytosis, probably due to steric constrains [6]. By combining live-cell imaging, single-particle tracking microscopy, and quantitative transfection-efficiency assays, a mechanistic evaluation of the transfection barriers involved in lipid-mediated gene/drug delivery was achieved and the interplay between the nanostructure composition and its final performances unveiled. For instance, it was found that Lipofectamine, contrary to alternative formulations, is able to efficiently avoid active intracellular transport along microtubules, and the subsequent degradation of the payload within acidic/digestive lysosomal compartments, a process that can be eventually further tuned by modulating the cholesterol content of the liposomal carrier [7, 8]: this result is achieved by random Brownian motion of Lipofectamine-containing vesicles within the cytoplasm.

It was also demonstrated that, following exposure to biological milieus (e.g. after systemic administration), lipid-based carriers get spontaneously covered by an outer biomolecular corona (BC) that defines many of their biological outcomes, such as the elicited immune response, biodistribution, and targeting abilities. In this regard, by conducting confocal fluorescence microscopy experiments and image correlation analyses, it was shown that the BC can be modulated to promote a neat switch of the cell entry mechanism and subsequent intracellular trafficking, for instance from macropinocytosis to clathrin-dependent endocytosis, thus targeting a specific endocytic route [9] (Fig. 2).

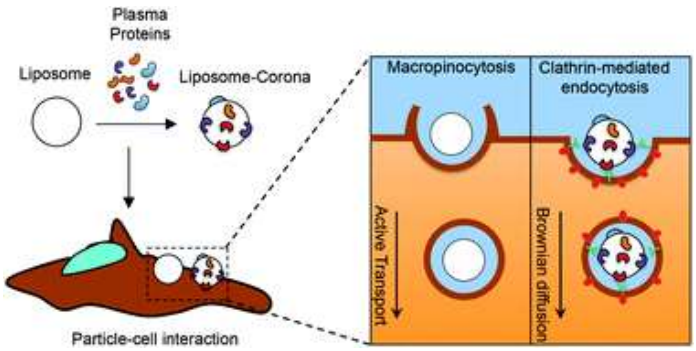

Figure 2. An apolipoprotein-enriched biomolecular corona switches the cellular uptake mechanism and trafficking pathway of lipid nanoparticles (taken from Ref. [9])

Depending on the specific *theranostic* application, the carrier can be engineered to include additional modules, as schematically sketched in the cartoon on the left. For instance, constant efforts at NEST are devoted to implement "Sensing" capabilities by means of GFP-derived mutants and/or environment-sensitive dyes; "Contrast Agents" are mainly built based on metallic and inorganic nanoparticles suitable for optical imaging and/or photoacoustic effects [10, 11]; finally, both existing and new "Drugs" are typically

employed in innovative configurations to increase their bioavailability and efficacy (e.g. doxorubicin linked to peptides or graphene-oxide [12]).

References

[1] S. Macchi, R. Nifosì, G. Signore, S. Di Pietro, C. Boccardi, F. D'Autilia, F. Beltram, F. Cardarelli, *Self-Aggregation Propensity of the Tat Peptide Revealed by UV-Vis, NMR and MD Analyses*, Phys. Chem. Chem. Phys. **19 (35)**, 23910 (2017).

[2] M. Jan Akhunzada, B. Chandramouli, N. Bhattacharjee, S. Macchi, F. Cardarelli, G. Brancato, *The Role of Tat Peptide Self-Aggregation in Membrane Pore Stabilization: Insights from a Computational Study*, Phys. Chem. Chem. Phys. **19 (40)**, 27603 (2017).

[3] S. Macchi, G. Signore, C. Boccardi, C. Di Rienzo, F. Beltram, F. Cardarelli, *Spontaneous Membrane-Translocating Peptides: Influence of Peptide Self-Aggregation and Cargo Polarity*, Sci. Rep. **5 (1)**, 16914 (2015).

[4] A. Fasoli, F. Salomone, M. Benedusi, C. Boccardi, G. Rispoli, F. Beltram, F. Cardarelli, *Mechanistic Insight into CM18-Tat11 Peptide Membrane-Perturbing Action by Whole-Cell Patch-Clamp Recording*, Molecules **19 (7)**, 9228 (2014).

[5] F. Salomone, M. Breton, I. Leray, F. Cardarelli, C. Boccardi, D. Bonhenry, M. Tarek, L.M. Mir, F. Beltram, *High-Yield Nontoxic Gene Transfer through Conjugation of the CM 18 -Tat 11 Chimeric Peptide with Nanosecond Electric Pulses*, Mol. Pharmaceutics **11 (7)**, 2466 (2014).

[6] D. Pozzi, C. Marchini, F. Cardarelli, F. Salomone, S. Coppola, M. Montani, M.E. Zabaleta, M.A. Digman, E. Gratton, V. Colapicchioni, G. Caracciolo, *Mechanistic Evaluation of the Transfection Barriers Involved in Lipid-Mediated Gene Delivery: Interplay between Nanostructure and Composition*, Biochimica et Biophysica Acta (BBA) – Biomembranes **1838 (3)**, 957 (2014).

[7] D. Pozzi, F. Cardarelli, F. Salomone, C. Marchini, H. Amenitsch, G.L. Barbera, G. Caracciolo, *Role of Cholesterol on the Transfection Barriers of Cationic Lipid/DNA Complexes*, Appl. Phys. Lett. **105 (7)**, 073701 (2014).

[8] F. Cardarelli, L. Digiacomo, C. Marchini, A. Amici, F. Salomone, G. Fiume, A. Rossetta, E. Gratton, D. Pozzi, G. Caracciolo, *The Intracellular Trafficking Mechanism of Lipofectamine-Based Transfection Reagents and Its Implication for Gene Delivery*, Sci. Rep. **6 (1)**, 25879 (2016).

[9] L. Digiacomo, F. Cardarelli, D. Pozzi, S. Palchetti, M.A. Digman, E. Gratton, A.L. Capriotti, M. Mahmoudi, G. Caracciolo, *An Apolipoprotein-Enriched Biomolecular Corona Switches the Cellular Uptake Mechanism and Trafficking Pathway of Lipid Nanoparticles*, Nanoscale **9 (44)**, 17254 (2017).

[10] R. Hakim, K. Damak, M. Gemmi, S. Luin, R. Maalej, A. Toncelli, *Pr 3+: BaY 2 F 8 Crystal Nanoparticles (24 Nm) Produced by High-Energy Ball Milling: Spectroscopic Characterization and Comparison with Bulk Properties*, J. Phys. Chem. C **119 (5)**, 2844 (2015).

[11] B. Silvestri, P. Armanetti, G. Sanità, G. Vitiello, A. Lamberti, G. Calì, A. Pezzella, G. Luciani, L. Menichetti, S. Luin, M. d'Ischia, *Silver-Nanoparticles as Plasmon-Resonant Enhancers for Eumelanin's Photoacoustic Signal in a Self-Structured Hybrid Nanoprobe*, Materials Science and Engineering: C **102**, 788 (2019).

[12] E. Quagliarini, R. Di Santo, D. Pozzi, P. Tentori, F. Cardarelli, G. Caracciolo, *Mechanistic Insights into the Release of Doxorubicin from Graphene Oxide in Cancer Cells*, Nanomaterials **10 (8)**, 1482 (2020).

1.3.29 Complex networks of organic nanowires: from coherent light emission to energy harvesting and biophysics

Organic nanowires are emerging as novel building blocks for photonic devices, energy nanogeneretors and smart substrates that can provide specific biophysical cues and direct stem-cell fate. We have investigated the properties of composite organic wires and filaments embedding various species of chromophores, including self-assembling rotaxane-type molecular systems, piezo-polymers and 2-dimensional materials. These composite materials are relevant for applications in optical amplifiers, lasers, chemical sensors, energy harvesting and tissue engineering.

Electrospinning is based on electrified jets of polymer solutions, which have to exhibit significant molecular entanglements, and it is nowadays the most promising method for producing organic nanofibers and nanowires due to its operational simplicity, low cost, and chemical versatility. Solutions are accelerated concomitantly to solvent evaporation, to deposit nanofiber-based coatings on solid surfaces, or to realize free-standing membranes. Active polymer nanofibers and nanowires, in the form of individual nanostructures or complex networks realized by such approach, exhibit better performances compared to conventional film-based materials and coatings [1]. Electrospinning is being developed in our group in order to realize new, active nanofibrous materials with applications in different scientific fields and technologies.

Figure 1a-d show an example of stimuli-responsive nanowires, realized by embedding a molecular motor in a polymer matrix [2]. Exposure to base and acid vapors induced the dethreading and rethreading of the molecular components in the solid wires (Fig. 1c-d). The light-induced photo-isomerization of the azobenzene molecules was also demonstrated in solid wires, making such composite systems responsive to both optical and chemical external stimuli. Interestingly, the dethreading of the axles from the rings enhanced significantly the Young's modulus of arrays made of aligned wires. These findings demonstrate the possibility of tailoring the macroscopic properties of such composite materials, by controlling the behavior of the molecular constituents at the nanoscale.

Another example of optically-active nanowires developed in our group is shown Fig. 1e-g, where near-infrared (NIR) emitting organic wires were realized by embedding light-emitting molecules in polymer fibers, obtaining optical gain up to 5 cm^{-1} [3]. The gain properties of macroscopic arrays made by many filaments can be tailored by controlling their assembly and mutual alignment. Recently, hybrid fibers and planar networks of polymer fibers with optical gain were realized which displayed lasing modes tailored by the topology of the fiber network [4-5].

The combination of electrospinning with nanopatterning technologies allows the generation of optically-pumped solid-state lasers, based on individual light-emitting nanofibers, which are textured by nanoimprint lithography [6]. Single-fiber distributed feedback lasers can be realized by Bragg gratings (with 400 nm - 600 nm period), imprinted directly onto the active nanowires. These devices show a threshold excitation fluence (750 μJ cm^{-2}) reduced by 40–50% with respect to nanopatterned, thin-film lasers made of the same molecular material, due to the higher field confinement which leads to correspondingly higher photonic density inside the active filaments (Fig. 2b) [6].

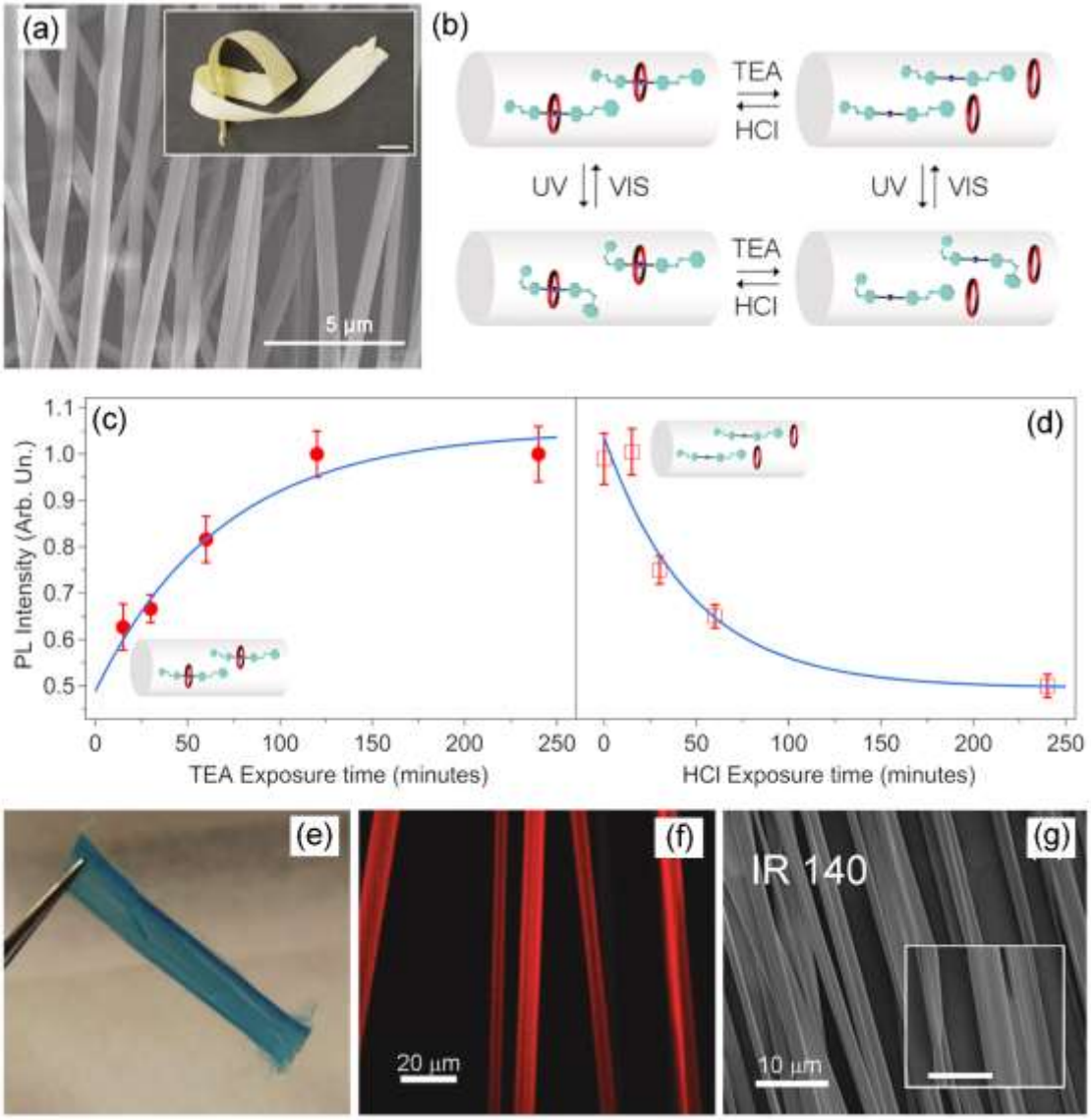

Figure 1. (a) SEM micrographs of polymer filaments doped with rotaxane-type molecular systems. Inset: photograph of an array made of such wires. Scale bar = 1 cm. (b) Schematics of the photo-isomerization processes of the azobenzene end-units of the axle and of the chemically-induced dethreading/rethreading processes of the axle and ring molecular components. Photo-isomerization processes occur upon exposure to ultraviolet (UV) and visible (Vis) light, whereas the dethreading/rethreading processes are induced by exposure to base/acid vapors (triethylamine, TEA, and HCl, respectively). (c)-(d) Photoluminescence (PL) intensity of polymer nanowires doped with molecular motors vs. base (c) and acid (d) vapors exposure times. These data evidence the reversible dethreading/rethreading processes that the axle and ring molecular components undergo inside polymer wires, upon chemical stimulation. Adapted from Ref. [2]. © 2014 American Chemical Society. (e) Photograph and (f) fluorescence confocal micrograph of an array of polymer wires doped with a NIR-emitting dye. (g) Scanning electron microscopy (SEM) images of polymer wires doped with a NIR-emitting dye. Inset scale bar = 10 µm. Adapted with permission from [3]. Copyright © 2014 WILEY-VCH Verlag GmbH & Co.

Analogously, electrospun piezoelectric nanofibers outperform thin films, in terms of self-poling capability and conformability to many surfaces. Aligned arrays of these nanofibers (Fig. 2c, d) in mutual contact exhibit improved voltage output due to electromechanical coupling of multiple filaments, together with large areas (up to tens of cm^2) and light weight, and they can be repeatedly bent and twisted

without fracture [7]. These features make functional polymer nanofibers very appealing for application in the fields of nanogenerators, self-powered systems, including implantable bioelectronics, smart wearables and body sensor networks, and ambient-assisted living.

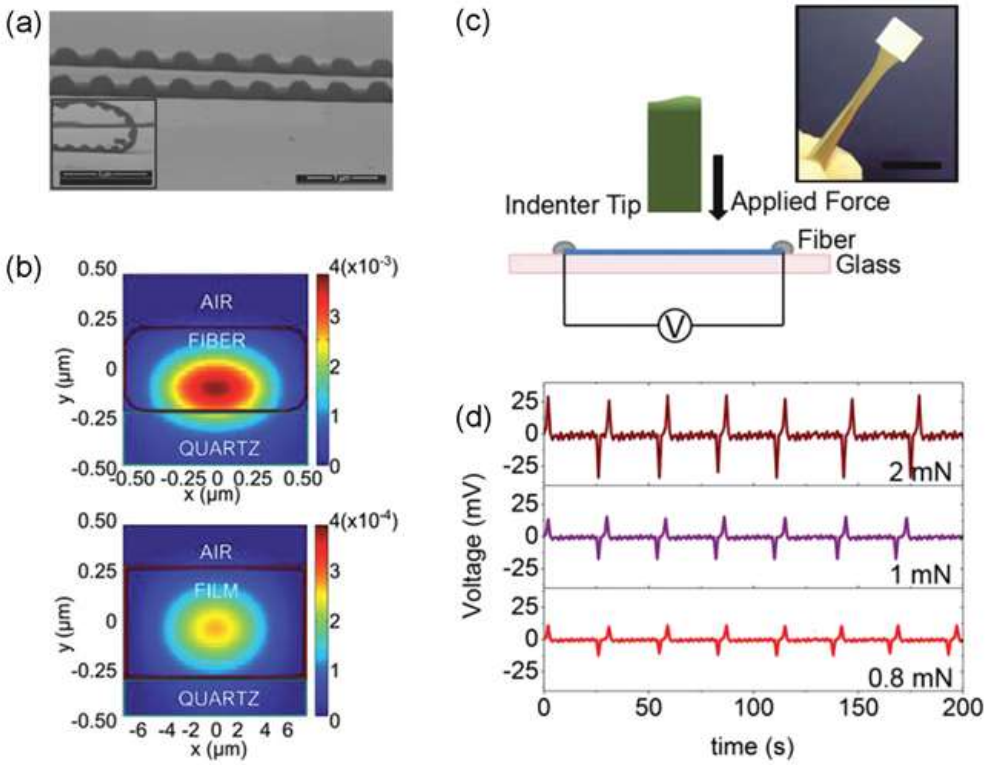

Figure 2. (a) Scanning electron micrograph of nanopatterned polymer fibers for lasing. Inset: bent patterned fibers. (b) Modeling of light propagating in the distributed feedback lasers. The maps show the normalized, real part of the Poynting vector component along the sample in-plane, longitudinal direction, calculated on a cross-section of a patterned fiber (top) and film (bottom), respectively. For the fiber, fields are much more confined in the transversal direction (see the different horizontal scales for the two maps). The fundamental transverse electric (TE) is calculated by Finite-Difference Time-Domain (FDTD) simulations. Adapted with permission from [6]. Copyright © 2014 WILEY-VCH Verlag GmbH & Co. KGaA, Weinheim. (c) Scheme of a developed set-up for force-indentation measurements on piezoelectric electrospun nanofibers (photograph in the inset). (d) Measured output voltages under various, repeatedly applied stresses. Adapted with permission from [7]. Copyright © 2014 The Authors. Published by WILEY-VCH Verlag GmbH & Co. KGaA, Weinheim.

Organic nanowire and their networks can be also specifically functionalized for realizing novel classes of smart substrates able to provide specific biophysical cues and direct the stem cell fate [8-9]. We developed a hybrid approach in which polymer nanofibers of polycaprolactone (PCL) realized by electrospinning are surface functionalized with graphene oxide (GO) by means of a layer-by-layer method schematized in Fig. 3a.

Fibrous scaffolds are particularly interesting for tissue engineering applications, as their nanofilaments structurally mimic the hierarchical organization of the natural extracellular matrix. We realized four types of PCL scaffolds: fibers with random and aligned orientation functionalized with GO and fibers with random and aligned orientation which undergo the same layer-by-layer processing except for the treatment with GO (Fig. 3b and 3c respectively). The employed method

guarantees uniform and homogeneous GO adsorption on the fiber surface, and the overall functionalization significantly affect the surface wettability by increasing the hydrophilicity of PCL. Such effect is fundamental for an efficient cell–substrate interaction.

Finally, we cultured primary neurospheres from DPSCs on the fibrous surfaces and assessed the substrates biocompatibility thus revealing no remarkable cytotoxic effects. In addition, the fiber orientation was found to influence the cell morphology through a cytoskeletal reorganization and a superior cell elongation on aligned fibers scaffolds when compared to the random oriented ones. Through the evaluation of the expression of several differentiation markers, we found that the different scaffolds selectively direct the fate of neurospheres toward four different lineages, such as osteoblastic, glial, fibroblastic, and neuronal as schematized in Fig. 3d. The confocal imaging of specific markers confirms these findings (Fig. 3e). Overall, the combination of wetting properties, protein adsorption capacity and effects on cell morphology of the substrate is able to specifically directs the cell commitment without the use of exogenous factors thus unveiling new potentialities for cellular programming.

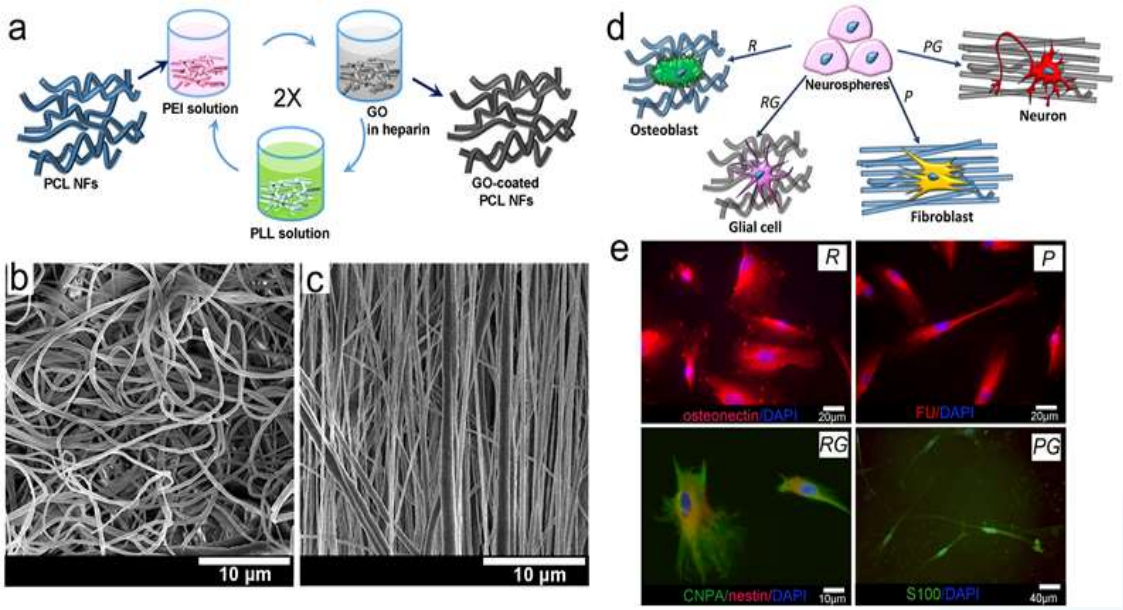

Figure 3. (a) Schematics of the stepwise coating of nanofibers by GO. Briefly, the surface of the scaffolds was activated by soaking in polyethyleneimine dissolved in PBS, then fibers were immersed into heparin with GO, followed by soaking in poly-l-lysine. After every step, fibers were washed in PBS. The immersion, washing, and soaking steps were repeated two times. (b,c) SEM images of random (b) and aligned (c) fibers. (d) Schematics of the different cell commitment: neurospheres from DPSCs show a differentiation propensity for osteoblastic, glial, fibroblastic, and neuronal cells on random fibers (R), random GO-coated fibers (RG), uniaxially aligned fibers (P) and uniaxially aligned GO-coated fibers (PG), respectively. (e) Immunofluorescence staining against osteonectin (red)/DAPI (blue), CNPase (green)/nestin (red)/DAPI (blue), FU (red)/DAPI (blue), and S100 (green)/DAPI (blue) respectively on neurosphere grown on substrate R, RG, P, and PG fibers. Adapted with permission from [9]. Copyright © 2019 WILEY-VCH Verlag GmbH & Co. KGaA, Weinheim.

The research leading to these results has received funding from the European Research Council under the European Union's Seventh Framework Programme (FP/2007-2013)/ERC Grant Agreement n. 306357 (ERC Starting Grant "NANO-

JETS") and under the European Union's Horizon 2020 Research and Innovation Programme (Grant Agreement no. 682157, "xPRINT").

References

[1] L. Persano, A. Camposeo, D. Pisignano, *Active polymer nanofibers for photonics, electronics, energy generation and micromechanics*, Prog. Polym. Sci. **43**, 48 (2015).

[2] V. Fasano, M. Baroncini, M. Moffa, D. Iandolo, A. Camposeo, A. Credi, D. Pisignano, *Organic nanofibers embedding stimuli-responsive threaded molecular components*, J. Am. Chem. Soc. **136**, 14245 (2014).

[3] G. Morello, M. Moffa, S. Girardo, A. Camposeo, D. Pisignano, *Optical gain in the near infrared by light-emitting electrospun fibers*, Adv. Funct. Mater. **24**, 5225 (2014).

[4] A. Portone, L. Romano, V. Fasano, R. Di Corato, A. Camposeo, F. Fabbri, F. Cardarelli, D. Pisignano, L. Persano, *Low-defectiveness exfoliation of MoS2 nanoparticles and their embedment in hybrid light-emitting polymer nanofibers*, Nanoscale **10**, 21748 (2018).

[5] M. Gaio, D. Saxena, J. Bertolotti, D. Pisignano, A. Camposeo, R. Sapienza, *A nanophotonic laser on a graph*, Nat. Commun. **10**, 226 (2019).

[6] L. Persano, A. Camposeo, P. Del Carro, V. Fasano, M. Moffa, R. Manco, S. D'Agostino, D. Pisignano, *Distributed Feedback Imprinted Electrospun Fiber Lasers*, Adv. Mater. **26**, 6542 (2014).

[7] L. Persano, C. Dagdeviren, C. Maruccio, L. De Lorenzis, D. Pisignano, *Cooperativity in the Enhanced Piezoelectric Response of Polymer Nanowires*, Adv. Mater. **26**, 7574 (2014).

[8] A. Portone, M. Moffa, C. Gardin, L. Ferroni, M. Tatullo, F. Fabbri, L. Persano, A. Piattelli, B. Zavan, D. Pisignano, *Lineage-Specific Commitment of Stem Cells with Organic and Graphene Oxide–Functionalized Nanofibers*, Adv. Funct. Mater. **29**, 1806694 (2019).

[9] A. Portone, A. G. Sciancalepore, G. Melle, G. S. Netti, G. Greco, L. Persano, L. Gesualdo, D. Pisignano, *Quasi-3D morphology and modulation of focal adhesions of human adult stem cells through combinatorial concave elastomeric surfaces with varied stiffness*, Soft Matter **15**, 5154 (2019).

1.3.30 Quantum Metrology

By making use of quantum-mechanical features, such as quantum superposition, entanglement, or squeezing, we are able to go beyond classical technologies. One of such promising ideas is "quantum metrology" because of its possible applications. When one wishes to estimate some quantity or parameter of a physical system, one typically tries to do it by analyzing data collected by performing a number of independent and identical experiments, or by sending a number of independent probes to the target.

In Ref. [1,8] we identified the optimal quantum pure states of identical bosonic particles for applications in quantum metrology, in particular in the estimation of a single parameter for the generic two-mode interferometric setup.

In Ref. [2,6] we introduced, a quantifier for the best achievable accuracy for temperature estimation via local measurements. In Ref. [10] a scheme for improving the sensitivity of quantum thermometry was proposed where the sensing quantum system used to recover the temperature of an external bath is dynamically coupled with an external ancilla (a meter) via an Hamiltonian coupling – see Fig. 1.

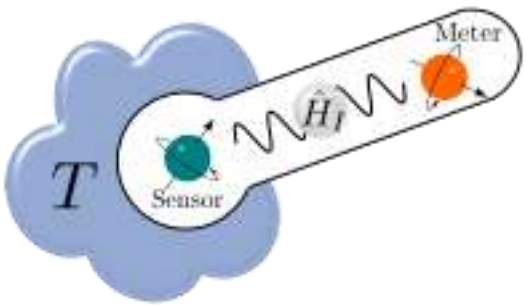

Figure 1. Schematic representation of the model discussed in Ref. [10] – figure taken from the paper. Here the temperature T is recovered by studying the effect it induces on the meter system that is coupled with a sensor that is in constant contact with the bath.

In Ref. [7,9] we studied the efficiency of estimation procedures where the temperature of an external bath is indirectly recovered by monitoring the transformations induced on a probing system that is put in thermal contact with the bath. In particular we compare the performances of sequential measurement schemes where the probe is initialized only once and measured repeatedly during its interaction with the bath, with those of measure and re-prepare approaches where instead, after each interaction-and-measurement stage, the probe is reinitialized into the same fiduciary state. From our analysis it is revealed that the sequential approach, while being in general not capable of providing the best accuracy achievable, is nonetheless more versatile with respect to the choice of the initial state of the probe, yielding on average smaller indetermination levels. In Ref. [4] the problem of estimating a parameter of a quantum system through a series of measurements performed sequentially on a quantum probe is analyzed in the general setting where the underlying statistics is explicitly non-i.i.d. In this setting we gave a generalization of the central limit theorem in the present context, which under fairly general assumptions shows that as the number N of measurement data increases the probability distribution of functionals of the data

(e.g., the average of the data) through which the target parameter is estimated becomes asymptotically normal and independent of the initial state of the probe.

In Ref. [11] the possibility of discriminating the statistics of a thermal bath using indirect measurements performed on quantum probes was presented. The scheme relies on the fact that, when weakly coupled with the environment of interest, the transient evolution of the probe toward its final thermal configuration, is strongly affected by the fermionic or bosonic nature of the bath excitations.

In Ref. [3] we presented a quantifier of non-classical correlations for bipartite, multi-mode Gaussian states. In Ref. [5] we considered bipartite systems as versatile probes for the estimation of transformations acting locally on one of the subsystems. We investigate what resources are required for the probes to offer a guaranteed level of metrological performance, when the latter is averaged over specific sets of local transformations. Our analysis contrasts and complements the recent series of studies focused on the minimum, rather than the average, performance of bipartite probes in local estimation tasks, which was instead determined by quantum correlations other than entanglement. We provide explicit prescriptions to characterize the most reliable states maximizing the average skew information, and elucidate the role of state purity, separability and correlations in the classification of optimal probes.

References

[1] A. De Pasquale, P. Facchi, G. Florio, V. Giovannetti, K. Matsuoka, K. Yuasa, *Two-Mode Bosonic Quantum Metrology with Number Fluctuations*, Physical Review A **92**, 042115 (2015).

[2] A. De Pasquale, D. Rossini, R. Fazio, V. Giovannetti, *Local quantum thermal susceptibility*, Nature Communications **7**, 12782 (2016).

[3] L. Rigovacca, A. Farace, A. De Pasquale, V. Giovannetti, *Gaussian discriminating strength*, Phys. Rev. A **92**, 042331 (2015).

[4] D. Burgarth, V. Giovannetti, A.N. Kato, K. Yuasa, *Quantum estimation via sequential measurements*, New J. Phys. **17**, 113055 (2015).

[5] A. Farace, A. De Pasquale, G. Adesso, V. Giovannetti, *Building versatile bipartite probes for quantummetrology*, New J. Phys. **18**, 013049 (2016).

[6] G. De Palma, A. De Pasquale, V. Giovannetti, *Universal locality of quantum thermal susceptibility*, Phys. Rev. A **95**, 052115 (2017).

[7] A. De Pasquale, K. Yuasa, V. Giovannetti, *Estimating temperature via sequential measurements*, Phys. Rev. A **96**, 012316 (2017).

[8] T. Matsubara, P. Facchi, V. Giovannetti, K. Yuasa, *Optimal Gaussian metrology for generic multimodeinterferometric circuit*, New J. Phys. **21**, 033014 (2019).

[9] V. Cavina, L. Mancino, A. De Pasquale, I. Gianani, M. Sbroscia, R.I. Booth, E. Roccia, R. Raimondi, V. Giovannetti, M. Barbieri, *Bridging thermodynamics and metrology in nonequilibrium quantum thermometry*, Phys. Rev. A **98**, 050101 (2018).

[10] A.H. Kiilerich, A. De Pasquale, V. Giovannetti, *Dynamical approach to ancilla-assisted quantum thermometry*, Phys. Rev. A **98**, 042124 (2018).

[11] D. Farina, V. Cavina, V. Giovannetti, *Quantum bath statistics tagging*, Phys. Rev. A **100**, 042327 (2019).

1.3.31 Quantum computation: protocols and process implementation

Part of the activity was devoted to design and possibly implement, new quantum protocols and platform for general purposes.

In Ref. [1] a nanoscale implementation of a Mach-Zhender interferometer was presented with spin-resolved quantum Hall states – see Fig. 1.

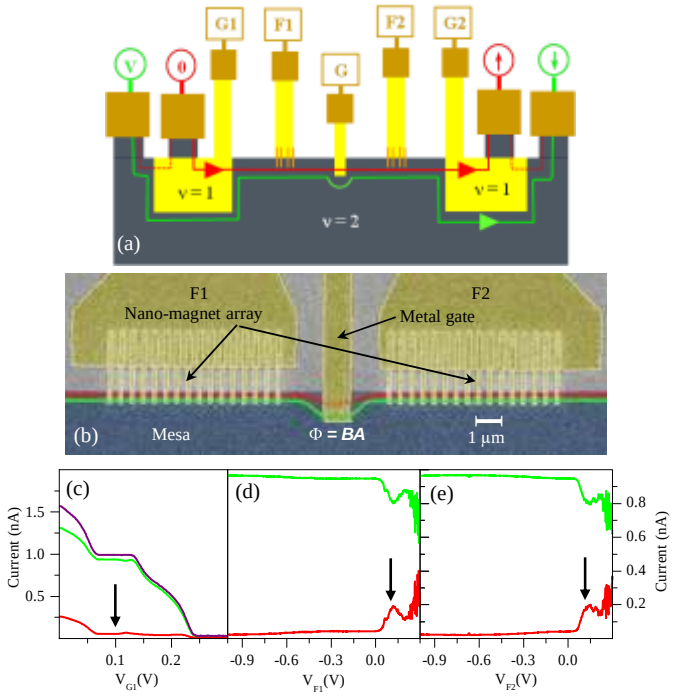

Figure 1. Schematics of the Mach-Zehnder interferometer implemented in Ref. [1] – figure from the paper.

Spontaneous synchronization is a fundamental phenomenon, important in many theoretical studies and applications. Recently this effect has been analyzed and observed in a number of physical systems close to the quantum mechanical regime. In Ref. [2] we proposed the mutual information as a useful order parameter which can capture the emergence of synchronization in very different contexts, ranging from semi-classical to intrinsically quantum mechanical systems.

In Ref. [3] a technique was proposed that enables one the creation of quantum discord between two distant nodes, each containing a cavity consist of the Bose-Einstein condensate, by applying a non-ideal Bell-like detection on the output modes of optical cavities.

In Ref. [4] we addressed the problem of realizing a reliable quantum memory based on zero-energy Majorana modes in the presence of experimental constraints on the operations aimed at recovering the information. In particular, we characterized the best recovery operation acting only on the zero-energy Majorana modes and the memory fidelity that can be therewith achieved.

On the basis of the quantum Zeno effect we showed [5] that a strong amplitude damping process applied locally on a part of a quantum system can have a beneficial effect on the dynamics of the remaining part of the system. Quantum

operations that cannot be implemented without the dissipation become achievable by the action of the strong dissipative process. In Refs. [7,8] the mathematical aspects of the problem were formalized and in Ref. [6] we generalize this idea by identifying decoherence-free subspaces (DFS's) as the subspaces in which the dynamics becomes more complex. Applying methods from quantum control theory we characterized the set of reachable operations within the DFS's. We provide three examples which become fully controllable within the DFS's while the control over the original Hilbert space in the absence of dissipation is trivial. In particular, we show that the (classical) Ising Hamiltonian is turned into a Heisenberg Hamiltonian by strong collective decoherence, which provides universal quantum computation within the DFS's.

In Ref. [9] we investigated the supercurrent in a hybrid topological Josephson junction consisting of two planes of topological insulator (TI) in a specific configuration, which allows both local (LAR) and crossed (CAR) Andreev processes at the interfaces with two conventional s-wave superconductors. In particular, we demonstrated that the voltage gating allows the manipulation of the entaglement symmetry of non-local Cooper pairs associated to the CAR process. We established a connection between the Josephson current-phase relationship of the system and the action of the two external fields, finding that they selectively modify the LAR or the CAR contributions. Remarkably, we found that the critical current of the junction takes a very simple form which reflects the change in the symmetry occurred to the entangled state and allows to determine the microscopic parameters of the junction.

As the possibility to decouple temporal and spatial variations of the electromagnetic field, leading to a wavelength stretching, has been recognized to be of paramount importance for practical applications, in Ref. [10] we generalize the idea of stretchability from the framework of electromagnetic waves to massive particles. A necessary and sufficient condition which allows one to identify energetically stable configuration of a 1D quantum particle characterized by arbitrary large spatial regions where the associated wave-function exhibit a flat, non-zero profile is presented, together with examples on well-known and widely used potential profiles and an application to 2D models.

In Ref. [11] we proposed a spatial analog of the Berry's phase mechanism for the coherent manipulation of states of non-relativistic massive particles moving in a two-dimensional landscape. In our construction the temporal modulation of the system Hamiltonian is replaced by a modulation of the confining potential along the transverse direction of the particle propagation. By properly tuning the model parameters the resulting scattering input-output relations exhibit a Wilczek-Zee non-abelian phase shift contribution that is intrinsically geometrical, hence insensitive to the specific details of the potential landscape.

References

[1] B. Karmakar, D. Venturelli, L. Chirolli, V. Giovannetti, R. Fazio, S. Roddaro, L.N. Pfeiffer, K.W. West, F. Taddei, V. Pellegrini, *Nanoscale Mach-Zehnder interferometer with spin-resolved quantum Hall edge states*, Phys. Rev. B **92**, 195303 (2015).

[2] V. Ameri, M. Eghbali-Arani, A. Mari, A. Farace, F. Kheirandish, V. Giovannetti, R. Fazio, *Mutual*

information as an order parameter for quantum synchronization, Phys. Rev. A **91**, 012301 (2015).
[3] M. Eghbali-Arani, H. Yavari, M.A. Shahzamanian, V. Giovannetti, S. Barzanjeh, *Generating quantum discord between two distant Bose–Einstein condensates with Bell-like detection*, JOSA B **32 (5)**, 798 (2015).
[4] M. Ippoliti, M. Rizzi, V. Giovannetti, L. Mazza, *Quantum memories with zero-energy Majorana modes and experimental constraints*, Phys. Rev. A **93**, 062325 (2016).
[5] D.K. Burgarth, P. Facchi, V. Giovannetti, H. Nakazato, S. Pascazio, K. Yuasa, *Exponential rise of dynamical complexity in quantum computing through projections*, Nat. Commun. **5**, 5173 (2014).
[6] C. Arenz, D. Burgarth, P. Facchi, V. Giovannetti, H. Nakazato, S. Pascazio, K. Yuasa, *Universal control induced by noise*, Phys. Rev. A **93**, 062308 (2016).
[7] D. Orsucci, D. Burgarth, P. Facchi, H. Nakazato, S. Pascazio, K. Yuasa, V. Giovannetti, *Hamiltonian purification*, J. of Math. Phys. **56**, 122104 (2015).
[8] C. Arenz, D. Burgarth, V. Giovannetti, H. Nakazato, K. Yuasa, *Lindbladian purification*, Quantum Sci. Technol. **2**, 024001 (2017).
[9] G. Blasi, F. Taddei, V. Giovannetti, A. Braggio, *Manipulation of Cooper pair entanglement in hybrid topological Josephson junctions*, Phys. Rev. B **99**, 064514 (2019).
[10] S. Cusumano, A. De Pasquale, G.C. La Rocca, V. Giovannetti, *Stretching potential engineering*, J. Phys A: Math. Theor. **53**, 035301 (2020).
[11] S. Cusumano, A. De Pasquale, V. Giovannetti, *Geometric Phase through Spatial Potential Engineering*, Phys. Rev. Lett. **124**, 190401 (2020).

1.3.32 Quantum Communication: efficiency thresholds, coding, and environment engineering

The study of how efficiently information can be preserved when transferring it via the use of quantum carriers, is central in quantum-information theory and represents a fundamental prerequisite to develop reliable quantum technologies. Our activity in the field covers a broad spectrum of different research lines which, among others, include the theoretical characterization of the optimal thresholds of the communication efficiency (capacities) attainable by several realistic quantum communication models (e.g. Bosonic quantum channels), the development of detection and coding schemes that allows one to reach such ultimate limits, the way in which partial engineering of the communication line environment can be used to in order to improve the overall quality of the signaling process, the study of non-Markovian effects.

Starting from previous results, in Refs. [1,2,8,10,12,14,20] generalizations of the longstanding Gaussian optimizer conjecture for Bosonic channels were proven. In particular in Ref. [8] an ordering between the quantum states emerging from a single mode gauge-covariant bosonic Gaussian channel was observed. Specifically it was shown that within the set of input density matrices with the same given spectrum, the element passive with respect to the Fock basis (i.e. diagonal with decreasing eigenvalues) produces an output which majorizes all the other outputs emerging from the same set. In Ref. [5] the set of linear maps sending the set of quantum Gaussian states into itself was explored: these transformations are in general not positive, a feature which can be exploited as a test to check whether a given quantum state belongs to the convex hull of Gaussian states. In Ref. [19] we derived several upper bounds on the quantum capacity of qubit and bosonic thermal attenuators.

In Ref. [4] an all-optical scheme for simulating non-Markovian evolution of a quantum system was proposed. It uses only linear optics elements and by controlling the system parameters allows one to control the presence or absence of information backflow from the environment.

In Ref. [3] a set of new functionals (called entanglement-breaking indices) has been introduced which characterize how many local iterations of a given (local) quantum channel are needed in order to completely destroy the entanglement between the system of interest over which the transformation is defined and an external ancilla. In Ref. [6] instead the set of Entanglement Saving quantum channels was characterized: these are completely positive, trace preserving transformations which when acting locally on a bipartite quantum system initially prepared into a maximally entangled configuration, preserve its entanglement even when applied an arbitrary number of times. In Ref. [22] a similar analysis was conducted for the case of dynamical semigroups, and in Ref. [23] a scheme was proposed to improve the entanglement survival via environment resetting.

In Ref. [18] reciprocal pairs of quantum channels were introduced as completely positive transformations which admit a rigid, distance-preserving, yet not completely-positive transformation that allows to reproduce the outcome of one from the corresponding outcome of the other, see Fig. 1. From a classical perspective these transmission lines should exhibit the same communication efficiency, interestingly enough however, it turns out that this is no longer the case in the quantum setting.

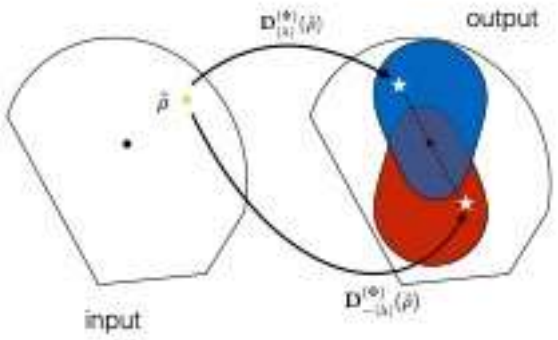

Figure 1. Graphical representation of output throughput of a quantum channel (blue region) of its reciprocal counterpart (red region) obtained by rigidly inverting the former (figure taken from [18]).

In Refs [7,15] we presented a new decoding protocol to realize transmission of classical information through a quantum channel at asymptotically maximum capacity, achieving the Holevo bound and thus the optimal communication rate. At variance with previous proposals, our scheme recovers the message bit by bit, making use of a series "yes-no" measurements, organized in bisection fashion, thus determining which codeword was sent in log(N) steps, N being the number of codewords. In Refs. [9,13,16] several schemes for the detection of low-intensity optical coherent signals ware studied which use probabilistic amplifier operated in the non-heralded version, improved applications of Hadamard receivers, and adaptive receivers. In Ref. [25] a dynamical model for Positive-Operator Valued Measures was presented. In Ref. [30] a perturbative to continuous-time quantum error correction was presented.

The distribution of entangled quantum systems among two or more nodes of a network is a key task at the basis of quantum communication, quantum computation and quantum cryptography. Unfortunately, the transmission lines used in this procedure can introduce so much perturbations and noise in the transmitted signal that prevent the possibility of restoring quantum correlations in the received messages either by means of encoding optimization or by exploiting local operations and classical communication. In Ref. [11] we presented a procedure which allows one to improve the performance of some of these channels. The mechanism underpinning this result is a protocol which we dub cut-and-paste, as it consists in extracting and reshuffling the sub-components of these communication lines, which finally succeed in "correcting each other". The proof of this counterintuitive phenomenon has a direct application in the realization of quantum information networks based on imperfect and highly noisy communication lines. In Ref. [17] instead we reported a bulk optics experiment demonstrating the possibility of restoring the entanglement distribution through noisy quantum channels by inserting a suitable unitary operation (filter) in the middle of the transmission process, see Fig. 2 below. We focus on two relevant classes of single-qubit channels consisting in repeated applications of rotated phase damping or rotated amplitude damping maps, both modeling the combined Hamiltonian and dissipative dynamics of the polarization state of single photons. Our results show that interposing a unitary filter between two noisy channels can significantly improve entanglement transmission.

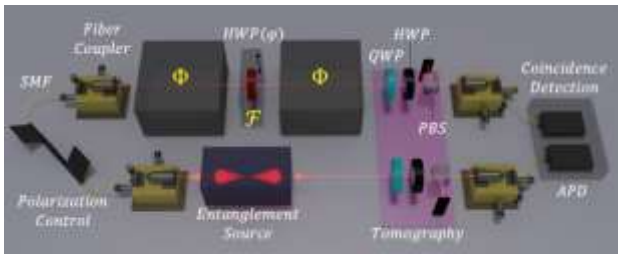

Figure 2. Scheme of the experimental setting used in Ref. [17]. The model uses a source of polarization entangled qubits which undergoes to noisy evolutions (grey boxes) and filtering operations (the F element of the figure). Figure taken from [17].

In Ref. [21] we considered the problem of correctly classifying a given quantum two-level system (qubit) which is known to be in one of two equally probable quantum states. We assumed that this task should be performed by a quantum machine which does not have at its disposal a complete classical description of the two template states, but can only have partial prior information about their level of purity and mutual overlap. Moreover, similarly to the classical supervised learning paradigm, we assumed that the machine can be trained by n qubits prepared in the first template state and by n more qubits prepared in the second template state. In this situation we were interested in the optimal process which correctly classifies the input qubit with the largest probability allowed by quantum mechanics. The problem was studied in its full generality for a number of different prior information scenarios and for an arbitrary size n of the training data. Finite size corrections around the asymptotic limit $n\to\infty$ were also derived. In Ref. [28] instead we derived the optimal performance of quantum state overlap estimation, a task which essential for at the decoding stage of any communication line.

In Ref. [24] the impossibility of undoing a mixing process was analyzed in the context of quantum information theory. The optimal machine to undo the mixing process was studied in the case of pure states, focusing on qubit systems. For simple but non-trivial cases we computed the analytical solution, comparing the performance of the optimal machine with other protocols. As a spin-off of this analysis in Ref. [29] we provided optimal bounds for the quantum capacity of the depolarizing channel.

In Ref. [27] we exploited an improved version of the Lieb-Robinson bound derived in [26], to estimate the quantum capacity of information transmission on spin-network communication lines.

In Refs. [31,32] quantum cascade networks where analyzed in which quantum systems are connected through unidirectional channels that can mutually interact giving rise to interference effects. In particular we showed how to compute master equations for cascade systems in an arbitrary interferometric configuration by means of a collisional model.

In Ref. [33] we studied the most efficient way to exploit a certain amount of entanglement to perform quantum teleportation protocols implemented using two-mode Gaussian states with a limited degree of entanglement and energy.

In Ref. [34] we showed how to recover complete positivity (and hence positivity) of the Redfield equation via a coarse grain average technique. We derived general bounds for the coarse graining time scale above which the positivity of the Redfield equation is guaranteed.

References

[1] V. Giovannetti, A.S. Holevo, A. Mari, *Theoretical and Mathematical Physics* **182**, 284 (2015).

[2] G. De Palma, A. Mari, S. Lloyd, V. Giovannetti, *Multimode quantum entropy power inequality*, Phys. Rev. A **91**, 032320 (2015).

[3] L. Lami, V. Giovannetti, *Entanglement–breaking indices*, J. of Math. Phys. **56**, 092201 (2015).

[4] J. Jin, V. Giovannetti, R. Fazio, *All-optical non-Markovian stroboscopic quantum simulator*, Phys. Rev. A **91**, 012122 (2015).

[5] G. De Palma, A. Mari, V. Giovannetti, A.S. Holevo, *Normal form decomposition for Gaussian-to-Gaussian superoperators*, J. Math. Phys. **56**, 052202 (2015).

[6] L. Lami, V. Giovannetti, *Entanglement-saving channels*, J. of Math. Phys. **57**, 032201 (2016).

[7] M. Rosati, V. Giovannetti, *Achieving the Holevo bound via a bisection decoding protocol*, J. Math. Phys. **57**, 062204 (2016).

[8] G. De Palma, D. Trevisan, V. Giovannetti, *Passive states optimize the output of bosonic Gaussian quantum channels*, IEEE Trans. Inf. Th. **62 (5)**, 2895 (2016).

[9] M. Rosati, A. Mari, V. Giovannetti, *Coherent-state discriminationvia nonheralded probabilistic amplification*, Phys. Rev. A **93**, 062315 (2016).

[10] G. De Palma, A. Mari, S. Lloyd, V. Giovannetti, *Passive states as optimal inputs for single-jump lossy quantum channels*, Phys. Rev. A **93**, 062328 (2016).

[11] A. Cuevas, A. Mari, A. De Pasquale, A. Orieux, M. Massaro, F. Sciarrino, P. Mataloni, V. Giovannetti, *Cut-and-paste restoration of entanglement transmission*, Phys. Rev. A **96**, 012314 (2017).

[12] G. De Palma, D. Trevisan, V. Giovannetti, *Gaussian States Minimize the Output Entropy of the One-Mode Quantum Attenuator*, IEEE Transactions on Information Theory **63 (1)**, 728 (2017).

[13] M. Rosati, A. Mari, V. Giovannetti, *Multiphase Hadamard receivers for classical communication on lossy bosonic channels*, Phys. Rev. A **94**, 062325 (2016).

[14] G. De Palma, D. Trevisan, V. Giovannetti, *The One-Mode Quantum-LimitedGaussian Attenuator and Amplifier have Gaussian Maximizers*, Annales Henri Poincaré **19**, 2919 (2018).

[15] M. Rosati, G. De Palma, A. Mari, V. Giovannetti, *Optimal quantum state discrimination via nested binary measurements*, Phys. Rev. A **95**, 042307 (2017).

[16] M. Rosati, A. Mari, V. Giovannetti, *Capacity of coherent-state adaptive decoders with interferometry and single-mode detectors*, Phys. Rev. A **96**, 012317 (2017).

[17] A. Cuevas, A. De Pasquale, A. Mari, A. Orieux, S. Duranti, M. Massaro, A. Di Carli, E. Roccia, J. Ferraz, F. Sciarrino, P. Mataloni, V. Giovannetti, *Amending entanglement-breaking channels via intermediate unitary operations*, Phys. Rev. A **96**, 022322 (2017).

[18] M. Rosati, V. Giovannetti, *Asymmetric information capacities of reciprocal pairs of quantum channels*, Phys. Rev. A **97**, 052318 (2018).

[19] M. Rosati, A. Mari, V. Giovannetti, *Narrow bounds for the quantum capacity of thermal attenuators*, Nature Communications **9**, 4339 (2018).

[20] G. De Palma, D. Trevisan, V. Giovannetti, L. Ambrosio, *Gaussian optimizers for entropic inequalities in quantum information*, J. of Math. Phys. **59 (8)**, 081101 (2018).

[21] M. Fanizza, A. Mari, V. Giovannetti, *Optimal Universal Learning Machines for Quantum State Discrimination*, IEEE Trans. Inf. Th. **65**, 5931 (2019).

[22] D. Gatto, A. De Pasquale, V. Giovannetti, *Degradation of entanglement in Markovian noise*, Phys. Rev. A **99**, 032307 (2019).

[23] T. Bullock, F. Cosco, M. Haddara, S.H. Raja, O. Kerppo, L. Leppäjärvi, O. Siltanen, N.W. Talarico, A. De Pasquale, V. Giovannetti, S. Maniscalco, *Entanglement protection via periodic environment resetting in continuous-time quantum-dynamical processes*, Phys. Rev. A **98**, 042301 (2018).

[24] F. Kianvash, M. Fanizza, V. Giovannetti, *Optimal quantum subtracting machine*, Phys. Rev. A **99**, 052319 (2019).

[25] A. De Pasquale et al., Phys. Rev. A **100**, 012130 (2019).
[26] S. Chessa, V. Giovannetti, *Time-polynomial Lieb-Robinson bounds for finite-range spin-network models*, Phys. Rev. A **100**, 052309 (2019).
[27] S. Chessa, M. Fanizza, V. Giovannetti, *Quantum-capacity bounds in spin-network communication channels*, Phys. Rev. A **100**, 032311 (2019).
[28] M. Fanizza, M. Rosati, M. Skotiniotis, J. Calsamiglia, V. Giovannetti, *Beyond the Swap Test: Optimal Estimation of Quantum State Overlap*, Phys. Rev. Lett. **124**, 060503 (2020).
[29] M. Fanizza, F. Kianvash, V. Giovannetti, *Quantum Flags and New Bounds on the Quantum Capacity of the Depolarizing Channel*, Phys. Rev. Lett. **125**, 020503 (2020).
[30] M. Ippoliti, L. Mazza, M. Rizzi, V. Giovannetti, *Perturbative approach to continuous-time quantum error correction*, Phys. Rev. A **91**, 042322 (2015).
[31] S. Cusumano, A. Mari, V. Giovannetti, *Interferometric quantum cascade systems*, Phys. Rev. A **95**, 053838 (2017).
[32] S. Cusumano, A. Mari, V. Giovannetti, *Interferometric modulation of quantum cascade interactions*, Phys. Rev. A **97**, 053811 (2018).
[33] P. Liuzzo-Scorpo, A. Mari, V. Giovannetti, G. Adesso*, Optimal Continuous Variable Quantum Teleportation with Limited Resources*, Phys. Rev. Lett. **119**, 120503 (2017).
[34] D. Farina, V. Giovannetti, *Open-quantum-system dynamics: Recovering positivity of the Redfield equation via the partial secular approximation*, Phys. Rev. A **100**, 012107 (2019).

1.4 Publications 2014-2020

The productivity of NEST scientists is significant and the sheer numbers that can be seen in the following histogram show that over 200 publications appear yearly in the scientific literature with NEST affiliation. We wish to underline that **all** these publications are in international peer-reviewed journals.

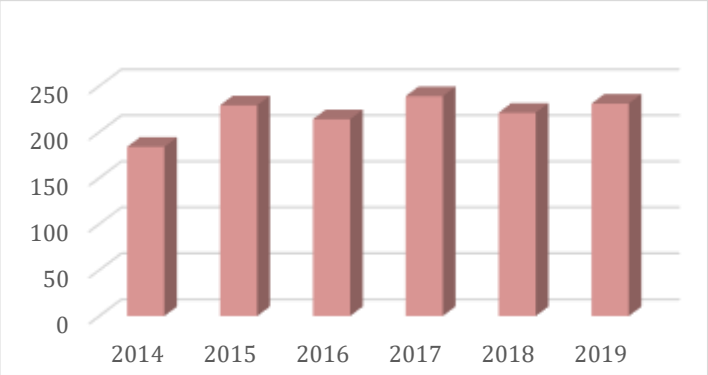

Number of publications with NEST affiliation
(Web of Science, September 2020)

In terms of visibility and impact of these articles it may be instructive to examine the number of yearly citations of NEST publications that are now approaching ten thousand per year. We must stress that these numbers represent an underestimate of the actual numbers owing to a rather large variety of abbreviations used by different publishers, but do indicate a good visibility with a constant growth that comforts us on the continued good quality of the scientific research carried out at NEST.

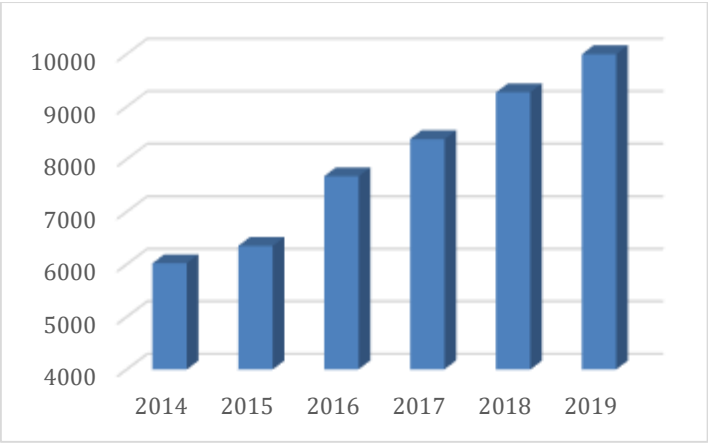

Number of citations of papers with NEST affiliation
(Web of Science, September 2020)

It is probably apparent from the material provided so far, but it is still of interest to analyze the diversity of areas in which NEST scientists are active as a means to

verify the degree of multidisciplinarity of the Laboratory. The following chart was generated by Web of Science analyzing the publications with NEST affiliation.

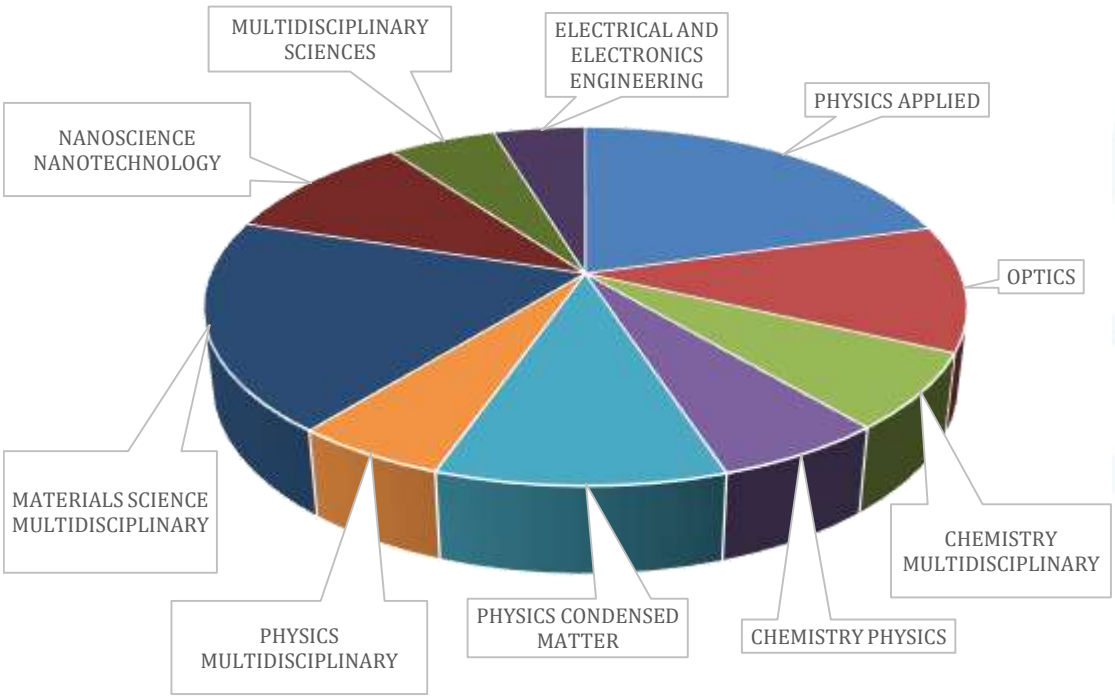

Subject areas of publications with NEST affiliation in the period 2014-2019.
(Web of Science, September 2020)

NEST has a large number of international collaborations. By analyzing the affiliations present in the publications of the period we can readily have an idea of how widespread this international network is:

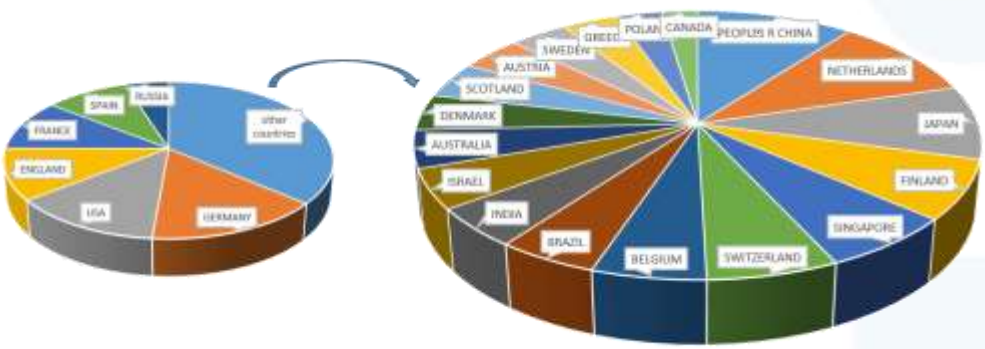

Nationalities and frequency of the co-authors in NEST publications
(Web of Science, September 2020)

1.5 Technology transfer 2014-2020

As already mentioned in Sec. 1.1, the establishment of the *Centro di Competenza Regionale sulle Nanotecnologie* at Laboratorio NEST was the starting point for an increasing effort to transfer the unique expertise, materials, and protocols developed at NEST to industrial enterprises in order to favor innovation. With the Centro di Competenza funding we were able to upgrade our clean room facility from class ISO7 to class ISO6, and to install state-of-the-art facilities for nanolithography and morphological characterization at the nanoscale. This created at NEST a favorable environment for a larger attention to the industrial potential of the research results produced and is leading to the establishment of the first spin-offs of the Laboratory.

In this section, we also mention an additional regional initiative that strengthened the Laboratory, the FELIX project (approved under the scientific responsibility of NEST director). This project led to the acquisition of funding for an additional upgrade of the scientific instrumentation available in the clean-room (high-resolution optical microscopy, a laser-writer optical-lithography system, a new cell for the CBE system), with the objective of making it even more accessible to the industrial enterprises of the area, in particular in the field of integrated electronics and photonics devices.

Finally, more recently (in 2019), NEST was also directly involved as innovation and demonstration node (IDN) of the *Centro di Competenza Nazionale su I4.0,* named ARTES4.0, a competence center dedicated to innovation and technology transfer in the field of Industry 4.0. In particular, the IDN NEST is directly involved in additive manufacturing, sensors and new materials for industry. This project funded in NEST a first set of new scientific facilities like a portable Raman system, a nanoparticle counter for Clean Room, a special microscope and an oven for

temperature, humidity and UV tests for characterization of additive manufactured objects. This makes NEST a reference and collaborating center for all the affiliated firms and those related to the national ARTES4.0 network.

In the period of reference NEST carried out a significant number of industrial collaborative projects with medium, small and large companies such as Microsoft Corp., Chiesi Pharmaceuticals, Exosomics, RiCO, COOPs, Bedimensional, Microtest, Maxim, SITAEL, Palladio, Carrara Marble Way, Salvatori, Cromology, Microport, Coswell, etc. in rather diverse areas such as

Characterization, fabrication and analysis at the nanoscale;
Agriculture;
Marble and stones;
Automotive;
Electronics;
Semiconductors;
Aerospace;
New and Functional Materials;
Photonics;
Leather production;
Cosmetics;
Nanomedicine and Pharmacology.

The industrial contracts are not only important for the revenues they generated in the period of reference and for the dedicated funding for research fellows (a dozen in the period considered in this report), but are a testimony to the significant competence accumulated by NEST scientists and to the quality of the technological platforms available.
As will be discussed in part 2 of this document, these are the assets on which the vision for the next five years of activity is based.

One additional element that must be cited in this section is the number of patents filed in this period. Consistently with the spirit of the NEST initiative, the partner institutions patent together deciding the distribution of ownership on case by case basis. The following table illustrates the patents active in the period of reference and the percentage of property of SNS

Laboratorio NEST active patents

Patent title	Patent authors	SNS %
THz semiconductor laser incorporating a controlled plasmon confinement waveguide	A. Tredicucci, F. Beltram, H. E. Beere, A.G. Davies, R. Koehler, E.H.Linfield	100
Metodo e dispositivo per misure di posizione e di massa	F. Beltram, G. Biasiol, V. Piazza, P. Pingue, L. Sorba, E. Strambini	100

Multiphoton photoreleasing system, based on click-chemistry functionalized gold nanoparticles, for biological applications	F. Beltram, S. Luin, V. Voliani, F. Ricci, G. Signore, R. Nifosì	27
Laser Thz a cascata quantica con risonatore micro-disco ed emissione verticale mediante una griglia di secondo-ordine	L. Mahler, A. Tredicucci, F. Beltram	100
Automatic passive control of liquid positioning in microfluidic chips	V. Piazza, F. Beltram, M. Travagliati, M. Cecchini, G. De Simoni	20
Method for the fabrication of dispersible three-dimensional nanoresonators for biological, medical and environmental applications	A. Bifone, A. Boni, V. Clericò, F. Recchia, A. Tredicucci, P. Pingue	10
Biosensore grafenico per l'analisi di esosomi in fluidi biologici, suoi procedimenti di preparazione e relativi usi	V. Voliani, C Coletti, G Signore, V Piazza, S Luin, F Beltram	30
Rivelatore di plasmoni completamente elettrico	R. Krahne, V. Pellegrini, I. Torre, M. Polini, A. Tomadin	20
Lab-on-chip basato su onde acustiche di superficie di Rayleigh (R-SAW) per analisi molecolari/oncologiche point-of-care	M. Cecchini, M. Agostini	50
Soluzione di contrasto per la caratterizzazione di campioni biologici tramite microscopia elettronica e correlativa	V. Cappello, G. Signore, S. Di Pietro, M. Santi, M. Gemmi, A. Moscardini	30

1.6 Funding

NEST scientists have a consistently good record in acquiring funds from all funding agencies thanks to a combination of their vision, excellent track record, and access to a very competitive technological platform made available to them by the synergistic effort of the participating institutions.
This latter aspect must not be underestimated. It would be impossible to present credible research proposal at any level without the availability of the necessary equipment, laboratory space and graduate student support that SNS, CNR, IIT, and SSSUP share at NEST.

In Sec. 1.1 we already mentioned that in the reference period NEST scientists managed research projects externally funded for a total exceeding **€ 34 million**. This figure must be compared to the total funding from SNS for NEST operation, about 1 million euros. If we limit the comparison to funds that were directly transferred by different agencies to SNS alone, we have **€ 10,5 million**, that is **over ten times what assigned by SNS** to NEST. Indeed, if we consider the overhead policy of Scuola Normale, this funding for NEST operation is about fully compensated.

Importantly, these figures do not include industrial collaborative contracts. This period has witnessed a very significant growth in the number and economic value of these contract (*conto terzi*). This was discussed in the previous section and we can estimate that NEST, overall, acquired over a million euro in this period. We shall further comment on this in part 2 of this document where collaboration with industrial enterprises will be much emphasized for the next 5-year period of the Laboratory.

The overall spending for these activities, of course, should include a number of other expenses such as building maintenance, salaries of the permanent staff, various utilities such as electric or heating. These are sizable figures.
Also, the other partners make available significant sums for NEST life. The fast growth of CNR staff, for example, has brought the CNR salaries for permanent staff to about 2,5 million euros yearly. Proponents regard this as one of the most important elements of success of the NEST initiative: Scuola Normale manages to drive a rather large operation with few people and limited running expenses thanks to the coordinated effort with CNR, IIT and SSSUP. This brings NEST to the size required for a degree of international visibility and credibility that ultimately leads to the creation of a highly-competitive team capable of supporting both training of undergraduate and graduate students, and research activity in line with the most competitive international standards.

1.7 Undergraduate and graduate training @ NEST

We list here graduate and undergraduate students that carried out their thesis work totally or partially at NEST under the supervision of NEST staff each year in the period of reference.

2014

PhD students

Matteo Agostini
Ilirjan Aliaj
Simone Barbarino
Filippo Begarani
Vezio Bianchi
Alberto Biella
Fulvio Bonsignore
Domenico Cassano
Tommaso Cavallucci
Domenica Convertino
Subhra Kanti De
Giacomo De Palma
Giuseppe De Vito
Ambra Del Grosso
Carmine Di Rienzo
Alessandro Farace
Gianmarco Ferri
Antonio Fornieri
Gianmarco Galbusera
Francesco Gobbo
Umesh Prasad Gomes
Stefano Guiducci
Nicholas Hemsworth
Aliaj Ilirjan
Abhishek Kumar
Sara Macchi
Subrata Mal
Cecilia Masciullo
Francesco Mazza
Sandro Meucci
Domenico Montemurro
Antonella Negro
Paola Parlanti
Davide Pellegrini
Liberato Pizza
David Porciani
Enrico Pracucci
Ahmed Ismail Ridoy
Caterina Rizzi
Lorenzo Romeo
Matteo Rosati
Antonio Rossi
Melissa Santi
Thomas Satzoukidis
Iacopo Torre
Marco Travagliati
Francesco Trovato
Andrea Ursic
Stefano Valentini
Raghunath Venkatramanan
Azzurra Volpi

Undergraduate students

Rosy Amodeo
Luca Matteo Barbieri
Vezio Bianchi
Simone Biasco
Leo Bourdet
Niccolò Calcini
Domenico Cassano
Tommaso Cavallucci
Francesco Colangelo
Sergio Lucio Debonis
Pierluigi Di Matteo
Emanuele Fiorino
Giuseppe Fiume
Leonardo Forcieri
Andrea Giuntoli
Gina Greco
Stefano Guiducci
Carlo Maria Lazzarini
Andrea Ottomaniello
Luca Pesce
Luigi Petrucco
Alessandro Ranalli
Giulio Romagnoli
Lorenzo Scipioni
Camilla Tossi
Shukla Vinay

Visiting students

Vahid Ameri Seyahooei
Léo Bourdet
F I De Rezende Aguiar
Philipp Rebmann

Mohammad Eghbali
Nicolò Forcellini
Imma Six
Guanqun Zhang

2015

PhD students

Matteo Agostini
Ilirjan Aliaj
Rosy Amodeo
Simone Barbarino
Filippo Begarani
Vezio Bianchi
Simone Biasco
Alberto Biella
Fulvio Bonsignore
Domenico Cassano
Tommaso Cavallucci
Roberta Cecchi
Alessandra Cecchini
Francesco Colangelo
Domenica Convertino
Olga Cozzolino
Stefano Cusumano
Subhra Kanti De
Giacomo De Palma
Giuseppe De Vito
Ambra Del Grosso
Carmine Di Rienzo
Abhishek Dubey
William Durso
Gianmarco Ferri
Antonio Fornieri
Gianmarco Galbusera
Marianna Galliani
Francesco Gobbo
Umesh Prasad Gomes
Gina Greco
Stefano Guiducci
Nicholas Hemsworth
Veronica Iacovacci
Sergio Iacopino
Aliaj Ilirjan
Maximillian Keck
Abhishek Kumar
Sara Macchi
Subrata Mal
Cecilia Masciullo
Francesco Mazza
Antonella Negro
Paola Parlanti
Davide Pellegrini
Sara Peruzzi
Vinoshene Pillai
Enrico Pracucci
Ahmed Ismail Ridoy
Lorenzo Romeo
Matteo Rosati
Antonio Rossi
Alice Rita Salgarella
Melissa Santi
Thomas Satzoukidis
Marco Terrigno
Giuliano Francesco Timossi
Iacopo Torre
Francesco Trovato
Davide Vaccaro
Stefano Valentini
Lorenzo Vannozzi
Raghunath Venkatramanan
Azzurra Volpi

Undergraduate students

Marco Albanesi
Lucia Angella
Simone Biasco
Mattia Cataldi
Francesco Colangelo
Giammarco Collemi
Enrico Dardanis
Pierluigi Di Matteo
Giuseppe Fiume
Leonardo Forcieri
Katia Garrasi
Gina Greco
Lennart Bours
Mario Miscuglio
Laura Mosti
Edoardo Mucchetti
Andrea Ottomaniello
Luigi Petrucco
Giulio Romagnoli
Michele Sanguanini
Raffaele Sarnataro
Francesca Fabiana Settembrini
Shukla Vinay
Francesco Vischi

Visiting students

Divya Balakrishnan
Lennart Bours
Ben Van Duppen
F I De Rezende Aguiar
Martin Meisner
Alina Mrenca
Luca Planat

2016

PhD students

Gerardo Abbandonato
Matteo Agostini
Ilirjan Aliaj
Rosy Amodeo
Federica Anastasi
Gian Marcello Andolina
Omer Arif
Filippo Begarani
Giulio Benetti
Bibek Bhandari
Vezio Bianchi
Simone Biasco
Alberto Biella
Gianmichele Blasi
Fulvio Bonsignore
Lennart Bours
Domenico Cassano
Tommaso Cavallucci
Roberta Cecchi
Francesco Colangelo
Domenica Convertino
Olga Cozzolino
Stefano Cusumano
Enrico Dardanis
Subhra Kanti De
Giacomo De Palma
Giuseppe De Vito
Ambra Del Grosso
Carmine Di Rienzo
Abhishek Dubey
William Durso
Paolo Andrea Erdman
Donato Farina
Gianmarco Ferri
Antonio Fornieri
Gianmarco Galbusera
Marianna Galliani
Francesco Gobbo
Umesh Prasad Gomes
Gina Greco
Stefano Guiducci
Nicholas Hemsworth
Sergio Iacopino
Aliaj Ilirjan
Maximillian Keck
Abhishek Kumar
Didi Angela Maria Lamers
Sara Macchi
Subrata Mal
Ana Katrina Mapanao
Giampiero Marchegiani
Cecilia Masciullo
Antonella Negro
Pietro Novelli
Paola Parlanti
Davide Pellegrini
Sara Peruzzi
Vinoshene Pillai
Louis Ponet
Enrico Pracucci
Matteo Rosati
Antonio Rossi
Alice Rita Salgarella
Melissa Santi
Vinay Shukla
Andrea Tagliani
Paolo Maria Tentori
Giuliano Francesco Timossi
Iacopo Torre
Francesco Trovato
Davide Vaccaro
Stefano Valentini
Verdiana Valvano
Lorenzo Vannozzi
Francesca Vannucchi
Raghunath Venkatramanan
Azzurra Volpi

Undergraduate students

Marco Albanesi
Lucia Angella
Luca Basta
Lennart Bours
Alessandro Mancari
Ivanie Mendes

Cristina Belllotti
Mattia Cataldi
Giammarco Collemi
Rosa D'Apice
Enrico Dardanis
Stefania Della Vecchia
Alessandra Della Vecchia
Pierluigi Di Matteo
Giorgio Domenichini
Ofelia Durante
Sara Fiori
Giuseppe Fiume
Leonardo Forcieri
Katia Garrasi
Fedor Getman
Laura Mosti
Sara Natalini
Andrea Ottomaniello
Giulia Panattoni
Elisa Petri
Luigi Petrucco
Alessio Ricci
Damiano Sallemi
Michele Sanguanini
Chiara Schirripa Spagnolo
Francesca Fabiana Settembrini
Teresa Tommasini
Yuri Venturini
Francesco Vischi

Visiting students

Lennart Bours
F I De Rezende Aguiar
Jaako Ilmari Mastomaki
Martin Meisner
Ivanie Mendes
Alina Mrenca
Patricia Pedraz
Sudipto Roy Singha
Klaudia Szatko
Ben Van Duppen

2017

PhD students

Gerardo Abbandonato
Alina Adamow
Matteo Agostini
Ilirjan Aliaj
Rosy Amodeo
Federica Anastasi
Gian Marcello Andolina
Omer Arif
Luca Basta
Filippo Begarani
Giulio Benetti
Bibek Bhandari
Simone Biasco
Gianmichele Blasi
Lennart Bours
Domenico Cassano
Tommaso Cavallucci
Roberta Cecchi
Sara Chiarugi
Sara Colanero
Francesco Colangelo
Domenica Convertino
Olga Cozzolino
Stefano Cusumano
Enrico Dardanis
Ambra Del Grosso
Francesca D'Elia
Daniele De Pasquale
Francesco Gobbo
Gina Greco
Stefano Guiducci
Nicholas Hemsworth
Sergio Iacopino
Maximillian Keck
Farzad Kianvash
Abhishek Kumar
Didi Angela Maria Lamers
Ana Katrina Mapanao
Giampiero Marchegiani
Elisa Martino
Cecilia Masciullo
Giulia Matteoli
Pietro Novelli
Andrea Ottomaniello
Paola Parlanti
Davide Pellegrini
Sara Peruzzi
Vinoshene Pillai
Louis Ponet
Enrico Pracucci
Claudio Puglia
Matteo Rosati
Antonio Rossi
Melissa Santi
Chiara Schirripa Spagnolo
Vinay Shukla

	William Durso	Andrea Tagliani
	Paolo Andrea Erdman	Paolo Maria Tentori
	Marco Fanizza	Giuliano Francesco Timossi
	Donato Farina	Iacopo Torre
	Gianmarco Ferri	Francesco Trovato
	Fabrizia Fontana	Lorenzo Vannozzi
	Antonio Fornieri	Francesca Vannucchi
	Gianmarco Galbusera	Isha Verma
	Marianna Galliani	Francesco Vischi
Undergraduate students	Alice Bettelli	Gabriele Nardi
	Vittorio Buccheri	Thea Papa
	Giovanna Capraro	Elisa Petri
	Rosa D'Apice	Giulia Piccinini
	Nicoletta Di Giorgi	Luca Piccinini
	Giorgio Domenichini	Dominic Prete
	Ofelia Durante	Claudio Puglia
	Leonardo Filareti	Aurora Russo
	Sara Fiori	Luca Salemi
	Gaia Germanese	Damiano Sallemi
	Fedor Getman	Eleonora Savi
	Andrea Iorio	Chiara Schirripa Spagnolo
	Giuseppe Lanza	Stefano Servino
	Veronica Leccese	Teresa Tommasini
	Roberta Mezzena	Yuri Venturini
	Andrea Morandi	
Visiting students	Manon Bischoff	Klaudia Szatko
	Luca Croin	Ben Van Duppen
	Zoe Dubois	Julian Wennmacher
	Ludovico Lami	Yu Yang
	Gwenael Le Gal	

2018

PhD students	Alina Adamow	Andrea Griesi
	Rosy Amodeo	Sergio Iacopino
	Federica Anastasi	Andrea Iorio
	Gian Marcello Andolina	Maximillian Keck
	Omer Arif	Vladislav Olegovich Khaustov
	Mahdi Asgari	Farzad Kianvash
	Luca Basta	Abhishek Kumar
	Filippo Begarani	Didi Angela Maria Lamers
	Simone Biasco	Ana Katrina Mapanao
	Gianmichele Blasi	Giampiero Marchegiani
	Lennart Bours	Elisa Martino
	Fabrizio Campanale	Cecilia Masciullo
	Domenico Cassano	Giulia Matteoli
	Tommaso Cavallucci	Nicola Melchioni
	Roberta Cecchi	Roberta Mezzena
	Ilaria Cesini	Gabriele Nardi
	Stefano Chessa	Andrea Ottomaniello

	Sara Chiarugi	Paola Parlanti
	Gaia Ciampalini	Davide Pellegrini
	Francesco Colangelo	Giulia Piccinini
	Domenica Convertino	Vinoshene Pillai
	Olga Cozzolino	Francesco Pisani
	Stefano Cusumano	Enrico Pracucci
	Laura Dalle Carbonare	Domenic Prete
	Ambra Del Grosso	Claudio Puglia
	Francesca D'Elia	Antonio Rossi
	Daniele De Pasquale	Melissa Santi
	William Durso	Chiara Schirripa Spagnolo
	Marco Fanizza	Vinay Shukla
	Gianmarco Ferri	Andrea Tagliani
	Fabrizia Fontana	Paolo Maria Tentori
	Gianmarco Galbusera	Giuliano Francesco Timossi
	Marianna Galliani	Silvia Travesari
	Francesco Garzella	Francesco Trovato
	Davide Giambastiani	Ayush Tyagi
	Giulia Giannone	Francesca Vannucchi
	Francesco Gobbo	Isha Verma
	Gina Greco	Francesco Vischi
Undergraduate students	Francesco Amato	Veronica Leccese
	Veronica Beatini	Giulia Lo Gerfo
	Vittorio Buccheri	Roberta Mezzena
	Giovanna Capraro	Andrea Morandi
	Lorenzo Ceccarelli	Maria Murace
	Simone Civita	Gabriele Nardi
	Gloria Conte	Emanuele Paoli
	Teresa Crisci	Thea Papa
	Federica Cruciani	Gabriele Parlanti
	Lorenzo De Marinis	Giulia Piccinini
	Alessia De Masi	Grazia Raciti
	Enrico De Paris	Aurora Russo
	Nicoletta Di Giorgi	Stefano Servino
	Sara Donato	Teresa Tommasini
	Francesco Garzella	Francesco Torre
	Gaia Germanese	Chiara Tremolanti
	Andrea Iorio	Maria Laura Vieri
	Giuseppe Lanza	Venera Zarbo
Visiting students	Marion Bonhomme	Oshrat Miller
	Dongni Chen	Konstantin Schneider
	Alexander Holm Kiilerich	Yu Yang
	Simon Joehr	Rong Zhang

2019

PhD students	Alina Adamow	Gina Greco
	Rosy Amodeo	Andrea Griesi
	Federica Anastasi	Sergio Iacopino

Gian Marcello Andolina
Omer Arif
Mahdi Asgari
Luca Basta
Federico Belliardo
Mario Bernardi
Federico Betti
Simone Biasco
Gianmichele Blasi
Lennart Bours
Fabrizio Campanale
Annalisa Carretta
Roberta Cecchi
Ilaria Cesini
Stefano Chessa
Sara Chiarugi
Gaia Ciampalini
M F Colombano Sosa
Elena Corradi
Olga Cozzolino
Laura Dalle Carbonare
Francesca D'Elia
William Durso
Naeimeh Eghbali Fam
Marco Fanizza
Fabrizia Fontana
Marianna Galliani
Francesco Garzella
Davide Giambastiani
Giulia Giannone
Andrea Iorio
Maximillian Keck
Vladislav Olegovich Khaustov
Farzad Kianvash
Didi Angela Maria Lamers
Ana Katrina Mapanao
Giampiero Marchegiani
Francesco Margheriti
Marco Martinelli
Elisa Martino
Giulia Matteoli
Nicola Melchioni
Roberta Mezzena
Gabriele Nardi
Andrea Ottomaniello
Giulia Piccinini
Luca Piccinini
Vinoshene Pillai
Francesco Pisani
Domenic Prete
Claudio Puglia
Chiara Schirripa Spagnolo
Andrea Tagliani
Paolo Maria Tentori
Giuliano Francesco Timossi
Ayush Tyagi
Francesca Vannucchi
Isha Verma
Francesco Vischi
Agata Zamborlin

Undergraduate students

Annachiara Albanese
Francesco Amato
Veronica Beatini
Luca Buoni
Giulio Cappelli
Giovanna Capraro
Michele Cardelli
Annalisa Carretta
Lorenzo Ceccarelli
Valentina Chiappa
Simone Civita
Gloria Conte
Monica Coraggioso
Federica Cruciani
Lorenzo De Marinis
Alessia De Masi
Enrico De Paris
Davide Degli Esposti
Fabio Dispinzeri
Sara Donato
Letizia Ferbel
Lorenzo Lavista
Giulia Lo Gerfo
Francesco Lunardelli
Chiara Massetti
Jacopo Menconi
Maria Murace
Elisa Ottalagana
Luca Palumbi
Emanuele Paoli
Gabriele Parlanti
Alessandro Porcelli
Grazia Raciti
Salvatore Ragusa
Marco Santucci
Luca Scaccini
Daniele Sonaglioni
Teresa Tommasini
Francesco Torre
Giacomo Venturi
Maria Laura Vieri
Boyu Wang
Lixuan Wei
Venera Zarbo

Visiting students

Johannes Dieplinger
Sayandip Ghosh
Konstantin Schneider
Harald Schmid
Yu Yang
Indra Yudhistira


Laboratorio
National Enterprise for nanoScience and nanoTechnology
NEST